Polyelectrolytes near Solid Surfaces

Thesis by
Christopher Balzer

In Partial Fulfillment of the Requirements for the
Degree of
Doctor of Philosophy in Chemical Engineering

CALIFORNIA INSTITUTE OF TECHNOLOGY
Pasadena, California

2023
Defended April 7, 2023

Christopher Balzer
ORCID: 0000-0002-9767-8437

ACKNOWLEDGEMENTS

I am privileged to have friends, family, colleagues, and mentors that have supported and guided my academic journey. I am beyond grateful for all of these people as they have fostered stimulating conversations, provided healthy distractions, and created lifelong memories for me. I am especially thankful to Dr. Mitchell Armstrong, Dr. Bin Mu, the Winston Churchill Foundation, Prof. Zhen-Gang Wang, and the Department of Energy Computational Science Fellowship program for taking a chance on me and giving me the opportunity to grow beyond what I thought myself capable.

I impart my deepest appreciation to Prof. Zhen-Gang Wang. His guidance, motivation, patience, and enthusiasm for research emboldened my research and helped me persevere during the various stages of my PhD. Besides my advisor, I would like to thank my thesis committee: Prof. John Brady, Prof. Kim See, and Dr. Amalie Frischknecht, for their encouragement and guidance during my time at Caltech. I give a special thanks to Amalie for hosting and advising me at Sandia National Laboratories for a summer; I thoroughly enjoyed our discussions and the opportunity to work outside of my usual area.

I would also like to thank all of the members of the Wang group. In particular, Dr. Yasemin Basdogan and Dr. Sriteja Mantha have been a constant source of joy for me and always manage to brighten my day. Over the years, my office mates, Dr. Chang Yun Son, Dr. Huikuan Chao, Dr. Leying Qing, Dr. Yasemin Basdogan, and Dr. Shensheng Chen, have always been willing to discuss research and the journey of life with me. I have learned more from them than they know. Outside of the Wang group, I am thankful for Dr. Andy Ylitalo, Dr. Camilla Kjeldbjerg, Dr. Austin Dulaney, Dr. Hyeongjoo Row, and Dr. Zhiwei Peng, for their friendship, support, and mentorship.

Above all else, I thank my father and late mother, who always provided me with the support and space to develop and pursue my wide interests.

ABSTRACT

Polyelectrolytes are ubiquitous in nature and in the products we use daily. The combination of their connectivity and charge lead to many useful properties in solution and near surfaces. Electrostatic forces dominate much of the behavior of charged species near solid surfaces; however, nonelectrostatic forces arising ion specific interactions or from varying polymer chemistry play an important role in tuning electrolyte and polyelectrolyte properties. The balance of these forces depends on factors like the salt concentration, solution pH, and properties of the surface. The current work outlines the thermodynamics of charged systems and investigates the structure and phase behavior of polyelectrolytes near solid surfaces. In particular, the work covers the thermodynamic aspects of preferential adsorption of small ions in electric double layers, polyelectrolyte adsorption, polymer-mediated interactions of surfaces using strong and weak electrolytes, surface phase transitions and contact angles of complex coacervates on solid surfaces, complexation-induced conformational phase transitions of polyelectrolyte brushes, and electro-swelling of weak polyelectrolyte brushes. The wide variety of problems addressed here reflects the variety of applications of polyelectrolytes and contexts in which polyelectrolytes appear.

PUBLISHED CONTENT AND CONTRIBUTIONS

(1) Balzer, C.; Zhang, P.; Wang, Z.-G. *Soft Matter* **2022**, *18*, 6326–6339, DOI: 10.1039/D2SM00859A.

(2) Bruch, D.; Balzer, C.; Wang, Z.-G. *The Journal of Chemical Physics* **2022**, *156*, 174704, DOI: 10.1063/5.0089260.

(3) Balzer, C.; Jiang, J.; Marson, R. L.; Ginzburg, V. V.; Wang, Z.-G. *Langmuir* **2021**, *37*, 5483–5493, DOI: 10.1021/acs.langmuir.1c00139.

(4) Balzer, C.; Qing, L.; Wang, Z.-G. *ACS Sustainable Chemistry & Engineering* **2021**, *9*, 9230–9239, DOI: 10.1021/acssuschemeng.1c01326.

In each of the above, C.B. participated in the conception of the project, conducted calculations, analyzed data, and participated in the writing of the manuscript.

TABLE OF CONTENTS

LIST OF ILLUSTRATIONS

Chapter I

INTRODUCTION

This introductory chapter gives an overview of polyelectrolytes, their uses, and the challenges associated with understanding their behavior near solid surfaces. The subsequent chapters address the theoretical description of inhomogenous charged systems in a variety of contexts, ranging from the structuring of small ions near a charged surface to surface phase transitions of polyelectrolytes.

This chapter includes content from our previously published article:

Balzer, C.; Jiang, J.; Marson, R. L.; Ginzburg, V. V.; Wang, Z.-G. *Langmuir* **2021**, *37*, 5483–5493, DOI: 10.1021/acs.langmuir.1c00139

Balzer, C.; Zhang, P.; Wang, Z.-G. *Soft Matter* **2022**, *18*, 6326–6339, DOI: 10.1039/D2SM00859A

I.1 Polyelectrolytes

Foundation

Polyelectrolytes are polymers with ionizable groups. When immersed in a solvent (usually water), the ionizable groups dissociate their counterions and impart positive or negative charge on the polymer. The most popular synthetic polyelectrolytes are poly(acrylic acid) (PAA) and poly(styrene sulfonate) (PSS). Naturally occurring biopolymer examples include alginate, pectin, and chitosan [3, 4]. Common proteins typically contain a collection of positive and negative ionizable groups based on the charge of amino acid residues, such as glutamic acid, arginine, aspartic acid, or lysine [5].

The presence of charge on a polymer leads to diverse structural and thermodynamic properties. Interactions between charges are long-ranged. Like-charges along the chain repel one another, yet the polymer connectivity prevents charges from separating. Compared to their neutral counterparts, polyelectrolytes take on a more extended conformation due to this internal repulsion, looking more like a rigid rod or so-called *cigar* rather than a random coil [6] (Figure I.1). In addition to intrachain interactions, the polymer interacts with other chains and small ions in solution, leading to polyelectrolyte conformations that depend on the local charge environment from other chains and solution, the sequence of ionizable groups, and the strength of the charge–charge interaction [7–10]. For example, adding salt, such as sodium chloride, to a polyelectrolyte solution will *screen* the charge–charge interactions, making the polymer conformation appear closer to that of a neutral polymer. Many other properties of polymer systems, such as the viscosity and overlap concentration,

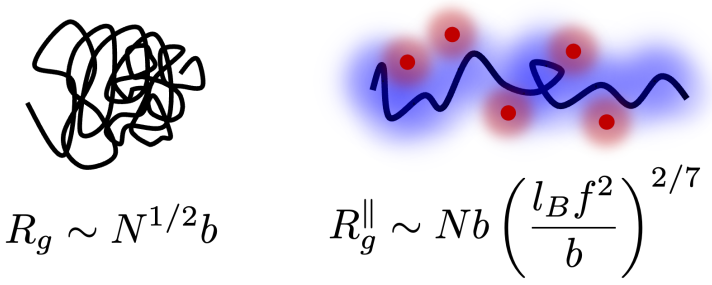

Figure I.1: Schematic of neutral polymer versus polyelectrolyte conformations. The scaling relationships show how the polymer size (radius of gyration) scale with the chain length. In the case of polyelectrolytes, the scaling is linear with the degree of polymerization N, but also depends on the strength of electrostatic interactions (Bjerrum length, l_B) and the fraction of charged monomers f in the backbone.

are derived from the polymer conformation, so the behavior of polyelectrolytes can differ greatly from neutral polymers [11]. Despite the vast conceptual and practical understanding gained since the term “polyelectrolyte“ was coined by Fuoss [12], a deceivingly simple question remains at the heart of polyelectrolyte research: how does the local ionic environment couple to the internal modes of polyelectrolytes?

Uses

Polyelectrolytes are truly ubiquitous materials, both in nature and in the products we use daily. The prevalence in nature and research interest is driven by their innate water solubility, ionic conductivity, strong ionic interactions that give rise to useful and sometimes befuddling solution properties, interaction with ions in solution, and surface activity [13]

Nature creatively and efficiently uses polyelectrolytes. DNA and RNA are polymers that carry a highly negative charge due to their phosphate backbones. Viruses, eukaryotes, and bacteria have all evolved to pack large amounts of DNA, despite the high charge density, into small volumes of the cell [14] in a way that must be accessible and reconfigurable. Cells create compartmentalized regions of cellular material via polyelectrolyte liquid–liquid phase separation to mediate cellular processes [15–17]. Even the disposal of said droplets is mediated by wetting of polyelectrolyte droplets in a elastocapillary-driven autophagy process [18, 19]. Several other compelling examples exist and are reviewed elsewhere [9].

Modern consumer products, emerging energy technologies, and novel biomedical technologies rely on the properties of polyelectrolytes [20–23]. The earliest and most popular application of polyelectrolytes is in colloidal dispersions [24, 25]. Inorganic colloids, such as metal-oxides, are often are used to modify the flow or optical properties of a solution. For example, titanium dioxide is the main white pigment used in paint formulations. These lyophobic colloidal particles tend to aggregate in solution, which degrades material performance. Polyelectrolytes can be added to the formulation to interact with the colloid surface and prevent aggregates from agglomerating (Figure I.2). If the polymer-colloid interaction is specifically tuned, a polyelectrolyte can act as a flocculant or coagulating agent, allowing separation of solid-liquid mixtures [22]. In personal care, shampoo products are complex formulations that rely on cation polyelectrolytes to carry anionic, dirt-finding surfactants to the hair and also lubricate the hair for better manageability [26, 27]. In the human body, the main component of mucous membranes are proteoglycans

(anionic polyelectrolytes), and researchers use the complexation between cationic biopolymers and these anionic polyelectrolytes to increase the efficacy in drug delivery [4]. Suffice to say that polyelectrolytes exist all around us and there are a myriad of ways that they are leveraged for practical uses. Many other applications will be discussed in the subsequent chapters. One can also read more about the historical developments of polyelectrolytes in the fantastic review by Dobrynin [28].

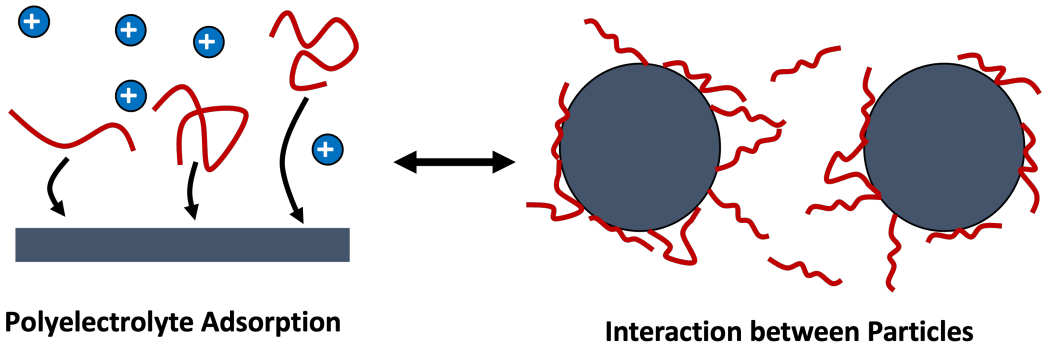

Figure I.2: Schematic showing polyelectrolyte adsorption and polymer-mediated interaction between surfaces. (left) Depiction of polyelectrolyte adsorption. (right) Depiction of two colloidal sized particles with adsorbed polyelectrolyte. The adsorbed polyelectrolyte provides an electrostatic and steric barrier that prevents the colloidal particles from aggregating.

The design space one must explore for polyelectrolytes (architecture and chemical sequence) and solution conditions (salt concentration, polyelectrolyte concentration, pH, solvent type, etc.) to address all of the applications above is too difficult to accomplish by experiments alone. Predicting and designing materials to have desirable properties for the applications above requires accurate theoretical descriptions of polyelectrolytes.

I.2 Challenges and Opportunities of Surfaces

Polyelectrolytes interact with themselves and the surrounding solution at multiple length-scales. The long-range nature of the electrostatic interactions leads polyelectrolytes to strongly interact with species of opposite charge. In an effort to minimize the electrostatic free energy, oppositely charged polyelectrolytes often form complexes or counterions may condense on the polyelectrolyte backbone [29–31]. The theoretical description of polyelectrolytes in bulk solutions relies on accurately describing the electrostatic correlations, which arise based on the local environment that surrounds a charged species [32]. Wolfgang Pauli said that “God made the

bulk. Surfaces were designed by the devil" [33]. The quote was not necessarily intended for thermodynamics of charged systems but the statement rings true. Surfaces take the complexity of bulk systems and add new length-scales, interactions, and inhomogeniety; however, the strong inhomogeniety imposed by a solid surface can sometimes simplify the electrostatic interactions. The presence of a solid surface, or other interface, permits local net charge in an electrolyte solution that is not possible in a bulk solution. In such a case, charge assembly is conceptually simple and many of the simpler electrostatic descriptions, such as mean-field theories, perform well since the relative effect of electrostatic correlations is reduced. To illustrate this idea, consider polyelectrolyte multi-layers prepared by layer-by-layer assembly, where a series of adsorption and washing steps of a polyelectrolyte on a charged substrate (Figure I.3). The attraction of opposite charges drives strong adsorption of the initial polyelectrolyte layer. Subsequent layers adsorb, or complex, due to the same electrostatic forces. The high degree of charge separation leads to layer-by-layer assembly being a reliable and robust way to create multi-layers of controlled thickness [34], enabling their use in a wide variety of contexts, such as encapsulation and preparation of films for drug delivery [35–37].

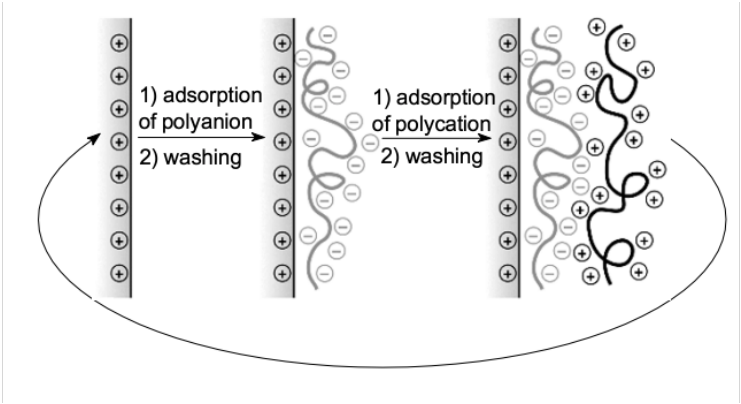

Figure I.3: Schematic of layer-by-layer assembly of polyelectrolyte multi-layer films. Reproduced from Izumrudov, V. A.; Mussabayeva, B. K.; Murzagulova, K. B. *Russian Chemical Reviews* **2018**, *87*, 192, DOI: 10.1070/RCR4767.

Much of the interesting behavior and applications of polyelectrolytes occur near surfaces. The applications follow two main themes: using polyelectrolytes to modify surface properties or using a surface to localize and mediate a process. For the first theme, the diversity of polymer chemistry and generality of charged assembly near a surface leads surface modification in many areas, such as lubrication [38, 39], biosensing [40], anti-fouling [41–43], and assembly of nanoparticles [44, 45].

The second theme is more elusive and underlies important of the open questions in polyelectrolyte research. Surface-mediated processes, like assembly, are often multicomponent and seen in biological systems. For example, recently, Gozen posited that solid surfaces, such as rocks and minerals, enabled the origin of life by providing a platform for surface-mediated subcompartmentalization of lipid assemblies and other non-trivial protocell structures, networks, and colonies [46] (Figure I.4).

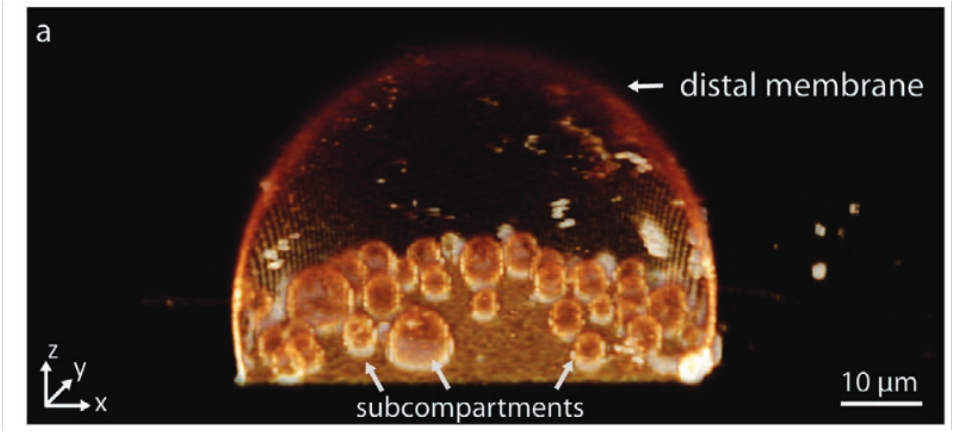

Figure I.4: Subcompartmentalization in surface-adhered model protocells. Confocal micrograph, reconstructed in 3D, showing a model protocell on a solid surface enveloping several subcompartments. Reproduced from Spustova, K.; Köksal, E. S.; Ainla, A.; Gözen, I. *Small* **2021**, *17*, 2005320, DOI: 10.1002/smll.202005320.

In the following chapters, we will traverse various aspects of polyelectrolytes near solid surfaces. A central theme of this work is the interplay between electrostatic and nonelectrostatic forces near a solid surface. Chapter II overviews the main principles of surface thermodynamics of charged systems, focusing on small ion systems, and applies a robust thermodynamic theory known as classical density functional theory to study the effect of preferential ion adsorption on the energy extraction from mixing fresh and salt water. Chapter III explores the interplay between nonelectrostatic and electrostatic adsorption in determining colloidal stability for both strong and weak polyelectrolyte dispersants. Chapter IV addresses the formation and growth of polyelectrolyte complexes as films and droplets on a solid surface for applications in underwater adhesives and other surface coatings. Chapter V investigates the responsive nature of strong and weak polyelectrolyte brushes by exploring complexation of oppositely charged polyelectrolytes and the electroresponsiveness of weak polyelectrolytes.

References

(1) Balzer, C.; Jiang, J.; Marson, R. L.; Ginzburg, V. V.; Wang, Z.-G. *Langmuir* **2021**, *37*, 5483–5493, DOI: 10.1021/acs.langmuir.1c00139.

(2) Balzer, C.; Zhang, P.; Wang, Z.-G. *Soft Matter* **2022**, *18*, 6326–6339, DOI: 10.1039/D2SM00859A.

(3) Lee, K. Y.; Mooney, D. J. *Progress in polymer science* **2012**, *37*, 106–126, DOI: 10.1016/j.progpolymsci.2011.06.003.

(4) Cazorla-Luna, R.; Martín-Illana, A.; Notario-Pérez, F.; Ruiz-Caro, R.; Veiga, M.-D. *Polymers* **2021**, *13*, 2241, DOI: 10.3390/polym13142241.

(5) Zhou, H.-X.; Pang, X. *Chemical Reviews* **2018**, *118*, 1691–1741, DOI: 10.1021/acs.chemrev.7b00305.

(6) Dobrynin, A. V.; Rubinstein, M. *Journal de Physique II* **1995**, *5*, 677–695, DOI: 10.1051/jp2:1995157.

(7) Overbeek, J. T. G. In *Macromolecular Chemistry–11*, Eisenberg, H., Ed.; Pergamon: 1977, pp 91–101, DOI: 10.1016/B978-0-08-020975-3.50004-9.

(8) Förster, S.; Schmidt, M. In *Physical Properties of Polymers*; Advances in Polymer Science; Springer: Berlin, Heidelberg, 1995, pp 51–133, DOI: 10.1007/3-540-58704-7_2.

(9) Rubinstein, M.; Papoian, G. A. *Soft Matter* **2012**, *8*, 9265–9267, DOI: 10.1039/C2SM90104H.

(10) Visakh, P. M. **2014**, 1–17, DOI: 10.1007/978-3-319-01680-1_1.

(11) Kitano, T.; Taguchi, A.; Noda, I.; Nagasawa, M. *Macromolecules* **1980**, *13*, 57–63, DOI: 10.1021/ma60073a011.

(12) Fuoss, R. M. *Science* **1948**, *108*, 545–550, DOI: 10.1126/science.108.2812.545.

(13) Schanze, K. S.; Shelton, A. H. *Langmuir* **2009**, *25*, 13698–13702, DOI: 10.1021/la903785g.

(14) Carrivain, P.; Cournac, A.; Lavelle, C., et al. *Soft Matter* **2012**, *8*, 9285–9301, DOI: 10.1039/C2SM25789K.

(15) Brangwynne, C. P.; Tompa, P.; Pappu, R. V. *Nature Physics* **2015**, *11*, 899–904, DOI: 10.1038/nphys3532.

(16) Yewdall, N. A.; André, A. A. M.; Lu, T.; Spruijt, E. *Current Opinion in Colloid & Interface Science* **2021**, *52*, 101416, DOI: 10.1016/j.cocis.2020.101416.

(17) Dinic, J.; Marciel, A. B.; Tirrell, M. V. *Current Opinion in Colloid & Interface Science* **2021**, *54*, 101457, DOI: 10.1016/j.cocis.2021.101457.

(18) Agudo-Canalejo, J.; Schultz, S. W.; Chino, H., et al. *Nature* **2021**, *591*, 142–146, DOI: 10.1038/s41586-020-2992-3.

(19) Kusumaatmaja, H.; May, A. I.; Knorr, R. L. *Journal of Cell Biology* **2021**, *220*, e202103175, DOI: 10.1083/jcb.202103175.

(20) Scranton, A. B.; Rangarajan, B.; Klier, J. In *Biopolymers II*, ed. by Peppas, N. A.; Langer, R. S., Springer: Berlin, Heidelberg, 1995, pp 1–54, DOI: 10.1007/3540587888_13.

(21) Bhatia, S. R.; Khattak, S. F.; Roberts, S. C. *Current Opinion in Colloid & Interface Science* **2005**, *10*, 45–51, DOI: 10.1016/j.cocis.2005.05.004.

(22) Farinato, R. S. In *Polyelectrolytes and Polyzwitterions*; ACS Symposium Series 937, Vol. 937; American Chemical Society: 2006, pp 153–168, DOI: 10.1021/bk-2006-0937.ch009.

(23) Papagiannopoulos, A. *Macromol* **2021**, *1*, 155–172, DOI: 10.3390/macromol1020012.

(24) De Vasconcelos, C. L.; Pereira, M. R.; Fonseca, J. L. C. *Journal of Dispersion Science and Technology* **2005**, *26*, 59–70, DOI: 10.1081/DIS-200040170.

(25) Hierrezuelo, J.; Sadeghpour, A.; Szilagyi, I.; Vaccaro, A.; Borkovec, M. *Langmuir* **2010**, *26*, 15109–15111, DOI: 10.1021/la102912u.

(26) Llamas, S.; Guzmán, E.; Ortega, F., et al. *Advances in Colloid and Interface Science* **2015**, *222*, 461–487, DOI: 10.1016/j.cis.2014.05.007.

(27) Cornwell, P. A. *International Journal of Cosmetic Science* **2018**, *40*, 16–30, DOI: 10.1111/ics.12439.

(28) Dobrynin, A. V. *Polymer* **2020**, *202*, 122714, DOI: 10.1016/j.polymer.2020.122714.

(29) Manning, G. S. *The Journal of Chemical Physics* **1969**, *51*, 924–933, DOI: 10.1063/1.1672157.

(30) Priftis, D.; Laugel, N.; Tirrell, M. *Langmuir* **2012**, *28*, 15947–15957, DOI: 10.1021/la302729r.

(31) Overbeek, J. T.; Voorn, M. J. *Journal of Cellular Physiology* **1957**, *49*, 7–26, DOI: 10.1002/jcp.1030490404.

(32) Shen, K.; Wang, Z. G. *Journal of Chemical Physics* **2017**, *146*, 84901, DOI: 10.1063/1.4975777.

(33) Mudunkotuwa, I. A.; Grassian, V. H. *Journal of Environmental Monitoring* **2011**, *13*, 1135, DOI: 10.1039/c1em00002k.

(34) Izumrudov, V. A.; Mussabayeva, B. K.; Murzagulova, K. B. *Russian Chemical Reviews* **2018**, *87*, 192, DOI: 10.1070/RCR4767.

(35) Jaber, J. A.; Schlenoff, J. B. *Current Opinion in Colloid & Interface Science* **2006**, *11*, 324–329, DOI: 10.1016/j.cocis.2006.09.008.

(36) Su, X.; Kim, B.-S.; Kim, S. R.; Hammond, P. T.; Irvine, D. J. *ACS Nano* **2009**, *3*, 3719–3729, DOI: 10.1021/nn900928u.

(37) Anselmo, A. C.; McHugh, K. J.; Webster, J.; Langer, R.; Jaklenec, A. *Advanced Materials* **2016**, *28*, 9486–9490, DOI: 10.1002/adma.201603270.

(38) Kreer, T. *Soft Matter* **2016**, *12*, 3479–3501, DOI: 10.1039/C5SM02919H.

(39) Zhulina, E. B.; Rubinstein, M. *Macromolecules* **2014**, *47*, 5825–5838, DOI: 10.1021/ma500772a.

(40) Ali, M.; Yameen, B.; Neumann, R., et al. *Journal of the American Chemical Society* **2008**, *130*, 16351–16357, DOI: 10.1021/ja8071258.

(41) Ma, S.; Ye, Q.; Pei, X.; Wang, D.; Zhou, F. *Advanced Materials Interfaces* **2015**, *2*, 1500257, DOI: 10.1002/admi.201500257.

(42) Higaki, Y.; Kobayashi, M.; Murakami, D.; Takahara, A. *Polymer Journal* **2016**, *48*, 325–331, DOI: 10.1038/pj.2015.137.

(43) Borzęcka, N. H.; Kozłowska, I.; Gac, J. M.; Bojarska, M. *Applied Surface Science* **2020**, *506*, 144658, DOI: 10.1016/j.apsusc.2019.144658.

(44) Pincus, P. **1991**, 2912–2919, DOI: 10.1021/ma00010a043.

(45) Marins, J. A.; Montagnon, T.; Ezzaier, H., et al. *ACS Applied Nano Materials* **2018**, *1*, 6760–6772, DOI: 10.1021/acsanm.8b01558.

(46) Gözen, İ. *Life* **2021**, *11*, 795, DOI: 10.3390/life11080795.

(47) Spustova, K.; Köksal, E. S.; Ainla, A.; Gözen, I. *Small* **2021**, *17*, 2005320, DOI: 10.1002/smll.202005320.

Chapter II

ELECTRIC DOUBLE LAYERS

A starting point to understand polyelectrolytes near solid surfaces is understanding the electric double layer (EDL) structure and thermodynamics of an electrolyte solution. The following chapter outlines the thermodynamics of a solution of small ions in contact with a charged (or uncharged) solid surface. The first half focuses on general surface thermodynamics for charge systems and the simplest model of the electrolyte system, known as Poisson-Boltzmann theory. All of the relevant thermodynamics for charged systems can be formulated at the Poisson-Boltzmann level. Next, we use a density-explicit thermodynamic framework to study preferential ion adsorption in capacitive double layer expansion (CDLE), where the controlled mixing of fresh and salty water can generate energy. The available *blue energy* (or salinity gradient energy) in a CDLE process is directly determined by the interplay between adsorption and release of ions from the electrodes at different salt concentrations. We explore the effect of asymmetric preferential ion adsorption at nanoporous anode and cathode surfaces as a means to enhance the available blue energy.

This chapter includes content from our previously published articles:

Bruch, D.; Balzer, C.; Wang, Z.-G. *The Journal of Chemical Physics* **2022**, *156*, 174704, DOI: 10.1063/5.0089260

Balzer, C.; Qing, L.; Wang, Z.-G. *ACS Sustainable Chemistry & Engineering* **2021**, *9*, 9230–9239, DOI: 10.1021/acssuschemeng.1c01326

I am thankful to Dorian Bruch and Dr. Leying Qing for their devotion to the projects we shared and their eagerness to understand the thermodynamics of charged systems.

II.1 Surface Thermodynamics of Electric Double Layers

We begin with a general discussion of surface thermodynamics for charged systems that will be used in subsequent chapters. Consider a planar, charged solid surface in contact with a fluid as depicted in Figure II.1. The internal energy for the system

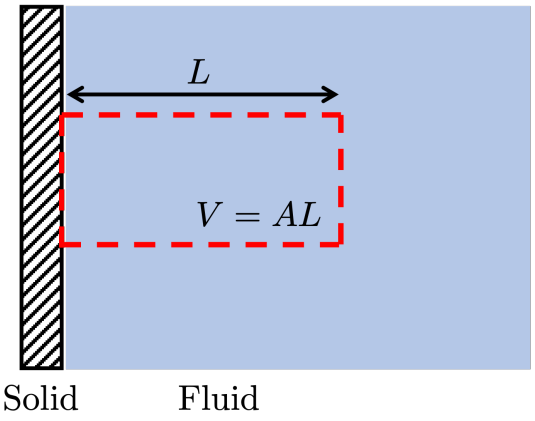

Figure II.1: Simple schematic of planar solid–liquid interface.

is described by the extensive variables S, V, A, N, and Q, corresponding to the entropy, volume, particle number, and surface charge, respectively.

$$U = TS - PV + \gamma A + \sum_{+,-} \mu_i N_i + \Psi Q \tag{II.1}$$

where T is temperature, P is pressure, γ is the surface tension, μ is the chemical potential of species i, and Ψ is the electrostatic potential of the surface. The differential form of the internal energy is

$$dU = TdS - PdV + \gamma dA + \sum_{+,-} \mu_i dN_i + \Psi dQ \tag{II.2}$$

From the geometry, the volume and area are related, $V = AL$. A key idea from Ref. 1 is that the surface charge Q and the surface potential Ψ are (1) thermodynamic quantities and (2) thermodynamic conjugate pairs for a charged planar surface. The consequences of this idea are clear when calculating thermodynamic quantities. For instance, if we have the grand free energy, or Landau energy, $W = U - TS - \sum_{+,-} \mu_i N_i$, the differential is

$$dW = -SdT - PdV + \gamma dA - \sum_{+,-} N_i d\mu_i + \Psi dQ \tag{II.3}$$

Calculating a pressure from this expression requires the derivative with respect to the volume, $P = -\left(\frac{\partial W}{\partial V}\right)_{T,A,\{\mu\},Q}$. The derivative is taken at constant Q and A,

which indicates that the surface charge density remains constant. Likewise, the surface tension has the derivative $\gamma = \left(\frac{\partial W}{\partial A}\right)_{T,V,\{\mu\},Q}$, where changing A at constant Q leads to a varying surface charge density. In this way, the grand potential is not the natural thermodynamic potential for calculating the surface tension. Increasing A with constant Q effectively discharges a surface. The natural way to think of surface tension is to consider a free energy change when increasing the area *without changing* the nature of the surface. The preferred thermodynamic potential is a grand-like potential $Y = W - \Psi Q$, where the surface tension is calculated as $\gamma = \left(\frac{\partial Y}{\partial A}\right)_{T,V,\mu,\Psi}$. Here, the surface is unchanged and only the area is perturbed in the differentiation.

The grand-like potential energy Y is also compatible with the Gibbsian picture of surface thermodynamics. The thermodynamic definition of surface tension introduced by Gibbs [3] is commonly used to calculate surface tension. The basis of Gibbs's formulation is to divide the inhomogeneous system into homogeneous *bulk* phases separated by a *surface* region. The surface tension is commonly evaluated using the integral form of the free energy such that $\gamma A = \Omega - \Omega_{\text{bulk}} = \Omega + P_{\text{bulk}} V$, where Ω is a type of grand free energy. The *bulk* subscript indicates that the surface region is in contact with a macroscopic, bulk phase. For a charged system, the common expression for surface tension is only valid when Ω is the "grand-like" free energy Y, not the grand free energy W, regardless of whether the system is characterized by constant surface charge or constant surface potential.

The thermodynamic potential Y leads to a useful Maxwell relation involving the surface tension. The differential form of the free energy is

$$dY = -SdT - PdV + \gamma dA - Nd\mu - Qd\Psi \tag{II.4}$$

One has the following Maxwell relation,

$$\left(\frac{\partial \gamma}{\partial \Psi}\right)_{T,V,\mu} = -\left(\frac{\partial Q}{\partial A}\right)_{T,V,\mu} = -\sigma \tag{II.5}$$

where σ is the surface charge density. The equation above is known as the Lippmann equation [4], which has been noted by several authors [5–9]. Because the capacitance is positive, the Lippmann equation shows that the surface tension is at a maximum when the surface charge density is zero.

What is the free energy of the fluid?

The thermodynamic arguments above are general and assume one has access to the free energy of the system, F or W. In reality, the challenge is determining the correct

free energy of the system. For an electrolyte solution, the minimum reasonable model is an ideal gas of point charges. Even for such a model, approximations are made to simplify the theory to a mean-field level, known as Poisson–Boltzmann theory. As we will later see, adding in effects beyond mean-field can be done in a perturbative manner by adding free energy contributions relative to a known free energy functional, such as that given by Poisson–Boltzmann theory.

II.2 Poisson-Boltzmann Theory

Theories of EDLs date back to Helmholtz and Perrin who captured the fundamental picture of the EDL [10]. As shown in Figure II.2, if a solid electrode surface carries charge, co-ions of the surface are repelled and the counter-ions are attracted to the surface. The double layer stores charge due to the polarization of the electrolyte solution. Guoy and Chapman built on the Helmholtz–Perrin framework to account for the fact that the ions can diffuse, leading to what is known as the Poisson–Boltzmann theory [11, 12]. Stern offered the next conceptual leap, describing the first layer of ions as bound to the surface with an adjacent diffuse layer [13]. In more recent years, several theories have been developed for electrolyte solutions to incorporate electrostatic correlation, finite size of the ions, image charges at an interface [14]. Some of these aspects will be discussed later in the chapter. The goal of the current section is develop the surface thermodynamics for a charged system. Consider the system depicted in Figure II.2. Poisson–Boltzmann theory can be

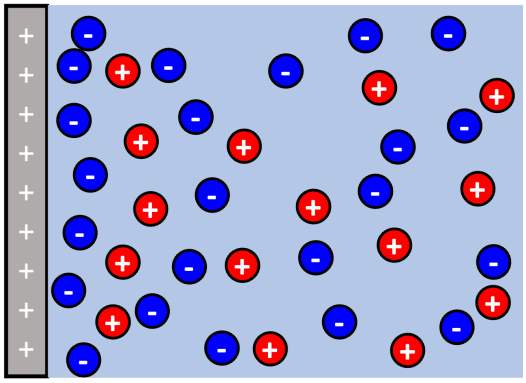

Figure II.2: Schematic of charged surface in contact with electrolyte solution.

derived by considering an ideal gas of point charges [15, 16]. The free energy of such a system includes 1) the translational entropy of each ion and 2) the Coulomb interactions between charges, $F = F_{\text{Ideal}} + F_{\text{Coul.}}$. For a system of monovalent ions ($Z_+ = -Z_- = 1$) with a bulk density of $\rho^b_\pm$, the Helmholtz free energy is

$$\beta F = \sum_{\alpha=+,-} \int \mathrm{d}\mathbf{r}\, \rho_\alpha(\mathbf{r}) \Big(\ln\left[\rho_\alpha(\mathbf{r}) v_\alpha\right] - 1 \Big) + \frac{\beta e^2}{8\pi\epsilon} \int \mathrm{d}\mathbf{r} \int \mathrm{d}\mathbf{r}' \frac{\rho_c(\mathbf{r})\rho_c(\mathbf{r}')}{|\mathbf{r}-\mathbf{r}'|} \quad \text{(II.6)}$$

where $\beta = 1/k_B T$ is the inverse temperature, v is the ion volume scale, e is the elementary charge, ϵ is the dielectric constant of the medium, and $\rho_c(\mathbf{r}) = \rho_+(\mathbf{r}) - \rho_-(\mathbf{r}) + \rho_{\text{ex}}$ is the charge density. ρ_{ex} are the fixed external charges. Using a standard field transformation for the Coulomb interactions [17], the free energy can be written as

$$\beta F = \sum_{\alpha=+,-} \int \mathrm{d}\mathbf{r}\, \rho_\alpha(\mathbf{r}) \Big(\ln\left[\rho_\alpha(\mathbf{r}) v_\alpha\right] - 1 \Big) + \int \mathrm{d}\mathbf{r} \left[\rho_c(\mathbf{r})\psi(\mathbf{r}) - \frac{1}{8\pi l_B} (\nabla\psi)^2 \right] \quad \text{(II.7)}$$

where ψ is the reduced electrostatic potential and $l_B = \beta e^2/4\pi\epsilon$ is the Bjerrum length. For a single surface in contact with an electrolyte solution, the relevant free energy is the grand potential energy, which is obtained through the Legendre transform of the Helmholtz free energy, $W = F - \mu_+ N_+ - \mu_- N_-$. To obtain equilibrium configurations, the grand potential energy is minimized with respect to the ion densities and maximized with respect to the electrostatic potential field. After applying the bulk condition, the following mean field equations govern the system.

$$\rho_\pm(\mathbf{r}) = \rho_\pm^b e^{\mp\psi(\mathbf{r})} \quad \text{(II.8)}$$

$$4\pi l_B \nabla^2 \psi(\mathbf{r}) = 2\rho_\pm \sinh(\psi) - \rho_{\text{ex}} \quad \text{(II.9)}$$

The first equation gives the density profiles for the ions, which only depend on the local value of the electrostatic potential. The second equation is the familiar Poisson equation. The corresponding grand potential energy is given as

$$\beta W = \int \mathrm{d}\mathbf{r} \left[-\frac{1}{8\pi l_B} (\nabla\psi)^2 + \rho_{\text{ex}}\psi - 2\rho_\pm^b \cosh(\psi) \right] \quad \text{(II.10)}$$

Poisson–Boltzmann theory continues to be a popular approach to describe charged systems but is only a starting point for describing the structure and thermodynamics of EDLs. The Poisson–Boltzmann level treatment of electrostatics fails to capture realistic electrolyte behavior [18–21], such as charge-inversion. For electrolyte solutions, classical density functional theory (cDFT) provides an alternative framework that addresses some of the limitations of Poisson–Boltzmann theory.

Classical Density of Functional Theory

The mathematical formalism of cDFT originates from the same seminal works of electronic DFT by Hohenberg and Kohn in 1964 [22] and Kohn and Sham in 1965 [23]. Hohenberg and Kohn proved that the ground-state energy of an electron gas is a unique functional of the electron density for any external potential. Further, the ground-state density can be found variationally – by minimizing the ground-state energy. Kohn and Sham postulated that a many-electron system could be represented by a noninteracting electron gas in an effective potential, providing a self-consistent method of arriving at the effective potential. Combined with Mermin's extension to non-zero temperatures in 1965 [24], these theorems enable straightforward calculation of a classical equilibrium density profile given knowledge of the intrinsic free energy of a system.

The key idea, and main challenge, of cDFT (and electronic DFT) lies in creating the free energy functional. Before considering construction of the free energy functional, the general grand potential energy for a one-component, small particle system will be derived.

For a system at constant temperature, volume, and external field $\phi(\mathbf{r})$, the grand free energy can be written as a Legendre transform of the intrinsic Helmholtz free energy $\mathcal{F}[\rho(\mathbf{r})]$ with respect to the number density $\rho(\mathbf{r})$ and external field $\psi(\mathbf{r})$. The intrinsic free energy is the Helmholtz free energy that is independent of the external field.

$$W[\rho(\mathbf{r})] = \mathcal{F}[\rho(\mathbf{r})] - \int d\mathbf{r}\phi(\mathbf{r})\rho(\mathbf{r}) \tag{II.11}$$

According to the Hohenberg and Kohn theorems, the minimum of the grand potential energy occurs at the equilibrium density distribution $\rho(\mathbf{r})$ so that $\frac{\delta W}{\delta \rho} = 0$. From thermodynamics, the following is also true, where V is the external potential.

$$F = W + \mu \int d\mathbf{r}\rho(\mathbf{r}) = \mathcal{F}[\rho(\mathbf{r})] + \int d\mathbf{r}V(\mathbf{r})\rho(\mathbf{r}) \tag{II.12}$$

Equating the first variations of Equations (II.11) and (II.12) with respect to the density evaluated at the equilibrium density shows that

$$\phi(\mathbf{r}) = \mu - V(\mathbf{r}) \tag{II.13}$$

Thus, the grand potential energy we seek to minimize can be written in terms of the intrinsic Helmholtz free energy and a contribution from the external and chemical potential.

$$W[\rho(\mathbf{r})] = \mathcal{F}[\rho(\mathbf{r})] - \mu \int d\mathbf{r}\rho(\mathbf{r}) + \int d\mathbf{r}V(\mathbf{r})\rho(\mathbf{r}) \tag{II.14}$$

Finally, one can divide the intrinsic free energy into an ideal part and excess part. The ideal part is the free energy of an ideal gas, while the excess contribution accounts for all deviations from ideality. In the equation below, Λ is the thermal de Broglie wavelength and β is the inverse temperature.

$$\begin{aligned}\beta W[\rho(\mathbf{r})] = \int d\mathbf{r}\rho(\mathbf{r}) \left[\ln(\rho(\mathbf{r})\Lambda^3) - 1)\right] + \beta \int d\mathbf{r}V(\mathbf{r})\rho(\mathbf{r}) \\ -\beta\mu \int d\mathbf{r}\rho(\mathbf{r}) + \beta\mathcal{F}_{ex}[\rho(\mathbf{r})]\end{aligned} \tag{II.15}$$

Here, it is worth noting the similarity to electronic DFT, where the intrinsic free energy is the sum of the Hartree energy of the electrons (known analytical form) and the exchange-correlation energy. The treatment of the exchange-correlation energy functional is where Kohn-Sham DFT can widely vary, including local density, gradient-corrected, and even second derivative functionals [25]. In the case of electronic DFT, the external potential arises from surrounding nuclei while the external potential in cDFT can originate from a number of different origins, such as a surface.

Minimization of the free energy in Equation (II.15) leads to an Euler-Lagrange equation for the equilibrium density. Note that Λ^3 has no effect on the density as it can be absorbed into the reference potential in the ideal part of the chemical potential.

$$\rho(\mathbf{r})\Lambda^3 = \exp\left[\beta\mu - \beta V(\mathbf{r}) - \beta\frac{\delta\mathcal{F}_{ex}(\mathbf{r})}{\delta n(\mathbf{r})}\right] \tag{II.16}$$

Excess Free Energy

As is clear in Equation (II.16), the excess free energy plays an essential role in dictating the equilibrium density profile. Deciding what physics to include in the excess free energy is the crux of cDFT. In addition to choosing physics to include in

the excess free energy, one must also choose from a variety of theoretical approaches to capture desired phenomena. For example, to include a finite size via a hard sphere contribution to the excess free energy, one could choose from early works of weighted/local density approximations or use one of the variations of fundamental measure theory (FMT) [26]. While there may be rules of thumb and room for intuition in deciding the functional, there is no "silver bullet" in choosing a free energy functional. The tailorability of cDFT is a considerable challenge to as well as an opportunity to use DFT for a wide variety of problems.

The initial applications of cDFT in the 1970's emphasized phase transitions and the structure of density distributions where different phases meet [27]. Excess free energy functionals consisted of local density or mean field approximations. To capture strong inhomogenieties in density and more complex phenomena like hydrogen bonding, weighted density approximations (WDAs), Rosenfeld's FMT [26], and the general class of statistically associating fluid theories (SAFTs) by Chapman were introduced [28]. With more robust free energy representations, applications extended to wetting transitions, freezing/melting transitions, complex fluid phenomena, and surfactant and gas adsorption [29]. Alongside those developments, cDFT has focused on the treatment of charged components, polymers or monomeric ions. The historical development of cDFT is linked to the refinements and new approaches in defining the excess free energy functional [27]. While these refinements are still ongoing [30–34], many recent applications in cDFT are focused on charged systems, specifically for energy applications. The following section will use the cDFT framework to study energy extraction from mixing fresh and saltwater.

II.3 Preferential Ion Adsorption in Blue Energy Applications

Introduction

Renewable alternatives to fossil fuels are urgently needed to address energy shortages and avoid further adverse environmental consequences [35]. The ocean provides several potential renewable energy sources, including wave power, ocean thermal energy, tidal energy, marine current energy, and salinity gradient energy [36, 37]. Salinity gradient energy (or so-called "blue energy") is the energy extracted from mixing freshwater and saltwater. Such mixing occurs in large quantities when rivers flow into the ocean, whereby part of the released free energy of the mixing process can be converted to useful work. This interesting approach to energy extraction was proposed by Pattle in 1954 [38], and then further developed by many researchers [39–42]. Popular engineered technologies include pressure retarded osmosis (PRO), reverse electrodialysis (RED), and capacitive mixing (CapMix) [43, 44]. The former two technologies are membrane-based and obtain high power density but widespread use is limited by low cost-efficiency and fouling [45, 46]. CapMix is an electrode-based technology and was originally proposed by Brogioli [47] in a seminal paper outlining what is now known as capacitive double layer expansion (CDLE) [48]. Subsequently, CapMix expanded to include two other variants based on CDLE: mixing entropy battery (MEB) [49] and capacitive Donnan potential (CDP) [50]. These processes have three corresponding reverse processes: capacitive deionization [51–53], desalination battery [54], and membrane capacitive deionization [55], respectively. Each variant of CapMix shows promise and has drawbacks, but CDLE has the benefit that no chemical reactions or ion-selective membranes are required as in MEB and CDP, respectively. CDLE uses two porous electrodes assembled as a capacitor to accumulate charged ions in the electrical double layer (EDL) to achieve the energy extraction from the saltwater and the freshwater [56]. Compared with other CapMix variants, CDLE also has a longer cycle life and favorable operating conditions, showing promise for several applications [57].

Figure II.3a shows the four states of the CDLE process involving two open and two closed circuits during the charging/discharging process. The corresponding thermodynamic cycle is shown in Figure II.3b. By alternating between saltwater and freshwater and switching between open/closed circuit states during the charging/discharging process, the enclosed area W in the thermodynamic cycle is the total useful work that can be extracted from the mixing process of the saltwater and the freshwater. A more detailed description of the CDLE process is available in previous literature [47, 56, 58] and is included in the Appendix for completeness.

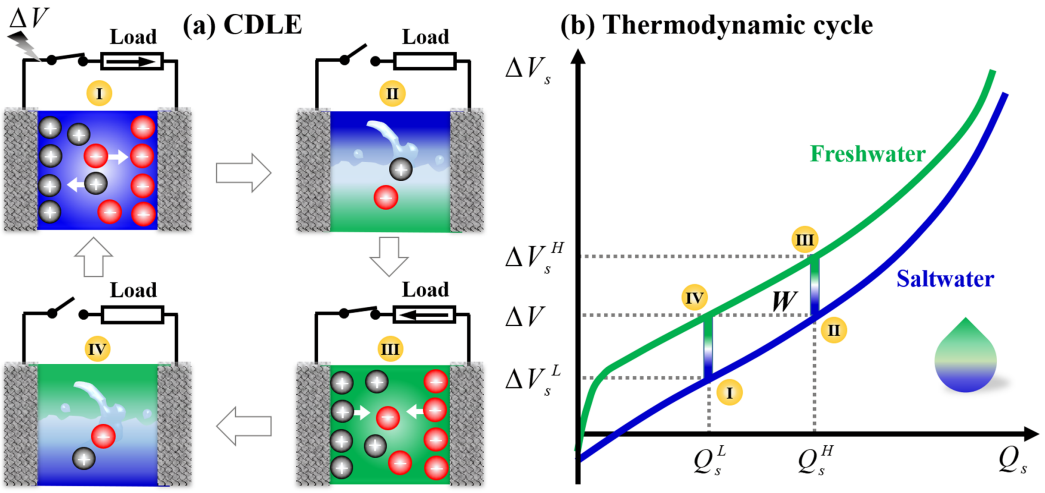

Figure II.3: Blue energy process graphic. (a) Schematic representation of the four states in CDLE process including two open-circuit and two closed-circuit states. (b) Thermodynamic cycle in the CDLE process. ΔV_s is the surface voltage difference (working voltage) between the positive and negative electrodes in the capacitor. Q_s is the surface charge density of the electrodes.

The available energy to extract W is closely associated with the fabrication and arrangement of porous electrode pair in electrolyte. Based on the idea proposed by Brogioli in 2009 [47], Brogioli and coworkers fabricated a larger dimensional prototype cell in a lab-scale stack with 8 cells [41]. Sales *et al.* increased the extracted efficiency of the Brogioli system by employing a membrane-modified supercapacitor and achieved the direct auto-generation of the current by alternating the saltwater and the freshwater [50]. Additionally, many experimental and theoretical studies have focused on the geometrical structure of the pore, interfacial interaction, and type of electrolytes on the energy extraction. For example, Jiménez *et al.* investigated the multi-ionic solution (*i.e.*, Mg^{2+},Na^{+},Cl^{-}) both theoretically and experimentally to find that divalent ions and larger ion sizes decrease the available energy [59, 60]. Using classical density functional theory (cDFT), Lian *et al.* found that hydrophilic electrodes can extract more blue energy compared to hydrophobic electrodes [58]. They further reported that multi-layer graphene electrodes can increase the extracted energy [61]. Furthermore, microporous electrodes show significant viability for energy extraction in the CDLE process and capacitive deionization [62, 63] due to the anomalous increase of capacitance at nanoscale pore size [64–67]. For supercapacitors, the capacitance was shown to be maximized when the pore size is close to the size of the ion diameter [68]; whereas, for the CDLE process, the ratio of the net energy output to the variation in the Gibbs free

energy between saltwater and freshwater (defined as the thermodynamic efficiency) was maximized when pore size is a few times the ion size [69].

The vast majority of experimental and theoretical work related to blue energy has focused on systems where both electrodes have the same properties. Experiments of different carbon-based electrodes have shown that a cell with two different electrode materials can give rise to differing "spontaneous potentials" due to specific ion adsorption and parasitic electrochemical reactions at the electrodes [40]. In the same experiments, the authors showed that operating the CDLE process close to the "spontaneous voltage" (difference between spontaneous potentials for the two electrodes) can significantly reduce, or even eliminate, the effect of self-discharge, which is a major limiting factor in the practical realization of CDLE.

As shown in Figure II.3b, the optimal energy extraction is given by the area enclosed in the thermodynamic curves of freshwater and saltwater at a given potential difference. Recent work by Chao and Wang suggested that the maximum of the differential capacitance shifts from zero voltage to finite voltage when there is preferential attraction of ions to the surface, which can significantly increase the energy storage capacity of supercapacitor (up to a 3-fold increase for some conditions) [70]. We expect that such a preferential attraction will similarly shift the operating curves of saltwater and the freshwater in the thermodynamic cycle for CDLE. For instance, at a positively charged surface, preferential attraction of cations will increase the surface potential. Since the different ion concentrations of freshwater and saltwater shift the potential by a different amount on each electrode, the degree of preferential attraction of ions can then be used to tune the available blue energy and shift the value of the potential difference ΔV where the maximum available energy occurs. The general effect of specific ion adsorption has been explained by a simple, Langmuir-like adsorption model [71]. However, to the best of our knowledge, the effects of asymmetric preferential adsorption on the operation of CapMix and on energy storage have not been systematically studied theoretically.

In this work, we use classical density functional theory (cDFT) to investigate the effect of preferential adsorption and pore size in like-charged slit-pores for the CDLE process. Our results show that preferential adsorption of counterions to the surface can increase the available blue energy, while preferential adsorption of coions decreases the available blue energy. Generally, the amount of available energy depends on the chosen potential difference and the pore size. However, when the pore size is more than a few times the ion size, we find a wide range of

operability. We also find that preferential adsorption shifts the maximum in the available energy closer to the spontaneous voltage and that significant energy can be extracted even at zero potential difference under certain conditions.

The rest of the article is organized as follows. We outline the model used to study the like-charged slit-pore with preferential attraction. From the prediction of density profiles using cDFT, we outline the process of calculating the available blue energy. We then systematically study the effects of the pore size and the strength of preferential attraction on the maximum extracted blue energy and the corresponding potential difference.

Methodology

We model an individual pore in the microporous electrodes as a like-charged slit-pore, where the surfaces carry either positive or negative charge as seen in Figure II.4. The slit-pore is a structure-less hard wall with pore size H. We use the the restricted primitive model (RPM) to describe the electrolyte solutions (*i.e.* saltwater and the freshwater) confined in the slit-pore. The solution is assumed to be a dielectric continuum, described by a relative dielectric constant, $\epsilon_r = 78.50$. The cations and the anions are modeled as hard spheres with the same ion diameter, $\sigma_+ = \sigma_- = \sigma = 0.425$ nm. The valency of cation and anion has $Z_+ = -Z_- = Z = 1$. The difference between saltwater and freshwater is only the bulk concentration. Approximately, the ion concentrations of saltwater and freshwater are 0.60M and 0.024M respectively, corresponding to the ionic strength of ocean and river water.

We focus on a 1:1 electrolyte to clearly present the effect of asymmetry between electrode materials. We note that using the RPM for a 1:1 electrolyte does not reflect the multi-ionic nature of any natural water source. In particular, seawater is made up of ions of differing size and valency. Further, the RPM ignores changes in the ions' hydration shell, which alters the solvated ion size and double layer structure as well as the dielectric constant at interfaces [72], in confinement [64, 73, 74], and with changing salt concentration [75, 76]. There is currently no widely accepted theory to describe the strong electrostatic correlation of multivalent ions [32] or to incorporate all solvation effects into cDFT [77]. While solvation, ion size disparity, and electrolyte valency are important for an accurate description of real electrolytes, tackling these issues is beyond the scope of this work; we expect the qualitative conclusions based on our simple 1:1 RPM model to hold. We direct the reader to works that have used cDFT for electric double layers to study size/valency

asymmetry [20, 21, 78], explicit solvent dipoles [79, 80], and ion hydration in confinement [81], as well as works that used a Poisson-Boltzmann level description to study at multi-ion effects for blue energy applications [59, 60].

After applying an external voltage, the counterions in the bulk solution adsorb into the porous electrodes due to the electrostatic attraction, resulting in the accumulation of counterions at the surface of the slit-pore and depletion of coions from the surface. These phenomena represent the typical adsorption and diffusion of ions in electrochemical system [21, 82]. To describe the preferential attraction between electrode materials and ions, we introduce a nonelectrostatic potential, described by a modified 9-3 potential.

$$\beta u_{93}(z) = 2\pi\beta\epsilon \left[\frac{1}{9}\left(\frac{\sigma}{2z}\right)^9 - \frac{1}{3}\left(\frac{\sigma}{2z}\right)^3 \right] \tag{II.17}$$

where z is the distance away from the surface of a single plate and ϵ is the energy parameter normalized by $\beta = \frac{1}{k_B T}$. k_B is the Boltzmann constant and T is the system temperature. The nonelectrostatic 9-3 potential is identical for both surfaces in the slit-pore. Therefore, the nonelectrostatic preferential attraction on the ions comes from both surfaces in the slit-pore, which is more pronounced in small slit-pore. In addition, ions are excluded from the surface at distances less than the radius of the ion, $\sigma/2$. Consequently, the nonelectrostatic external preferential attraction on the ions V^{ext} is

$$V^{\text{ext}}(z) = \begin{cases} u_{93}(z) + u_{93}(H-z) & \sigma/2 \le z \le H - \sigma/2 \\ \infty & \text{otherwise} \end{cases} \tag{II.18}$$

The 9-3 potential has a minimum at the contact distance from the surface. Therefore, V^{ext} is negative in the available space of the slit-pore, providing a purely attractive force on ions.

To minimize the number of adjustable parameters, we consider three situations ($f = 0$, $f < 0$ and $f > 0$) to characterize the preferential attraction of electrode materials on the ions. Particularly, $f < 0$ corresponds to adsorption of counterions on the surface (Fig. II.4a), while $f > 0$ corresponds to adsorption of the coions on the surface of the slit-pore (Fig. II.4b). For $f = 0$, there is no nonelectrostatic preferential attraction in the slit-pore, in which case the ion adsorption is determined only by the electrostatic and hard sphere interactions at the charged surfaces. Simplifying the system to these three cases amounts to considering *symmetric* ($f = 0$) and *antisymmetric* ($f < 0$ and $f > 0$) electrodes, which are limiting cases for

the combination of two electrode materials. This has important implications when comparing to previous experiments, which will be detailed later on.

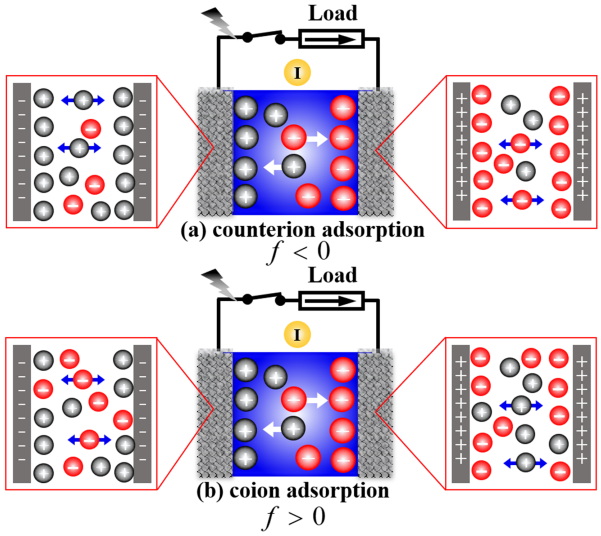

Figure II.4: Schematic representation of two preferential attraction on the ions in state I. (a) $f < 0$, where electrodes have a preferential adsorption for the counterions.(b) $f > 0$, where electrodes have a preferential adsorption for the coions. Note that anions are counterions for positive electrode, and cations are counterions for the negative electrode. Likewise, cations are coions for positive electrode, and anions are coions for negative electrode.

cDFT has been extensively employed to investigate the adsorption and diffusion of ions in electrochemical systems [83, 84]. For an open system, the grand potential $\Omega[\{\rho_i(\mathbf{r})\}]$ is expressed as a functional of the density profiles of ions, $\{\rho_i(\mathbf{r})\}$,

$$\Omega[\{\rho_i(\mathbf{r})\}] = F[\{\rho_i(\mathbf{r})\}] + \sum_i \int d\mathbf{r}\rho_i(\mathbf{r})[V_i^{\text{ext}}(\mathbf{r}) - \mu_i] \tag{II.19}$$

where μ_i is the chemical potential of component i. $F[\{\rho_i(\mathbf{r})\}]$ is the Helmholtz free energy including two parts: the ideal gas contribution $F^{\text{id}}[\{\rho_i(\mathbf{r})\}]$ and the excess part due to the intermolecular interaction $F^{\text{ex}}[\{\rho_i(\mathbf{r})\}]$,

$$F[\{\rho_i(\mathbf{r})\}] = F^{\text{id}}[\{\rho_i(\mathbf{r})\}] + F^{\text{ex}}[\{\rho_i(\mathbf{r})\}] \tag{II.20}$$

The ideal part has a known form but the excess part must be approximated. In an electrochemical system, the excess free energy includes several contributions: the excluded volume effects $F^{\text{hs}}[\{\rho_i(\mathbf{r})\}]$, the electrostatic correlation $F^{\text{el}}[\{\rho_i(\mathbf{r})\}]$, and the direct (mean-field) Coulomb interaction $F^{\text{c}}[\{\rho_i(\mathbf{r})\}]$, and the van der Waals interaction between ions $F^{\text{vdW}}[\{\rho_i(\mathbf{r})\}]$.

$$F^{\text{ex}}[\{\rho_i(\mathbf{r})\}] = F^{\text{hs}}[\{\rho_i(\mathbf{r})\}]+F^{\text{el}}[\{\rho_i(\mathbf{r})\}]+F^{\text{c}}[\{\rho_i(\mathbf{r})\}]+F^{\text{vdW}}[\{\rho_i(\mathbf{r})\}] \tag{II.21}$$

In this work, we neglect the effects of van der Waals interactions ($F^{\mathrm{vdW}}[\{\rho_i(\mathbf{r})\}] = 0$). For the hard sphere interactions, we use the modified fundamental measure theory (MFMT) [85], which has been shown to accurately predict hard sphere packing near a planar surface. In addition to the mean-field Coulomb contribution, the electrostatic correlation contribution is added to account for the local electrostatic environment around an ions with finite size. Several theoretical approaches exist for approximating electrostatic correlation [32]. We use a 2$^{\mathrm{nd}}$ order perturbation theory around a bulk reference fluid using the mean spherical approximation (MSA) [86], which adequately describes the ion density profiles for a 1:1 electrolyte of the same size [21, 32]. Without electrostatic correlation and hard sphere interactions, our theory would be identical to the classical Poisson-Boltzmann theory. The expression of Helmholtz free energy functional is given in the Appendix.

Minimizing Eq. II.19, $\frac{\delta\Omega[\{\rho_i(\mathbf{r})\}]}{\delta\rho_i(\mathbf{r})} = 0$, we obtain the density profile of ions at equilibrium.

$$\rho_i(\mathbf{r}) = \frac{1}{\Lambda_i^3} \exp\left[\beta\left(\mu_i - V_i^{ext}(\mathbf{r}) - \frac{\delta F^{ex}[\{\rho_i(\mathbf{r})\}]}{\delta\rho_i(\mathbf{r})}\right)\right] \tag{II.22}$$

where Λ_i is the thermal wavelength, which has no thermodynamic effects on the density distribution and can be absorbed into the definition of the bulk density. The last term in Eq. II.22 defines the local excess chemical potential $\mu_i^{ex}(\mathbf{r})$. Because the slit-pore surface is homogeneous, we only consider density and field variations perpendicular to the surface, *i.e.* in the z direction. The excess chemical potential due to the direct Coulomb interaction is $\mu_i^c(z) = Z_i e\psi(z)$, where e is the elementary charge and $\psi(z)$ is the average electrostatic potential that is found by solving the Poisson equation. For a like-charged slit-pore with both surfaces carrying surface charge density, Q_s, the Poisson equation can be written as

$$\epsilon_0\epsilon_r\nabla^2\psi(z) = -[\rho_c(z) + Q_s\delta(z) + Q_s\delta(z-H)], \tag{II.23}$$

where $\rho_c(z) = e\sum_i Z_i\rho_i(z)$; ϵ_0 is the vacuum permittivity; and $\delta(z)$ is the Dirac delta function. By integrating Eq. II.23 between 0^- and 0^+, the boundary condition for $\psi(z)$ at $z = 0$ is obtained

$$-\epsilon_0\epsilon_r \left.\frac{\partial\psi(z)}{\partial z}\right|_{z=0} = Q_s \tag{II.24}$$

Since both sides of the slit-pore have the same charges (negative or positive), the system is symmetric across the mid-plane, and the boundary condition for $z = H$ is

similarly $\epsilon_0\epsilon_r\psi'(H) = Q_s$. Integrating Eq. II.23 from $z = 0^-$ to $z = H^+$ and noting the potential is constant inside the conducting electrodes,

$$2Q_s + \int_0^H \rho_c(z)dz = 0 \tag{II.25}$$

The full potential profile can be obtained by integrating Eq. II.23 from 0^- to z twice,

$$\psi(z) = V_s - \frac{Q_s}{\epsilon_0\epsilon_r}z - \frac{1}{\epsilon_0\epsilon_r}\int_0^z (z - z')\rho_c(z')dz' \tag{II.26}$$

where V_s is the surface potential. The density profiles and electric potential are solved iteratively and self-consistently. Starting from a given Q_s and an initial guess of the density profiles (the bulk concentrations), the local chemical potential from hard sphere and electrostatic correlations are calculated. The Poisson equation (Eq. II.23) is then solved with Eq. II.26 up to a constant V_s. The surface potential V_s is then determined such that electroneutrality is preserved (Eq. II.25), where V_s enters in the Boltzmann weight in the charge density. Eq. II.22 is used to obtain an updated guess for the density profile. The new guess and previous guess are linearly *mixed* in a Picard updating scheme. The iterative process is repeated until the maximum relative error between the input guess and newly obtained density is less than an error threshold ($< 10^{-6}$).

Results and Discussion

The EDL structure at the electrode surface depends on both the pore size and the strength of the attractive potential between the electrode surface and ions. Figure II.5 shows density profiles for ions in freshwater at a variety of wall-ion attractive strengths (Fig. II.5a&b) and pore sizes (Fig. II.5c&d) for a representative surface charge density. In Figure II.5a, the counterions have preferential attraction to the surface ($f < 0$), leading to enhanced counterion adsorption at the surface and decreased width of the counterion adsorption layer. The thinner adsorption layer is evident in the length scale required for the density profile to return to the bulk value. Increasing $\beta\epsilon$ within reasonable range has a negligible effect for $f > 0$ as the preferential adsorption of coions is not favorable enough to overcome the electrostatic repulsion near the surface (Figure II.5b). As a result, the density profiles for the counterions appear to overlap for a wide range of $\beta\epsilon$. In Figure II.5c, with preferential adsorption of counterions to the surface ($f < 0$), the contact-density varies non-monotonically with the pore size. In the figure, one can see that the contact-density increases from a pore size of $H/\sigma = 1.5$ (black) to $H/\sigma = 3.0$ (blue) but then slightly decreases for larger pore sizes. Without preferential adsorption,

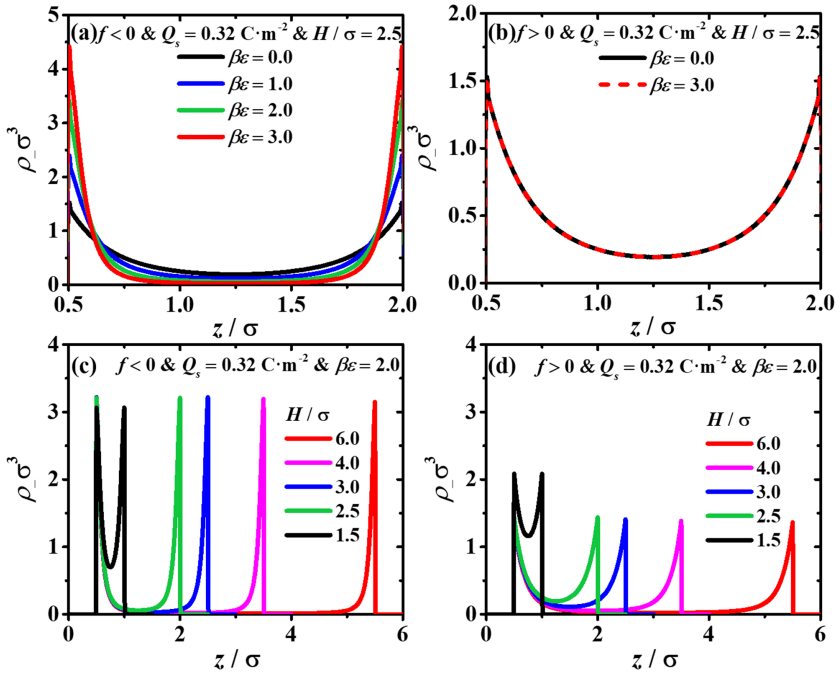

Figure II.5: Density profiles for anions in freshwater (0.024 M) near positively charged surface for various pore sizes (H) and surface affinities ($\beta\epsilon$). The top row shows the effect of $\beta\epsilon$ at constant H for (a) $f < 0$ and (b) $f > 0$. The bottom row shows the effect of pore size at constant $\beta\epsilon$ for (c) $f < 0$ and (d) $f > 0$.

one would expect monotonic decrease of the contact density with pore size – similar to $f > 0$ (see Fig. II.5d), where the coions have preferential adsorption [87]. These density profiles indicate a complex interplay between the pore size and the balance of nonelectrostatic and electrostatic adsorption. When the pore size is much larger than the width of the EDL, the density of ions returns to the bulk value far from the surface. If the pore size is smaller than the width of the EDL, the midplane value of the density exceeds the bulk value for counterions so that the ion adsorption structure is dominated by the first layer of adsorbed counterions [88].

The relationship between surface charge density (Q_s) and surface potential (V_s) is central to calculating the available electrical energy in the thermodynamic cycle of the CDLE process. This relationship is directly accessible in our cDFT calculations as we fix the surface charge density and calculate the surface potential self-consistently with the density profiles. In the absence of preferential adsorption, we expect the surface potential to increase monotonically with the surface charge density and be symmetric about the origin for both electrodes. In particular, with zero surface charge density, the surface potential is zero. However, with preferential

adsorption, there can be a non-zero surface potential even with zero surface charge density – either cations or anions accumulate on the surface. Figure II.6 shows the effect of asymmetric preferential adsorption at the anode and cathode in fresh and saltwater on the relationship between Q_s and V_s. Figures II.6a&d show that for an uncharged cell ($Q_s = 0$), the cathode (black/red) and anode (blue/green) have a non-zero surface potential. The surface potential for $Q_s = 0$ in the saltwater curves is equal to the "spontaneous potential" [40] for an electrode material in the absence of parasitic electrochemical reactions. This is the point where Q_s vs. V_s curves have zero potential difference if one used the *same material* for both electrodes, which does not correspond to the $f > 0$ or $f < 0$ cases. Generally, the spontaneous potential does not need to occur with $Q_s = 0$ but does here because we do not model any electrochemical reactions. The sign of the surface potential for $Q_s = 0$ depends on whether $f < 0$ or $f > 0$. For $f < 0$, at the anode, anions accumulate at the electrode surface, leading to a negative surface potential. The preferential adsorption effectively shifts the V_s-Q_s curve for both the anode and the cathode. Because $f < 0$ and $f > 0$ are each antisymmetric cases, the shift on the anode and cathode are equal in magnitude but opposite in sign. The degree to which preferential adsorption

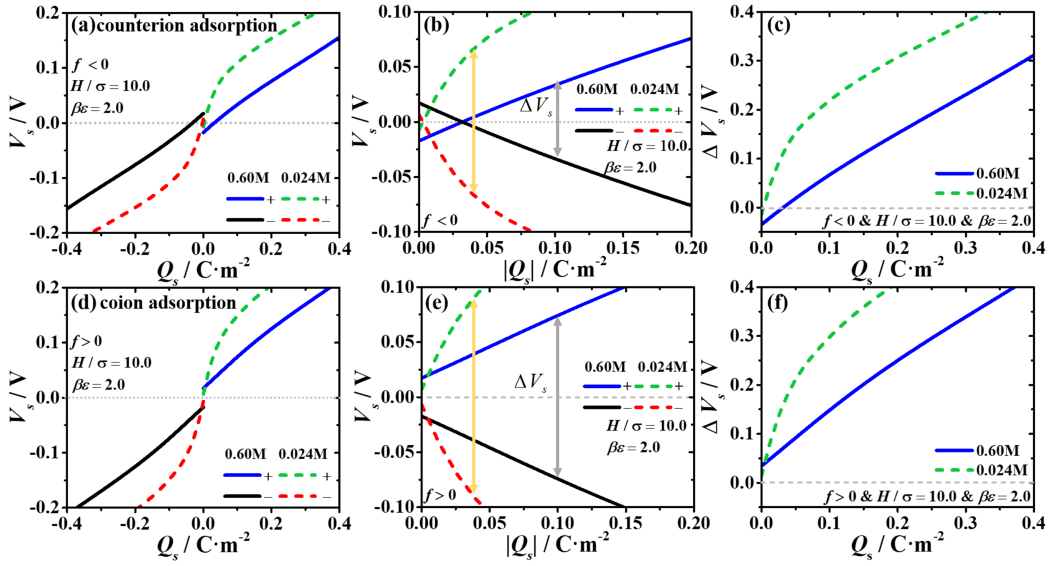

Figure II.6: Relationship between electric potential and surface charge density for $H/\sigma = 10$ and surface affinity $\beta\epsilon = 2$. (a) Surface potential versus the surface charge density for $f < 0$. (b) Illustration of working voltage calculation obtained from matching the magnitude of the surface charge density at in the anode and cathode curves in (a). (c) Working voltage versus surface charge density for $f < 0$. (d-f) are the same as (a-c) with $f > 0$.

impacts the surface potential depends on the salt concentration (Fig. II.6a&d). A higher salt concentration will result in more ions being accumulated on the neutral surface driven by the wall-ion attractive potential, which results in the larger shift of the surface potential in saltwater. Here, the saltwater and freshwater curves have a surface potential of $|V_s(Q_s = 0)| \approx 17$ mV and $|V_s(Q_s = 0)| \approx 7$ mV, respectively. The magnitude of this shift will also increase as the strength of preferential attraction increases, which we will explore later on.

The working voltage (ΔV_s) is calculated as the difference between the anode and cathode surface potential at the same magnitude of the surface charge density. This is indicated in Figures II.6b&e by the arrows for ΔV_s at a given $|Q_s|$. For a given surface charge density, the working voltage is decreased for $f < 0$ and increased for $f > 0$ compared to the case with no preferential adsorption. For the conditions in Figure II.6, the point where the anode/cathode curves cross occurs at $|Q_s| \approx 0.03$ C/m^2 and $|Q_s| \approx 0.005$ C/m^2 for the salt and freshwater respectively. The "spontaneous voltage" in previous literature [40] is the difference between the spontaneous potentials of the two different electrode materials. Because of the antisymmetry of $f < 0$ and $f > 0$, the spontaneous voltage is twice the value of the spontaneous potential at the anode (positive electrode). Figures S2 and S3 show the spontaneous voltage for different pore sizes and strengths of preferential attraction. The key feature is that the spontaneous voltage is negative for $f < 0$ and positive for $f > 0$ if $\beta\epsilon > 0$.

Figures II.6c&f show the relationship between the working voltage and the surface charge density at two different salt concentrations for $f < 0$ and $f > 0$. The amount of energy available to extract is directly related to the area between the freshwater and saltwater curves. The difference in working potential when switching from saltwater to freshwater is known as the voltage rise [71]. Because the magnitude of the preferential adsorption effect depends on the salt concentration, the magnitude of the shift in the saltwater ΔV_s versus Q_s curve is greater than the shift in the freshwater curve. For $f < 0$, such an effect increases the voltage rise (provides more energy output) compared to no preferential adsorption. Conversely, the two curves can shift closer together so that voltage rise, and hence the available energy, is reduced when $f > 0$. We will quantitatively analyze the effect on the available energy later in this work.

Figure II.7 highlights the relationship between the pore size and salt concentration for the ΔV_s vs. Q_s curves. For most applications, the saltwater concentration is

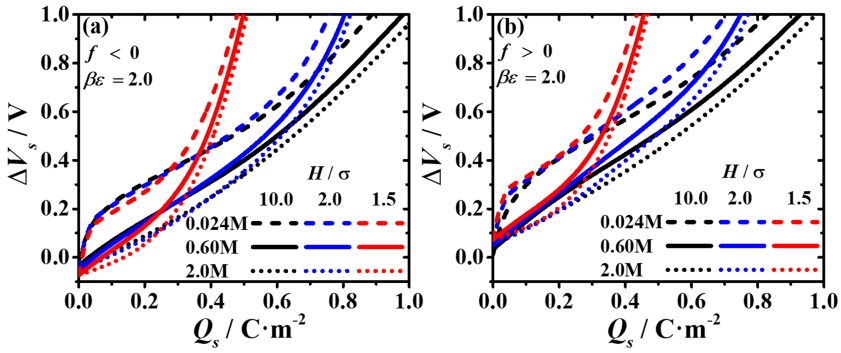

Figure II.7: Working voltage versus surface charge density for various salt concentrations and pore sizes with (a) $f < 0$ and (b) $f > 0$. The depth of the ion-wall potential is fixed at $\beta\epsilon = 2.0$.

fixed, whether from a natural reservoir or industrial process. However, saltwater can have a higher salt concentration than seawater so we include 2.0 M for comparison. For moderate surface charge density, the working voltage decreases with increasing salt concentration. This indicates that a larger difference in fresh and saltwater concentrations increases the voltage rise and the available energy available per cycle. At sufficiently high surface potential, the number of ions in the slit-pore and the surface charge density will saturate. On the ΔV_s vs. Q_s curves, saturation corresponds to a divergence of ΔV_s. In the relevant voltage range (less than 1 V), saturation is not reached, but we see effects of approaching saturation for small pore sizes, indicated in Figure II.7 for $H/\sigma = 1.5$ (red) by the fast rise of ΔV_s for each salt concentration. Such a fast rise in ΔV_s is prevalent to a lesser extent for $H/\sigma = 2.0$ (blue) and not present for $H/\sigma = 10.0$ (black), signifying that the saturation value for Q_s increases with pore size. The prominence of saturation effects at small pore size is due to the fact that only a smaller amount of ions can be drawn into the nano-sized slit than a larger pore. Saturation of the surface charge density is relevant for blue energy as the saturation surface charge density is insensitive to salt concentration. As saturation is approached, the difference in ΔV_s vs. Q_s curves for different salt concentrations becomes smaller, resulting in less energy being extracted from the CDLE process.

The potential difference ΔV uniquely determines the four states involved in the CDLE process as seen graphically in Figure II.3. In CDLE literature, ΔV is referred to as the "base voltage" and is equal to the "external voltage" for infinite charging time [40]; however, we use a generic "potential difference" to avoid confusion with the external potential in the cDFT framework. From a choice of ΔV, we identify

the Q_s^L and Q_s^H (Figure 1) and then numerically integrate between the freshwater and saltwater curves (ΔV_s vs. Q_s). We note that this ideal thermodynamic cycle does not take into account the power loss from self-discharge, which results from the tendency of the electrodes to move toward their spontaneous potential in open-circuit conditions, such as when switching from saltwater to freshwater. Self-discharge will be present when the potential difference is different from the spontaneous voltage. This power loss can be significant and increases as the distance between the potential difference and spontaneous voltage increases [40, 57].

Figure II.8 shows the energy available to extract from the CDLE process as a function of ΔV for various pore sizes. Two important parameters are the maximum available energy W_M and the ΔV^M that give the maximum energy. For pore sizes less than $H/\sigma = 3$, the energy has a maximum near $\Delta V = 0.25\ V$ and exhibits a notably lower maximum value in the available energy than pore sizes greater than $H/\sigma = 3$. Both phenomena can be explained by the electrode surface approaching saturation of the surface charge density as described above. Below $H/\sigma = 3$, the available energy also exhibits multiple shoulders, rather than a single, smooth peak. The shoulders

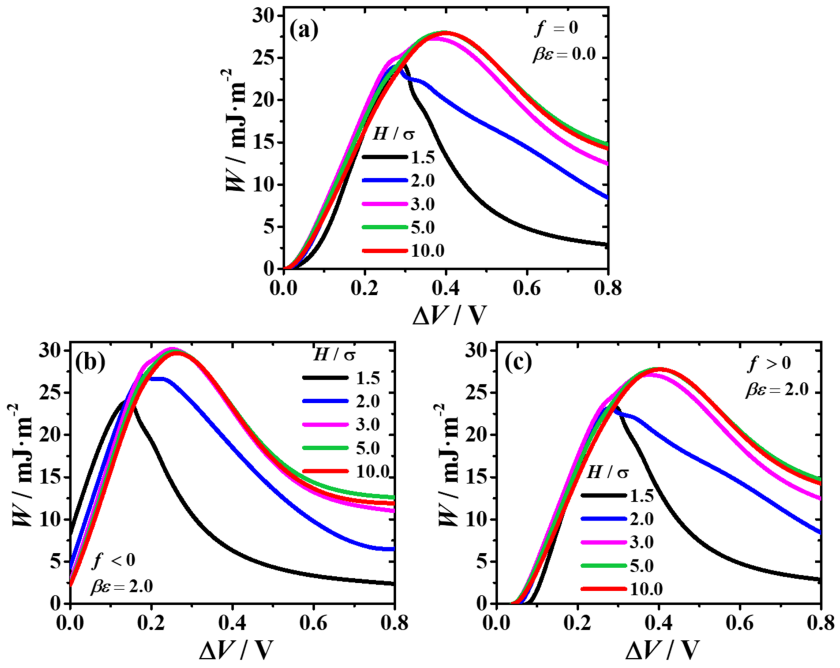

Figure II.8: Available blue energy W versus the potential difference ΔV for various pore sizes and types of interaction with the surface. Panels show cases (a) without preferential attraction ($f = 0$), (b) counterions attracted to surface ($f < 0$), and (c) coions attracted to the surface ($f > 0$).

are not numerical artifacts but, rather, reflect the strong oscillatory nature of the capacitance when the pore size is only a few times larger than the ion size [82]. For pore sizes above $H/\sigma = 3$, the available energy reaches a maximum around $\Delta V = 0.4\,V$. After the pore size has reached $H/\sigma \approx 4$, the energy profile is relatively insensitive to pore size, which is consistent with findings from previous work [69]. With preferential adsorption of counterions ($f < 0$), the amount of available energy increases for pore sizes above $H/\sigma = 1.5$. The pore size that provides the maximum available energy is closer to $H/\sigma = 3$, indicated by the pink curve in Figure II.8b. However, the more significant effect is that the locations of the maximums ΔV^M are shifted to lower potential differences ($\Delta V^M \approx 0.3V$), an effect that results from the shift in the V_s-Q_s curves. For $f > 0$, increasing $\beta\epsilon$ has nearly the opposite effect compared to $f < 0$. Namely, ΔV^M slightly increases and W_M decreases. We say nearly opposite because for the pore size $H/\sigma = 1.5$, the maximum energy W_M decreases with increasing $\beta\epsilon$, which is also true for $f < 0$.

To further highlight one of the key effects of preferential adsorption on the available energy, Figure II.9 shows the effect of increasing the depth of nonelectrostatic potential at a given pore size of $H/\sigma = 5$. For $f < 0$, increasing $\beta\epsilon$ leads to a lower ΔV^M, which is beneficial for the stability of the CDLE process as high working voltages can lead to electrolyte/electrode decomposition. More importantly, the ability to tune ΔV^M has practical implications as experiments [40, 57] have shown that matching ΔV to the spontaneous voltage offsets the power loss due to self-discharge. An important note for $f < 0$ is that with sufficient $\beta\epsilon$, a considerable amount of energy is available even for $\Delta V = 0$. For $f > 0$, ΔV^M increases with increasing $\beta\epsilon$, and increasing $\beta\epsilon$ only decreases the available energy. An essential

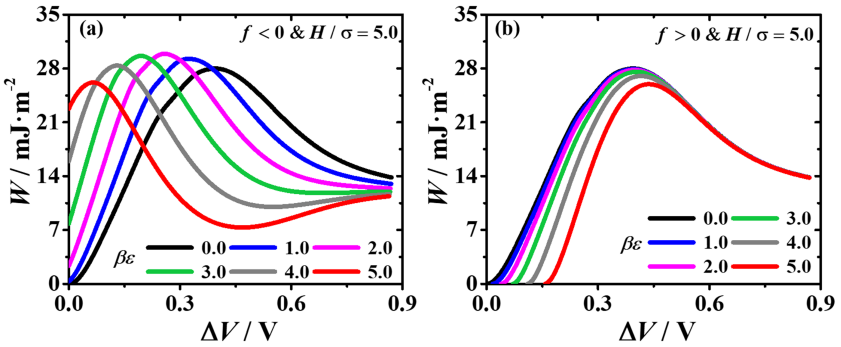

Figure II.9: Available blue energy W versus the potential difference ΔV for various strengths of interaction with the surface. Panels (a) and (b) show the case where counterions and coions are attracted to the surface, respectively.

relationship is the relation between the shifting ΔV^M and spontaneous voltage at different conditions. Namely, ΔV^M decreases with increasing $\beta\epsilon$ for $f < 0$ but, as previously noted, the spontaneous voltage also decreases. Figures S4 and S5 show the relationship between pore size and $\beta\epsilon$ on the distance of ΔV^M from the spontaneous voltage. The negative slopes in these plots indicates that surfaces with any degree of preferential adsorption (for both $f < 0$ and $f > 0$) moves ΔV^M closer to the spontaneous voltage than indifferent surfaces ($\beta\epsilon = 0$). In other words, the shift in ΔV^M with changing $\beta\epsilon$ is faster than the change in the spontaneous voltage for $f < 0$ and slower than the change in the spontaneous voltage for $f > 0$. For either case, the preferential adsorption shifts ΔV^M toward the spontaneous voltage.

The maximum of the available energy clearly varies non-monotonically with the depth of the external potential, evidenced by the peak of the curve for $\beta\epsilon = 2.0$ being the largest value for W_M. The available energy relies on the difference in the EDL response at different salt conditions. For small $\beta\epsilon$, the addition of nonelectrostatic adsorption enhances the electrostatic effects for $f < 0$. However, at high values of $\beta\epsilon$, the strong adsorption at the surface can lead to saturation of the surface charge density, regardless of salt concentration.

The above results suggest a nontrivial relationship in the available energy and potential difference as a function of the pore size and strength of nonelectrostatic potential. To present a complete picture, we computed the maximum available energy with various wall-ion attraction strengths and pore sizes. The maximum available energy W_M and the corresponding potential difference ΔV^M are given in Figure II.10 as a heat map. We find the non-monotonic behavior in the maximum energy with increasing $\beta\epsilon$ for $f < 0$ persists for all pore sizes above $H/\sigma = 2$. However, a monotonically decreasing behavior exists for $f > 0$ and $H/\sigma < 2$. Both results are consistent with the previous discussion. By tuning $\beta\epsilon$ and the pore size H/σ, we obtain the optimal condition for energy extraction. Comparing the optimal energy and the operation condition for $f < 0$ and $f > 0$, we find that the optimal energy for $f < 0$ (30.7 mJ/m^2) is larger than that for $f > 0$ (28.0 mJ/m^2). For $f < 0$, the globally optimal value for W_M occurs with $\beta\epsilon \approx 2.8$ and $H/\sigma \approx 3$; however, the peak is broad so the values of $\beta\epsilon \in [2, 3]$ result in similar values for W_M. The potential difference ΔV^M decreases as $\beta\epsilon$ increases for all pore sizes for $f < 0$ as expected, while the behavior of ΔV^M as $\beta\epsilon$ increases for $f > 0$ is a function of the pore size. In total, Figure II.10 suggests that electrode materials should be designed (1) with a large enough pore size to avoid the detrimental performance

effects of surface charge saturation and (2) with characteristics consistent with $f < 0$ to maximize the available energy and lower the potential difference.

Figure II.11 shows the heat map of the maximum available energy W_M and the corresponding potential difference ΔV^M in the plane of $\beta\epsilon$ and H/σ for a higher saltwater concentration (2.0 M). The extracted maximum energy significantly increases for this higher saltwater concentration. An important difference between 0.6 M and 2.0 M for saltwater is where the peak of the available energy is for $f < 0$. For 2.0 M, the peak is at a much lower value of $\beta\epsilon$ than for saltwater of 0.6 M, which indicates that the effect of preferential adsorption is more accessible with a higher saltwater concentrations. By comparing the contours at $\beta\epsilon = 0$ and $\beta\epsilon$ where W_M has an absolute maximum in Figures II.10a & II.11a, the peak value for 2.0 M saltwater is only ≈3% higher compared to no preferential adsorption, while for the 0.6 M case it is ≈10% higher (we note that our calculations do not consider the diffusion of ions into the pore or the energy cost associated with self-discharge [57] so such a 10% overall increase may not be practically obtainable). This suggest that while the optimal value is more accessible (in terms of $\beta\epsilon$) at higher salt concentrations, the

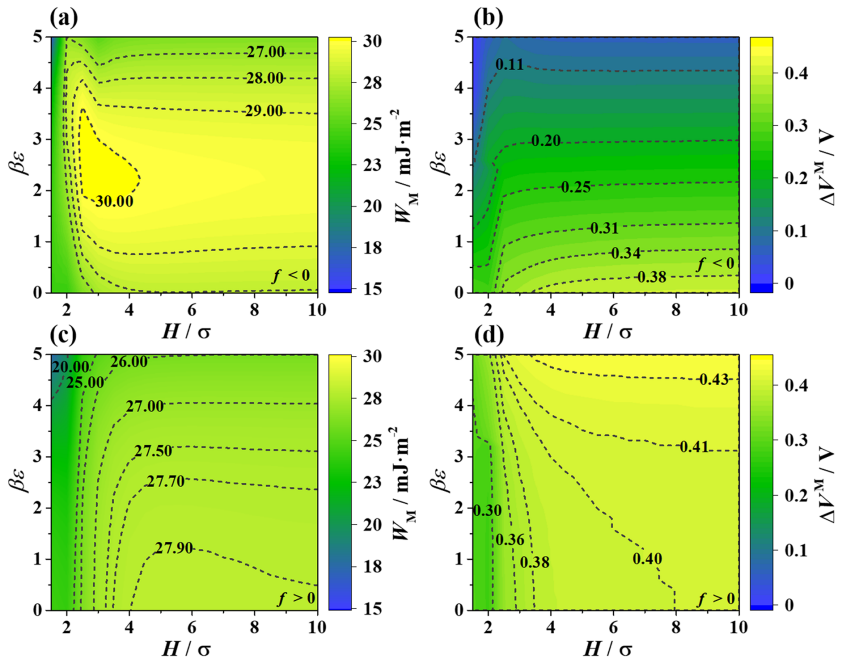

Figure II.10: Heat map of (a) the maximum available energy W_M and (b) the corresponding potential difference ΔV^M in the plane of $\beta\epsilon$ and H/σ for $f < 0$. Panels (c-d) are identical to (a-b) with $f > 0$. The concentration of freshwater is 0.024 M, and the concentration of saltwater is 0.6 M.

effect of preferential adsorption is more beneficial closer to seawater concentrations (0.6 M). For both saltwater concentrations, for $f < 0$, the absolute maximum occurs with pore sizes near $H/\sigma = 3.0$. Kong *et al.* reported that the thermodynamic efficiency was maximized around 1 nm, suggesting that the pore size for maximum energy extraction and maximum efficiency may coincide. However, the definition of thermodynamic efficiency for the CDLE cycle is unsettled as several measures have been proposed to calculate the maximum amount of work from the cycle [52, 69, 89]. Figures S6 and S7 show the same heat maps as Figures II.10 and II.11, respectively, with the *per area* energy divided by $2H$ to give a *per electrolyte volume* measure of the energy. These figures indicate that the smallest pore sizes give the most available energy, but this measure clearly neglects the electrode volume and is specific to the planar geometry in this study.

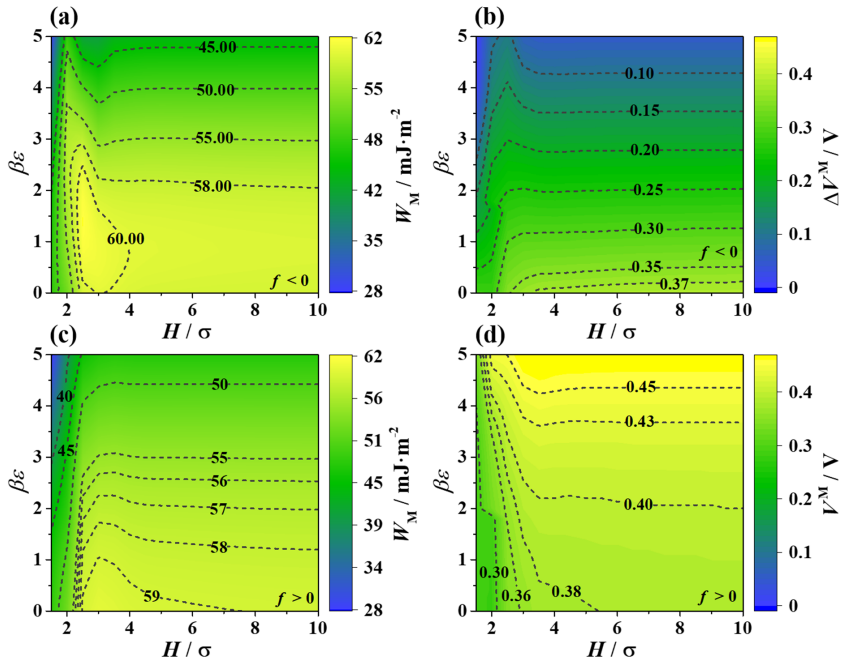

Figure II.11: Heat map of (a) the maximum available energy W_M and (b) the corresponding potential difference ΔV^M in the plane of $\beta\epsilon$ and H/σ for $f < 0$. Panels (c-d) are identical to (a-b) with $f > 0$. The concentration of freshwater is 0.024 M, and the concentration of saltwater is 2.0 M.

Conclusion

In this work, we use preferential adsorption of counterions or coions to tune the relationship between voltage difference and surface charge density for freshwater and saltwater in the CDLE thermodynamic cycle. We systematically investigated the effect of nonelectrostatic preferential adsorption between the surface and the ions on the energy extraction. Compared to pure electrostatic adsorption, we find that the preferential adsorption of *counterions* increases the available energy extraction while decreasing the potential difference of maximum energy for most pore sizes. With sufficient preferential adsorption, significant energy can be extracted even with zero applied potential difference. The preferential adsorption of coions decreases the available energy extraction and increases the potential difference of maximum energy. We also show that preferential adsorption shifts the potential difference of maximum energy closer to the spontaneous voltage (for both $f < 0$ and $f > 0$), though it is not possible to quantify the energy cost of operating away from the spontaneous voltage within a purely thermodynamic framework. Furthermore, we find that above $H/\sigma \approx 4$, the available energy extraction is roughly constant, indicating a wide range of pore sizes for material design. We have also shown that a larger concentration difference between the freshwater and the saltwater significantly increases the available energy, but the effect of preferential adsorption is weaker. The results presented here give insight to selection and design of electrode materials that can utilize the preferential adsorption to optimize the amount of energy that can be extracted in blue energy applications.

Appendix

Description of CDLE Process

Figure II.12a shows the four states of the CDLE process involving two open and two closed circuits during the charging/discharging process. The corresponding thermodynamic cycle is shown in Figure II.12b. The charging process takes the system from state I to state II. In state I, the external circuit is closed and the porous electrodes are surrounded by saltwater. The cell is charged from Q_s^L to Q_s^H, which has a corresponding adsorption of charged counterions to the electrode surfaces. The surface voltage increases from ΔV_s^L to the potential difference ΔV (also called the "base voltage" and "external voltage" in the limit of infinite charging time). From state II to III, the external circuit is opened and the saltwater is replaced with the freshwater. In this process, the surface charge density remains fixed because the circuit is open, and the surface voltage difference increases to a higher surface

voltage, ΔV_s^H. The surface voltage increases due to the inverse relation between the electrostatic potential difference and the ion concentration of the solution [47]. In state III, the two porous electrodes are surrounded by freshwater. After closing the external circuit, the surface charge density gradually decreases from Q_s^H to Q_s^L, and the corresponding surface voltage difference from ΔV_s^H to ΔV, resulting in a reverse current in the closed circuit. In state IV, the circuit is opened again, and the freshwater is replaced with the saltwater. The surface voltage difference decreases from ΔV to ΔV_s^L with a surface charge density Q_s^L.

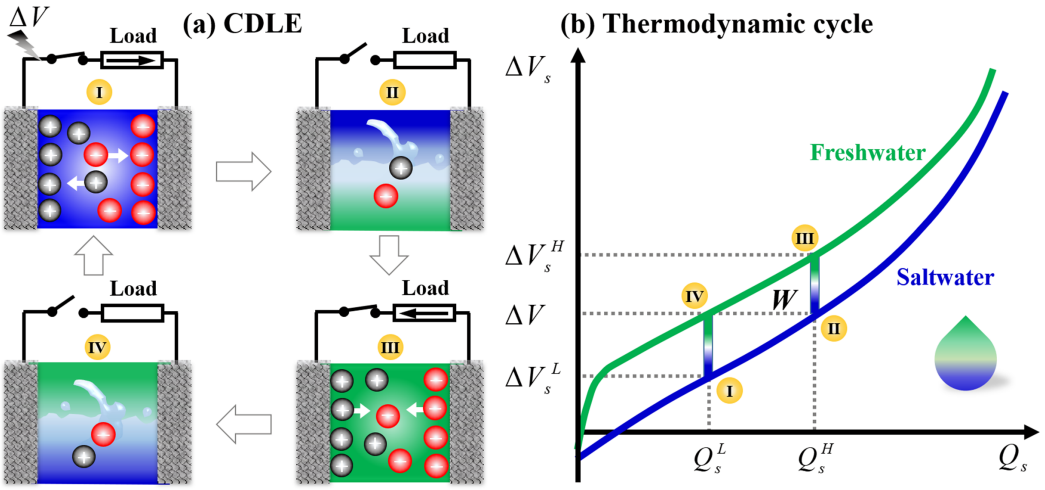

Figure II.12: Blue energy process graphic. (a) Schematic representation of the four states in CDLE process including two open-circuit and two closed-circuit states. (b) Thermodynamic cycle in the CDLE process. ΔV_s is the applied surface voltage difference between the positive and negative electrodes in the capacitor. Q_s is the surface charge density of the electrodes. Same as Figure 1 in the main text. Reproduced here for completeness.

Classical Density Functional Theory for Electrolyte System

In an inhomogeneous and open system with fixed chemical potential, system temperature, and volume, the grand potential is minimized at the equilibrium state [90],

$$\frac{\delta\Omega[\{\rho_i(\mathbf{r})\}]}{\delta\rho_i(\mathbf{r})} = 0, \tag{II.27}$$

In general, the grand potential is expressed as a functional of the local density profiles of species, $\Omega[\{\rho_i(\mathbf{r})\}]$.

$$\Omega[\{\rho_i(\mathbf{r})\}] = F[\{\rho_i(\mathbf{r})\}] + \sum_i \int d\mathbf{r}\rho_i(\mathbf{r})[V_i^{ext}(\mathbf{r}) - \mu_i], \tag{II.28}$$

where μ_i is the chemical potential of species, i, and determined by the thermodynamic condition of bulk system. $V_i^{ext}(\mathbf{r})$ is the external potential. The key quantity in the grand potential is the intrinsic Helmholtz free energy, $F[\{\rho_i(\mathbf{r})\}]$, which is separated into two contributions: the ideal gas part $F^{id}[\{\rho_i(\mathbf{r})\}]$ and the excess term due to the intermolecular interaction $F^{ex}[\{\rho_i(\mathbf{r})\}]$.

$$F[\{\rho_i(\mathbf{r})\}] = F^{id}[\{\rho_i(\mathbf{r})\}] + F^{ex}[\{\rho_i(\mathbf{r})\}] \tag{II.29}$$

The ideal gas term is

$$\beta F^{id}[\{\rho_i(\mathbf{r})\}] = \sum_i \int d\mathbf{r}\rho_i(\mathbf{r})\{\ln[\rho_i(\mathbf{r})\Lambda_i^3] - 1\}, \tag{II.30}$$

and taking derivative of the ideal gas free energy with respect to the density, we obtain the ideal chemical potential

$$\mu_i^{id}(\mathbf{r}) = \ln[\rho_i(\mathbf{r})\Lambda_i^3] \tag{II.31}$$

Combining Eqs. (II.27), (II.28), (II.29) and (II.31), the density profiles of ion species have

$$\rho_i(\mathbf{r}) = \frac{1}{\Lambda_i^3}\exp\left[\beta\left(\mu_i - V_i^{ext}(\mathbf{r}) - \frac{\delta F^{ex}[\{\rho_i(\mathbf{r})\}]}{\delta\rho_i(\mathbf{r})}\right)\right] \tag{II.32}$$

The excess free energy $F^{ex}[\{\rho_i(\mathbf{r})\}]$ captures additional physical effects by accounting for any intermolecular interactions beyond the ideal gas. For the electrochemical system, three contributions are included: the hard-sphere repulsions (also call excluded volume effect or steric effect), $F^{hs}[\{\rho_i(\mathbf{r})\}]$, the electrostatic correlation contribution, $F^{el}[\{\rho_i(\mathbf{r})\}]$, and the direct coulomb interaction, $F^{c}[\{\rho_i(\mathbf{r})\}]$.

$$F^{ex}[\{\rho_i(\mathbf{r})\}] = F^{hs}[\{\rho_i(\mathbf{r})\}] + F^{el}[\{\rho_i(\mathbf{r})\}] + F^{c}[\{\rho_i(\mathbf{r})\}] \tag{II.33}$$

In Eq. (II.33), the first term is obtained by the modified fundamental measure theory (MFMT) extended by Yu and Wu [85], according to the original FMT proposed by Rosenfeld. [91]

$$\beta F^{hs}[\rho(\mathbf{r})] = \int \Phi^{hs}[n_\alpha(\mathbf{r})]d\mathbf{r}, \tag{II.34}$$

where Φ^{hs} is the reduced excess Helmholtz energy density, and depends on six weighted densities, $n_\alpha(\mathbf{r})$. [92]

$$\Phi^{hs} = -n_0\ln(1-n_3) + \frac{n_1n_2 - \mathbf{n}_{V_1}.\mathbf{n}_{V_2}}{1-n_3} + \frac{n_2^3 - 3n_2\mathbf{n}_{V_2}\cdot\mathbf{n}_{V_2}}{36\pi}\left[\frac{\ln(1-n_3)}{n_3^2} + \frac{1}{n_3(1-n_3)^2}\right] \tag{II.35}$$

where six weighted densities $n_0(\mathbf{r})$, $n_1(\mathbf{r})$, $n_2(\mathbf{r})$, $n_3(\mathbf{r})$, $\mathbf{n}_{V_1}(\mathbf{r})$, and $\mathbf{n}_{V_2}(\mathbf{r})$ are related to the weight functions $\omega_i^{(\alpha)}(\mathbf{r})$, $\alpha = 0,\ 1,\ 2,\ 3,\ V_1,\ V_2$.

$$n_\alpha(\mathbf{r}) = \sum_i n_{\alpha,i}(\mathbf{r}) = \sum_i \int \rho_i(\mathbf{r}')\omega_i^{(\alpha)}(\mathbf{r}-\mathbf{r}')d\mathbf{r}' \tag{II.36}$$

The weight functions is employed to describe the geometry of the hard-sphere particle, mainly including two scalar functions associated with the volume and surface area, and a surface vector function.

$$\omega_i^{(3)}(\mathbf{r}) = \theta(\sigma_i/2 - |\mathbf{r}|) \tag{II.37}$$

$$\omega_i^{(2)}(\mathbf{r}) = \delta(\sigma_i/2 - |\mathbf{r}|) \tag{II.38}$$

$$\omega_i^{(V_2)}(\mathbf{r}) = \frac{\mathbf{r}}{|\mathbf{r}|}\delta(\sigma_i/2 - |\mathbf{r}|) \tag{II.39}$$

Another three weight functions are

$$\omega_i^{(1)}(\mathbf{r}) = \omega_i^{(2)}(\mathbf{r})/(2\pi\sigma_i) \tag{II.40}$$

$$\omega_i^{(0)}(\mathbf{r}) = \omega_i^{(2)}(\mathbf{r})/(\pi\sigma_i^2) \tag{II.41}$$

$$\omega_i^{(V_1)}(\mathbf{r}) = \omega_i^{(V_2)}(\mathbf{r})/(2\pi\sigma_i) \tag{II.42}$$

$\theta(\mathbf{r})$ is the Heaviside step function, and $\delta(\mathbf{r})$ is the Dirac delta function. In Eq.(II.33), the second term because of the electrostatic correlation is obtained by a quadratic functional Taylor expansion with respect to the bulk density of ions by neglecting the higher-order correlations.

$$\begin{aligned}\beta F^{el}[\{\rho_i(\mathbf{r})\}] =& \beta F^{el}[\{{\rho_i}^b\}] + \sum_i \int d\mathbf{r}\Delta C_i^{(1)el}[\rho_i(\mathbf{r}) - {\rho_i}^b] \\ &- \frac{1}{2}\sum_{i,j}\int\int d\mathbf{r}d\mathbf{r}'\Delta C_{ij}^{(2)el}(|\mathbf{r}-\mathbf{r}'|)\times[\rho_i(\mathbf{r}) - {\rho_i}^b]\times[\rho_j(\mathbf{r}') - {\rho_j}^b]\end{aligned} \tag{II.43}$$

where ${\rho_j}^b$ is the bulk density of ions. $\Delta C_i^{(1)el}$ and $\Delta C_i^{(2)el}$ represent one-order and two-order direct correlation functions, respectively.

$$\Delta C_i^{(1)el} = -\left.\frac{\delta\beta F^{el}}{\delta\rho_i(\mathbf{r})}\right|_b \tag{II.44}$$

$$\Delta C_{ij}^{(2)el}(|\mathbf{r}-\mathbf{r}'|) = -\left.\frac{\delta^2\beta F^{el}}{\delta\rho_i(\mathbf{r})\delta\rho_j(\mathbf{r}')}\right|_b \tag{II.45}$$

The one-order DCF is clearly proportional to the excess chemical potential in the bulk fluid; the two-order DCF can be expressed as

$$\Delta C_{ij}^{(2)el}(r) = C_{ij}(r) - C_{ij}^{hs}(r) - C_{ij}^{c}(r) \tag{II.46}$$

where $C_{ij}^{c}(r) = -l_B Z_i Z_j / r$ is the direct Coulomb correlation. The two-body DCF can be obtained from the mean-spherical approximation (MSA). [86, 93] For $0 \leq r \leq \left|\sigma_i - \sigma_j\right| /2$,

$$C_{ij}(r) - C_{ij}^{hs}(r) = -2l_B[-Z_i N_j + X_i(N_i + \Gamma X_i) - \frac{\sigma_i}{3}(N_i + \Gamma X_i)^2] \tag{II.47}$$

and for $\left|\sigma_i - \sigma_j\right| /2 \leq r \leq (\sigma_i + \sigma_j)/2$,

$$rC_{ij}(r) - rC_{ij}^{hs}(r) = l_B[(\sigma_i - \sigma_j)L_1 - rL_2 + r^2 L_3 + r^4 L_4] \tag{II.48}$$

where

$$L_1 = \frac{X_i + X_j}{4}(S_i - S_j) - \frac{\sigma_i - \sigma_j}{16}[(S_i + S_j)^2 - 4N_i N_j] \tag{II.49}$$

$$L_2 = (X_i - X_j)(N_i - N_j) + (X_i^2 + X_j^2)\Gamma + (\sigma_i + \sigma_j)N_i N_j - \frac{\sigma_i S_i^2 + \sigma_j S_j^2}{3} \tag{II.50}$$

$$L_3 = \frac{X_i}{\sigma_i}S_i + \frac{X_j}{\sigma_j}S_j + N_i N_j - \frac{S_i^2 + S_j^2}{2} \tag{II.51}$$

$$L_4 = \frac{S_i^2}{6\sigma_i^2} + \frac{S_j^2}{6\sigma_j^2} \tag{II.52}$$

The parameters used in here have $S_i = N_i + \Gamma X_i$, $\Gamma = \sqrt{\pi l_B \sum_i \rho_i^b X_i^2}$, and $N_i = \frac{X_i - Z_i}{\sigma_i}$. In addition, X_i can be solved through the following two equations:

$$(1 + \Gamma\sigma_i)X_i + \nu\sigma_i^2 \sum_j \rho_j^b \sigma_j X_j = Z_i \tag{II.53}$$

$$\nu \equiv (\pi/2)\left[1 - (\pi/6)\sum_i \rho_i^b \sigma_i^3\right]^{-1} \tag{II.54}$$

Then, we have

$$X_i = \frac{Z_i}{1 + \Gamma\sigma_i} - \frac{\nu\sigma_i^2}{1 + \Gamma\sigma_i}\left[\sum_j \frac{\rho_j^b \sigma_j Z_j}{1 + \Gamma\sigma_j} \Big/ \left(1 + \nu\sum_j \frac{\rho_j^b \sigma_j^3}{1 + \Gamma\sigma_j}\right)\right] \tag{II.55}$$

In Eq. (II.33), the last term from the direct coulomb interaction has

$$F^c[\{\rho_i(\mathbf{r})\}] = \sum_i \psi(\mathbf{r}) Z_i e \rho_i(\mathbf{r}) - \frac{\epsilon_0 \epsilon_r}{2}[\nabla\psi(\mathbf{r})]^2 \tag{II.56}$$

where $\psi(\mathbf{r})$ is the average electrostatic potential. In general, $\psi(\mathbf{r})$ can be solved by Poisson equation.

Trends in Spontaneous Voltage

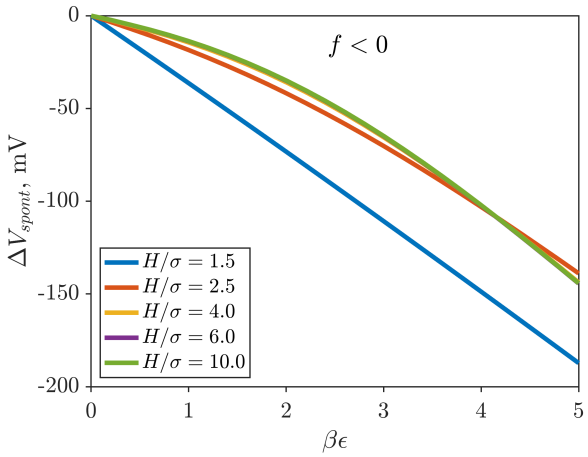

Figure II.13: Spontaneous voltage for $f < 0$ and a variety of pore sizes and preferential adsorption strengths. The concentration of saltwater is 0.6 M.

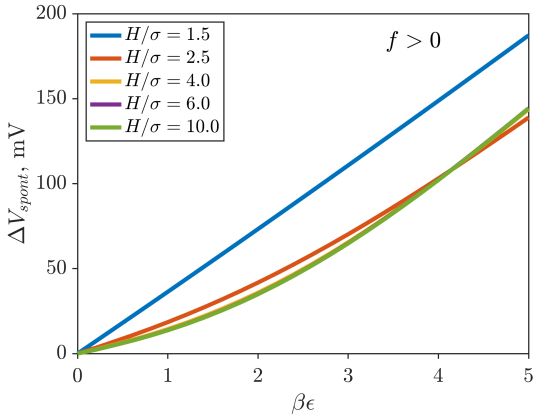

Figure II.14: Spontaneous voltage for $f > 0$ and a variety of pore sizes and preferential adsorption strengths. The concentration of saltwater is 0.6 M. The lines for $H/\sigma = 6$ and $H/\sigma = 10$ overlap.

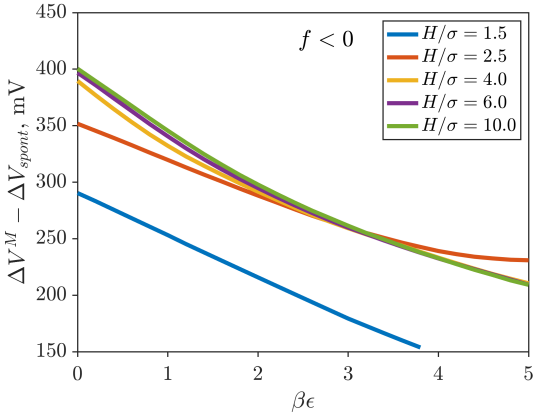

Figure II.15: Difference between the potential difference of maximum energy and the spontaneous voltage for $f < 0$ and a variety of pore sizes and preferential adsorption strengths. The concentration of freshwater is 0.024 M, and the concentration of saltwater is 0.6 M.

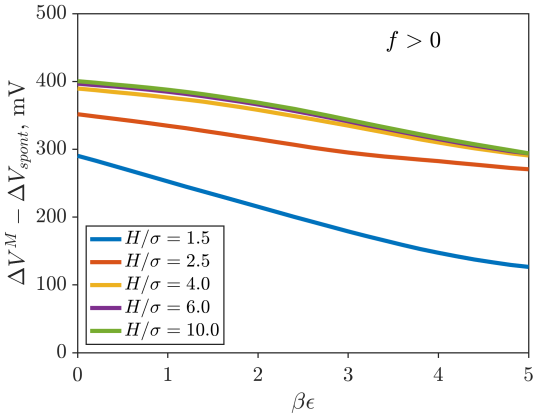

Figure II.16: Difference between the potential difference of maximum energy and the spontaneous voltage for $f > 0$ and a variety of pore sizes and preferential adsorption strengths. The concentration of freshwater is 0.024 M, and the concentration of saltwater is 0.6 M.

Maximum Energy per Volume of Electrolyte

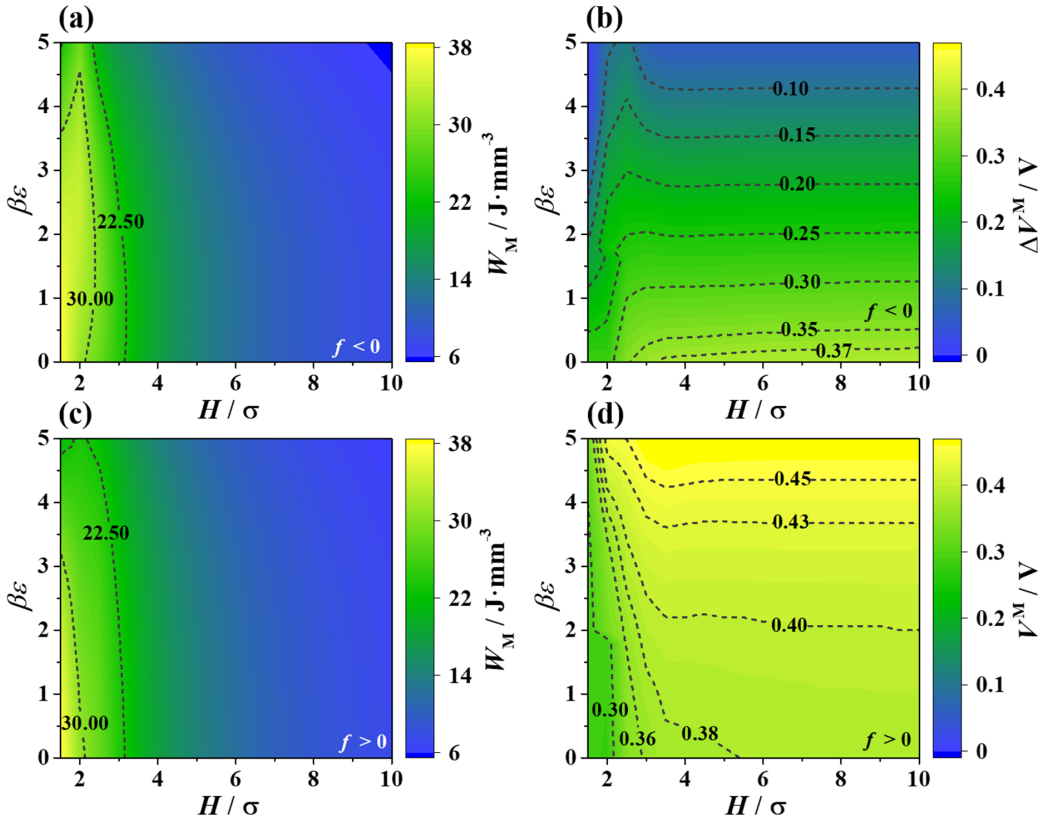

Figure II.17: Heat map of (a) the maximum available energy W_M per volume of electrolyte and (b) the corresponding potential difference ΔV^M in the plane of $\beta\epsilon$ and H/σ for $f < 0$. Panels (c-d) are identical to (a-b) with $f > 0$. The concentration of freshwater is 0.024 M, and the concentration of saltwater is 0.6 M.

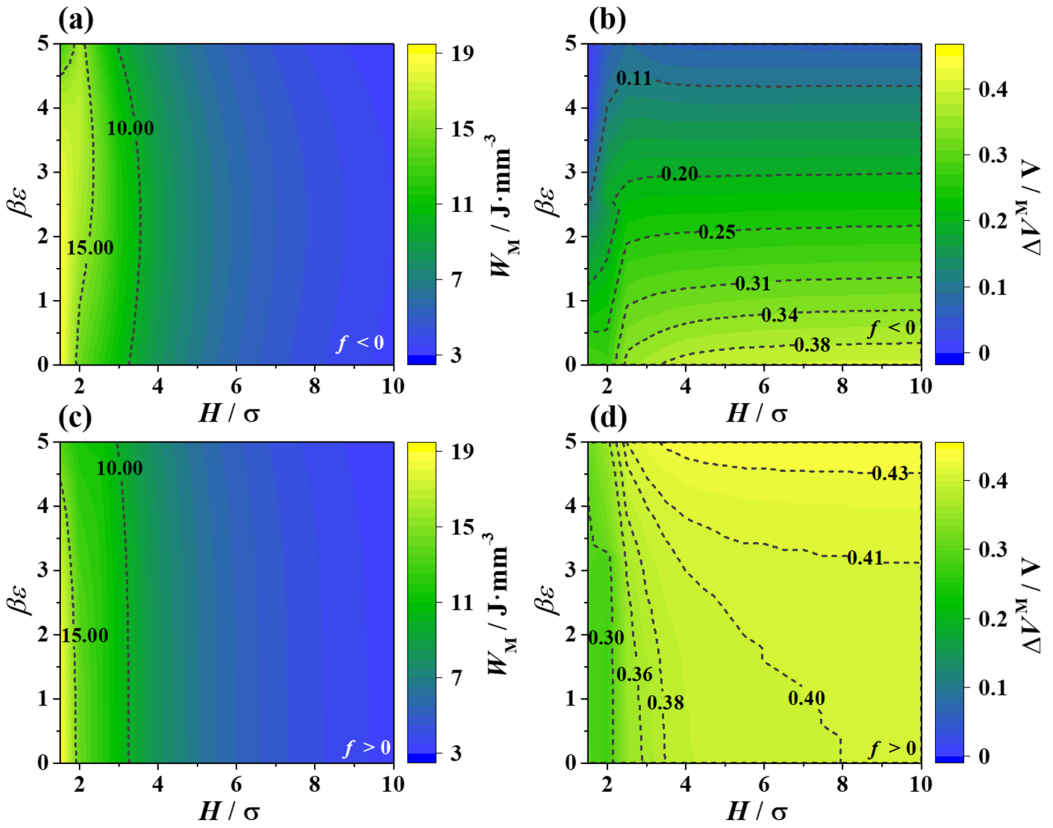

Figure II.18: Heat map of (a) the maximum available energy W_M per volume of electrolyte and (b) the corresponding potential difference ΔV^M in the plane of $\beta\epsilon$ and H/σ for $f < 0$. Panels (c-d) are identical to (a-b) with $f > 0$. The concentration of freshwater is 0.024 M, and the concentration of saltwater is 2.0 M.

References

(1) Bruch, D.; Balzer, C.; Wang, Z.-G. *The Journal of Chemical Physics* **2022**, *156*, 174704, DOI: 10.1063/5.0089260.

(2) Balzer, C.; Qing, L.; Wang, Z.-G. *ACS Sustainable Chemistry & Engineering* **2021**, *9*, 9230–9239, DOI: 10.1021/acssuschemeng.1c01326.

(3) Gibbs, J. W., *On the Equilibrium of Heterogeneous Substances - Part I*, 1874; Vol. 3, DOI: 10.1017/cbo9780511710377.051.

(4) Lippmann, G. *Annales de Chimie et de Physique* **1875**, *5*, 494–549.

(5) Quilliet, C.; Berge, B. *Current Opinion in Colloid and Interface Science* **2001**, *6*, 34–39, DOI: 10.1016/S1359-0294(00)00085-6.

(6) Mugele, F.; Baret, J. C. *Journal of Physics Condensed Matter* **2005**, *17*, 705–774, DOI: 10.1088/0953-8984/17/28/R01.

(7) Quinn, A.; Sedev, R.; Ralston, J. *Journal of Physical Chemistry B* **2005**, *109*, 6268–6275, DOI: 10.1021/jp040478f.

(8) Guangze, H.; Jianjia, M. *Continuum Mechanics and Thermodynamics* **2018**, *30*, 817–823, DOI: 10.1007/s00161-018-0644-8.

(9) Láng, G. G. *Journal of Solid State Electrochemistry* **2020**, *24*, 3039–3047, DOI: 10.1007/s10008-020-04745-5.

(10) Helmholtz, H. *Annalen der Physik* **1879**, *243*, 337–382, DOI: 10.1002/andp.18792430702.

(11) Gouy, M. *Journal de Physique Théorique et Appliquée* **1910**, *9*, 457–468, DOI: 10.1051/jphystap:019100090045700.

(12) Chapman, D. L. *The London, Edinburgh, and Dublin Philosophical Magazine and Journal of Science* **1913**, *25*, 475–481, DOI: 10.1080/14786440408634187.

(13) Stern, O. *Z. Elektrochem* **1924**, *30*, 508–516.

(14) Wu, M.; Li, W.; Li, S.; Feng, G. *RSC Advances* **2017**, *7*, 28945–28950, DOI: 10.1039/c7ra00443e.

(15) Reiner, E. S.; Radke, C. J. *Journal of the Chemical Society, Faraday Transactions* **1990**, *86*, 3901–3912.

(16) Wang, Z.-G. In *Variational Methods in Molecular Modeling*, Wu, J., Ed.; Molecular Modeling and Simulation; Springer: Singapore, 2017, pp 1–29, DOI: 10.1007/978-981-10-2502-0_1.

(17) Fredrickson, G., *The Equilibrium Theory of Inhomogeneous Polymers*; Oxford University Press: New York, 2007, DOI: 10.1093/acprof:oso/9780198567295.001.0001.

(18) Wang, Z. G. *Physical Review E - Statistical, Nonlinear, and Soft Matter Physics* **2010**, *81*, DOI: 10.1103/PhysRevE.81.021501.

(19) Salerno, K. M.; Frischknecht, A. L.; Stevens, M. J. *Journal of Physical Chemistry B* **2016**, *120*, 5927–5937, DOI: 10.1021/acs.jpcb.6b01392.

(20) Yu, Y. X.; Wu, J.; Gao, G. H. *Journal of Chemical Physics* **2004**, *120*, 7223–7233, DOI: 10.1063/1.1676121.

(21) Jiang, J.; Ginzburg, V. V.; Wang, Z. G. *Soft Matter* **2018**, *14*, 5878–5887, DOI: 10.1039/c8sm00595h.

(22) Hohenberg, P.; Kohn, W. *Physical Review* **1964**, *136*, DOI: 10.1103/PhysRev.136.B864.

(23) Kohn, W.; Sham, L. J. *Physical Review* **1965**, *140*, DOI: 10.1103/PhysRev.140.A1133.

(24) Mermin, N. D. *Physical Review* **1965**, *137*, DOI: 10.1103/PhysRev.137.A1441.

(25) Becke, A. D. *Journal of Chemical Physics* **2014**, *140*, 18–301, DOI: 10.1063/1.4869598.

(26) Roth, R. *Journal of Physics Condensed Matter* **2010**, *22*, 18, DOI: 10.1088/0953-8984/22/6/063102.

(27) Wu, J.; Li, Z. *Annual Review of Physical Chemistry* **2007**, *58*, 85–112, DOI: 10.1146/annurev.physchem.58.032806.104650.

(28) Tripathi, S.; Chapman, W. G. *Journal of Chemical Physics* **2005**, *122*, DOI: 10.1063/1.1853371.

(29) Wu, J. *AIChE Journal* **2006**, *52*, 1169–1193, DOI: 10.1002/aic.10713.

(30) Evans, R.; Oettel, M.; Roth, R.; Kahl, G. *Journal of Physics Condensed Matter* **2016**, *28*, DOI: 10.1088/0953-8984/28/24/240401.

(31) Jiang, J.; Cao, D.; Henderson, D.; Wu, J. *Physical Chemistry Chemical Physics* **2014**, *16*, 3934–3938, DOI: 10.1039/c3cp55130j.

(32) Jiang, J.; Cao, D.; Henderson, D.; Wu, J. *Journal of Chemical Physics* **2014**, *140*, 044714, DOI: 10.1063/1.4862990.

(33) Emborsky, C. P.; Feng, Z.; Cox, K. R.; Chapman, W. G. *Fluid Phase Equilibria* **2011**, *306*, 15–30, DOI: 10.1016/j.fluid.2011.02.007.

(34) Gallegos, A.; Ong, G. M. C.; Wu, J. *The Journal of Chemical Physics* **2021**, *155*, 241102, DOI: 10.1063/5.0066774.

(35) Chu, S.; Majumdar, A. *Nature* **2012**, *488*, 294–303.

(36) Isaacs, J. D.; Schmitt, W. R. *Science* **1980**, *207*, 265–273.

(37) Lanjewar, S.; Mukherjee, A.; Muzamil Rehman, L.; Roy, A. In *Advances in Membrane Technologies*; IntechOpen: 2020, DOI: 10.5772/intechopen.86953.

(38) Pattle, R. *Nature* **1954**, *174*, 660.

(39) Ma, M.; Zhao, S.; Liu, H.; Xu, Z. *AIChE Journal* **2017**, *63*, 1785–1791, DOI: 10.1002/aic.15708.

(40) Brogioli, D.; Ziano, R.; Rica, R. A., et al. *Energy and Environmental Science* **2012**, *5*, 9870–9880, DOI: 10.1039/c2ee23036d.

(41) Brogioli, D.; Zhao, R.; Biesheuvel, P. *Energy & Environmental Science* **2011**, *4*, 772–777.

(42) Rica, R. A.; Brogioli, D.; Ziano, R.; Salerno, D.; Mantegazza, F. *The Journal of Physical Chemistry C* **2012**, *116*, 16934–16938.

(43) Cipollina, A.; Micale, G., *Sustainable energy from salinity gradients*; Woodhead Publishing: Cambridge, UK, 2016.

(44) Jia, Z.; Wang, B.; Song, S.; Fan, Y. *Renewable and Sustainable Energy Reviews* **2014**, *31*, 91–100.

(45) Logan, B. E.; Elimelech, M. *Nature* **2012**, *488*, 313–319.

(46) Härtel, A.; Janssen, M.; Samin, S.; Van Roij, R. *Journal of Physics Condensed Matter* **2015**, *27*, 194129, DOI: 10.1088/0953-8984/27/19/194129.

(47) Brogioli, D. *Physical Review Letters* **2009**, *103*, DOI: 10.1103/PhysRevLett.103.058501.

(48) Rica, R. A.; Ziano, R.; Salerno, D., et al. *Entropy* **2013**, *15*, 1388–1407.

(49) La Mantia, F.; Pasta, M.; Deshazer, H. D.; Logan, B. E.; Cui, Y. *Nano Letters* **2011**, *11*, 1810–1813, DOI: 10.1021/nl200500s.

(50) Sales, B.; Saakes, M.; Post, J., et al. *Environmental Science & Technology* **2010**, *44*, 5661–5665.

(51) Hatzell, K. B.; Hatzell, M. C.; Cook, K. M., et al. *Environmental Science and Technology* **2015**, *49*, 3040–3047, DOI: 10.1021/es5055989.

(52) Moreno, D.; Hatzell, M. C. *Journal of Physical Chemistry C* **2018**, *122*, 22480–22486, DOI: 10.1021/acs.jpcc.8b05940.

(53) Dixit, M. B.; Moreno, D.; Xiao, X.; Hatzell, M. C.; Hatzell, K. B. *ACS Materials Letters* **2019**, *1*, 71–76, DOI: 10.1021/acsmaterialslett.9b00106.

(54) Pasta, M.; Wessells, C. D.; Cui, Y.; La Mantia, F. *Nano Letters* **2012**, *12*, 839–843.

(55) Zhang, J.; Hatzell, K. B.; Hatzell, M. C. *Environmental Science and Technology Letters* **2017**, *4*, 470–474, DOI: 10.1021/acs.estlett.7b00395.

(56) Yip, N. Y.; Brogioli, D.; Hamelers, H. V.; Nijmeijer, K. *Environmental Science and Technology* **2016**, *50*, 12072–12094, DOI: 10.1021/acs.est.6b03448.

(57) Iglesias, G. R.; Fernández, M. M. In *Interface Science and Technology*; Elsevier B.V.: 2018; Vol. 24, pp 119–140, DOI: 10.1016/B978-0-12-811370-7.00006-1.

(58) Lian, C.; Kong, X.; Liu, H.; Wu, J. *Journal of Physics Condensed Matter* **2016**, *28*, DOI: 10.1088/0953-8984/28/46/464008.

(59) Fernández, M. M.; Ahualli, S.; Iglesias, G. R., et al. *Journal of Colloid and Interface Science* **2015**, *446*, 307–316, DOI: 10.1016/j.jcis.2014.08.009.

(60) Jiménez, M. L.; Ahualli, S.; Fernández, M. M. In *Interface Science and Technology*; Elsevier B.V.: 2018; Vol. 24, pp 39–62, DOI: 10.1016/B978-0-12-811370-7.00003-6.

(61) Lian, C.; Zhan, C.; Jiang, D. E.; Liu, H.; Wu, J. *Journal of Physical Chemistry C* **2017**, *121*, 14010–14018, DOI: 10.1021/acs.jpcc.7b02827.

(62) Suss, M.; Porada, S.; Sun, X., et al. *Energy & Environmental Science* **2015**, *8*, 2296–2319.

(63) Porada, S.; Zhao, R.; Van Der Wal, A.; Presser, V.; Biesheuvel, P. *Progress in Materials Science* **2013**, *58*, 1388–1442.

(64) Chmiola, J.; Yushin, G.; Gogotsi, Y., et al. *Science* **2006**, *313*, 1760–1763.

(65) Huang, J.; Sumpter, B. G.; Meunier, V. *Angewandte Chemie* **2008**, *120*, 530–534.

(66) Feng, G.; Cummings, P. T. *The Journal of Physical Chemistry Letters* **2011**, *2*, 2859–2864.

(67) Jiang, D. E.; Meng, D.; Wu, J. *Chemical Physics Letters* **2011**, *504*, 153–158, DOI: 10.1016/j.cplett.2011.01.072.

(68) Largeot, C.; Portet, C.; Chmiola, J., et al. *Journal of the American Chemical Society* **2008**, *130*, 2730–2731.

(69) Kong, X.; Gallegos, A.; Lu, D.; Liu, Z.; Wu, J. *Physical Chemistry Chemical Physics* **2015**, *17*, 23970–23976, DOI: 10.1039/c5cp03514g.

(70) Chao, H.; Wang, Z. G. *Journal of Physical Chemistry Letters* **2020**, *11*, 1767–1772, DOI: 10.1021/acs.jpclett.0c00023.

(71) Brogioli, D.; Ziano, R.; Rica, R. A.; Salerno, D.; Mantegazza, F. *Journal of Colloid and Interface Science* **2013**, *407*, 457–466, DOI: 10.1016/j.jcis.2013.06.050.

(72) Gongadze, E.; Iglič, A. *Bioelectrochemistry* **2012**, *87*, 199–203, DOI: 10.1016/j.bioelechem.2011.12.001.

(73) Jäckel, N.; Simon, P.; Gogotsi, Y.; Presser, V. *ACS Energy Letters* **2016**, *1*, 1262–1265, DOI: 10.1021/acsenergylett.6b00516.

(74) Fumagalli, L.; Esfandiar, A.; Fabregas, R., et al. *Science* **2018**, *360*, 1339–1342.

(75) Levy, A.; Andelman, D.; Orland, H. *Physical Review Letters* **2012**, *108*, DOI: 10.1103/PhysRevLett.108.227801.

(76) Gavish, N.; Promislow, K. *Physical Review E* **2016**, *94*, 12611, DOI: 10.1103/PhysRevE.94.012611.

(77) Hartel, A. *Journal of Physics Condensed Matter* **2017**, *29*, 423002, DOI: 10.1088/1361-648X/aa8342.

(78) Lu, H.; Nordholm, S.; Woodward, C. E.; Forsman, J. *Journal of Chemical Physics* **2018**, *148*, 193814, DOI: 10.1063/1.5013134.

(79) Henderson, D.; Jiang, D. E.; Jin, Z.; Wu, J. *Journal of Physical Chemistry B* **2012**, *116*, 11356–11361, DOI: 10.1021/jp305400z.

(80) Warshavsky, V.; Marucho, M. *Physical Review E* **2016**, *93*, DOI: 10.1103/PhysRevE.93.042607.

(81) Qing, L.; Tao, J.; Yu, H., et al. *AIChE Journal* **2020**, *66*, e16938, DOI: 10.1002/aic.16938.

(82) Jiang, D. E.; Jin, Z.; Wu, J. *Nano Letters* **2011**, *11*, 5373–5377, DOI: 10.1021/nl202952d.

(83) Jiang, D. E.; Wu, J. *Journal of Physical Chemistry Letters* **2013**, *4*, 1260–1267, DOI: 10.1021/jz4002967.

(84) Osti, N. C.; Gallegos, A.; Dyatkin, B., et al. *The Journal of Physical Chemistry C* **2018**, *122*, 10476–10481.

(85) Yu, Y.-X.; Wu, J. *The Journal of Chemical Physics* **2002**, *117*, 10156–10164.

(86) Blum, L. *Molecular Physics* **1975**, *30*, 1529–1535, DOI: 10.1080/00268977500103051.

(87) Lian, C.; Gallegos, A.; Liu, H.; Wu, J. *Physical Chemistry Chemical Physics* **2017**, *19*, 450–457.

(88) Qing, L.; Li, Y.; Tang, W., et al. *Langmuir* **2019**, *35*, 4254–4262, DOI: 10.1021/acs.langmuir.9b00088.

(89) Boon, N.; Van Roij, R. *Molecular Physics* **2011**, *109*, 1229–1241, DOI: 10.1080/00268976.2011.554334.

(90) Hansen, J.-P.; McDonald, I. R., *Theory of simple liquids*; Elsevier: 1990.

(91) Rosenfeld, Y. *Journal of Physics: Condensed Matter* **2002**, *14*, 9141–9152.

(92) Li, Z.; Wu, J. *Physical Review E* **2004**, *70*, 031109.

(93) Hiroike, K. *Molecular Physics* **1977**, *33*, 1195–1198.

Chapter III

REVERSIBLE POLYELECTROLYTE ADSORPTION AND MEDIATED INTERACTIONS BETWEEN SURFACES

The connectivity innate to polyelectrolytes distinguishes their adsorption behavior from the small ion systems discussed in the previous chapter. A connected chain has a limited number of conformations near a planar surface compared to a bulk solution, leading to an entropic force that depletes polymer. The presence of charges along the polymer further influences the chain conformation and leads to rich adsorption behavior near a solid surface, especially when changing solution conditions (*i.e.* salt concentration). The polymer-mediated interaction between two solid surfaces is directly connected to the properties of the adsorbed polymer layers. Nonelectrostatic interactions with a surface can significantly impact the adsorption of polyelectrolytes to charged surfaces. This chapter explores the interplay between nonelectrostatic and electrostatic adsorption adsorption of strong and weak polyelectrolytes to planar surfaces and the resultant polymer-mediated surface interaction. For strong polyelectrolytes, polymer classical density functional theory is utilized to capture all of the relevant and competing forces. For weak polyelectrolytes, to focus on the charge regulation, a self-consistent field theory is developed.

This chapter includes content from our previously published article:

Balzer, C.; Jiang, J.; Marson, R. L.; Ginzburg, V. V.; Wang, Z.-G. *Langmuir* **2021**, *37*, 5483–5493, DOI: 10.1021/acs.langmuir.1c00139

I am thankful to the Dow Chemical Company for their partial support of the work in this chapter and the wonderful discussions during the course of the project with Dr. Chang Yun Son, Dr. Valeriy Ginzburg, Dr. Tom Kalantar, Dr. Christopher Tucker, and Dr. Anthony Van Dyk. For the weak polyelectrolytes, much of theory stems Prof. Zhen-Gang Wang's initial notes on the topic.

III.1 Strong Polyelectrolytes

Introduction

The adsorption of polyelectrolytes to solid surfaces has been widely studied for several decades. Interest in the topic has persisted due to the wide parameter space of polyelectrolyte solutions and the corresponding variety of adsorption behaviors and mediated interactions that arise from the subtle interplay among electrostatic effects, excluded volume, and chain connectivity of polyelectrolyte near a solid surface [2–9]. Forsman summarized the difficulty in isolating the effect of these subtleties and how they manifest in experimental measurements and theoretical predictions of polyelectrolyte-mediated forces[10]. Forsman concluded that despite significant progress, there is a lack of consensus on the effect of polyelectrolyte addition on the resulting force. Such unresolved issues in polyelectrolyte adsorption and mediated interaction of solid surfaces are relevant for many industrial applications, including stabilization of colloidal suspensions, waste water treatment, papermaking, and biomedical applications [11–15].

The vast majority of studies of polyelectrolyte adsorption and mediated interaction – both experimental [6, 16–21] and theoretical [19, 22–33] – focus on surfaces that carry an opposite charge to the polyelectrolyte backbone, where the adsorption is primarily driven by electrostatic attraction to the surface. There have also been efforts focused on electrostatically driven like-charged polyelectrolyte adsorption to induce long-range repulsion [34–37], where multivalent ion adsorption provides enough overcharging to drive adsorption of a like-charged polymer secondary layer[31, 38]. Whether like-charged or oppositely charged, the adsorption is driven by electrostatics in these works. When the adsorption is purely electrostatic, bringing two surfaces with adsorbed polymer results in long-range repulsion and short-range attraction due to the overlap of adsorbed polymer layers and a bridging effect between the polymer and both surfaces, respectively [5, 33, 35–37, 39–42].

A particularly interesting facet is the role of nonelectrostatic adsorption on the adsorption behavior and the resulting polymer-mediated interaction. Nonelectrostatic interactions include any non-ionic interactions, such as hydrogen bonding or hydrophobic interactions. The presence of nonelectrostatic adsorption complicates the balance of electrostatic effects near the surface, particularly upon salt addition. Adding salt to a polyelectrolyte solution can lead to monotonically increasing[27, 43–49], decreasing[31, 50, 51], or non-monotonic[32, 38, 49, 52–54] behavior in the adsorbed amount of polyelectrolyte. A recent review states that the adsorbed

mass “normally increases“ with monovalent salt addition [42], while mean-field theory would suggest only decreasing adsorption with salt addition for pure electrostatic adsorption [55]. The wide range of qualitatively different behaviors for the adsorbed amount upon salt addition have been historically attributed to effects of nonelectrostatic polymer-surface affinity[44]. More recently, Forsman showed that including electrostatic correlation in a classical density functional theory (cDFT) captures the non-monotonic behavior of the adsorbed amount upon salt addition for oppositely-charged systems without the inclusion of nonelectrostatic affinity to the surface [32]. The system-dependent behavior upon salt addition and seemingly conflicting explanations in the literature demonstrate the need to understand and isolate the role of nonelectrostatic adsorption. Nonelectrostatic attraction to the surface and the corresponding balance with electrostatic interactions undoubtedly plays a role in the polyelectrolyte-mediated interactions.

In this work, we use a previously developed cDFT framework [56] to characterize the effect of the strength of nonelectrostatic adsorption, salt addition, and polyelectrolyte charge density on the polyelectrolyte adsorption and corresponding mediated interaction. The cDFT framework has two main advantages over self-consistent field theory (SCFT) approaches from previous works [22, 39, 57] : cDFT is better able to describe density profiles even in the absence of electrostatics[58], and cDFT takes into account electrostatic correlations not present in mean-field treatment of electrostatics [29, 33, 56, 59]. Previous works have not focused specifically on the role of nonelectrostatic attraction in relation to both adsorption and polyelectrolyte mediated-interactions. We focus on the surfaces that carry the same charge as the polymer to reflect common systems where nonelectrostatic adsorption likely plays a prominent role. For example, polyacrylic acid has been shown to adsorb to a like-charge surface, such as silica or titanium dioxide at high pH, where zeta potentials on the order of -10 mV have been measured [37, 60, 61]. Our results show that the presence of nonelectrostatic attraction can substantially enhance polyelectrolyte adsorption, which displaces counterion adsorption at the surface. Interestingly, we find that upon salt addition the adsorbed amount can decrease, increase, or vary non-monotonically for a neutral surface depending on the nonelectrostatic attraction strength, while only increasing for sufficiently negatively charged surface within the parameters studied. The interplay between the surface charge density and strength of the nonelectrostatic attraction determine which of the the three regimes is dominant. Further, we show that with sufficient strength of nonelectrostatic attraction, the polyelectrolyte forms thin adsorption layer that leads to an extended double-layer,

providing a long-range repulsive barrier between two like-charge surfaces that can overcome the dispersive (Hamaker) attraction between two colloids. Despite the variety of regimes for adsorption upon salt addition, the height of the repulsive barrier always decreases with salt addition.

Methodology

To study the polyelectrolyte adsorption and interaction, we model a polyelectrolyte solution in a slit-pore between homogeneous surfaces as shown in Figure III.1. The density functional theory with incompressibility used here was reported in a previous work [56] so only the main details will be reproduced. The polyelectrolyte solution is made up of polyions with N segments, small ions, and solvent. The species have diameter σ_i, and each non-solvent species has valence Z_i – the solvent is neutral. Z_i is positive for positively charged species and negative for negatively charged species. The polyelectrolyte chains are represented by tangentially-connected charged hard spheres [62]. The counterion to the polyelectrolyte is treated as identical to the salt ions.

The incompressible cDFT assumes a fixed local packing fraction, $\eta = \sum_i \rho_i(\mathbf{r})v_i$, where $\rho_i(\mathbf{r})$ is the local density and v_i is the species volume. i refers to the solvent, small ions ($\pm$), and polyelectrolytes (p). We have chosen a packing fraction of

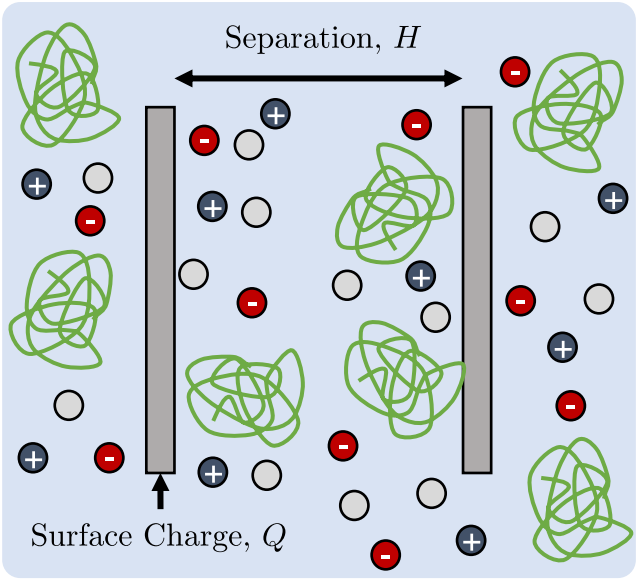

Figure III.1: Generic schematic of polyelectrolyte solution in a slit-pore geometry. The polymer (green) is uniformly charged and is linear. The polymer, salt ions, and solvent (gray) are in contact with a bulk reservoir.

$\eta = 0.5$ throughout this work. Note that the incompressibility condition is added to the free energy functional as a constraint. In the cDFT framework, the free energy is fully specified as a functional of the density profiles $\{\rho_i(\mathbf{r})\}$. For the system considered in this work, the grand potential can be written as

$$W[\rho_p(\mathbf{R}), \{\rho_\alpha(\mathbf{r})\}, \rho_s(\mathbf{r}), \phi(\mathbf{r}), \lambda(\mathbf{r})] = F_{\text{id}} + \int d\mathbf{r} f_{\text{ex}}[\{\rho_i(\mathbf{r})\}, \phi(\mathbf{r}); \mathbf{r}]$$
$$+ \int d\mathbf{R}\rho_p(\mathbf{R})\Big[\Psi_p(\mathbf{R}) - \mu_p\Big] + \sum_\alpha \int d\mathbf{r}\rho_\alpha(\mathbf{r})\big[\psi_\alpha(\mathbf{r}) - \mu_\alpha\big] + \int d\mathbf{r}\rho_s(\mathbf{r})\big[\psi_s(\mathbf{r}) - \mu_s\big]$$
$$+ \int d\mathbf{r}\lambda(\mathbf{r})\Big[\sum_i v_i\rho_i(\mathbf{r}) - \eta\Big] \quad \text{(III.1)}$$

where F_{id} is the ideal contribution, $\mathbf{R}$ represents the $3N$-dimensional position vector for the entire chain and $d\mathbf{R} = \prod_{m=1}^{N} d\mathbf{r}_m$. α refers only to small ions (salts and counterions). $\phi(\mathbf{r})$ is the electric potential. $\Psi_p(\mathbf{R})$ is the external potential that acts on individual polymer segments, and $\psi_\alpha(\mathbf{r})$ and $\psi_s(\mathbf{r})$ are the external potential for small ions and solvent respectively. μ_i is the chemical potential. $\lambda(\mathbf{r})$ is a Lagrange multiplier used to enforce the incompressibility condition. The overall segment density $\rho_p(\mathbf{r})$ is related to the polymer chain density $\rho_p(\mathbf{R})$ as

$$\rho_p(\mathbf{r}) = \sum_{m=1}^{N} \rho_{sm}(\mathbf{r}) = \sum_{m=1}^{N} \int d\mathbf{R}\delta(\mathbf{r} - \mathbf{r}_m)\rho_p(\mathbf{R}) \quad \text{(III.2)}$$

where $\delta(\mathbf{r})$ is the Dirac-delta function. The ideal free energy is given by

$$\beta F_{\text{id}} = \int d\mathbf{R}\rho_p(\mathbf{R})\Big[\ln(\rho_p(\mathbf{R})a_p^N) - 1\Big] + \int d\mathbf{R}\rho_p(\mathbf{R})\beta V_b(\mathbf{R}) +$$
$$\sum_\alpha \int d\mathbf{r}\rho_\alpha(\mathbf{r})\Big[\ln(\rho_\alpha(\mathbf{r})a_\alpha) - 1\Big] + \int d\mathbf{r}\rho_s(\mathbf{r})\Big[\ln(\rho_s(\mathbf{r})a_s) - 1\Big] \quad \text{(III.3)}$$

where a_i is a volume scale that has no thermodynamic consequence as it merely shifts the chemical potential by a constant. The bonding potential $V_b(\mathbf{R})$ is given for a freely-jointed chain model.

$$\exp[-\beta V_b(\mathbf{R})] = a_p^{N-1} \prod_{m=1}^{N-1} \frac{\delta(|\mathbf{r}_{m+1} - \mathbf{r}_m| - \sigma_p)}{4\pi\sigma_p^2} \quad \text{(III.4)}$$

The excess free energy density f_{ex} can be written as the sum of f_{hs}, f_{C}, f_{el}, f_{ch}, and f_{vdW} which respectively account for hard-core excluded volume interaction, mean-field Coulomb interaction, nonbonded electrostatic correlation, chain connectivity correlation, and van der Waals attraction. In this work, we ignore the effect of

van der Waals attraction between system components, $f_{\mathrm{vdW}} = 0$. The Coulomb interaction is given by

$$f_{\mathrm{C}}[\phi(\mathbf{r}), \{\rho_{i'}(\mathbf{r})\}; \mathbf{r}] = \sum_{i'} \phi(\mathbf{r}) Z_{i'} e_0 \rho_{i'}(\mathbf{r}) - \frac{\epsilon_r \epsilon_0}{2} \left[\nabla\phi(\mathbf{r})\right]^2 \tag{III.5}$$

where $\phi(\mathbf{r})$) is the electrostatic potential. i' refers to non-solvent components – small ions and polyelectrolytes. We use a functional Taylor expansion to account for nonbonded electrostatic correlation [59]

$$f_{\mathrm{el}}[\{\rho_{i'}(\mathbf{r})\}; \mathbf{r}] \approx f_{\mathrm{el}}[\{\rho_{i'}^{\mathrm{ref}}(\mathbf{r})\}; \mathbf{r}] + \sum_{i'} \int d\mathbf{r} \frac{\delta f_{\mathrm{el}}[\{\rho_{i'}^{\mathrm{ref}}(\mathbf{r})\}]}{\delta \rho_{i'}^{\mathrm{ref}}(\mathbf{r})} \left[\rho_{i'}(\mathbf{r}) - \rho_{i'}^{\mathrm{ref}}(\mathbf{r})\right] + \ldots \tag{III.6}$$

where the nonbonded electrostatic correlation for the reference fluid is obtained using the mean spherical approximation (MSA) [63–65],

$$\beta f_{\mathrm{el}}[\{\rho_{i'}^{\mathrm{ref}}(\mathbf{r})\}; \mathbf{r}] = \frac{\Gamma^3(\mathbf{r})}{3\pi} - l_B \sum_i \rho_i Z_i \left(\frac{Z_i - Z_i^{\mathrm{eff}}}{\sigma_i}\right) \tag{III.7}$$

In Equation III.7, $\Gamma(\mathbf{r})$ is the MSA screening parameter; $l_B = \beta e_0^2 / 4\pi\epsilon_r\epsilon_0$ is the Bjerrum length with e_0 and $\epsilon_r\epsilon_0$ being the elementary charge and electric permittivity, respectively; and $Z_i^{\mathrm{eff}} = (Z_i - \chi\sigma_i^2)/(1 + \Gamma\sigma_i)$ can be considered an effective valence. The screening parameter Γ is given by the implicit relationship

$$\Gamma^2(\mathbf{r}) = \pi l_B \sum_{i'} \rho_{i'}^{\mathrm{ref}}(\mathbf{r}) \left(Z_{i'}^{\mathrm{eff}}\right)^2 \tag{III.8}$$

and χ is given by

$$\chi = \sum_{i'} \frac{\rho_{i'}^{\mathrm{ref}}(\mathbf{r}) \sigma_{i'} Z_{i'}}{1 + \Gamma\sigma_{i'}} \Bigg/ \left[\frac{2(1-\eta)}{\pi} + \sum_{i'} \frac{\rho_{i'}^{\mathrm{ref}}(\mathbf{r}) \sigma_{i'}^3}{1 + \Gamma\sigma_{i'}}\right] \tag{III.9}$$

In this work, we use the Reference Fluid Density (RFD) scheme developed by Gillespie and co-workers [66] for the reference density as opposed to using the bulk density as a reference. We use a first-order approximation in Eq. III.6, which is shown to be nearly as accurate as the second-order expansion with RFD in our previous work [59].

We use first-order TPT (TPT-1) [67–70] to account for the connectivity correlation, which has been successfully used for uncharged polymer systems [71–73]. The free energy density can be written as the sum of hard-sphere and electrostatic correlation contributions.

$$f_{\mathrm{ch}}[\{\rho_{i'}(\mathbf{r})\}; \mathbf{r}] = f_{\mathrm{ch}}^{\mathrm{hs}}[\{\rho_{i'}(\mathbf{r})\}; \mathbf{r}] + f_{\mathrm{ch}}^{\mathrm{el}}[\{\rho_{i'}(\mathbf{r})\}; \mathbf{r}] \tag{III.10}$$

The hard sphere part can be written in terms of the pair distribution function at contact $g(\sigma_p, \{\rho_{i'}(\mathbf{r})\})$

$$\beta f_{\mathrm{ch}}^{\mathrm{hs}}[\{\rho_{i'}(\mathbf{r})\};\mathbf{r}] = \frac{(1-N)\rho_p(\mathbf{r})}{N} \ln g(\sigma_p, \{\rho_{i'}(\mathbf{r})\}) \tag{III.11}$$

The electrostatic correlation part can be written as a functional Taylor expansion

$$f_{\mathrm{ch}}^{\mathrm{el}}[\{\rho_{i'}(\mathbf{r})\};\mathbf{r}] \approx f_{\mathrm{ch}}^{\mathrm{el}}[\{\rho_{i'}^{\mathrm{ref}}(\mathbf{r})\};\mathbf{r}] + \sum_{i'} \int d\mathbf{r} \frac{\delta f_{\mathrm{ch}}^{\mathrm{el}}[\{\rho_{i'}^{\mathrm{ref}}(\mathbf{r})\}]}{\delta \rho_{i'}^{\mathrm{ref}}(\mathbf{r})} \left[\rho_{i'}(\mathbf{r}) - \rho_{i'}^{\mathrm{ref}}(\mathbf{r})\right] + \ldots \tag{III.12}$$

where we use a first-order approximation to maintain consistency with the non-bonded electrostatic correlation. The energy density for a reference density is given by

$$\beta f_{\mathrm{ch}}^{\mathrm{el}}[\{\rho_{i'}^{\mathrm{ref}}(\mathbf{r})\};\mathbf{r}] = \frac{(1-N) l_B \rho_p^{\mathrm{ref}}(\mathbf{r}) \left[Z_i^2 - (Z_i^{\mathrm{eff}})^2\right]}{N\sigma_p} \tag{III.13}$$

To account for the hard sphere excluded volume effect, we use a functional based on a local density approximation (LDA) combined with the Boublík-Mansoori-Carnarhan-Starling-Leland (BMCSL) equation of state [74, 75]. The functional has the form

$$\beta f_{\mathrm{hs}}[\{\rho_i(\mathbf{r})\};\mathbf{r}] = -\xi_0 \ln(1-\xi_3) + \frac{\xi_1\xi_2}{1-\xi_3} + \frac{\xi_2^3}{36\pi}\left[\frac{\ln(1-\xi_3)}{\xi_3^2} + \frac{1}{\xi_3(1-\xi_3)^2)}\right] \tag{III.14}$$

where $\xi_3 = \pi \sum_i \rho_i(\mathbf{r})\sigma_i^3/6$, $\xi_2 = \pi \sum_i \rho_i(\mathbf{r})\sigma_i^2$, $\xi_1 = \sum_i \rho_i(\mathbf{r})\sigma_i/2$, $\xi_0 = \sum_i \rho_i(\mathbf{r})$. Clearly, ξ_3 is the equal to the local packing fraction and is equal to η by the incompressibility condition. The effects of excluded-volume interactions in Eq. III.14 are especially important for systems where the solvent, monomers, and ions have different sizes. In the limit where all species have the same size, σ, and the packing fraction η is uniform, the variables ξ_0, ξ_1, ξ_2, and ξ_3 become constants, and the free energy from excluded-volume becomes a pure additive constant. In this regard, the cDFT calculation with $\sigma_p = \sigma_\alpha = \sigma_s = \sigma$ and constant η is similar to a “compressible" self-consistent field theory, where the incompressibility condition is enforced by adding a “void“ component with volume fraction equal to $1-\eta$. Jain *et al.* showed that cDFT and compressible SCFT predict similar thermodynamic behavior for neutral polymers between hard walls if $\eta \geq 0.5$ [58, 76]. The advantage of cDFT over SCFT stems from a more accurate description of the density fluctuations near the walls (even for the equal diameter case) and

also, from the straight-forward generalization to the case of non-equal diameters, in addition to being more compatible with the treatment of electrostatic correlations.

Extremizing the grand potential (Eq. III.1) with respect to the densities and introduced fields - $\lambda(\mathbf{r})$ and $\phi(\mathbf{r})$ - results in the following equations,

$$\rho_p(\mathbf{R})a_p^N = \exp\left\{\beta\Big[\mu_p - V_b(\mathbf{R}) - \sum_{m=1}^{N}\Lambda_p(\mathbf{r_m})\Big]\right\} \tag{III.15}$$

$$\rho_\alpha(\mathbf{r})a_\alpha = \exp\left\{\beta\left[\mu_\alpha - \Lambda_\alpha(\mathbf{r})\right]\right\} \tag{III.16}$$

$$\eta\lambda(\mathbf{r})v_s = \beta\left[\mu_s - \psi_s - \frac{\partial f_{\text{ex}}}{\partial\rho_s(\mathbf{r})}\right] - \ln\Big(\rho_s(\mathbf{r})a_s\Big) \tag{III.17}$$

$$\epsilon_r\epsilon_0\nabla^2\phi(\mathbf{r}) = \sum_{i'} Z_i e_o \rho_{i'}(\mathbf{r}) \tag{III.18}$$

$$\eta = \sum_i \rho_i(\mathbf{r})v_i \tag{III.19}$$

where Λ_p and Λ_α are effective fields for monomers and small ions, respectively:

$$\Lambda_p(\mathbf{r}) = \frac{\partial f_{\text{ex}}}{\partial\rho_p(\mathbf{r})} + \psi_p(\mathbf{r}) + Z_p e_0\phi(\mathbf{r}) + \lambda(\mathbf{r})v_p \tag{III.20}$$

$$\Lambda_\alpha(\mathbf{r}) = \frac{\partial f_{\text{ex}}}{\partial\rho_\alpha(\mathbf{r})} + \psi_\alpha(\mathbf{r}) + Z_\alpha e_0\phi(\mathbf{r}) + \lambda(\mathbf{r})v_\alpha \tag{III.21}$$

In this work, we consider the effect of non-electrostatic adsorption of the polymer. This effect is accounted for using the external potential $\psi_p(\mathbf{r})$, which acts on each *monomer* independently. We use a modified *9-3* potential for this interaction with the surface, u_{93}^p. Because we consider a slit-pore geometry, ψ_p and u_{93}^p only vary in the z-direction, perpendicular to the surface.

$$u_{93}^p(z) = 2\pi\epsilon\left[\frac{1}{9}\left(\frac{\sigma_p}{2z}\right)^9 - \frac{1}{3}\left(\frac{\sigma_p}{2z}\right)^3\right] \tag{III.22}$$

Such a potential has a minimum at $\sigma_p/2$. Combined with the hard sphere condition near the surface, the external potential for the monomer can be written as follows

$$\psi_p(z) = \begin{cases} u_{93}^p(z) + u_{93}^p(H-z) & \sigma_p/2 \le z \le H - \sigma_p/2 \\ \infty & \text{otherwise} \end{cases} \tag{III.23}$$

Numerical Implementation

The density of monomers and small ions vary only in the z-direction. The monomer density is obtained using Equations III.2, III.4, and III.15.

$$\rho_p(z)a_p = \exp[\beta\mu_p] \sum_{m=1}^{N} \exp[-\beta\Lambda_p(z)] G_m(z) G_m^{'}(z) \tag{III.24}$$

For small ions,

$$\rho_\alpha(z)a_\alpha = \exp[\beta\mu_\alpha - \beta\Lambda_\alpha(z)] \tag{III.25}$$

The chain propagators are given by the recurrence relation

$$G_m(z) = \frac{1}{2\sigma_p} \int_{z-\sigma_p}^{z+\sigma_p} dz' \exp[-\beta\Lambda_p(z')] G_{m-1}(z') \tag{III.26}$$

for $m = 1, \ldots, N$ with the initial condition of $G_1(z) = 1$. The complementary propagator for linear homopolymers satisfies $G'_m(z) = G_{N+1-m}(z)$. In this work, we fix the surface charge density on the surfaces in the slit-pore, Q. The electrostatic potential from Eq. III.18 can be exactly solved in 1D to give

$$\begin{aligned}\beta e_0\phi(z) = \beta e_0\phi(0) + 4\pi l_B \sum_i \int_0^H Z_i\rho_i(z')(z - zz'/H)dz' \\ + 4\pi l_B \sum_i \int_0^z Z_i\rho_i(z')(z' - z)dz'\end{aligned} \tag{III.27}$$

with boundary conditions $d\psi(z)/dz|_{z=0} = -d\psi(z)/dz|_{z=H} = -Q/\epsilon_r\epsilon_0$ and charge neutrality condition

$$2Q = -\sum_i \int_{0^-}^{H^+} Z_i e_0 \rho_i(z')dz' \tag{III.28}$$

The density profiles $\{\rho_i(z)\}$ are solved with Picard iterations, starting from uniform density profiles corresponding to the bulk densities of individual components.

Results and Discussion

We consider the polyelectrolyte solution where the monomers of polyelectrolyte, salt ions (and counterions), and solvent have the same diameter (σ = 5 Å). The salts to be monovalent ($Z_+ = -Z_- = 1$). Recall that we treat the polyelectrolyte counterion as identical to the salt ions. In this work, we exclusively consider polyanions so that the counterion is identical to the salt cation. We treat the polyelectrolyte as a weak acid where only a portion of the monomers have dissociated. In our model, this amounts to smearing the charge over all monomers so that $Z_p = -0.5$ if 50% are

dissociated. This valency is fixed and does not change with the local environment. Unless otherwise noted, we use $N = 50$ and $Z_p = -0.5$ for the results shown. We model the solution to have a constant dielectric constant ($\epsilon_r = 80$) and temperature ($T = 300\ K$).

Using a fractional valency is an approximation and reflects a drawback of TPT-1 in its treatment of intrachain correlation; TPT-1 can only capture connectivity at the level of nearest neighbor [77, 78]. Although it is desirable to consider a model where only some of the monomers are charged, doing so will lose the chain connectivity contribution to the electrostatic correlation if the charges are not nearest-neighbors on the chain. Using fractional charge on every monomer allows us to maintain the effects of chain connectivity on the electrostatic correlation, which can be important for certain phenomena [79]. Accounting for electrostatic correlation in an inhomogenous polyelectrolyte solution is a challenging, multiscale problem [80, 81]. To date, there is no widely accepted theory that fully captures electrostatic correlation at all length scales and concentration regimes. Tackling this issue is beyond the scope of this work.

To highlight the effect of nonelectrostatic adsorption in this work, we start by considering the salt-free adsorption profile near a single surface in the absence of nonelectrostatic attraction. *Salt-free* indicates only the polyelectrolyte, counterion, and solvent are in the system. Near a like-charge surface, we expect depletion due to the entropic penalty that restricts conformations near the surface and electrostatic repulsion of the like-charge polymer. Figure III.2 shows the density profiles for the polyanion and counterions near a like-charge surface for different bulk densities. Note that the densities are normalized relative to the bulk concentration. The thickness of the polyanion depletion layer decreases as the bulk density increases due to increased screening of the surface and the increased osmotic pressure of the polyanion [56]. For low bulk densities, a double-layer forms near the surface due to the strong adsorption of counterions near the surface to compensate the surface charge. Such strong counterion adsorption causes a slight enhancement in polyanion density away from the surface. For the highest bulk densities, the counterion is also slightly depleted at the surface and replaced by solvent at the surface. This occurs because with higher bulk density, less adsorption (relative to the bulk) is necessary to compensate the surface charge density so counterions tend to associate with the polyelectrolytes that are depleted at the surface. For clarity of presentation, through the rest of this work, we fix the bulk monomer density of polyelectrolyte to be

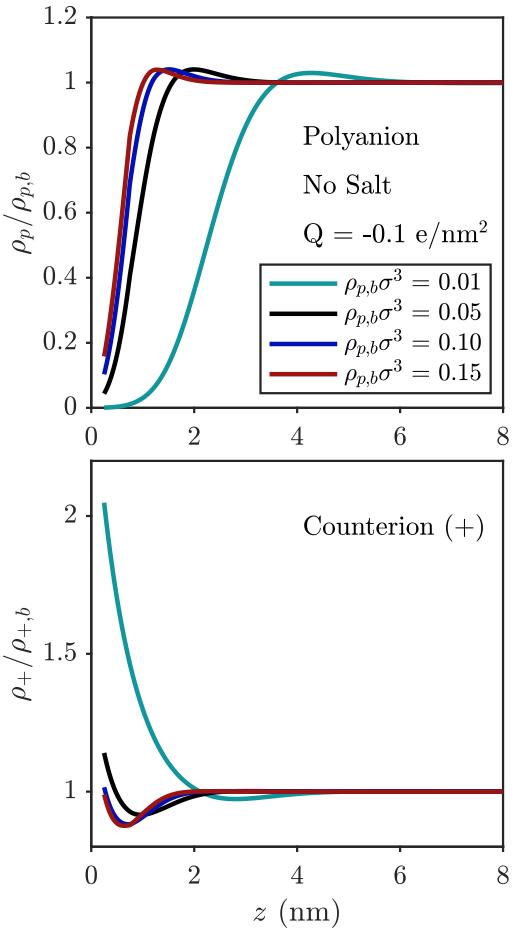

Figure III.2: Polyelectrolyte (top) and counterion (bottom) adsorption profiles with no added salt for varying bulk polymer concentrations without nonelectrostatic adsorption. The polymer chain length is $N = 50$; the valency of the polyelectrolyte is $Z_p = -0.5$; and the surface carries a negative charge of $Q = -0.1$ e/nm^2.

$\rho_{p,b}\sigma^3 = 0.01$, corresponding to a volume fraction $\approx 0.5\%$. Results for varying monomer density can be found in the Supporting information and will be referred to throughout the article.

Upon addition of salt in the absence of nonelectrostatic adsorption, an increase of screening decreases the width of the depletion layer (Figure III.3). In Figure III.3, above a threshold of added salt, there is no enhancement of the polymer density far from the surface as polyelectrolyte no longer participates in the electric double-layer (EDL). In other words, the surface charge density is screened by the salt ions within the depletion layer of the polyelectrolyte. This is reflected by the fact that the cation density for $\rho_{s,b} = 0.1$ drops to the bulk value within the depletion region of the

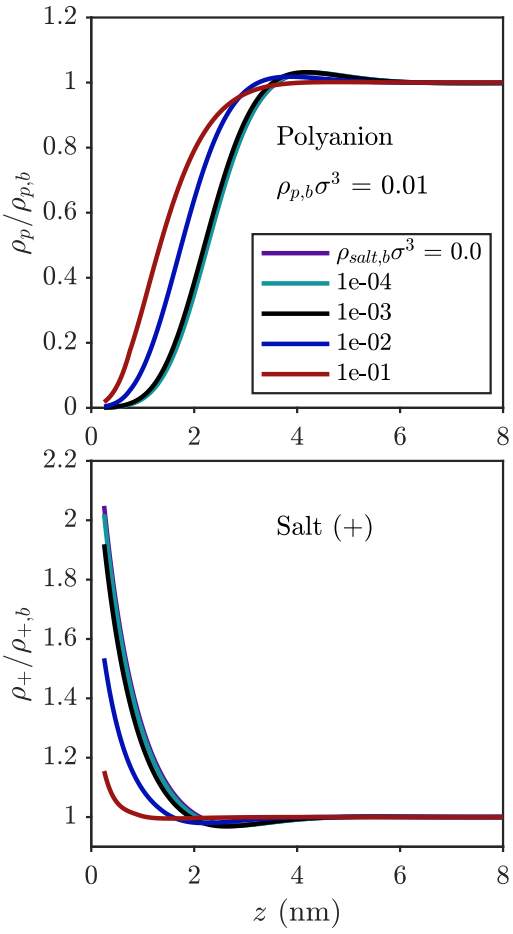

Figure III.3: Polyelectrolyte (top) and counterion (bottom) adsorption profiles for varying salt concentrations polymer concentration without nonelectrostatic adsorption. The polymer chain length is $N = 50$; the valency of the polyelectrolyte is $Z_p = -0.5$; and the surface carries a negative charge of $Q = -0.1$ e/nm^2.

polymer density < 1 nm. At such a salt concentration, the polyanion effectively behaves like a neutral polymer near the surface.

If the effect of a nonelectrostatic potential can overcome the entropic penalty and electrostatic repulsion, we expect strong adsorption at the surface. Figure III.4 shows the adsorption profiles for polyelectrolyte near the surface with various strengths of nonelectrostatic attraction. Increasing $\beta\epsilon$ increases the depth of the nonelectrostatic potential. With increasing $\beta\epsilon$, the polymer forms a thin layer at the surface. The presence a discontinuous derivative in the monomer density profile in Figure 4 at 0.75 nm (1.5σ) is a common feature in polymer cDFT and is a direct result of using a freely-jointed chain model, where the propagator is excluded from the surface

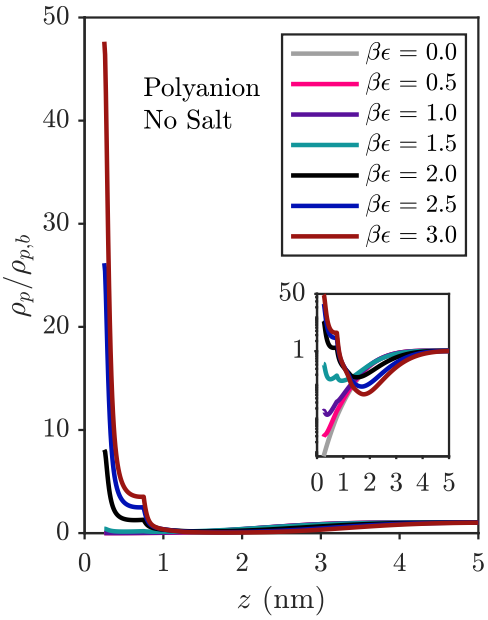

Figure III.4: Polyelectrolyte adsorption profiles with no salt for varying depths of nonelectrostatic potential between the surface and monomers. The inset depicts the same adsorption profile in a semi-log format to highlight the depletion. The bulk polyelectrolyte monomer density is $\rho_{p,b}\sigma^3 = 0.01$; the polymer chain length is $N = 50$; the valency of the polyelectrolyte is $Z_p = -0.5$; and the surface carries a negative charge of $Q = -0.1$ e/nm^2.

when there is strong adsorption in the first layer near the surface. The monomer density changes from depletion to adsorption at $\beta\epsilon \approx 2.0$, which corresponds to a potential well depth of just under 3 kT. The inset of Figure III.4 indicates that as the adsorption at the surface increases, there is more depletion in the secondary adsorption layer due to enhanced adsorption of the counterions. This indicates that as the nonelectrostatic attraction strength increases so does the local charge separation to form an electric double layer. The increased polyelectrolyte adsorption both draws in more counterion to balance the charge with more polymer adsorption at the surface and displaces counterions from the adsorption layer adjacent to the surface. Note the difference from Figure III.2, where the counterion formed the initial layer at the surface and the polymer provided the secondary adsorption layer.

The transition from depletion to adsorption depends on the salt concentration. In particular, overcoming the electrostatic barrier to adsorb on a like-charge surface requires sufficient strength of nonelectrostatic attraction. For a high salt concentration, increased charge screening dampens the electrostatic repulsion such that

the nonelectrostatic attraction only needs to overcome the entropic penalty at the surface. Figure III.5a illustrates this by showing the adsorbed amount as a function of the nonelectrostatic attraction strength. The adsorbed amount is calculated as $\Gamma_{ex} = \int_0^\infty (\rho_p(z) - \rho_{p,b})dz$. The point where the adsorbed amount crosses zero is roughly where the polyelectrolyte crosses from being depleted to being adsorbed. For higher salt concentration, electrostatic effects are not as dominant so that the transition occurs at lower $\beta\epsilon$. It is well known that nonelectrostatic effects become more prominent in high salt regimes [28]. Also, the effect of salt addition is apparent by looking at the adsorbed amount from low salt (purple/green) to high salt (red) for any given $\beta\epsilon$. Salt addition increases the adsorbed amount for all $\beta\epsilon$ for the like-charge surface.

Due to the variety of qualitative behaviors upon salt addition that have been reported, we also present the adsorbed amount of the polyanion for a neutral surface in Figure III.5b. As $\beta\epsilon$ is increased, the effect of salt addition transitions from monotonically decreasing to monotonically increasing the adsorbed amount. This transition is clear when observing the two end points of $\beta\epsilon = 0$ and $\beta\epsilon = 3$. For $\beta\epsilon = 0$, the adsorbed amount decreases when adding salt as salt ions displace the polymer at the surface, while the adsorbed amount increases upon salt addition for $\beta\epsilon = 3$, where increased screening reduces intrachain repulsion. For the parameters studied here, the transition occurs around $\beta\epsilon = 1.0$, which corresponds to a potential-well depth of 1.2 kT. Such a depth of nonelectrostatic interaction should be within a reasonable range to see experimentally. The balance of nonelectrostatic and electrostatic effects with adsorbed amount presented here agrees qualitatively with the concept of screening-enhanced or screening-reduced adsorption [44].

The effect of salt addition is more interesting near the transition. As stated above, as the salt concentration increases, the transition from depletion to adsorption requires a lower threshold of the nonelectrostatic attraction strength. Because the threshold value of $\beta\epsilon$ decreases with salt, there will be a portion of the $\beta\epsilon$ axis where the adsorbed amount is non-monotonic with increasing salt (inset of Figure III.5b). In the non-monotonic regime, the adsorbed amount initially decreases with increasing salt and then increases. To the best of our knowledge, such a non-monotonic salt trend has not been previously reported. In oppositely-charged systems, the non-monotonic relationship of adsorbed amount goes from increasing to decreasing with added salt [19, 32, 44]. While the results presented here are not for an oppositely-charged surface, these three different regimes in the adsorbed amount upon salt

addition highlight the complexity that nonelectrostatic effects can bring and help contextualize the variety of results from polyelectrolyte adsorption measurements cited in the introduction.

By our prediction, the non-monotonic range is unlikely to be seen experimentally as the difference in the adsorbed amounts across all salt concentrations is relatively small and the range of $\beta\epsilon$ for this regime is narrow. However, identical calculations without electrostatic correlation yield an even narrower range of the non-monotonic regime (Figure S1), suggesting that stronger electrostatic correlation will likely make this non-monotonic regime more prominent. The TPT-1 treatment of the chain connectivity is known to underestimate the electrostatic correlation [81]. Other theories with different treatment of the electrostatic correlation, including that by Forsman and Nordholm [33], could produce a more pronounced non-monotonic regime. We further note that the presence of only one regime (monotonically increasing) upon salt addition for the like-charge surface ($Q = -0.1$ e/nm^2) is not a universal phenomenon. We expect that increasing the bulk polymer concentration or decreasing the magnitude of the surface charge density will lead to all three regimes being present as seen for the neutral surface in Figure III.5b. The effect of the bulk polymer concentration on the excess adsorption can be found in Figures S2 and S3. Figure S2 shows that the negatively charged surface can achieve the three regimes for higher bulk monomer concentrations, as evidenced by the adsorbed amount for the highest salt concentration crossing the curves for the lower salt concentrations.

The above analysis discussed the adsorption of polyelectrolytes onto an isolated surface. We now turn our attention to the role of polyelectrolytes in mediating colloidal forces between two adjacent particles. As one brings the two surfaces together, the polyelectrolyte-mediated interaction force (referred to as “force" from hereafter) between the surfaces depends on the salt concentration and the strength of the nonelectrostatic adsorption. Note that because of the slit-pore geometry, it is convenient to use the force per unit area, which can be calculated by $\Pi = -(\partial W/\partial H)$ (obtained via numerical differentiation), where H is the surface separation. Figure III.6 shows the effect of increasing $\beta\epsilon$ on the force. In Figure III.6a, when $\beta\epsilon = 0.0$, polyelectrolyte is depleted from the slit-pore, leading to monotonically decaying force profile with the separation distance. Note that in the absence of polyelectrolyte, the force should indeed monotonically decay with the separation distance, as described by Poisson-Boltzmann theory. A decaying force profile is maintained until the nonelectrostatic adsorption is strong enough to keep polymer

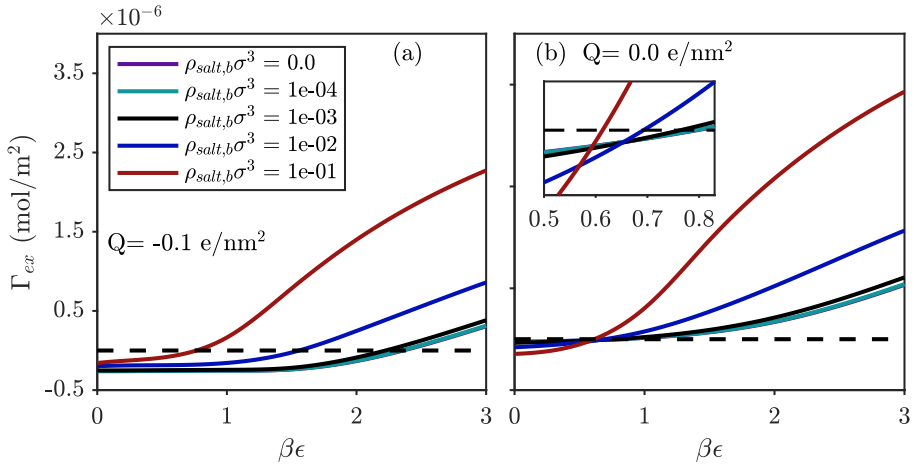

Figure III.5: Adsorbed amount as a function of the depth of the nonelectrostatic potential for varying salt concentrations. (a) Adsorption on like-charge surface with $Q = -0.1$ e/nm^2. (b) Adsorption on neutral surface. The curves for $\rho_{salt,b}\sigma^3 = 0.0$ and $\rho_{salt,b}\sigma^3 = 1\times10^{-4}$ are indistinguishable in both panels. The inset in (b) shows the transition region for the salt effects. The bulk polyelectrolyte monomer density is $\rho_{p,b}\sigma^3 = 0.01$; and the polymer chain length is $N = 50$ and the valency of the polyelectrolyte is $Z_p = -0.5$

on the surface on close approach. For $\beta\epsilon = 3$, the adsorbed polyelectrolyte layer creates an extended double layer of counterions, providing a repulsive barrier starting from ≈ 4 *nm*. At 2 *nm*, the adsorbed polyelectrolyte layers begin to overlap. At separations closer than 2 *nm*, there is short range attraction, corresponding to the bridging effect where the polymer feels the attractive potential to both surfaces. While the polymer effectively adsorbs to both surfaces here, bridging generally does not imply that the polymer is strictly adsorbed to both surfaces, but only that the polymer chains favor being stretched between both surfaces [30, 40]. With stronger nonelectrostatic adsorption, the repulsive barrier heightens due to more adsorption/overlap of the polyelectrolyte and EDL layers and the attractive region deepens due to more favorable bridging. Experimentally, this has consequences in direct force measurements using an AFM probe as polymers that provide the largest repulsive barrier on approach could also show the deepest attraction on retraction of the AFM probe. For $\beta\epsilon = 2$, the prominent repulsive barrier at $H \approx 1.5$ results from the overlap of adsorbed polyelectrolyte. This effect is also seen in $\beta\epsilon = 3$ as a "shoulder" peak to the left of the main repulsive barrier. The combined effects of bridging and overlap of strongly adsorbed polymer are difficult to separate.

An important question is whether the polymer-mediated repulsion is strong enough to overcome the dispersive interactions that generally cause colloidal particles to attract each other. The attraction between macroscopic particles can be modeled using a Hamaker potential [82]. For two flat surfaces, the force between the two surfaces is $\Pi_h = -A/6\pi H^3$, where A is the Hamaker constant. Adding the Hamaker contribution to the force calculated from the cDFT model results in Figure III.6a, Figure III.6b shows that with sufficiently strong non-electrostatic adsorption, the repulsive barrier resulting from polyelectrolytes can overcome the Hamaker attraction. With no polyelectrolyte, the EDL repulsion is not sufficient to create a repulsive barrier, leading to aggregation of the colloids. Due to the depletion when $\beta\epsilon = 0$, the force profile for $\beta\epsilon = 0$ is nearly identical to that of a system with no polyelectrolyte for the same salt concentration. Figures S4 and S5 show the interaction profiles for various bulk monomer concentrations. In Figure S4, one can see that increasing the bulk monomer concentration leads to depletion effects at small separations for $\beta\epsilon = 0$ and generally a smaller repulsive barrier, likely due to combined depletion and increased screening of the surface charge and interchain repulsion. As seen in Figure S5, because the Hamaker potential decays rapidly, these subtle changes in the length scale and strength of the repulsive interaction can significantly impact the behavior across $\beta\epsilon$ values. Most notably, the peak height of the repulsive barrier decreases with increasing bulk monomer concentration.

Increasing the salt concentration increases the adsorbed amount for the like-charge surface, but does not increase the repulsive barrier. Figure III.7 shows the force profile for a given value of $\beta\epsilon$ at various salt concentrations. The height of the repulsive barrier significantly decreases with increasing salt content, which is attributed to the shorter range of the double-layer at high salt concentration due to screening. When the double layers do overlap, the length scale is within the range where bridging causes short-range attraction. The depth of the attractive bridging region also increases because adsorption is more favorable at high salt concentrations. The net effect is that increasing salt concentration in the presence of nonelectrostatic repulsion turns the long-range repulsive surface interaction into a predominantly attractive surface interaction. The same qualitative salt trend can be seen for different bulk monomer concentrations (Figure S6). We note that in systems where there is pure electrostatic adsorption on an oppositely charged surface, others have reached similar conclusions of weakened repulsion and stronger short-range bridging attraction upon salt addition [42].

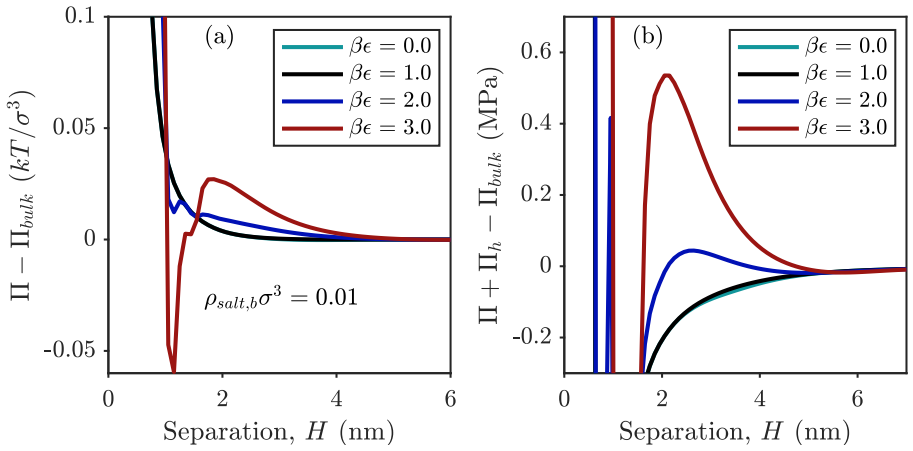

Figure III.6: Polyelectrolyte-mediated force between surfaces as a function of surface separation for varying strengths of nonelectrostatic attraction to the surface. (a) Without Hamaker attractive potential. The curves for $\beta\epsilon = 0.0$ and $\beta\epsilon = 1.0$ are indistinguishable. (b) With Hamaker attractive potential. The Hamaker constant is 5×10^{-20} J. The bulk polyelectrolyte monomer density is $\rho_{p,b}\sigma^3 = 0.01$; the bulk salt concentration is $\rho_{salt,b}\sigma^3 = 0.01$; the polymer chain length is $N = 50$; the valency of the polyelectrolyte is $Z_p = -0.5$; and the surface carries a negative charge of $Q = -0.1$ e/nm^2.

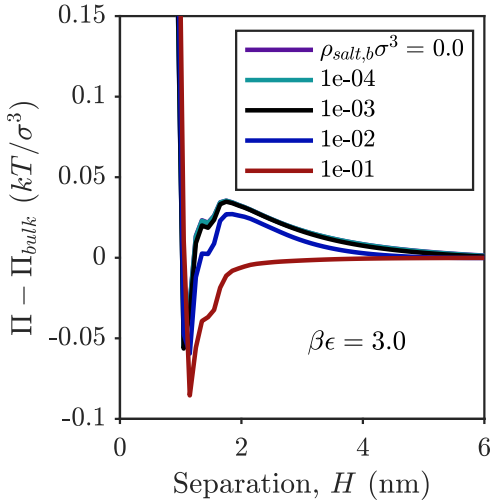

Figure III.7: Polyelectrolyte-mediated force between surfaces for varying bulk concentrations of added salt. The bulk polyelectrolyte monomer density is $\rho_{p,b}\sigma^3 = 0.01$; the polymer chain length is $N = 50$; the valency of the polyelectrolyte is $Z_p = -0.5$; and the surface carries a negative charge of $Q = -0.1$e/nm^2.

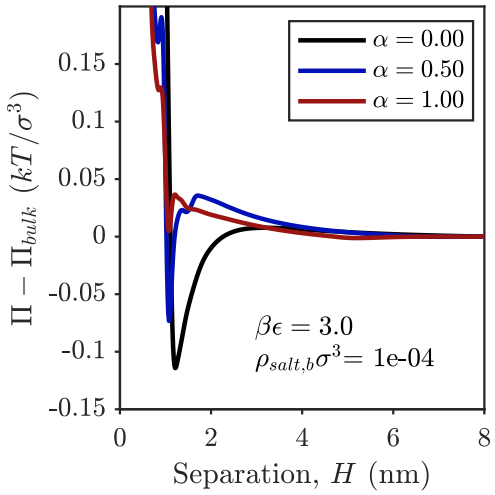

Figure III.8: Polyelectrolyte-mediated force between surfaces for varying polyelectrolyte charge densities. The bulk polyelectrolyte monomer density is $\rho_{p,b}\sigma^3 = 0.01$ and the polymer chain length is $N = 50$; and the surface carries a negative charge of $Q = -0.1$ e/nm^2.

The polyelectrolyte charge density plays an important role in like-charge adsorption as one of the barriers to adsorption is the electrostatic repulsion from the surface. Figure III.8 illustrates the effect of the backbone charge density on the force profile. α is the fraction of charged monomers that goes into the calculation of Z_p for the polyelectrolyte. At one extreme of $\alpha = 0$, where the polymer is neutral, nonelectrostatic adsorption leads to enhanced adsorption of the polymer. However, the polymer only contributes to the bridging-type attraction with no repulsive barrier. Increasing the polyelectrolyte charge density yields a repulsive barrier and a shallower short-range attraction from bridging. Notably, for $\alpha = 1$ (all monomers dissociated so that $Z_p = -1$), the repulsive barrier appears to be shorter range than, say, $\alpha = 0.5$. This repulsive peak at $H \approx 1.5$ *nm* is different in character from the long-range repulsion that results from mutual repulsion from EDL layers seen in $\alpha = 0.5$. The peak arises due to the overlap of adsorbed polyelectrolyte layers, rather than the double-layer repulsion. This difference is similar to what is seen for $\beta\epsilon = 2$ in Figure III.6. Such an effect occurs when the adsorption is not favorable enough to induce bridging.

Lastly, we examine the effect of chain length on the force profile. As explained in our earlier work [56], the force profile is insensitive to the chain length at fixed monomer density (Fig. III.9). Even with nonelectrostatic polyelectrolyte adsorption,

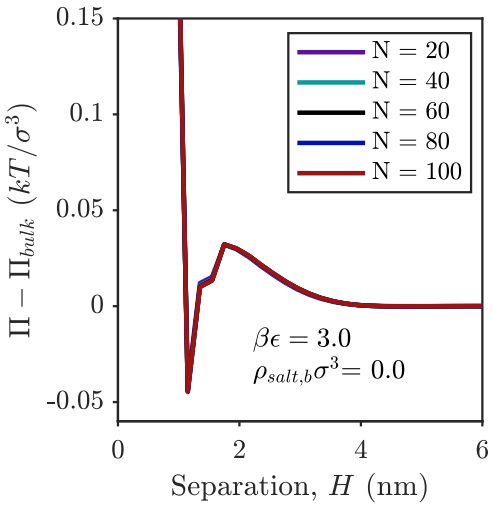

Figure III.9: Polyelectrolyte-mediated force between surfaces for varying polyelectrolyte chain lengths. The bulk polyelectrolyte monomer density is $\rho_{p,b}\sigma^3 = 0.01$; the valency of the polyelectrolyte is $Z_p = -0.5$; and the surface carries a negative charge of $Q = -0.1$ e/nm^2.

the dominant length scale for the interaction in the semi-dilute regime is set by the Debye length. Strictly speaking, the length scale is set by the correlation length, but cDFT cannot capture the coupled effects of electrostatic correlation and chain conformation [81]. at the given salt and polylelectrolyte concentration. Additionally, Figure III.9 implies that the width of the adsorption layer does not change with the chain length as the length scale for the repulsion is the same for all curves.

Conclusion

In this work, the effect of nonelectrostatic adsorption affinity of polyelectrolytes near a like-charged surface was characterized for a variety of polyelectrolyte and solution conditions. Upon salt addition, three regimes of adsorbed amount are observed for the neutral surface as a function of the strength of nonelectrostatic potential (decreasing, non-monotonic, increasing). The non-monotonic trend of initially decreasing then increasing has not previously been reported in literature. For the negatively charged surface, the adsorbed amount only increases with added salt at low bulk monomer concentration but can achieve all three regimes for higher bulk concentration. Such a result underscores the delicate balance between the electrostatic and nonelectrostatic forces and rationalizes the variety of behaviors observed in experimental measurements upon salt addition. Experimentally, the salt behaviors also suggests that minor changes in the nonelectrostatic potential or

surface charge density that can occur from varying pH, for example, can qualitatively change the salt effects for adsorption. Increasing the strength of the nonelectrostatic potential generally increases the height of the long-range repulsive peak in the mediated interaction but also deepens the short-range bridging attractive region. The long-range nature of the repulsive barrier results from an extended double-layer created from the polymer displacing counterions at the surface. When adding salt, the height of the repulsive barrier decreases and the bridging attraction deepens. Such a salt trend is also found when adding salt for pure electrostatic adsorption, indicating that adsorption profile rather than the interaction force, is more reflective of the effect of nonelectrostatic adsorption. Further, the results for the polyelectrolyte charge density indicate that adsorption alone does not provide a repulsive barrier - sufficient charge along the backbone is required to create a long-range electric double layer. The range of the repulsive barrier tends to decrease with increasing charge fraction. All of these results together have implications for selection and design of polyelectrolytes and solution conditions (i.e., salt, pH) for coating and dispersion applications.

Appendix

No Electrostatic Correlation

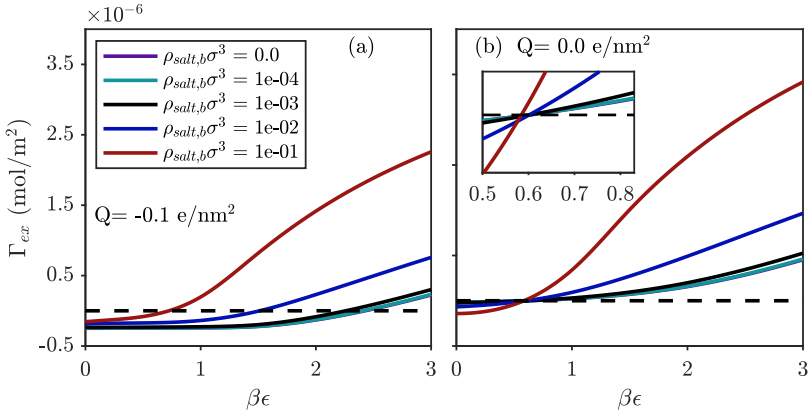

Figure III.10: Adsorbed amount as a function of the depth of the nonelectrostatic potential for varying salt concentrations with no electrostatic correlation. (a) Adsorption on like-charge surface with $Q = -0.1$ e/nm^2. (b) Adsorption on neutral surface. The curves for $\rho_{salt,b}\sigma^3 = 0.0$ and $\rho_{salt,b}\sigma^3 = 1 \times 10^{-4}$ are indistinguishable in both panels. The inset in (b) shows the transition region for the salt effects. The bulk polyelectrolyte monomer density is $\rho_{p,b}\sigma^3 = 0.01$; and the polymer chain length is $N = 50$ and the valency of the polyelectrolyte is $Z_p = -0.5$

Varying Monomer Bulk Concentration - Adsorption

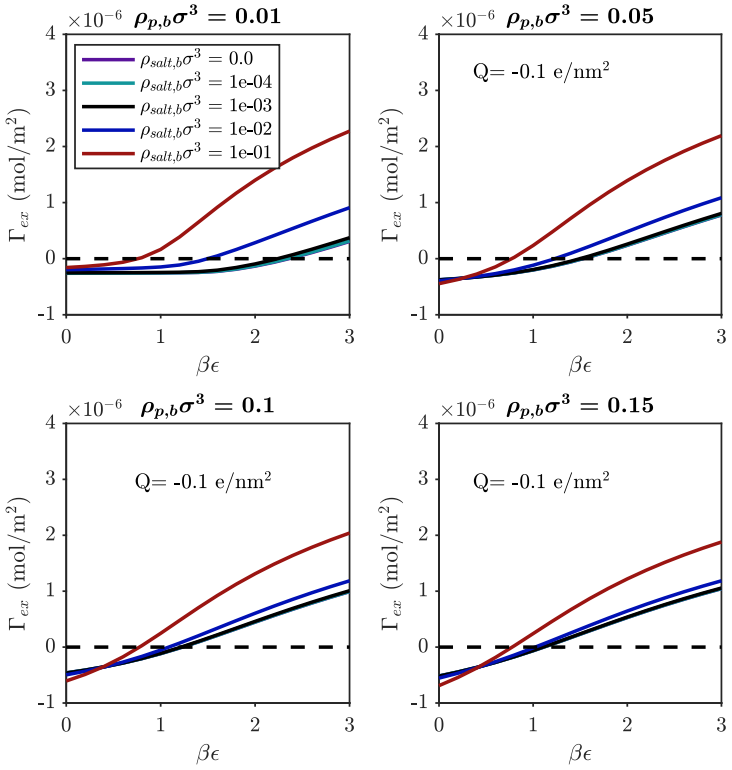

Figure III.11: Adsorbed amount as a function of the depth of the nonelectrostatic potential for varying salt concentrations for a negatively charged surface ($Q = -0.1\text{e/nm}^2$). Each panel is for a different bulk concentration. The curves for $\rho_{salt,b}\sigma^3 = 0.0$ and $\rho_{salt,b}\sigma^3 = 1 \times 10^{-4}$ are indistinguishable in most panels. The polymer chain length is $N = 50$ and the valency of the polyelectrolyte is $Z_p = -0.5$.

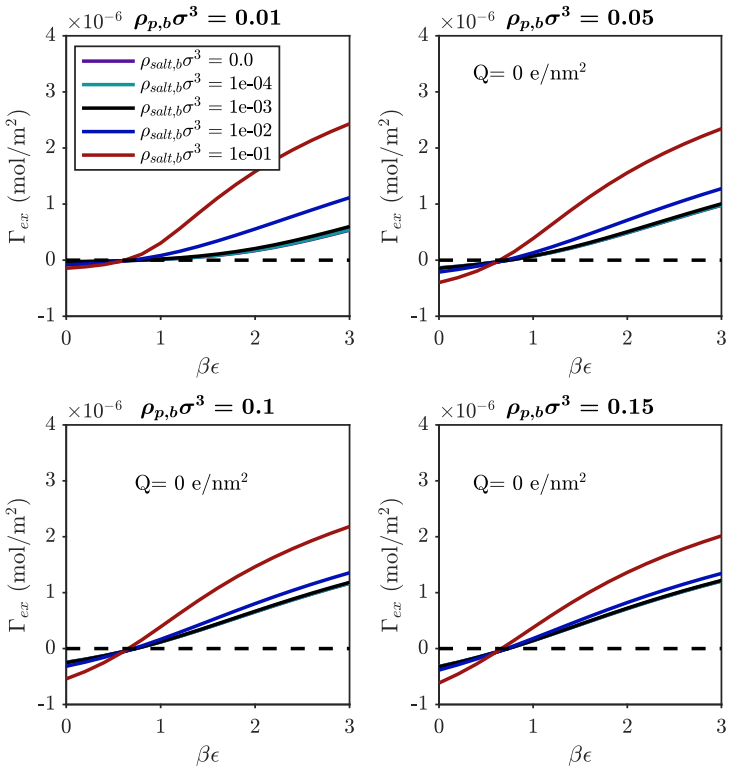

Figure III.12: Adsorbed amount as a function of the depth of the nonelectrostatic potential for varying salt concentrations for a neutral surface. Each panel is for a different bulk concentration. The curves for $\rho_{salt,b}\sigma^3 = 0.0$ and $\rho_{salt,b}\sigma^3 = 1\times10^{-4}$ are indistinguishable in most panels. The polymer chain length is $N = 50$ and the valency of the polyelectrolyte is $Z_p = -0.5$.

Varying Monomer Bulk Concentration - Interaction

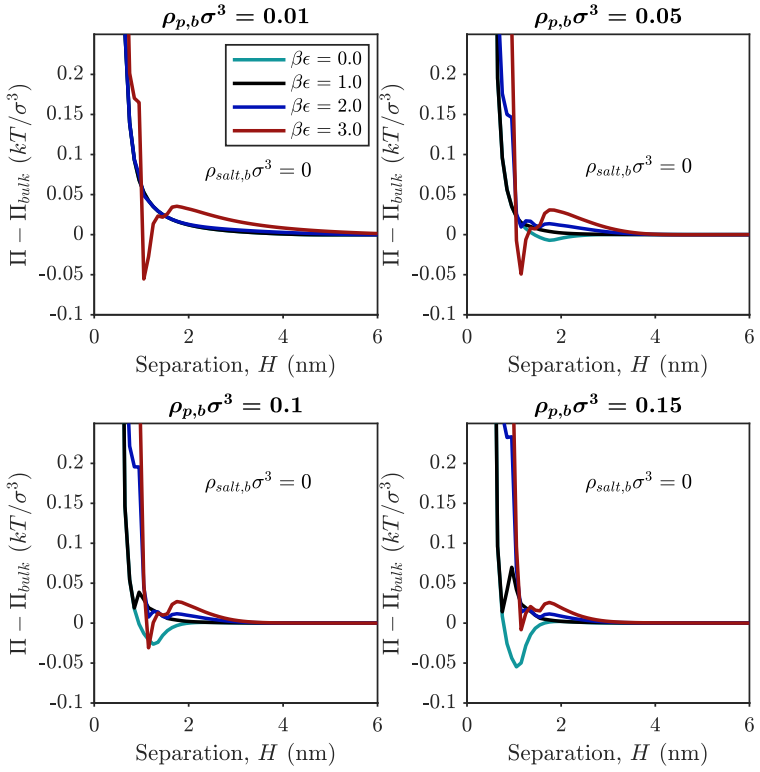

Figure III.13: Polyelectrolyte-mediated force between surfaces as a function of surface separation for varying strengths of nonelectrostatic attraction to the surface without the Hamaker attractive potential. The bulk salt concentration is $\rho_{salt,b}\sigma^3 = 0.0$; the polymer chain length is $N = 50$; the valency of the polyelectrolyte is $Z_p = -0.5$; and the surface carries a negative charge of $Q = -0.1$ e/nm^2.

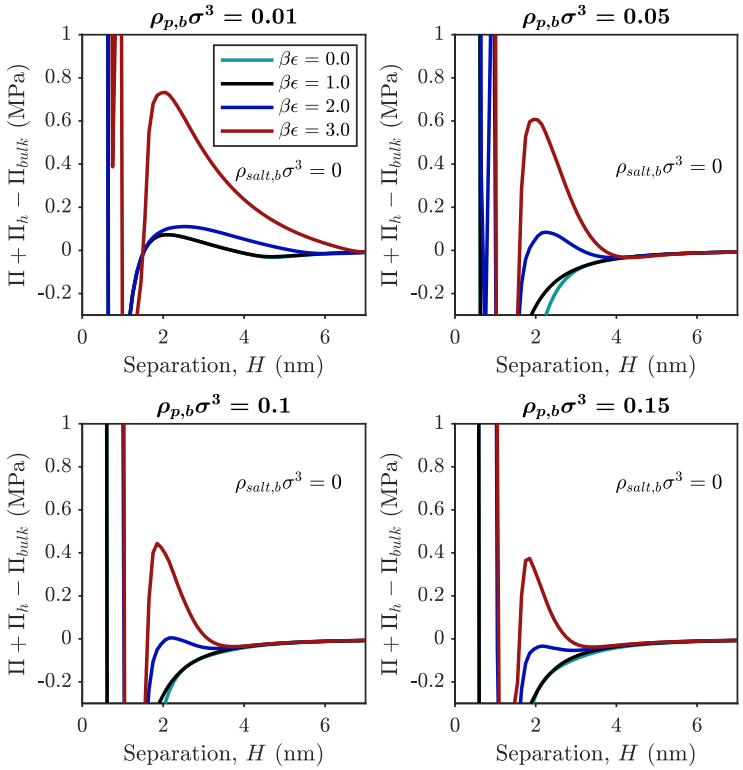

Figure III.14: Polyelectrolyte-mediated force between surfaces as a function of surface separation for varying strengths of nonelectrostatic attraction to the surface with the Hamaker attractive potential. The Hamaker constant is 5×10^{-20} J. The bulk salt concentration is $\rho_{salt,b}\sigma^3 = 0.0$; the polymer chain length is $N = 50$; the valency of the polyelectrolyte is $Z_p = -0.5$; and the surface carries a negative charge of $Q = -0.1$ e/nm^2.

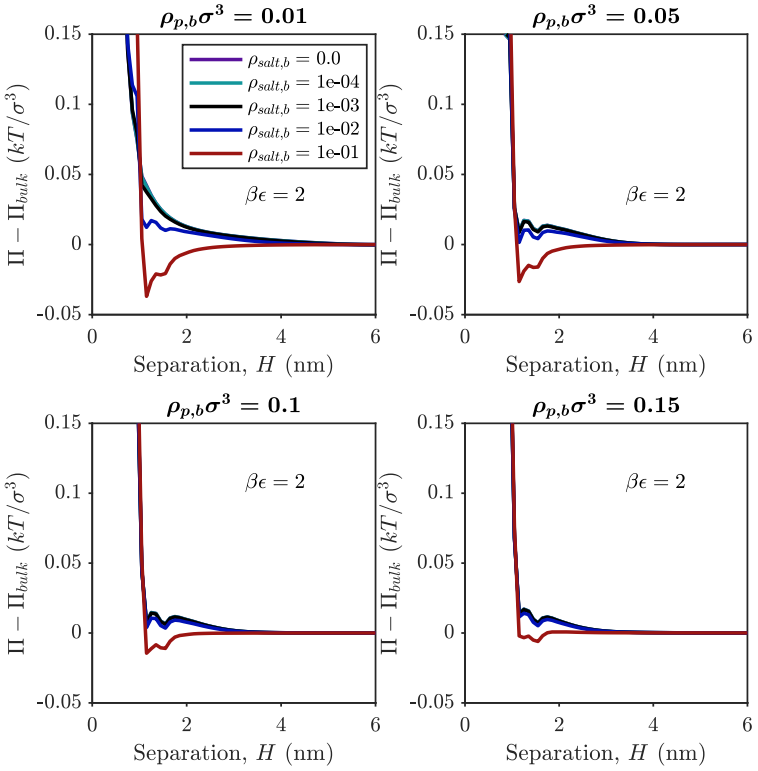

Figure III.15: Polyelectrolyte-mediated force between surfaces for varying bulk concentrations of added salt. The polymer chain length is $N = 50$; the valency of the polyelectrolyte is $Z_p = -0.5$; and the surface carries a negative charge of $Q = -0.1\text{e/nm}^2$.

III.2 Weak Polyelectrolytes

Introduction

Weak polyelectrolytes are polyelectrolytes where the backbone charge is not fixed. Monomer units, or even multiple sites on a monomer, have the ability to protonate or deprotonate according to the acid-base equilibrium. The ubiquitous examples are those of amino acids, such as glutamic acid, arginine, aspartic acid, or lysine [83]. Experiments on synthetic weak polyelectrolytes started in the late 1930s [84–86], where the pH response of common polyelectrolytes was measured.

The power and promise of weak polyelectrolytes stems from the fact that they are responsive materials. The charge state depends on the local electrostatic potential and the local solution conditions. By tuning the local environment and changing the charge along a polymer backbone, the conformational properties can change dramatically. This section will give an overview of weak polyelectrolytes, derive a mean-field theory that accounts for acid-base equilibrium, and apply the theory to adsorption of weak polyelectrolytes to a planar surface.

Toy Example

First, we will consider a toy example of proton binding using a cell model outlined by Koper [87]. The benefit of the cell model is that one can gain intuition for the weak polyelectrolyte system without worrying about the chain conformation or model details. The system is a polymer chain with N discrete sites (monomers). Each monomer has a site where a proton can either be bound or dissociated. The result is that each monomer can take on two states, charged or uncharged. The charge state of a polymer chain can be described by $\sigma = \{\sigma_1, \sigma_2, ..., \sigma_N\}$, where σ is either zero or one, charged or uncharged, respectively. Figure III.16 shows an example of states for a short chain. The state of the system is fully specified by σ.

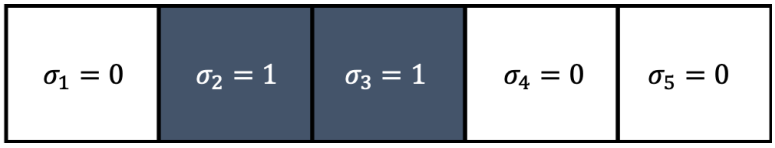

Figure III.16: Schematic of charge states along a polymer chain with $N = 5$

Following the result from Koper [87], the system can be viewed as a grand canonical system with a fixed proton chemical potential (μ_p), binding sites (N), and temperature. The energy of a given microstate with only pairwise interactions is captured in the equation below. The proton chemical potential can be related to the pH and pKa

of the polymer and the coupling constant J is positive to indicate a repulsive interaction between occupied (protonated) sites. In general $J_{i,j}$ depends on the distance between sites.

$$E(\{\sigma\}) = -\mu_p \sum_{i=1}^{N} \sigma_i + \frac{1}{2} \sum_{i \neq j}^{N} J_{i,j} \sigma_i \sigma_j \tag{III.29}$$

The partition function is the weighted sum over all of the microstates,

$$\Xi = \sum_{\{\sigma\}} e^{-E(\{\sigma\})} = \sum_{\sigma_1=\{0,1\}} \sum_{\sigma_2=\{0,1\}} \cdots \sum_{\sigma_N=\{0,1\}} e^{\mu_p \sum_{i=1}^{N} \sigma_i - \frac{1}{2} \sum_{i \neq j}^{N} J_{i,j} \sigma_i \sigma_j} \tag{III.30}$$

Relationship between μ_p and pH

Koper defines the effective chemical potential of the proton to be the following [87]

$$\beta \mu_p / \ln(10) = \mathrm{pK_a} - \mathrm{pH} \tag{III.31}$$

where $\mathrm{pH} = -\log(\mathrm{a_p})$ and $\mathrm{pK_a} = -\log(\mathrm{K})$. a_p is the activity of a proton and K is the microscopic constant corresponding to proton binding when all other sites are dissociated. Intuitively, if the pH of the solution is higher than the $\mathrm{pK_a}$, then there is a penalty for a proton to bind to a monomer.

Only Nearest Neighbor Interactions

With only nearest neighbor interactions, the energy of a microstate is

$$E(\{\sigma\}) = -\mu_p \sum_{i=1}^{N} \sigma_i + J \sum_{i=1}^{N-1} \sigma_i \sigma_{i+1} \tag{III.32}$$

where J is now constant for each interacting site. The partition function can be written as the following.

$$\Xi = \sum_{\sigma_1=\{0,1\}} \sum_{\sigma_2=\{0,1\}} \cdots \sum_{\sigma_N=\{0,1\}} e^{\beta\mu_p(\sigma_1+\sigma_2+\ldots+\sigma_N) - \beta J(\sigma_1\sigma_2+\sigma_2\sigma_3+\ldots+\sigma_{N-1}\sigma_N)} \tag{III.33}$$

Rewriting,

$$\Xi = \sum_{\sigma_1=\{0,1\}} \sum_{\sigma_2=\{0,1\}} \cdots \sum_{\sigma_N=\{0,1\}} e^{\beta\mu_p\sigma_1 - \beta J\sigma_1\sigma_2 + \beta\mu_p\sigma_2 - \beta J\sigma_2\sigma_3 + \ldots} \tag{III.34}$$

$$\Xi = \sum_{\sigma_1=\{0,1\}} \sum_{\sigma_2=\{0,1\}} \cdots \sum_{\sigma_N=\{0,1\}} e^{\beta\mu_p\sigma_N} \prod_{i=1}^{N-1} e^{\beta\mu_p\sigma_i - \beta J\sigma_i\sigma_{i+1}} \tag{III.35}$$

Defining $z = e^{\beta\mu_p}$ and $u = e^{-\beta J}$,

$$\Xi = \sum_{\sigma_1=\{0,1\}} \sum_{\sigma_2=\{0,1\}} \dots \sum_{\sigma_N=\{0,1\}} z^{\sigma_N} \prod_{i=1}^{N-1} z^{\sigma_i} u^{\sigma_i \sigma_{i+1}} \tag{III.36}$$

One can write the product term as a matrix consisting of the four elements from the four different possibilities for site states. Namely, the combinations are $\{\sigma_1, \sigma_2\} = \{[1,1],[1,0],[0,1],[0,0]\}$. Here, specifying a state $\{\sigma_1, \sigma_2\}$ gives the index in the matrix.

$$T_{\sigma_i,\sigma_{i+1}} = \begin{bmatrix} 1 & 1 \\ z & zu \end{bmatrix}$$

$$\Xi = \sum_{\sigma_1=\{0,1\}} \sum_{\sigma_2=\{0,1\}} \dots \sum_{\sigma_N=\{0,1\}} T_{\sigma_1,\sigma_2} T_{\sigma_2,\sigma_3} \dots T_{\sigma_{N-2}\sigma_{N-1}} (T_{\sigma_{N-1}\sigma_N} z^{\sigma_N})$$

Each monomer takes the same states so that this is a product of identical sums,

$$\Xi = \sum_{\sigma_1=\{0,1\}} T^{N-2} \sum_{\sigma_{N-1}=\{0,1\}} \sum_{\sigma_N=\{0,1\}} (T_{\sigma_{N-1}\sigma_N} z^{\sigma_N})$$

Where T is the generic transfer matrix. Summing over the last monomer,

$$\Xi = \sum_{\sigma_1=\{0,1\}} T^{N-2} \sum_{\sigma_{N-1}=\{0,1\}} \left(\begin{bmatrix} 1 \\ z \end{bmatrix} + z \begin{bmatrix} 1 \\ zu \end{bmatrix} \right)$$

The last product can be written as the product of $T^2(1,0)^T$.

$$\Xi = \sum_{\sigma_1=\{0,1\}} T^N \begin{bmatrix} 1 \\ 0 \end{bmatrix}$$

Summing over all values of σ is equivalent to the following matrix multiplication,

$$\Xi = \begin{bmatrix} 1 & 1 \end{bmatrix} T^N \begin{bmatrix} 1 \\ 0 \end{bmatrix}$$

Explicitly,

$$\Xi = \begin{bmatrix} 1 & 1 \end{bmatrix} \begin{bmatrix} 1 & 1 \\ z & zu \end{bmatrix}^N \begin{bmatrix} 1 \\ 0 \end{bmatrix}$$

Small and Long Chain Limits

In the small chain limit $N = 1$, then the partition function is exactly

$$\Xi = 1 + z = 1 + e^{\beta\mu_p} \tag{III.37}$$

One can obtain the average occupancy via the proper derivative of the partition function or through the definition of the average σ.

$$\langle\sigma\rangle = \theta = \frac{1 \times 0 + e^{\beta\mu_p} \times 1}{1 + e^{\beta\mu_p}} = \frac{e^{\beta\mu_p}}{1 + e^{\beta\mu_p}} \tag{III.38}$$

$$\langle\sigma\rangle = \theta = \frac{\partial \ln \Xi}{\partial\beta\mu} = \frac{1}{1 + e^{\beta\mu_p}} \frac{\partial(1 + e^{\beta\mu_p})}{\partial\beta\mu} = \frac{e^{\beta\mu_p}}{1 + e^{\beta\mu_p}} \tag{III.39}$$

In either case, one can write this in a more familiar style utilizing the definition of the effective chemical potential from above.

$$\theta = \frac{1}{1 + e^{\beta(pH - pKa)}} = \frac{1}{1 + \frac{K_a}{a_p}} \tag{III.40}$$

In the long chain limit $N = \infty$, then the partition function is dominated by the largest eigenvalue of T. The eigenvalue can be computed analytically as

$$\Xi = \lambda_{max}^N \tag{III.41}$$

The maximum eigenvalue can be calculated

$$\lambda_{max} = \frac{1 + zu + \sqrt{(1 - zu)^2 + 4z}}{2} \tag{III.42}$$

Taking the proper derivative, one can calculate the average occupancy

$$\theta = \frac{1}{N} \frac{\partial \ln \Xi}{\partial\beta\mu} = z \frac{\partial \ln \lambda_{max}}{\partial z} = \frac{z}{\lambda_{max}} \frac{\partial \lambda_{max}}{\partial z} = \left[2 + \frac{\lambda_{max}}{z} \frac{1 - zu}{1 - u - \lambda_{max} u}\right]^{-1} \tag{III.43}$$

In these two limits, one can plot the average occupancy as a function of the pH as shown in Figure III.17. The penalty arising from nearest neighbor interactions leads to the step-like profile for the occupancy.

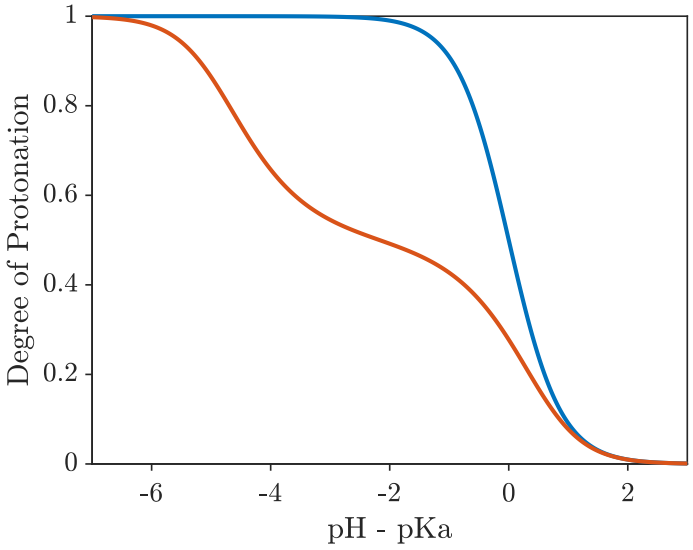

Figure III.17: Degree of protonation (average occupancy) as a function of the pH in short (blue) and long (red) chain limit. Parameters $\beta J = 5$ and $\beta\mu_p = \ln(10)(\text{pH} - \text{pK}_a)$ with $\text{pK}_a = 7$

.

Theory

Consider a polyelectrolyte solution made up pH-responsive, linear polyelectrolytes, salt ions and water. Each monomer in the chain is a pH-responsive group whose charge state is determined by local acid-base equilibria. For simplicity, we consider each monomer to have only one dissociable proton and one available protonation site.

$$\begin{aligned} HM + H_2O &\longleftrightarrow M^- + H_3O^+ \\ HM + H_2O &\longleftrightarrow MH_2^+ + OH^- \end{aligned} \tag{III.44}$$

In the equations above, M is a generic monomer that can be basic or acidic. The reactions above are dictated by acid-dissociation, $K_{a,1}$ and $K_{a,2}$, respectively. Similarly, water can dissociated and at room temperature pure water has $pK_a = 7$.

$$2H_2O \longleftrightarrow OH^- + H_3O^+ \tag{III.45}$$

We consider the salt ions, denoted + and − to be strong electrolytes with valency Z_+, Z_- with $Z_- < 0$. In the following theory, we make several simplifications. We neglect the size of the bare proton and assume all of the other species have the same size, denoted b. This length scale also sets our volume scale for all species to be $v = b^3$.

From the acid-base relationships, the monomers and water can each take on 3 distinct states – neutral, protonated, or deprotonated. To model the protonation and deprotonation, we introduce protonation variables. For example, we use s_i^w to denote the state of a given water molecule i. s_i^w can take on values of -1, 0, or 1, corresponding to deprotonated, neutral, or protonated, respecitvely. Likewise, the monomer state of the j-th monomer on the i-th chain can be tracked the same way using $s_{i,j}^M$. Such a model is similar to that of Nakamura and Wang [88] in the context of salt-doped block copolymers and more recently, in classical density functional theory by Gallegos, Ong, and Wu [89].

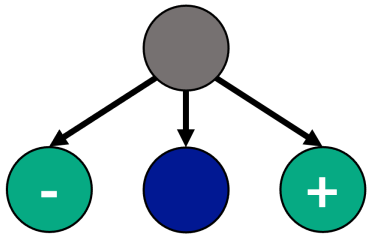

Figure III.18: Schematic of Ising-like configurational states for monomers and water.

For a system of n_w water molecules, n_p polymer chains with N total segments, n_+ cations, and n_- anions, the Hamiltonian can be written as follows.

$$\begin{aligned}\beta H = -\beta a_w \sum_{i=1}^{n_w} (s_i^w)^2 + \sum_{i=1}^{n_p}\sum_{j=1}^{N} \beta a_M^j (s_{i,j}^M) \\ + \sum_{i=1}^{n_p}\sum_{j=1}^{N-1} \beta h(\mathbf{r}_{i,j+1} - \mathbf{r}_{i,j}) + \int d\mathbf{r} \beta u_{\text{surf}}(\mathbf{r}) \hat{\rho}_{HM}(\mathbf{r}) \\ + \frac{\beta}{2} \int d\mathbf{r} \int d\mathbf{r}' \hat{\rho}_c(\mathbf{r}) C(\mathbf{r}, \mathbf{r}') \hat{\rho}_c(\mathbf{r}')\end{aligned} \tag{III.46}$$

The first two terms in Eq. III.46 account for the binding and unbinding of protons from the water and monomers, respectively. The third term accounts for the connectivity of the polymer chain. Later on, we will specify the form of $h(\mathbf{r})$ to be Gaussian. The fourth term is an attractive potential between the neutral form of the monomers and the surface. While we don't specify the form of u_{surf}, the fact that it is attractive is important for the following field theory. The last term is the energy from electrostatics, where $C(\mathbf{r}, \mathbf{r}')$ is the Coulomb operator.

The system is open since all components can exchange with the bulk reservoir. The partition function for the system is below, where μ_i is the chemical potential of component i. The partition function is given below with incompressibility and the "protonation potential", λ.

$$\begin{aligned}\Omega = \sum_{n_p}\sum_{n_w}\sum_{n_+}\sum_{n_-} \frac{\exp(\beta\mu_p n_p + \beta\mu_w n_w + \beta\mu_+ n_+ + \beta\mu_- n_-)}{n_p! v^{n_p} N n_w! v^{n_w} n_+! v^{n_+} n_-! v^{n_-}} \\ \times \int \mathcal{D}\{\mathbf{R}\} \sum_{\{s^w\}}\sum_{\{s^M\}} \delta(\hat{\rho}_w(\mathbf{r}) + \hat{\rho}_M(\mathbf{r}) + \hat{\rho}_+(\mathbf{r}) + \hat{\rho}_-(\mathbf{r}) - 1/v) \\ \times \exp\Big[-\beta H + \beta\lambda\Big(\sum_{k=1}^{n_w} s_k^w + \sum_{i=1}^{n_p}\sum_{j=1}^{N} s_{i,j}^M\Big)\Big]\end{aligned} \tag{III.47}$$

Performing the field transformations for the incompressibility and the electrostatic interactions, the Hamiltonian and the partition function become

$$\begin{aligned}\beta H = -\beta a_w \sum_{i=1}^{n_w}(s_i^w)^2 + \sum_{i=1}^{n_p}\sum_{j=1}^{N}\beta a_M^j(s_{i,j}^M) + \sum_{i=1}^{n_p}\sum_{j=1}^{N-1}\beta h(\mathbf{r}_{i,j+1} - \mathbf{r}_{i,j}) \\ + \int d\mathbf{r}\beta u_{\text{surf}}\hat{\rho}_{HM}(\mathbf{r}) + \beta\int d\mathbf{r}\Big[\hat{\rho}_c(\mathbf{r})i\psi(\mathbf{r}) - \frac{1}{2}\epsilon\big(\nabla\psi(\mathbf{r})\big)^2\Big] \\ -i\beta\eta(\mathbf{r})\Big(\hat{\rho}_w(\mathbf{r}) + \hat{\rho}_M(\mathbf{r}) + \hat{\rho}_+(\mathbf{r}) + \hat{\rho}_-(\mathbf{r}) - 1/v\Big)\end{aligned} \tag{III.48}$$

$$\begin{aligned}\Omega = \sum_{n_p}\sum_{n_w}\sum_{n_+}\sum_{n_-} \frac{\exp(\beta\mu_p n_p + \beta\mu_w n_w + \beta\mu_+ n_+ + \beta\mu_- n_-)}{n_p! v^{n_p} N n_w! v^{n_w} n_+! v^{n_+} n_-! v^{n_-}} \\ \int \mathcal{D}\eta \int \mathcal{D}\psi \int \mathcal{D}\{\mathbf{R}\} \sum_{\{s^w\}}\sum_{\{s^M\}} \exp\Big[-\beta H + \beta\lambda\Big(\sum_{k=1}^{n_w} s_k^w + \sum_{i=1}^{n_p}\sum_{j=1}^{N} s_{i,j}^M\Big)\Big]\end{aligned} \tag{III.49}$$

Introducing a field for the protonated density with $\delta(\rho_{HM}(\mathbf{r}) - \hat{\rho}_{HM}(\mathbf{r}))$ and using identify transformations, the Hamiltonian becomes

$$\begin{aligned}\beta H = -\beta a_w \sum_{i=1}^{n_w}(s_i^w)^2 + \sum_{i=1}^{n_p}\sum_{j=1}^{N}\beta a_M^j(s_{i,j}^M) + \sum_{i=1}^{n_p}\sum_{j=1}^{N-1}\beta h(\mathbf{r}_{i,j+1} - \mathbf{r}_{i,j}) \\ +\beta\int d\mathbf{r}\Big[\hat{\rho}_c(\mathbf{r})i\psi(\mathbf{r}) - \frac{1}{2}\epsilon\big(\nabla\psi(\mathbf{r})\big)^2\Big] \\ -i\beta\eta(\mathbf{r})\Big(\hat{\rho}_w(\mathbf{r}) + \hat{\rho}_M(\mathbf{r}) + \hat{\rho}_+(\mathbf{r}) + \hat{\rho}_-(\mathbf{r}) - 1/v\Big) + \int d\mathbf{r}\beta u_{\text{surf}}(\mathbf{r})\rho_{HM}(\mathbf{r}) \\ +i\int d\mathbf{r}\beta w_{HM}(\mathbf{r})\rho_{HM}(\mathbf{r}) - \sum_{i=1}^{n_p}\sum_{j=1}^{N} i w_{HM}(\mathbf{r}_{i,j})(1 - |s_{i,j}^M|)\end{aligned} \tag{III.50}$$

Carrying out the summation over the binding variables in the partition function gives

$$\Omega = \int \mathcal{D}\rho_{HM} \int \mathcal{D}\eta \int \mathcal{D}\psi \exp\Big[e^{\beta\mu_w} q_w(\psi,\eta) + e^{\beta\mu_+} q_+(\psi,\eta) + e^{\beta\mu_-} q_-(\psi,\eta) + e^{\beta\mu_p} Q_p(w_{HM},\psi,\eta) + \int d\mathbf{r}\Big(\frac{1}{8\pi l_B}\big(\nabla(i\beta e\psi)\big)^2 - \frac{i\beta\eta}{v}\Big) - \int d\mathbf{r}\beta u_{\text{surf}}(\mathbf{r})\rho_{HM} - i\int d\mathbf{r}\beta w_{HM}\rho_{HM}\Big] \tag{III.51}$$

The single particle partition functions are

$$q_w(\psi,\eta) = \frac{1}{v}\int d\mathbf{r}\Big(e^{i\beta\eta} + e^{i\beta\eta - i\beta e\psi + \beta\lambda + \beta a_w} + e^{i\beta\eta + i\beta e\psi - \beta\lambda + \beta a_w}\Big) \tag{III.52}$$

$$q_+(\psi,\eta) = \frac{1}{v}\int d\mathbf{r} e^{i\beta\eta - i\beta e\psi Z_+} \tag{III.53}$$

$$q_-(\psi,\eta) = \frac{1}{v}\int d\mathbf{r} e^{i\beta\eta - i\beta e\psi Z_-} \tag{III.54}$$

The single chain partition function is

$$Q_p(w_{HM},\psi,\eta) = \frac{1}{v^N}\int d\mathbf{r}^N \exp\Big[-\sum_{j=1}^{N-1}\beta h(\mathbf{r}_{j+1}-\mathbf{r}_j) + \sum_{j=1}^{N}\beta\xi_j(\mathbf{r_j})\Big] \tag{III.55}$$

where $\xi_i(\mathbf{r})$ is the effective field for each monomer. The monomer-specificity goes into the microscopic binding constant βa_i.

$$\beta\xi_j(\mathbf{r}) = i\beta\eta + \ln\Big[\exp(i\beta w_{HM}) + \exp(i\beta e\psi - \beta\lambda + \beta a^j_{M_1}) + \exp(-i\beta e\psi + \beta\lambda - \beta a^j_{M_2})\Big] \tag{III.56}$$

At this point, we will redefine and nondimensionalize some quantities for convenience and clarity in manipulating the equations. The dissociation constants: $K^W = \exp(\beta a_w)$ and $K_j^{D_k} = \exp(\beta a^j_{M_k})$. All of the integrations of $\mathbf{r}$ can be nondimensionalized by the segment length b. Knowing that the fluctuating fields will turn out to be purely imaginary from the saddle point approximation, we can rewrite drop the imaginary parts of the above equations. The partition functions become the following.

$$\Omega = \int \mathcal{D}\rho_{HM} \int \mathcal{D}\eta \int \mathcal{D}\psi \exp\Big[e^{\beta\mu_w} q_w(\psi,\eta) + e^{\beta\mu_+} q_+(\psi,\eta) + e^{\beta\mu_-} q_-(\psi,\eta) + e^{\beta\mu_p} \ln Q_p(w_{HM},\psi,\eta) + \int d\mathbf{r}\Big(\frac{1}{8\pi l_B}\big(\nabla(\beta e\psi)\big)^2 - \beta\eta\Big) - \int d\mathbf{r}\beta u_{\text{surf}}(\mathbf{r})\rho_{HM} - \int d\mathbf{r}\beta w_{HM}\rho_{HM}\Big] \tag{III.57}$$

$$q_w(\psi,\eta) = \int d\mathbf{r}\Big(e^{\beta\eta} + K^W e^{\beta\eta-\beta e\psi+\beta\lambda} + K^W e^{\beta\eta+\beta e\psi-\beta\lambda}\Big) \tag{III.58}$$

$$q_+(\psi,\eta) = \int d\mathbf{r} e^{\beta\eta-\beta e\psi Z_+} \tag{III.59}$$

$$q_-(\psi,\eta) = \int d\mathbf{r} e^{\beta\eta-\beta e\psi Z_-} \tag{III.60}$$

$$Q_p(w_{HM},\psi,\eta) = \int d\mathbf{r}^N \exp\Big[-\sum_{j=1}^{N-1} \beta h(\mathbf{r}_{j+1}-\mathbf{r}_j) + \sum_{j=1}^{N} \beta\xi_j(\mathbf{r_j})\Big] \tag{III.61}$$

$$\beta\xi_j(\mathbf{r}) = \beta\eta + \ln\Big[\exp(\beta w_{HM}) + K_j^{D_1}\exp(\beta e\psi-\beta\lambda) + K_j^{D_2}\exp(-\beta e\psi+\beta\lambda)\Big] \tag{III.62}$$

Writing out the single chain partition function

$$Q_p(w_{HM},\psi,\eta) = \int d\mathbf{r}^N \exp\Big[\beta\xi_1(\mathbf{r_1})\Big]\exp\Big[-\beta h(\mathbf{r}_2-\mathbf{r}_1)+\beta\xi_2(\mathbf{r_2})\Big]\times\ldots \exp\Big[-\beta h(\mathbf{r}_{j+1}-\mathbf{r}_j)+\beta\xi_j(\mathbf{r_j})\Big]\exp\Big[-\beta h(\mathbf{r}_N-\mathbf{r}_{N-1})+\beta\xi_N(\mathbf{r_N})\Big] \tag{III.63}$$

Defining a recursive propagator

$$q(j,\mathbf{r}) = \exp\Big[\beta\xi_j(\mathbf{r})\Big]\int d\mathbf{r}'\exp\Big[-\beta h(\mathbf{r}-\mathbf{r}')\Big]q(j-1,\mathbf{r}') \tag{III.64}$$

with initial condition $q(1,\mathbf{r}) = \exp\Big[\beta\xi_1(\mathbf{r})\Big]$. We similarly have the complimentary propagator

$$q^*(j,\mathbf{r}) = \exp\Big[\beta\xi_j(\mathbf{r})\Big]\int d\mathbf{r}'\exp\Big[-\beta h(\mathbf{r}-\mathbf{r}')\Big]q(j+1,\mathbf{r}') \tag{III.65}$$

with initial condition $q^*(N,\mathbf{r}) = \exp\Big[\beta\xi_N(\mathbf{r})\Big]$.

Saddle Point Approximation

For convenience, we start by defining the density operators. With $v = b^3$, the reduced density is the same as the volume fraction. We'll use the volume fraction for convenience ϕ.

$$\phi_w(\mathbf{r}) = e^{\beta\mu_w}\frac{\delta q_w(\psi,\eta)}{\delta\beta\eta} = e^{\beta\mu_w}\left(e^{\beta\eta} + K^W e^{\beta\eta-\beta e\psi+\beta\lambda} + K^W e^{\beta\eta+\beta e\psi-\beta\lambda}\right) \quad \text{(III.66)}$$

$$\phi_+(\mathbf{r}) = e^{\beta\mu_+}\frac{\delta q_+(\psi,\eta)}{\delta\beta\eta} = e^{\beta\mu_+}e^{\beta\eta-\beta e\psi Z_+} \quad \text{(III.67)}$$

$$\phi_-(\mathbf{r}) = e^{\beta\mu_-}\frac{\delta q_-(\psi,\eta)}{\delta\beta\eta} = e^{\beta\mu_-}e^{\beta\eta-\beta e\psi Z_-} \quad \text{(III.68)}$$

$$\phi_M(\mathbf{r}) = e^{\beta\mu_p}\sum_{j=1}^{N}\frac{\delta Q_p}{\delta\beta\xi_j} = e^{\beta\mu_p}\sum_{j=1}^{N}\frac{\delta Q_p}{\delta\beta\xi_j} = e^{\beta\mu_p}\sum_{j=1}^{N} q(j,\mathbf{r})\exp\Big[-\beta\xi_j(\mathbf{r})\Big]q^*(j,\mathbf{r}) \quad \text{(III.69)}$$

The variation with respect to the density field ρ_{HM} gives the following

$$w_{HM} = -u_{\text{surf}} \quad \text{(III.70)}$$

Taking the variation with respect to the incompressibility and electric potential fields give

$$\phi_w + \phi_+ + \phi_- + \phi_M = 1 \quad \text{(III.71)}$$

$$\frac{-1}{4\pi l_B}\nabla^2\psi = \phi_c \quad \text{(III.72)}$$

Or equivalently (useful later)

$$e^{\beta\mu_w+\beta\eta} = \frac{1-\phi_+-\phi_--\phi_M}{1+K^W e^{-\beta e\psi+\beta\lambda}+K^W e^{\beta e\psi-\beta\lambda}} = f_{H_2O}(1-\phi_+-\phi_--\phi_M) \quad \text{(III.73)}$$

$$\frac{-1}{4\pi l_B}\nabla^2\psi = \phi_w\left(f_{H_3O^+}-f_{OH^-}\right)+\phi_M\left(f_{H_2M^+}-f_{M^-}\right)+Z_+\phi_++Z_-\phi_- \quad \text{(III.74)}$$

with the following fractions defined

$$f_{H_2O} = \frac{1}{1+K^W e^{-\beta e\psi+\beta\lambda}+K^W e^{\beta e\psi-\beta\lambda}} \quad \text{(III.75)}$$

$$f_{H_3O^+} = \frac{K^W e^{-\beta e\psi+\beta\lambda}}{1+K^W e^{-\beta e\psi+\beta\lambda}+K^W e^{\beta e\psi-\beta\lambda}} \quad \text{(III.76)}$$

$$f_{OH^-} = \frac{K^W e^{\beta e\psi-\beta\lambda}}{1+K^W e^{-\beta e\psi+\beta\lambda}+K^W e^{\beta e\psi-\beta\lambda}} \quad \text{(III.77)}$$

The fractions for the monomers are weighted by the segment densities

$$f_{HM_j} = \frac{e^{-\beta u_{\text{surf}}}}{e^{-\beta u_{\text{surf}}} + K_j^{D_1} e^{\beta e\psi - \beta\lambda} + K_j^{D_2} e^{-\beta e\psi + \beta\lambda}} \tag{III.78}$$

$$f_{HM} = \frac{\sum_{j=1}^{N} \phi_{M,j} f_{HM_j}}{\sum_{j=1}^{N} \phi_{M,j}} \tag{III.79}$$

$$f_{M_j^-} = \frac{K_j^{D_1} e^{\beta e\psi - \beta\lambda}}{e^{-\beta u_{\text{surf}}} + K_j^{D_1} e^{\beta e\psi - \beta\lambda} + K_j^{D_2} e^{-\beta e\psi + \beta\lambda}} \tag{III.80}$$

$$f_{M^-} = \frac{\sum_{j=1}^{N} \phi_{M,j} f_{M_j^-}}{\sum_{j=1}^{N} \phi_{M,j}} \tag{III.81}$$

Determining Binding Constants

To obtain values for K^w and K_j^D for the acid-base reactions, we must connect the expressions to the conventional acid-base equilibrium. To do this, we will use the fact that for pure water, $K_a^W \approx 10^{-14}(M^2)$ and $c_w^0 \approx 1000/18 = 55.56M$. From our definitions,

$$\frac{f_{H_3O^+} f_{OH^-}}{f_{H_2O}} = (K^W)^2 \tag{III.82}$$

In terms of molarity,

$$\frac{[H_3O^+][OH^-]}{[H_2O]^2} = \frac{10^{-14}}{[H_2O]^2} = (K^W)^2 \tag{III.83}$$

Since the fraction of $f_{H_2O} \approx 1$, then $K^W = 10^{-8.74}$. Similarly for the equilibria for each monomer in the absence of an electric field,

$$\frac{[H_3O^+][M_j^-]}{[H_2O][HM_j]} = K^W K_j^{D_1} = K_{a,1}^{M_j}/c_w^0 \tag{III.84}$$

$$\frac{[OH^-][H_2M_j^+]}{[H_2O][HM_j]} = K^W K_j^{D_2} = K_{a,2}^{M_j}/c_w^0 \tag{III.85}$$

In either case, $K_j^{D_k} = K_{a_k}^{M_j}/(K_a^W)^{1/2} = 10^{7 - pK_{a_k}^{M_j}}$. By specifying the pK_a of the monomer sequence, all of the dissociation constants can be obtained.

The protonation potential $\beta\lambda$ is determined by the pH and the total water concentration in the absence of an electric field. Starting with the definition of $f_{H_3O^+}$,

$$f_{H_3O^+} = \frac{K^W e^{\beta\lambda}}{1 + K^W e^{\beta\lambda} + K^W e^{-\beta\lambda}} \tag{III.86}$$

Making a quadratic equation

$$K^W(f_{H_3O^+}-1)e^{2\beta\lambda}+f_{H_3O^+}e^{\beta\lambda}+K^W f_{H_3O^+}=0 \tag{III.87}$$

Solving the quadratic and taking the only possible solution

$$e^{\beta\lambda}=\frac{f_{H_3O^+}+\sqrt{f_{H_3O^+}^2+4(K^W)^2 f_{H_3O^+}(1-f_{H_3O^+})}}{2K^W(1-f_{H_3O^+})} \tag{III.88}$$

Substituting $f_{H_3O^+}=[H_3O^+]/c_w$,

$$e^{\beta\lambda}=\frac{[H_3O^+]/c_w+\sqrt{\left([H_3O^+]/c_w\right)^2+4(K^W)^2[H_3O^+]/c_w(1-[H_3O^+]/c_w)}}{2K^W(1-[H_3O^+]/c_w)} \tag{III.89}$$

$$e^{\beta\lambda}=[H_3O^+]\frac{1+\sqrt{1+4\frac{c_w(K^W)^2}{[H_3O^+]}(1-[H_3O^+]/c_w)}}{2c_wK^W(1-[H_3O^+]/c_w)} \tag{III.90}$$

We know in pure water that $[H_3O^+]=10^{-pH}$ ($c_w=c_w^0$),

$$e^{\beta\lambda}=10^{-pH}\frac{1+\sqrt{1+4c_w^0(K^W)^2\times 10^{pH}(1-10^{-pH}/c_w^0)}}{2c_w^0K^W(1-10^{-pH}/c_w^0)} \tag{III.91}$$

Results

While the theory above is developed above for polyacids and polybases, we will consider a polyacid for the results below. For polymer dispersants, formulations typically have a basic pH and use a polyacid. We consider a linear, homopolymer, polyacid dispersant with $pK_a = 5$. The strong polyelectrolytes considered in our earlier work interacted with the surface via electrostatic interactions and also non-electrostatic interactions. For weak polyelectrolytes, we model the nonelectrostatic interaction with the surface as only applying to the protonated form of the acid. Namely, the interaction of protonated states interacts with the surface via the following attractive potential, which coarsely represents a favorable coordination with the surface groups (i.e. hydrogen bonding).

$$u_{\text{surf}}(z)=-\beta\epsilon(1-z)\Theta(1-z) \tag{III.92}$$

Potential of mean force calculations for polyacrylic on aluminum oxide indicate that the neutral residue has a more attractive interaction than the protonated[1]. From the

[1]Unpublished simulation results by Chang Yun Son as part of the Dow University Partnership Initiative

theory, the spatially-dependent, average ionized fraction is

$$f_{M^-}(z) = \frac{K^D e^{\beta e\psi(z)-\beta\lambda}}{e^{-\beta u_{\text{surf}}(z)} + K^D e^{\beta e\psi(z)-\beta\lambda}} \approx \frac{10^{\text{pH}-\text{pK}_a} e^{\beta e\psi(z)}}{e^{-\beta u_{\text{surf}}(z)} + 10^{\text{pH}-\text{pK}_a} e^{\beta e\psi(z)}} \tag{III.93}$$

For $\epsilon = 0$ (no surface preference), Equation III.93 indicates that the charge fraction increases with increasing pH, decreasing pK_a, or increasing electrostatic potential. The parameter $\beta\epsilon$ shifts local equilibrium in the vicinity toward the neutral state to have a picture like Figure III.19. For adsorption to a negatively charged surface, as

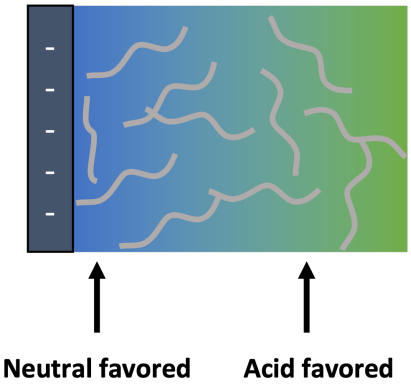

Figure III.19: Schematic showing neutral state preferred in the vicinity of the surface.

is the case of alumina or titanium oxide at a basic pH, the electrostatic potential and the preferential adsorption create a neutral favored environment near the surface. Figure III.20 shows the monomer density profiles as for different values of $\beta\epsilon$. As $\beta\epsilon$ increases, the fraction of ionized monomers in vicinity of the surface significantly decreases with almost no ionized monomers for $\beta\epsilon = 12$. At the same time, the monomer density dramatically increases (though not discontinuously), raising to nearly 100 times the bulk concentration at the surface.

A key point to keep in mind is the length scale of the effect on the charge fraction and the density profiles. The charge fraction is only affected from the bulk value on the length scale of the potential u_{surf}. In Figure III.20, the fraction returns to a bulk value at approximately 0.2 nm. However, the density profiles clearly vary over a larger length scale. This indicates that the first layer of adsorption, which is primarily neutralized, is *dragging* a significant amount of charge monomers along with it. The physical picture is that of neutral *trains* adsorbed to the surface with charge *tails* extending from the surface (Figure III.21).

The physical picture presented above is encouraging for the mediated interaction between surfaces. The extended, charged tails can overlap and provide a barrier to

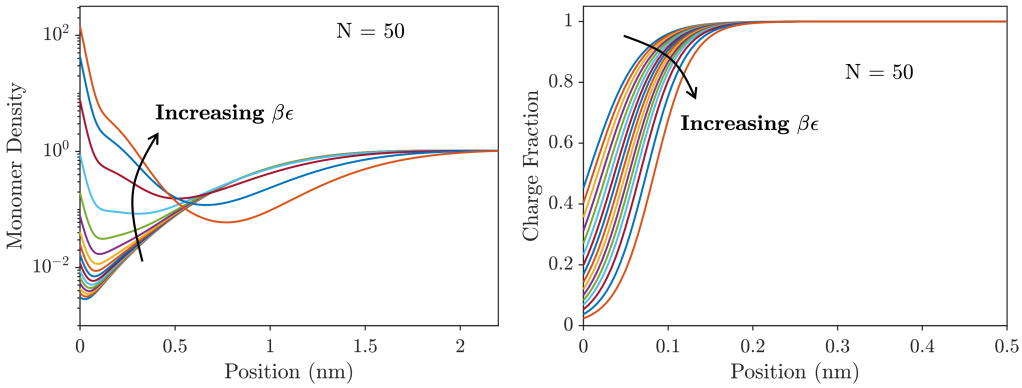

Figure III.20: Monomer density (left) and ionized monomer fraction (right) profiles for a polymer dispersant with pK_a = 5 in a pH=9 solution with no added salt (only counterions) in contact with a surface with fixed surface charge density of -0.1 $\frac{e}{nm^2}$. The bulk density of monomers is ϕ_M^{bulk} = 0.1% and $\beta\epsilon$ values range from 9 to 12.

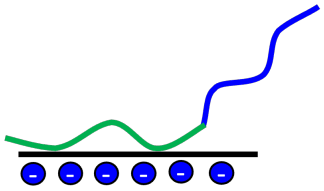

Figure III.21: Schematic for adsorption of weak polyelectrolyte with preferential interaction of neutral residues with the surface.

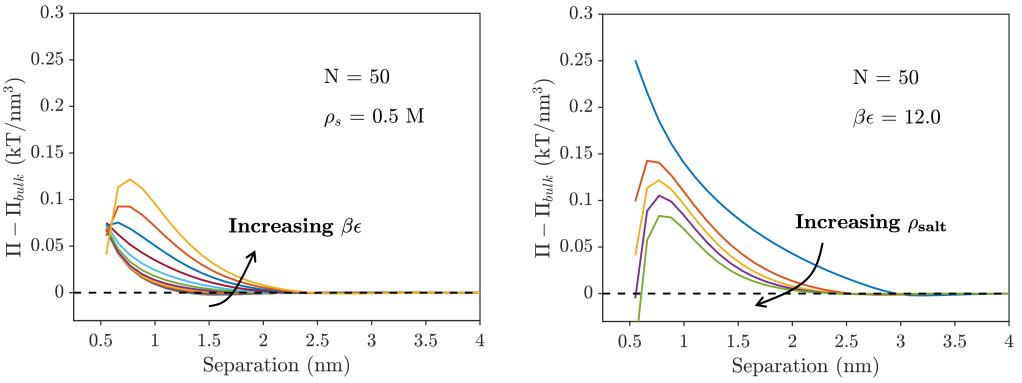

Figure III.22: Interaction force between two surfaces (left) for various neutral residue–surface interaction strengths $\beta\epsilon$ ranging from 9 to 12 and (right) for various salt concentrations from no added salt to 1 M. Polymer dispersant pK_a = 5, pH=9, fixed surface charge density of -0.1 $\frac{e}{nm^2}$. The bulk density of monomers is ϕ_M^{bulk} = 0.1%.

further approach for two colloidal sized particles. Figure III.22 shows the disjoining pressure between two surfaces. With increasing $\beta\epsilon$, the amount of adsorbed polymer increases, including the charged tails. When bringing the two surfaces together, the adsorbed layers overlap. The ion repulsion in the charged tails leads to net repulsion between the surfaces. Increasing the salt concentration decreases penalty of tails overlapping due to screening.

Conclusion

We presented a microscopic model that naturally accounts for the charge regulation of weak polyelectrolytes at the mean-field level based on Ising-like configurational states. By building in a preferential adsorption of neutral monomers for a polyacid, monomers near the surface are neutralized, leading to trains of neutral monomers and extended tails of charged monomers. Such a conformation is ideal for imparting repulsion between two particles. Indeed, a repulsive barrier is seen when two layers of charged tails overlap. Unfortunately, for all of the systems here, none of the repulsive barriers are strong enough to overcome the Hamaker potential. There are a few possible reasons. The self-consistent field theory underestimates the packing and other correlation effects that would be present with such strong adsorption. We aim to incorporate these real ion effects into a more realistic model. Nevertheless, the self-consistent field framework captures the main physics of weak polyelectrolytes near a solid surface.

References

(1) Balzer, C.; Jiang, J.; Marson, R. L.; Ginzburg, V. V.; Wang, Z.-G. *Langmuir* **2021**, *37*, 5483–5493, DOI: 10.1021/acs.langmuir.1c00139.

(2) Gregory, J. *Journal of Colloid And Interface Science* **1973**, *42*, 448–456, DOI: 10.1016/0021-9797(73)90311-1.

(3) Marra, J.; Hair, M. L. *Journal of Physical Chemistry* **1988**, *92*, 6044–6051, DOI: 10.1021/j100332a041.

(4) Åkesson, T.; Woodward, C.; Jönsson, B. *The Journal of Chemical Physics* **1989**, *91*, 2461–2469, DOI: 10.1063/1.457006.

(5) Miklavic, S. J.; Woodward, C. E.; Jönsson, B.; Åkesson, T. *Macromolecules* **1990**, *23*, 4149–4157, DOI: 10.1021/ma00220a019.

(6) Popa, I.; Gillies, G.; Papastavrou, G.; Borkovec, M. *Journal of Physical Chemistry B* **2009**, *113*, 8458–8461, DOI: 10.1021/jp904041k.

(7) Üzüm, C.; Christau, S.; Von Klitzing, R. *Macromolecules* **2011**, *44*, 7782–7791, DOI: 10.1021/ma201466a.

(8) Üzüm, C.; Makuska, R.; Von Klitzing, R. *Macromolecules* **2012**, *45*, 3168–3176, DOI: 10.1021/ma202763m.

(9) Maroni, P.; Montes Ruiz-Cabello, F. J.; Cardoso, C.; Tiraferri, A. *Langmuir* **2015**, *31*, 6045–6054, DOI: 10.1021/acs.langmuir.5b01103.

(10) Forsman, J. *Current Opinion in Colloid and Interface Science* **2006**, *11*, 290–294, DOI: 10.1016/j.cocis.2006.09.003.

(11) Scranton, A. B.; Rangarajan, B.; Klier, J. *Advances in Polymer Science* **1995**, *122*, DOI: 10.1007/3540587888_13.

(12) Claesson, P. M.; Dedinaite, A.; Rojas, O. J. *Advances in Colloid and Interface Science* **2003**, *104*, 53–74, DOI: 10.1016/S0001-8686(03)00036-8.

(13) Howe, A. M.; Wesley, R. D.; Bertrand, M.; Côte, M.; Leroy, J. *Langmuir* **2006**, *22*, 4518–4525, DOI: 10.1021/la053327s.

(14) Bolto, B.; Gregory, J. *Water Research* **2007**, *41*, 2301–2324, DOI: 10.1016/j.watres.2007.03.012.

(15) Kohay, H.; Bilkis, I. I.; Mishael, Y. G. *Journal of Colloid and Interface Science* **2019**, *552*, 517–527, DOI: 10.1016/j.jcis.2019.05.079.

(16) Maurdev, G.; Meagher, L.; Ennis, J.; Gee, M. L. *Macromolecules* **2001**, *34*, 4151–4158, DOI: 10.1021/ma001237i.

(17) Gillies, G.; Lin, W.; Borkovec, M. *Journal of Physical Chemistry B* **2007**, *111*, 8626–8633, DOI: 10.1021/jp069009z.

(18) Hierrezuelo, J.; Sadeghpour, A.; Szilagyi, I.; Vaccaro, A.; Borkovec, M. *Langmuir* **2010**, *26*, 15109–15111, DOI: 10.1021/la102912u.

(19) Xie, F.; Nylander, T.; Piculell, L., et al. *Langmuir* **2013**, *29*, 12421–12431, DOI: 10.1021/la4020702.

(20) Moazzami Gudarzi, M.; Trefalt, G.; Szilagyi, I.; Maroni, P.; Borkovec, M. *Journal of Physical Chemistry C* **2015**, *119*, 15482–15490, DOI: 10.1021/acs.jpcc.5b04426.

(21) Xie, F.; Lu, H.; Nylander, T.; Wågberg, L.; Forsman, J. *Langmuir* **2016**, *32*, 5721–5730, DOI: 10.1021/acs.langmuir.6b00668.

(22) Böhmer, M. R.; Evers, O. A.; Scheutjens, J. M. *Macromolecules* **1990**, *23*, 2288–2301, DOI: 10.1021/ma00210a027.

(23) Pryamitsyn, V.; Ganesan, V. *Macromolecules* **2014**, *47*, 6095–6112, DOI: 10.1021/ma501014u.

(24) Pandav, G.; Pryamitsyn, V.; Errington, J.; Ganesan, V. *Journal of Physical Chemistry B* **2015**, *119*, 14536–14550, DOI: 10.1021/acs.jpcb.5b07905.

(25) Forsman, J. *Current Opinion in Colloid and Interface Science* **2017**, *27*, 57–62, DOI: 10.1016/j.cocis.2016.10.001.

(26) Andelman, D.; Joanny, J. F. *Comptes Rendus de l'Academie des Sciences - Series IV: Physics, Astrophysics* **2000**, *1*, 1153–1162, DOI: 10.1016/S1296-2147(00)01130-6.

(27) Dobrynin, A. V.; Deshkovski, A.; Rubinstein, M. *Macromolecules* **2001**, *34*, 3421–3436, DOI: 10.1021/ma0013713.

(28) Wang, Q. *Macromolecules* **2005**, *38*, 8911–8922, DOI: 10.1021/ma050960b.

(29) Li, Z.; Wu, J. *Physical Review Letters* **2006**, *96*, 048302, DOI: 10.1103/PhysRevLett.96.048302.

(30) Turesson, M.; Akesson, T.; Forsman, J. *Langmuir* **2007**, *23*, 9555–9558, DOI: 10.1021/la7017852.

(31) Wang, L.; Liang, H.; Wu, J. *Journal of Chemical Physics* **2010**, *133*, 7230, DOI: 10.1063/1.3463426.

(32) Forsman, J. *Langmuir* **2012**, *28*, 5138–5150, DOI: 10.1021/la3000735.

(33) Forsman, J.; Nordholm, S. *Langmuir* **2012**, *28*, 4069–4079, DOI: 10.1021/la2045459.

(34) Luque-Caballero, G.; Martín-Molina, A.; Quesada-Pérez, M. *Journal of Chemical Physics* **2014**, *140*, 174701, DOI: 10.1063/1.4872263.

(35) Tiraferri, A.; Maroni, P.; Borkovec, M. *Physical Chemistry Chemical Physics* **2015**, *17*, 10348–10352, DOI: 10.1039/c5cp00910c.

(36) Bassalah, M. E.; Cerdà, J. J.; Sintes, T.; Aschi, A.; Othman, T. *European Polymer Journal* **2017**, *96*, 55–68, DOI: 10.1016/j.eurpolymj.2017.08.045.

(37) Muráth, S.; Sáringer, S.; Somosi, Z.; Szilágyi, I. *Colloids and Interfaces* **2018**, *2*, 32, DOI: 10.3390/colloids2030032.

(38) Turesson, M.; Labbez, C.; Nonat, A. *Langmuir* **2011**, *27*, 13572–13581, DOI: 10.1021/la2030846.

(39) Israëls, R.; Leermakers, F. A.; Fleer, G. J. *Macromolecules* **1995**, *28*, 1626–1634, DOI: 10.1021/ma00109a040.

(40) Claesson, P. M.; Poptoshev, E.; Blomberg, E.; Dedinaite, A. *Advances in Colloid and Interface Science* **2005**, *114-115*, 173–187, DOI: 10.1016/j.cis.2004.09.008.

(41) Podgornik, R.; Ličer, M. *Current Opinion in Colloid and Interface Science* **2006**, *11*, 273–279, DOI: 10.1016/j.cocis.2006.08.001.

(42) Szilagyi, I.; Trefalt, G.; Tiraferri, A.; Maroni, P.; Borkovec, M. *Soft Matter* **2014**, *10*, 2479–2502, DOI: 10.1039/c3sm52132j.

(43) Blaakmeer, J.; Böhmer, M. R.; Cohen Stuart, M. A.; Fleer, G. J. *Macromolecules* **1990**, *23*, 2301–2309, DOI: 10.1021/ma00210a028.

(44) Van de Steeg, H. G.; Stuart, M. A.; de keizer, A.; Bijsterbosch, B. H. *Langmuir* **1992**, *8*, 2538–2546, DOI: 10.1021/la00046a030.

(45) Rehmet, R.; Killmann, E. *Colloids and Surfaces A: Physicochemical and Engineering Aspects* **1999**, *149*, 323–328, DOI: 10.1016/S0927-7757(98)00329-X.

(46) Mészáros, R.; Thompson, L.; Bos, M.; De Groot, P. *Langmuir* **2002**, *18*, 6164–6169, DOI: 10.1021/la011776w.

(47) Popa, I.; Cahill, B. P.; Maroni, P.; Papastavrou, G.; Borkovec, M. *Journal of Colloid and Interface Science* **2007**, *309*, 28–35, DOI: 10.1016/j.jcis.2007.01.050.

(48) Seyrek, E.; Hierrezuelo, J.; Sadeghpour, A.; Szilagyi, I.; Borkovec, M. *Physical Chemistry Chemical Physics* **2011**, *13*, 12716–12719, DOI: 10.1039/c1cp20654k.

(49) Maroni, P.; Montes Ruiz-Cabello, F. J.; Tiraferri, A. *Soft Matter* **2014**, *10*, 9220–9225, DOI: 10.1039/c4sm02093f.

(50) Rojas, O. J.; Claesson, P. M.; Muller, D.; Neuman, R. D. *Journal of Colloid and Interface Science* **1998**, *205*, 77–88, DOI: 10.1006/jcis.1998.5596.

(51) Stoll, S.; Chodanowski, P. *Macromolecules* **2002**, *35*, 9556–9562, DOI: 10.1021/ma020272h.

(52) Van de Steeg, H. G.; de Keizer, A.; Stuart, M. A.; Bijsterbosch, B. H. *Colloids and Surfaces A: Physicochemical and Engineering Aspects* **1993**, *70*, 77–89, DOI: 10.1016/0927-7757(93)80498-4.

(53) Enarsson, L. E.; Wågberg, L. *Langmuir* **2008**, *24*, 7329–7337, DOI: 10.1021/la800198e.

(54) Jiang, M.; Popa, I.; Maroni, P.; Borkovec, M. *Colloids and Surfaces A: Physicochemical and Engineering Aspects* **2010**, *360*, 20–25, DOI: 10.1016/j.colsurfa.2010.01.070.

(55) Shafir, A.; Andelman, D.; Netz, R. R. *Journal of Chemical Physics* **2003**, *119*, 2355–2362, DOI: 10.1063/1.1580798.

(56) Jiang, J.; Ginzburg, V. V.; Wang, Z. G. *Journal of Chemical Physics* **2019**, *151*, 214901, DOI: 10.1063/1.5123172.

(57) Israëls, R.; Scheutjens, J. M.; Fleer, G. J. *Macromolecules* **1993**, *26*, 5405–5413, DOI: 10.1021/ma00072a018.

(58) Jain, S.; Ginzburg, V. V.; Jog, P., et al. *Journal of Chemical Physics* **2009**, *131*, 20901, DOI: 10.1063/1.3177009.

(59) Jiang, J.; Ginzburg, V. V.; Wang, Z. G. *Soft Matter* **2018**, *14*, 5878–5887, DOI: 10.1039/c8sm00595h.

(60) Fazio, S.; Guzmán, J.; Colomer, M. T.; Salomoni, A.; Moreno, R. *Journal of the European Ceramic Society* **2008**, *28*, 2171–2176, DOI: 10.1016/j.jeurceramsoc.2008.02.017.

(61) Wiśniewska, M.; Urban, T.; Grządka, E.; Zarko, V. I.; Gun'ko, V. M. *Colloid and Polymer Science* **2014**, *292*, 699–705, DOI: 10.1007/s00396-013-3103-x.

(62) Woodward, C. E. *The Journal of Chemical Physics* **1991**, *94*, 3183–3191, DOI: 10.1063/1.459787.

(63) Blum, L. *Molecular Physics* **1975**, *30*, 1529–1535, DOI: 10.1080/00268977500103051.

(64) Høye, J. S.; Stell, G. *The Journal of Chemical Physics* **1977**, *67*, 439–445, DOI: 10.1063/1.434887.

(65) Blum, L.; Rosenfeld, Y. *Journal of Statistical Physics* **1991**, *63*, 1177–1190, DOI: 10.1007/BF01030005.

(66) Gillespie, D.; Nonner, W.; Eisenberg, R. S. *Journal of Physics Condensed Matter* **2002**, *14*, 12129–12145, DOI: 10.1088/0953-8984/14/46/317.

(67) Wertheim, M. S. *Journal of Statistical Physics* **1984**, *35*, 35–47, DOI: 10.1007/BF01017363.

(68) Wertheim, M. S. *Journal of Statistical Physics* **1984**, *35*, 19–34, DOI: 10.1007/BF01017362.

(69) Wertheim, M. S. *The Journal of Chemical Physics* **1986**, *85*, 2929–2936, DOI: 10.1063/1.451002.

(70) Wertheim, M. S. *The Journal of Chemical Physics* **1988**, *88*, 1145–1155, DOI: 10.1063/1.454233.

(71) Segura, C. J.; Vakarin, E. V.; Chapman, W. G.; Holovko, M. F. *Journal of Chemical Physics* **1998**, *108*, 4837–4848, DOI: 10.1063/1.475893.

(72) Yu, Y. X.; Wu, J. *Journal of Chemical Physics* **2002**, *117*, 2368–2376, DOI: 10.1063/1.1491240.

(73) Yu, Y. X.; Wu, J. *Journal of Chemical Physics* **2002**, *116*, 7094–7103, DOI: 10.1063/1.1463435.

(74) Roth, R.; Evans, R.; Lang, A.; Kahl, G. *Journal of Physics Condensed Matter* **2002**, *14*, 12063–12078, DOI: 10.1088/0953-8984/14/46/313.

(75) Roth, R. *Journal of Physics Condensed Matter* **2010**, *22*, 18, DOI: 10.1088/0953-8984/22/6/063102.

(76) Jog, P. K.; Ginzburg, V. V.; Srivastava, R., et al. In *Advances in Chemical Engineering*; Academic Press Inc.: 2010; Vol. 39, pp 131–164, DOI: 10.1016/S0065-2377(10)39003-X.

(77) Jiang, J.; Liu, H.; Hu, Y.; Prausnitz, J. M. *Journal of Chemical Physics* **1998**, *108*, 780–784, DOI: 10.1063/1.475438.

(78) Jiang, J. W.; Blum, L.; Bernard, O.; Prausnitz, J. M. *Molecular Physics* **2001**, *99*, 1121–1128, DOI: 10.1080/00268970110043414.

(79) Zhang, P.; Shen, K.; Alsaifi, N. M.; Wang, Z. G. *Macromolecules* **2018**, *51*, 5586–5593, DOI: 10.1021/acs.macromol.8b00726.

(80) Dobrynin, A. V.; Rubinstein, M. *Progress in Polymer Science (Oxford)* **2005**, *30*, 1049–1118, DOI: 10.1016/j.progpolymsci.2005.07.006.

(81) Shen, K.; Wang, Z. G. *Journal of Chemical Physics* **2017**, *146*, 84901, DOI: 10.1063/1.4975777.

(82) Israelachvili, J. N.; Adams, G. E. *Journal of the Chemical Society, Faraday Transactions 1: Physical Chemistry in Condensed Phases* **1978**, *74*, 975–1001, DOI: 10.1039/F19787400975.

(83) Zhou, H.-X.; Pang, X. *Chemical Reviews* **2018**, *118*, 1691–1741, DOI: 10.1021/acs.chemrev.7b00305.

(84) Kern, W. *Zeitschrift für Physikalische Chemie* **1939**, *184A*, 197–210, DOI: 10.1515/zpch-1939-18416.

(85) Katchalsky, A.; Spitnik, P. *Journal of Polymer Science* **1947**, *2*, 432–446, DOI: 10.1002/POL.1947.120020409.

(86) Gamble, D. S. *Canadian Journal of Chemistry* **1970**, *48*, 2662–2669, DOI: 10.1139/v70-450.

(87) Koper, G. J.; Borkovec, M. *Polymer* **2010**, *51*, 5649–5662, DOI: 10.1016/j.polymer.2010.08.067.

(88) Nakamura, I.; Wang, Z. G. *Soft Matter* **2012**, *8*, 9356–9367, DOI: 10.1039/c2sm25606a.

(89) Gallegos, A.; Ong, G. M. C.; Wu, J. *The Journal of Chemical Physics* **2021**, *155*, 241102, DOI: 10.1063/5.0066774.

Chapter IV

SURFACE PHASE TRANSITIONS

Phase separation is usually thought of and studied in the context of macrophase separation, where two coexisting form arbitrarily large domains. When the domain size is finite, the phase separation is deemed microphase separation. The canonical example of microphase separation is that of a diblock copolymer, where unfavorable interaction between A- and B-type blocks leads to regions of A-rich (B-poor) and B-rich (A-poor) that cannot be macroscopic due to the chain connectivity [1]. Surface phase transitions are similar to microphase separation in that the surface effects and phases are localized to a finite region. The strength and length scale of the surface interaction plays a significant role in the phase behavior near a solid interface. This chapter considers the wetting behavior of polyelectrolyte complex coacervates and controlling wettability using electrostatic manipulation of the surface.

This chapter includes content from our previously published article:

Balzer, C.; Zhang, P.; Wang, Z.-G. *Soft Matter* **2022**, *18*, 6326–6339, DOI: 10.1039/D2SM00859A

I am thankful to Prof. Pengfei Zhang for the initial notes and guidance on the inhomogeneous theory used throughout this chapter. I would also like to thank Dr. Andy Ylitalo for enticing me to pursue polyelectrolyte complex coacervation. Andy's excitement for the topic was contagious, and our shared project was one of the highlights of my time at Caltech. I also thank Sam Varner for fruitful discussions on surface phase transitions over the years.

IV.1 Wetting Behavior of Complex Coacervates

The wetting behavior of complex coacervates underpins their use in many emerging applications of surface science, particularly wet adhesives and coatings. Many factors dictate if a coacervate phase will condense on a solid surface, including solution conditions, the nature of the polymer–substrate interaction, and the underlying supernatant–coacervate bulk phase behavior. In this work, we use a simple inhomogeneous mean-field theory to study the wetting behavior of complex coacervates on solid surfaces both off-coexistence (wetting transitions) and on-coexistence (contact angles). We focus on the effects of salt concentration, the polycation/polyanion surface affinity, and the applied electrostatic potential on the wettability. We find that the coacervate generally wets the surface via a first order wetting transition with second order transitions possible above a surface critical point. Applying an electrostatic potential to a solid surface always improves the surface wettability when the polycation/ polyanion–substrate interaction is symmetric. For asymmetric surface affinity, the wettability has a nonmonotonic dependence with the applied potential. We use simple scaling and thermodynamic arguments to explain our results.

Introduction

Polyelectrolyte complex coacervation is a type of associative liquid-liquid phase separation where oppositely charged polyelectrolytes separate into a coacervate phase (polymer-rich) and a supernatant phase (polymer-depleted) [3]. In the past few decades, there has been broad interest in complex coacervation due to its wide range of applications across scientific disciplines. For example, complex coacervation has proven to be an efficient means of encapsulation [4], enabling its use in the food [5–8], textile [9–12], and agricultural industries [13]. Emerging technologies of complex coacervates include targeted drug delivery [14, 15], fabrication of hydrogels [16], and development of wet adhesives [17].

Utilizing complex coacervation relies on understanding the factors that influence the bulk phase behavior and interfacial properties. Knowing the location of the two-phase boundary for a variety of solution conditions is crucial to exploit the phase transition. There are many factors that contribute to the bulk phase behavior, such as the salt concentration, valency of salt ions, charge state of the polyelectrolytes, chain length, temperature, and sequence of the polymer backbone, which have each been explored with experiments and theory [3, 18–20]. In the past decade, there has also been significant progress in characterizing the interfacial properties of the coacervate–supernatant interface — notably, the interfacial tension [21, 22]. Exper-

iments and theory of symmetric mixtures of polyelectrolytes have characterized the scaling of interfacial tension with the salt concentration relative to the critical salt concentration [23–31] ($\gamma \sim [\phi_{\pm}^{\mathrm{crit}} - \phi_{\pm}]^{3/2}$) and with the chain length [24, 26, 32]. Simulations and theory also give access to additional interfacial properties, such interface thickness and excess adsorption [27]. Access to the interfacial profiles is particularly important for asymmetric mixtures of polyelectrolytes, where local charge separation can lead to spatially varying, and usually nonmonotonic, profiles of the electrostatic potential [30, 33].

Compared to the coacervate–supernatant interface, the supernatant and coacervate phases near solid surfaces are relatively unexplored. Of central importance for solid substrates is the adsorption and corresponding wetting (or drying) behavior of the coacervate phase. The contact angle (at the substrate-coacervate-supernatant equilibrium) will determine the coacervate's ability to coat a surface. Few works have reported contact angles for these systems, partly due to the difficultly of measuring the contact angle *in situ* [22]. Contact angles are predominantly reported for their relevance to experimental measurements of the interfacial tension, such as colloidal probe atomic force microscopy (CP-AFM) and surface force apparatus (SFA). For example, in measuring interfacial tension with CP-AFM, Spruijt and coworkers presented the contact angle of a coacervate phase in the corresponding supernatant phase on a silica surface for different salt concentrations, reporting contact angles less than 45° and a transition to complete wetting (zero contact angle) above 1 M [23]. Lim *et al.* found that salt solutions in the Hofmeister series at a single salt concentration give contact angles ranging from 25° to above 90° (nonwetting) [34]. In SFA measurements, the interfacial tension is measured via an extrapolation of the pull-off force to zero separation $\gamma = (1/4\pi)(F_{\mathrm{pull},0}/R)\cos\theta$, where R is related to the geometry of the probe. In these measurements, the contact angle has been assumed to be zero (complete wetting) so that $\cos\theta \approx 1$ [21, 24, 35]. Such an assumption dismisses the role of the surface. Overall, the lack of experimental data leaves many open questions. For instance, how do different surface types and solution conditions affect wettability?

Understanding how complex coacervates wet surfaces can inform design of complex coacervates for applications on solid surfaces, like wet adhesives. The performance of wet adhesives critically depends on their ability to wet a substrate in complex and challenging environments, such as the human body [36]. Recently, there has been a proliferation of wet adhesive materials inspired by the adhesives created by marine

organisms [17, 37], notably the sandcastle worm [38–42] and seawater mussel [35, 43–47]. Both of these creatures secrete glue-like proteins that undergo coacervation (complex coacervation or single-component coacervation), wet the adhering surface, and cure into a strong adhesive [48]. Most of the bio-inspired adhesives mimic these glue protein sequences, particularly in their inclusion of 3,4-dihydroxyphenylalanine (DOPA) residues, which serve to both enhance adsorption of the adhesive to the surface and aid in curing the adhesive after oxidation [38, 49]. As emphasized by Waite [49], mimicking the residue composition of marine life proteins alone does not capture the complexity of mussel adhesion. The success of mussels in adhering to a variety of surfaces [44] depends on their ability to intricately prepare the surface properties and solution in the proximity of the surface for their adhesive proteins. Replicating the versatility of marine life requires a fundamental understanding of the important factors that influence, and can be used to control, the wetting process.

In this work, we seek to understand and characterize the wetting behavior of symmetric polyelectrolyte complexes near a charged surface. Motivated by the variety of adsorption mechanisms proposed in biological systems [47], we study the effect of salt concentration on the wetting transitions and the contact angle when the polyelectrolyte complexes have nonelectrostatic and/or electrostatic interaction with the surface. To elucidate the main physics in this system, we use a simple inhomogeneous mean-field theory extended from a theory for studying the interfacial behavior of polyelectrolyte complex coacervates developed by Zhang and Wang [30]. The central difference from Ref. 30 is that the polyelectrolyte solution, either coacervate or supernatant, is in contact with a solid surface rather than its coexisting phase. Under the conditions studied, we find that the supernatant to coacervate wetting transition generally occurs via a first order prewetting transition with a second order transition occurring as one approaches the bulk critical salt concentration. Applying an electrostatic potential to the surface shifts the surface critical point away from the bulk critical point and always improves the wettability (lowers contact angles) when polycation and polyanion have identical nonelectrostatic attraction to the surface. However, asymmetry in nonelectrostatic attraction can lead to nonmonotonic changes of the contact angle with the applied potential. Our main finding is that electrostatic manipulation of the substrate is an efficacious method for controlling wettability. Contact angles can be substantially altered by applying small potentials ($\sim$ 10 mV), which is a direct result of the low supernatant–coacervate interfacial tension. By studying the effects of electrowetting and nonelectrostatic affinity (i.e. polymer chemistry), this work can serve to guide future design of coacervate

materials for applications such as encapsulation, coatings, and adhesives.

Theoretical Formulation

To study the wetting behavior, we model a polyelectrolyte solution in contact with a solid surface. Both the model and the theory are similar to that presented by Zhang and Wang [30] so only the main details will be reproduced. The polyelectrolyte solution consists of polycations (p_+), polyanions (p_-), salt ions (+ and −), and solvent (s), which we describe as coarse-grained beads. The polyanions and polycations have N_{p_+} and N_{p_-} segments where each segment represents a coarse-grained monomer. The monomers and salt ions have valency Z_i, where i is the species. Z_i is positive for positively charged species and negative for negative charges. For the current work, we treat the polyelectrolytes as strong polyelectrolytes where all monomers are fully dissociated and carry the same charge. We treat all species as having the same volume scale of v with a corresponding length scale $\sigma = v^{1/3}$. Further, for simplicity, the counterions dissociated from the polyelectrolytes are assumed to be the same as the corresponding salt ions. Far from the solid surface, the polyelectrolyte solution can be considered uniform with its composition described by the corresponding bulk densities, $\rho^{\mathrm{B}} = \{\rho^{\mathrm{B}}_{p_+}, \rho^{\mathrm{B}}_{p_-}, \rho^{\mathrm{B}}_{+}, \rho^{\mathrm{B}}_{-}, \rho^{\mathrm{B}}_{s}\}$. Here, the polyelectrolyte density $\rho_{p_\pm}$ is the segment (monomer) density. Because the volume scale is the same for all components, it is convenient to work with the volume fractions of each component, and assume incompressibility $\sum_i \phi_i = v \sum_i \rho_i = 1$.

In a homogeneous solution, the Helmholtz free energy density f_{B} can be written as the sum of three different parts, f_{id}, f_{el}, and f_{ch}. These additive free energy terms respectively account for the mixing entropy of the species, electrostatic correlation of a solution of disconnected ions, and the additional electrostatic correlation due to the connectivity of charges along the polyelectrolyte backbone. We do not include any other inter-species interactions like (i.e. Flory–Huggins χ) into the theory in order to focus on the effect of electrostatics; however, these terms can be easily included. The mixing entropy is given by

$$\beta v f_{\mathrm{id}} = \sum_{i=p_+,p_-} \frac{\phi_i}{N_i} \ln(\phi_i) + \sum_{i=+,-} \phi_i \ln(\phi_i) + \left(1 - \sum_{i=p_+,p_-,+,-} \phi_i\right) \ln\left(1 - \sum_{i=p_+,p_-,+,-} \phi_i\right) \quad \text{(IV.1)}$$

where $\beta = 1/k_B T$ is defined by the Boltzmann constant k_B and temperature T. The

electrostatic correlation is treated at the Debye–Hückel level,

$$\beta v f_{\mathrm{el}} = -\frac{1}{4\pi}\left[\ln(1+\kappa\sigma) - \kappa\sigma + \frac{(\kappa\sigma)^2}{2}\right] \tag{IV.2}$$

where κ is the inverse Debye screening length defined as $\kappa\sigma = \sqrt{4\pi(l_{\mathrm{B}}/\sigma)\sum_{i=p_\pm,\pm} Z_i^2\phi_i}$. The Bjerrum length has the usual definition of $l_{\mathrm{B}} = \beta e^2/4\pi\epsilon_0\epsilon_r$, where e is the elementary charge, ϵ_0 is the vacuum permitivity, and ϵ_r is the relative dielectric constant of the medium. The first order thermodynamic perturbation theory [50] (TPT1) framework is commonly used to describe the chain connectivity contribution to the electrostatic correlation, but Zhang and Wang recently developed a TPT1-like expression for electrostatic correlation at the Debye–Hückel level that we employ here. We direct readers to Ref. 30 for the full discussion on the derivation. For polyelectrolytes with charge on each segment, the free energy contribution is

$$\beta v f_{\mathrm{ch}} = \frac{l_{\mathrm{B}}/\sigma}{1+\kappa\sigma}\sum_{i=p_+,p_-}\frac{N_i-1}{N_i}Z_i^2\phi_i \tag{IV.3}$$

With the homogeneous free energy, one can study the bulk phase behavior by calculating the coexisting supernatant–coacervate phase diagram. Since the focus of this work is the role of the solid surface, we provide only a brief description of the supernatant–coacervate phase diagram and direct interested readers to our other works that give a more detailed description [51–53]. For a symmetric polyelectrolyte mixture ($\rho^{\mathrm{B}}_{p_+} = \rho^{\mathrm{B}}_{p_-}$, $N_{p_+} = N_{p_-}$, $Z_{p_+} = -Z_{p_-}$), as considered in this work, the coexisting concentrations are determined by the equality of chemical potential for each component in the coexisting phases (i.e. $\mu_i^I = \mu_i^{II}$) and equality of osmotic pressure, $\Pi_{\mathrm{B}} = \sum_{i=p_\pm,\pm}\mu_i\rho_i - f_{\mathrm{B}}$. The set of chemical potentials $\{\mu_i\}_{i=p_\pm,\pm}$ are measured with respect to the chemical potential of the solvent, which can be taken as a constant (zero) due to incompressibility. When the polyelectrolyte mixture is symmetric, the polycation/polyanion and cation/anion concentrations are equal within the same phase. For a given l_{B}, there are 4 unknowns ($\rho^I_{p_\pm}$,$\rho^{II}_{p_\pm}$, $\rho^I_\pm$, and $\rho^{II}_\pm$) with 3 independent equations (2 for chemical potential equality and one for osmotic pressure equality). The phase diagram is constructed by specifying one of the unknown components and solving for the other 3 unknowns using a Newton-Raphson approach. By scanning over $\rho^{II}_\pm$, for example, one can construct a phase diagram in the salt–polymer plane.

We extend the homogeneous free energy f_{B} to the inhomogeneous case by using a local approximation of the bulk free energy density and introducing additional

mean-field level free energy contributions to account for the inhomogeneous spatial densities. Namely, the Helmholtz free energy for a polyelectrolyte solution in contact with a planar, homogeneous surface is

$$F = A\int_0^\infty dz\Big[f_{\mathrm{B}}(\{\rho(z)\}) + \sum_{i=p_+,p_-}\frac{k_BT\,b^2}{6}\left(\frac{d\sqrt{\rho_i(z)}}{dz}\right)^2 + \sum_{i=p_\pm,\pm} eZ_i\rho_i(z)\psi(z) - \frac{\epsilon_0\epsilon_r}{2}\left(\frac{d\psi(z)}{dz}\right)^2 + eQ_s\psi(z)\delta(z) + b\sum_{i=p_+,p_-}\eta_i\rho_i(z)\delta(z)\Big] \quad \text{(IV.4)}$$

where A is the area of the planar surface, b is the Kuhn length (equivalent to σ in this work), $\psi(z)$ is the mean electrostatic potential, eQ_s is the surface charge density, η is a nonelectrostatic interaction parameter between the polyelectrolyte and solid surface, and $\delta(z)$ is the Dirac delta function. In the expression above, we have assumed that the density variation only takes place in the direction perpendicular to the surface. The first term in Eq. (IV.4) is the free energy density of the homogeneous solution evaluated with the local density. The second term is the Lifshitz entropy that arises from the ground-state dominance approximation in mean-field theory to account for the conformation entropy penalty of the polymer chains due to density inhomogeneity [54]. The third and forth terms are the mean-field energy contributions that arise from local net charge. The final two terms in Eq. (IV.4) account for the solid surface. The term involving Q_s is the surface contribution to the electrostatic free energy that arises from the charge accumulated on the solid surface. The last term accounts for the nonelectrostatic interaction between monomer residues and the surface, which is localized to the surface via the Dirac delta function. We do not include any nonelectrostatic surface interaction for the salt ions in order to focus on the polyelectrolyte adsorption. Treating the polyelectrolyte–substrate interaction this way follows previous studies of neutral polymer [55, 56] and polyelectrolyte adsorption [57, 58]. Physically, $\eta_{p_\pm}$ does not represent the bare interaction of the monomers with the surface. Instead, $\eta_{p_\pm}$ is a combination of the hard wall repulsion and short range attraction with the surface. As we will see below, a value of zero for $\eta_{p_\pm}$ corresponds to a polyelectrolyte that is indifferent to the surface (neither adsorbing or depleted).

At this point, we emphasize that our theory is a simplified representation of an inhomogeneous system. Treating the electrostatic correlation at the Debye–Hückel level is only valid when electrostatic correlation is relatively weak (i.e. low salt

concentration or small surface potentials) and is known to generally overestimate the electrostatic correlation for disconnected beads, while the TPT1 approach underestimates the electrostatic correlation for polyelectrolytes [59]. The majority of works studying complex coacervation have employed a Debye–Hückel electrostatic correlation term with no size correction and no chain connectivity correction, as is the case in VO theory [3]. Currently, there is no widely accepted theory to describe electrostatic correlation in polyelectrolyte solutions, especially for inhomogeneous systems. Additionally, using a local incompressibility assumption only coarsely captures the solvent–monomer or solvent–ion contacts that exist in real solutions. A hard sphere model may be more realistic but requires commensurate theoretical treatment of electrostatic correlation.

Throughout this work, we will consider systems with a constant electrostatic potential on the surface or constant surface charge density. For a solution in contact with a single surface maintained at constant surface potential ψ_0, the thermodynamic potential that is minimized at equilibrium is

$$\begin{aligned} Y = F - eQ_sA\psi_0 - \sum_{i=p_\pm,\pm} \mu_i \mathcal{N}_i = \\ = A\int_0^\infty dz\Big[f_{\mathrm{B}}(\{\rho(z)\}) + \sum_{i=p_\pm,\pm} eZ_i\rho_i(z)\psi(z) - \frac{\epsilon_0\epsilon_r}{2}\left(\frac{d\psi(z)}{dz}\right)^2 \\ + \frac{k_BT\ b^2}{6}\sum_{i=p_+,p_-}\left(\frac{d\sqrt{\rho_i(z)}}{dz}\right)^2 + b\sum_{i=p_+,p_-}\eta_i\rho_i(z)\delta(z) \\ - \sum_{i=p_\pm,\pm}\mu_i\rho_i(z)\Big] \end{aligned} \tag{IV.5}$$

where $\mathcal{N}_i = A\int_0^\infty \rho_i(z)dz$. Note that the electrostatic surface term is subtracted by the Legendre transform to account for the energy of charging/discharging the surface [60]. For a fixed surface charge density, the relevant free energy is $W = F - \sum_{i=p_\pm,\pm}\mu_i\mathcal{N}_i$. Y and W are equivalent when either Q_s or ψ_0 are zero. We note again that the salt and polyelectrolyte chemical potentials are measured with respect to the pure solvent, which naturally results from the incompressibility condition ($v\sum_{i=p_\pm,\pm,s}\rho_i = 1$). To obtain equilibrium configurations, we extremize the relevant inhomogeneous free energy with respect to the densities and electrostatic potential field to obtain the mean-field equations. Starting with the electrostatic potential, we obtain the Poisson equation

$$\sum_{i=p_\pm,\pm} eZ_i\rho_i(z) + \epsilon_0\epsilon_r\frac{d^2\psi}{dz^2} = 0 \tag{IV.6}$$

For the polyelectrolyte densities,

$$\frac{\delta f_{\mathrm{B}}(\{\rho(z)\})}{\delta \rho_{p_\pm}(z)} + b\eta_{p_\pm}\delta(z) - \frac{k_B T\, b^2}{6\sqrt{\rho_{p_\pm}(z)}} \frac{d^2\sqrt{\rho_{p_\pm}(z)}}{dz^2} + eZ_{p_\pm}\psi(z) - \mu_{p_\pm} = 0 \quad \text{(IV.7)}$$

For small ions,

$$\frac{\delta f_{\mathrm{B}}(\{\rho(z)\})}{\delta \rho_{\pm}(z)} + eZ_{\pm}\psi(z) - \mu_{\pm} = 0 \quad \text{(IV.8)}$$

For fixed surface charge density, the boundary condition for the electrostatic potential is $\epsilon_0\epsilon_r \frac{d\psi}{dz}\Big|_{z=0} = -eQ_s$. For fixed surface potential, the boundary condition is simply given by the specified potential at the surface, $\psi(0) = \psi_0$. In either case, far from the surface, the potential can be defined to be zero, $\psi(z \to \infty) = 0$, where we also have $\frac{d\psi}{dz}\Big|_{z\to\infty} = 0$. For the polymer volume fraction, the boundary condition near the surface can be obtained by integrating Eq. (IV.7) from 0^- to 0^+. Only the terms defined at the surface remain, and one obtains

$$\left.\frac{d\sqrt{\rho_{p_\pm}(z)}}{dz}\right|_{z=0} = 6b^{-1}\beta\eta_{p_\pm}\sqrt{\rho_{p_\pm}(0)} \quad \text{(IV.9)}$$

As mentioned above, $\eta_{p_\pm}$ is not the bare interaction with the surface but serves as an effective boundary condition for the polymer density. In the absence of a polymer–substrate interaction, the entropic penalty of a polymer chain near a solid surface should lead to depletion [55]. A value of zero for $\eta_{p_\pm}$ indicates the slope of the density profile is zero at the surface, which corresponds to some degree of attraction to overcome the usual depletion arising from loss of conformations near the surface. Likewise, in the absence of electrostatic effects, the sign of $\eta_{p_\pm}$ determines whether the polyelectrolyte is adsorbing or depleted from the surface. These subtleties result from using a continuous chain model (Lifshitz entropy) and have been discussed in detail elsewhere [1]. Far from the surface, the polyelectrolyte volume fractions return to the bulk solution conditions.

We conclude this section by writing the functional form of the surface tension. The surface tension is equal to the excess grand potential energy for constant surface potential system [60]. Subtracting the grand potential energy of the homogeneous

system ($Y_0 = -\Pi_B V$) gives

$$\gamma = \frac{Y - Y_0}{A} = \int_0^\infty dz \Big[f_B(\{\rho(z)\}) - f_B(\{\rho^B\}) + e \sum_{i=p_\pm,\pm} Z_i \rho_i(z)\psi(z) - \frac{\epsilon_0 \epsilon_r}{2}\left(\frac{d\psi(z)}{dz}\right)^2 + \frac{k_B T b^2}{6} \sum_{i=p_+,p_-} \left(\frac{d\sqrt{\rho_i(z)}}{dz}\right)^2 - \sum_{i=p_\pm,\pm} \mu_i \Big(\rho_i(z) - \rho_i^B\Big)\Big] + b \sum_{i=p_+,p_-} \eta_i \rho_i(0) \quad \text{(IV.10)}$$

The expression above can be used to compute either the supernatant–solid or coacervate–solid surface tension. The only difference is the choice of bulk composition. Namely, the choice of $\{\rho^B\}$ will specify whether the bulk solution is on the supernatant or coacervate side of the phase diagram. We note that the surface tension obtained from Eq. IV.10 is not the true surface tension but the excess surface tension relative to that of a pure solvent. However, the (constant) contribution to the surface tension from the pure solvent has no bearing on the properties of interest in this work (e.g. the contact angle).

Numerical Considerations

The mean-field equations above are solved by discretizing the spatial coordinate from the surface to a distance far enough from the surface where the volume fraction is sufficiently close to the bulk concentration ($z > 50b$). The set of discretized mean-field equations can be written as $\mathbf{F}(\mathbf{X}) = 0$, where $\mathbf{X} = [\{\phi(z)\}, \psi(z)]$. This nonlinear system of equations can be solved in a variety of ways, including relaxation methods or quasi-Newton approaches. We found that reformulating the problem in terms of fixed-point iterations, where one solves $\mathbf{X} = \mathbf{G}(\mathbf{X}) = \mathbf{X} + \mathbf{F}(\mathbf{X})$, and solving using Anderson Acceleration [61] led to the fastest convergence. The convergence criterion was considered met when the maximum value of $\mathbf{F}(\mathbf{X})$ was less than an error tolerance (10^{-10}).

Results and Discussion

We will explore the wetting behavior both off- and on-coexistence. Both refer to locations or trajectories relative to the supernatant–coacervate phase diagram. As the name implies, off-coexistence refers to starting with a system prepared in the one-phase region of the phase diagram and changing a state variable that brings the system closer to the two-phase region. On-coexistence refers to trajectories of the

phase diagram that are restricted to the binodal surface, where the contact angle is defined. In this work, in order to reduce the overall number of parameters, we will focus on a single phase diagram constructed in the salt–polyelectrolyte plane. We fix the number of segments for each chain $N_{p_+} = N_{p_-} = N = 100$, the Bjerrum length $l_B/\sigma = 1.785$, and valencies of each species $Z_{p_+} = -Z_{p_-} = Z_+ = -Z_- = 1$ to mimic similar conditions in our earlier work [30]. For $\sigma = 0.4$ nm, the Bjerrum length corresponds to a relative dielectric of $\epsilon_r \approx 80$ at room temperature.

The resulting supernatant–coacervate phase diagram is shown in Figure IV.1. Figure IV.1 shows that the tie-lines connecting the supernatant (dilute) and coacervate (dense) phases are slightly negatively sloped and that above a threshold salt concentration ($\phi_\pm^B = 0.115$), the two phases are indistinguishable. One common feature in the theoretical prediction of bulk phase diagrams of complex coacervates is that the polyelectrolyte concentration in the supernatant phase is exceedingly low [62–67]. In most current theories, including this work, the physical picture of the supernatant phase is a *uniformly mixed* polyelectrolyte solution. In reality, the oppositely charged polyions in the supernatant phase are likely to form dispersed clusters made up of two or more polyions [68–72]. Such a distinction undoubtedly influences the behavior of the supernatant near a solid surface. We recognize this as a limitation of our study; however, using a uniformly mixed assumption allows for the complete phase diagram (Fig. IV.1), which is useful for mapping surface phase transitions relative to the binodal. The phase diagram near the critical salt concentration is not available when accounting for the polyion clusters in the supernatant phase [71]. Further, we expect many aspects of the wetting behavior to be similar, which we will revisit later on.

The focus of off-coexistence trajectories is whether, and how, the coacervate phase forms on the surface from an unsaturated solution. From Cahn's classical wetting theory [73], reaching coexistence starting from an undersaturated solution generally leads to one of two scenarios. The first is complete wetting, where a macroscopically large, dense film forms on the surface at coexistence. Complete wetting is a surface transition that can be first or second order, depending on whether the film thickness diverges discontinuously or continuously at coexistence, respectively [74]. The second scenario is partial wetting, where the film thickness remains finite at coexistence. To study this, we increase the bulk polymer concentration ($\phi_{p_\pm}^B$) from an undersaturated solution to the saturated solution at a fixed bulk salt concentration, which is a horizontal path (left to right) on the phase diagram in Figure IV.1. Note

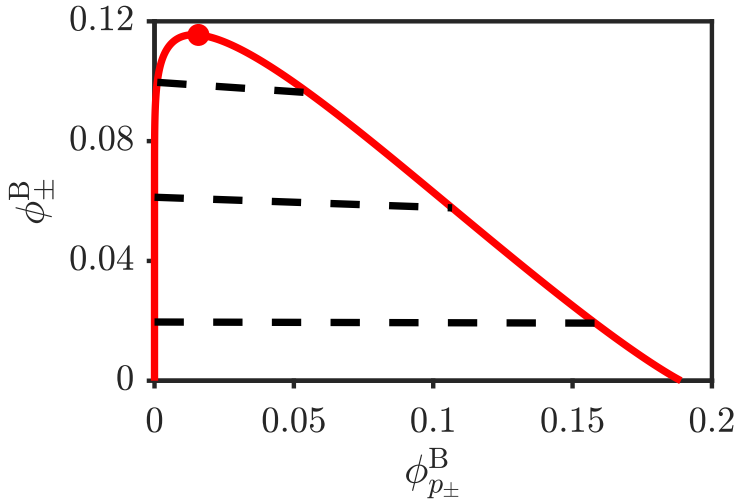

Figure IV.1: Supernatant–coacervate bulk phase diagram in the salt–polyelectrolyte plane for $N = 100$ and $l_{\mathrm{B}}/\sigma = 1.785$. Dashed black lines indicate tie-lines. Red point indicates the bulk critical point.

that $\phi^{\mathrm{B}}_{\pm}$ is the overall salt concentration that includes the added salt ions and counterions to the polyelectrolytes so that increasing $\phi^{\mathrm{B}}_{p_\pm}$ for fixed $\phi^{\mathrm{B}}_{\pm}$ amounts to removing added salt. We calculate the excess adsorption $\Gamma_{\mathrm{ex},i}b^2 = \int_0^\infty \left[\phi_i(x) - \phi_i^{\mathrm{B}}\right]dx$ to measure the presence of the coacervate film.

Nonelectrostatic Wetting

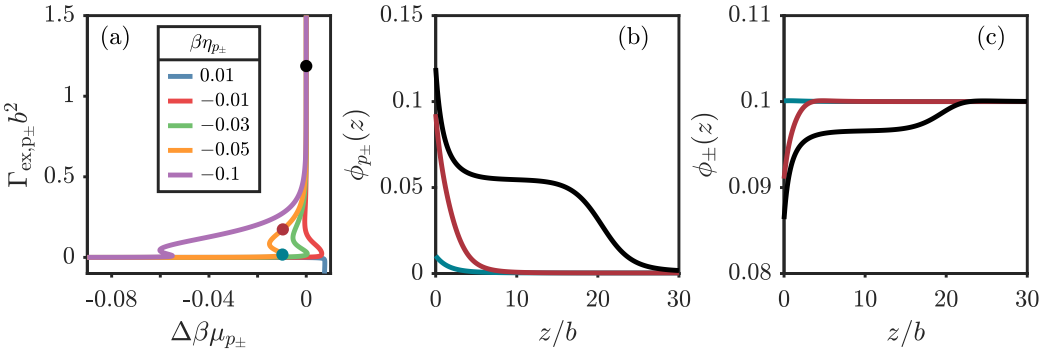

Figure IV.2: Adsorption isotherms and density profiles for nonelectrostatic adsorption. (a) Polyelectrolyte adsorption isotherms for various nonelectrostatic attraction strengths at a constant bulk salt concentration of $\phi^{\mathrm{B}}_{\pm} = 0.1$. $\Delta\beta\mu_{p_\pm} = \beta\mu_{p_\pm} - \beta\mu^{\mathrm{coex}}_{p_\pm}$ is a measure of the distance from coexistence. Corresponding (b) polyelectrolyte and (c) salt density profiles before and after the prewetting transition for $\beta\eta_{p_+\pm} = -0.05$. Line colors match the circular markers in (a). For (a), values of $\beta\eta_\pm < -0.01$ undergo complete wetting via a prewetting transition.

Figure IV.2 shows adsorption isotherms and interfacial profiles for symmetrically adsorbing polyelectrolytes on a charge-neutral surface for $\phi_{\pm}^{\mathrm{B}} = 0.1$. Symmetric adsorption means that both polycation and polyanion have identical nonelectrostatic affinity to the surface ($\eta_{p_+} = \eta_{p_-} = \eta_{p_\pm}$). Without an applied potential on the surface or non-zero surface charge density, there is no charge separation so the positive/negative interfacial profiles are identical. The quantity $\Delta\beta\mu_{p_\pm} = \beta\mu_{p_\pm} - \beta\mu_{p_\pm}^{\mathrm{coex}}$ measures the chemical potential difference from the chemical potential of the supernatant phase at coexistence. $\Delta\beta\mu_{p_\pm} < 0$ corresponds to an undersaturated supernatant phase in contact with the surface while $\Delta\beta\mu_{p_\pm} < 0$ corresponds to a supersaturated, metastable supernatant phase in contact with the surface. Figure IV.2a shows the adsorption isotherms for representative values of $\eta_{p_\pm}$. A key feature in this plot is the presence of turning points in the excess adsorption curves. The turning points mark surface spinodals and thus, are an indication of a first order transition. The section of the adsorption isotherm connecting two surface spinodals is thermodynamically unstable. See the Appendix for more detail on turning points and thermodynamic stability.

Surface phase coexistence is determined by the crossing of the relevant surface excess free energy (Figure IV.13). For $\beta\eta_{p_\pm} = -0.1$ (purple line in Figure IV.2a), a first order transition happens near $\Delta\beta\mu_{p_\pm} \approx -0.06$ and then the excess adsorption diverges continuously. A surface transition off-coexistence where the excess adsorption jumps to a finite value is known as a prewetting transition [75], corresponding to coexistence between a thin and thick coacervate layer on the surface [76]. Such a transition is illustrated in the interfacial profiles in Figure IV.2b. The red and green lines correspond to coexisting surface phases before and after the transition, respectively. Before the transition (green line), a small amount of polyelectrolyte adsorbs on the surface. After the prewetting transition (red line), there is strong adsorption in the immediate vicinity of the surface, which continuously grows into a macroscopically thick film upon further increase in the bulk concentration (black line). The black curve in Figure IV.2b reaches a plateau around $z/b = 10$. The same is true in the salt density profiles. As the bulk concentration approaches the binodal, the composition of the plateau approaches the coexisting coacervate phase determined by the phase diagram in Figure IV.1. The negative tie-lines explain why the coacervate layer depletes salt from the surface. The behavior of the tie-line slope is an active research area [3]. Neitzel and coworkers recently measured positively sloped tie-lines for low charge density polyelectrolytes [77], which would change the trend in salt composition of the wetted coacervate layer.

In Figure IV.2a, a less favorable polymer–surface interaction shifts or eliminates the prewetting transition. The curve for $\beta\eta_{p_\pm} = -0.01$ exhibits partial wetting. As opposed to the other curves, there is no crossing of the supernatant and coacervate surface excess free energy (Figure IV.14). In other words, a coacervate layer on the surface can only exist as metastable state on the supernatant side of the phase diagram for $\beta\eta_{p_\pm} = -0.01$. For $\beta\eta_{p_\pm} = 0.01$, the excess adsorption is actually negative and decreases with bulk concentration, which indicates drying rather than wetting. In that case, the surface also cannot support a coacervate layer. The results presented at this point are similar to that of Monteillet and coworkers that studied coacervation at an oil–water interface using self-consistent field theory [78]. In their work, the formation of a coacervate at the oil-water interface also proceeded via a first order prewetting transition.

By scanning over many salt concentrations, we track the full behavior of the wetting transition. Figure IV.3 shows the surface phase diagram for $\beta\eta_{p_\pm} = -0.05$ plotted on top of the bulk phase diagram. The green line is the surface spinodal for the supernatant on the surface. Crossing this line from left to right on the diagram results in spontaneous formation of the coacervate layer on the surface (wetting). When the green line falls below the binodal (red), the surface spinodal exists in the metastable region for the bulk supernatant phase. The pink line is the coacervate surface spinodal, where the (metastable) coacervate surface layer must dewet the surface. The black line is the surface coexistence point determined by the crossing point of the relevant free energy (see Figure IV.13). Because the surface coexistence line extends off the bulk binodal (red), this line is also known as the prewetting line. As one approaches the critical bulk salt concentration, there is no distinction of supernatant or coacervate phases so the surface transition should be second order in the proximity of the bulk critical point [73]. Indeed, the three lines in the surface phase diagram converge on a surface critical point. Above that point but below the bulk critical point, a horizontal trajectory on the phase diagram leads to a continuous divergence of the excess adsorption, which is consistent with a second order wetting transition. For low salt, the surface coexistence line eventually intersects with the bulk binodal, which we define as the wetting salt concentration, $\phi_\pm^{\text{wet}}$. For the conditions in Figure IV.3, this occurs at $\phi_\pm^{\text{wet}} \approx 0.053$. One can draw analogy to the wetting temperature typical in liquid-vapor systems [79, 80]. The existence of surface spinodals below the wetting salt concentration, called extended wetting, is also expected from classical wetting theory when polyelectrolyte–surface interaction is favorable [81]. When this occurs, the wetted coacervate surface phase can only

exist on the surface as a metastable state since there is no crossing of the free energy (see Figure IV.14).

When the nonelectrostatic adsorption is asymmetric ($\eta_{p_+} \neq \eta_{p_-}$), the interfacial profiles for the polyions will differ from one another and this charge separation gives rise to a spatially varying electrostatic potential. Figure IV.4 shows the adsorption isotherms for asymmetric adsorption on a charge-neutral surface ($Q_s = 0$), where we keep $\eta_{p_-} = 0$ while varying the strength of the polycation attraction to the surface η_{p_+}. With $\eta_{p_-} = 0$, polyanions are indifferent to the surface so the formation of the coacervate on the surface must be driven by the adsorption of polycation. Compared to Figure IV.2, the values of η_{p_+} to induce complete wetting are necessarily higher since polycations must *drag* polyanions to the surface via electrostatic attraction to induce a surface phase transition. The curve for $\beta\eta_{p_+} = -0.1$ in Figure IV.4 looks qualitatively similar to $\beta\eta_{p_\pm} = -0.05$ in Figure IV.2a. Another noticeable difference for asymmetric adsorption is the disappearance of turning points for $\beta\eta_{p_+} \leq -0.15$. The excess adsorption diverges continuously, which indicates a second order transition (Figure IV.15). Second order wetting transitions are usually associated with systems where long range fluid–fluid interactions are dominant over the short range fluid-solid interaction [82], as is the case near the bulk critical point.

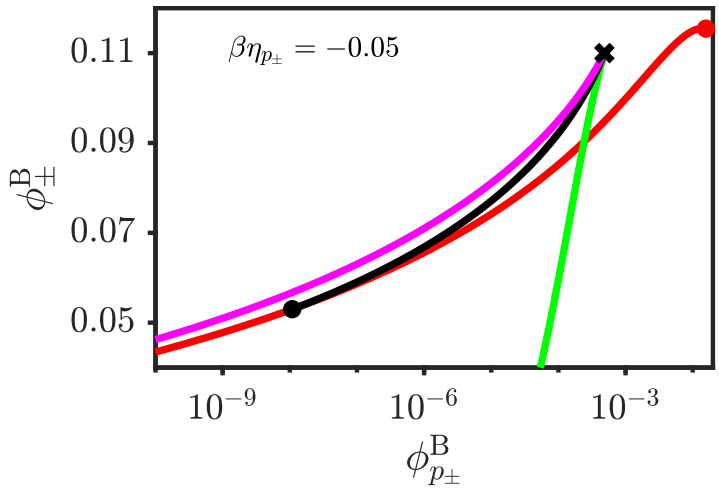

Figure IV.3: Surface phase diagram for $\beta\eta_{p_+\pm} = -0.05$ superimposed on bulk phase diagram (red). Lines correspond to supernatant surface spinodal (green), supernatant–coacervate surface coexistence (black), and coacervate surface spinodal (pink). Symbols correspond to the wetting salt concentration (●), the surface critical point (✖), and the bulk critical point (●).

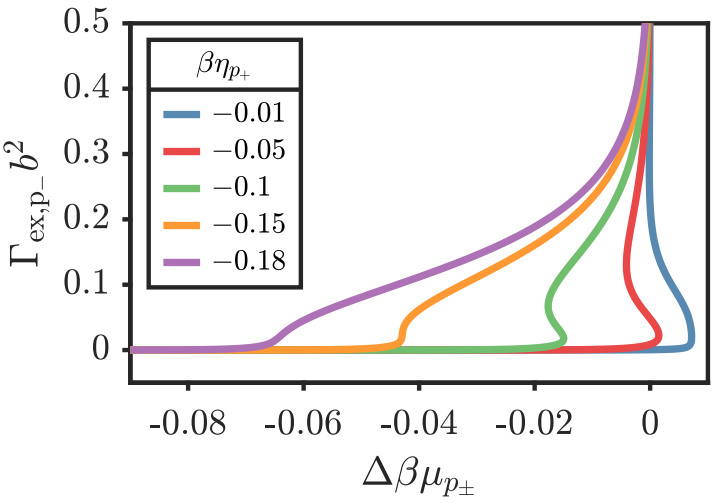

Figure IV.4: Polyelectrolyte adsorption isotherms for asymmetric nonelectrostatic attraction strengths ($\eta_{p_+} < 0$ and $\eta_{p_-} = 0$) at a constant bulk salt concentration of $\phi_\pm^{\mathrm{B}} = 0.1$. $\Delta\beta\mu_{p_\pm} = \beta\mu_{p_\pm} - \beta\mu_{p_\pm}^{\mathrm{coex}}$ is a measure of the distance from coexistence.

The emergence of a second order transition indicates that the electrostatic attraction between adsorbed polycation and indifferent polyanion has an enhanced role in the wetting transition compared to its role in symmetric adsorption, pushing the surface critical point to lower salt concentrations. This result may at first seem nonintuitive since the second order transition develops when the short range polycation–surface interaction (η_{p_+}) becomes *more* favorable. However, increasing η_{p_+} increases the local charge separation near the surface. There must be sufficient charge separation to see the effect of long range electrostatics. At the same salt concentration, for symmetric adsorption, we find only first order transitions when increasing $\beta\eta_{p_\pm}$. The balance of the long range and short range forces is tied to both the strengths and intrinsic length scales of those forces, so we expect nontrivial phenomena to arise from this competition when varying factors like the monomer charge fraction or the salt concentration. Exploring each of these factors is beyond the scope of the current work.

Electrowetting

Now, we consider the effect of applying an electric potential on the surface transition and surface phase diagram. We consider symmetric adsorption where $\beta\eta_{p_\pm} = -0.05$ with a positive applied surface potential ($\psi_0 > 0$). A positive electrostatic potential will enhance the attraction of the polyanion to the surface and repel the

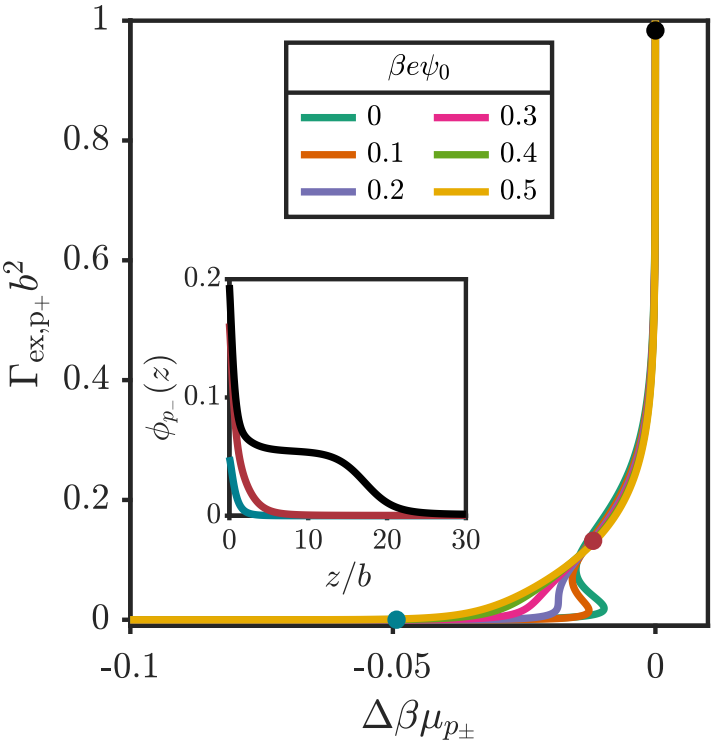

Figure IV.5: Polycation adsorption isotherms with $\beta\eta_{p_\pm} = -0.05$ for various surface potentials $\beta e\psi_0$ at a constant bulk salt concentration of $\phi_\pm^{\mathrm{B}} = 0.1$. $\Delta\mu_{p_\pm} = \mu_{p_\pm} - \mu_{p_\pm}^{\mathrm{coex}}$ is a measure of the distance from coexistence. (Inset) Polyanion density profiles for $\beta e\psi = 0.3$ corresponding to the matching solid colored points on the adsorption isotherm. For reference, 1 $\beta e\psi \approx 22$ mV.

polycation. The adsorption of salt ions will similarly be affected. For a single salt concentration of $\phi_\pm^{\mathrm{B}} = 0.1$, we show the adsorption isotherm of the polycation for various applied potentials in Figure IV.5. We show the polycation adsorption since the main driving force for its adsorption is the nonelectrostatic interaction with the surface. The polyanion will have higher adsorption for increasing applied potentials to compensate for the positive surface charge density. Figure IV.5 indicates that as the applied potential increases, the surface transition evolves from a first order prewetting transition to a second order transition. The switch is reflected in the absence of turning points in the curve for $\beta e\psi_0 = 0.5$. This result is similar to the asymmetric nonelectrostatic adsorption discussed previously, where the charge separation enhances the role of long range electrostatic forces.

The inset of Figure IV.5 shows the polyanion density profiles along the adsorption isotherm for $\beta e\psi_0 = 0.3$. In the region very close to the surface, the adsorption of

polyanion is greatly enhanced. Upon approaching the binodal, the coacervate layer grows out of the strongly adsorbing surface layer. The coacervate layer that grows approaches same composition for all values of $\beta e\psi_0$, since, as stated earlier, the eventual composition of the coacervate film is determined by the tie-line on Figure IV.1. The interfacial profiles for all species, potential profiles, and charge density are shown in Figure IV.16 for $\beta e\psi_0 = 0.3$. The charge density and potential profile return to bulk values of zero within $z/b = 5$. After this distance, despite the coacervate layer on the surface, the effect of electrostatic adsorption is screened out. Further, Figure IV.16 shows that the potential profile and charge density crosses zero, which is a sign of strong charge accumulation at the surface and is typical of polyelectrolyte adsorption [83–85]. Practically, these findings are advantageous since one can alter the wetting properties (order of the transition, wetting salt concentration, etc.) by applying a potential without disrupting the coacervate film composition far from the surface. We briefly note that because the nonelectrostatic parameters for polycation and polyanion are equal ($\beta\eta_{p_\pm} = -0.05$), applying a negative surface potential rather than a positive one has the same overall effect with the labels for positive/negative species reversed.

The wetting transition is intimately tied to our description of the supernatant phase as uniformly mixed. Figures IV.16a&b show that the wetting transition proceeds by initially forming a dense layer of one polyion. We hypothesize that obtaining the same degree of charge separation is unlikely if the supernatant phase is made up of polyion clusters. For this reason, we expect that the assumption of a uniformly mixed supernatant phase overestimates the prevalence of charge separation and thus, the electrostatic effect on the order of the wetting transition. However, we do not currently have a method of describing the adsorption of such polyion clusters to a solid surface.

The crossover from a first order to second order wetting transition in Figure IV.5 indicates that the salt concentration corresponding to the surface critical point ($\phi_\pm^*$) has moved below $\phi_\pm^{\mathrm{B}} = 0.1$ for applied potentials greater than $\beta e\psi_0 = 0.2$. There are several works that describe how the surface or interfacial tension decreases for small applied potentials (within the linear regime) for solid surfaces [86, 87] and even liquid–liquid interfaces [88]. However, the location of the surface critical point does not have an obvious scaling relationship. Using a simple scaling analysis, we hope to give a physical reason for movement of $\phi_\pm^*$. The wetting transition corresponds to replacing the supernatant–solid interface with coacervate–solid and supernatant–

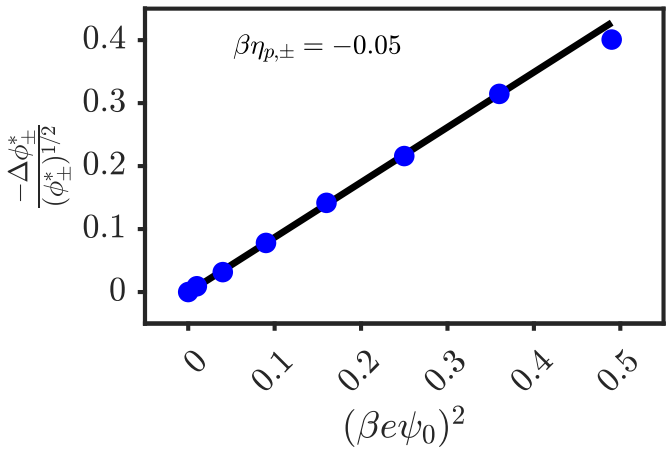

Figure IV.6: Rescaled salt concentration of the surface critical point, $\phi^*_\pm$, versus the applied potential for $\beta\eta_{p_\pm} = -0.05$. Rescaled variables are $\Delta\phi^*_\pm = \phi^*_\pm - \left(\phi^*_\pm\right)_{\psi_0=0}$ with $\left(\phi^*_\pm\right)_{\psi_0=0} = 0.11$ (Figure IV.3). The solid black line indicates the scaling of $-\Delta\phi^*_\pm/\left(\phi^*_\pm\right)^{1/2} \sim \psi_0^2$ fit to the first 3 points predicted points.

coacervate interfaces. Along the prewetting line (black line in Figure IV.3), the condition for surface phase coexistence is $S = \gamma_{\text{sup,co}} + \gamma_{\text{co,solid}} - \gamma_{\text{sup,solid}} = 0$, where S is the spreading coefficient. Below the bulk critical point, $\gamma_{\text{sup,co}} > 0$ and we can combine the other two terms to represent the effect of adsorption of the coacervate phase compared to the supernatant phase, $F_{\text{ads}}/A = \gamma_{\text{co,solid}} - \gamma_{\text{sup,solid}}$. For favorable adsorption, $F_{\text{ads}}/A < 0$. Thus, the prewetting line is determined by balancing $\gamma_{\text{sup,co}}$ and F_{ads}/A. When applying an electric potential, we consider how $\phi^*_\pm$ should change. We maintain that $S = 0$ so that $\Delta\gamma_{\text{sup,co}} + \Delta F_{\text{ads}}/A = 0$, where the Δ indicates the change from no applied potential ($\psi_0 = 0$). As mentioned in the introduction, the scaling of the interfacial tension with salt concentration is well studied, $\gamma_{\text{sup,co}} \sim (\phi^{\text{crit}}_\pm - \phi^\pm)^{3/2}$. Further, $\Delta F_{\text{ads}}/A$ should scale with the energy stored in the electric double layer, $\Delta F_{\text{ads}}/A \sim -eQ_s\psi_0$. Small applied potentials lead to small changes in $\phi^*_\pm$. Expanding the difference from zero potential to linear order, $\Delta\gamma_{\text{sup,co}} \sim \left(\phi^*_\pm\right)_{\psi_0=0} - \phi^*_\pm \equiv -\Delta\phi^*_\pm$, and for small potentials, $Q_s \sim \kappa\psi_0/l_{\text{B}}$. Assuming the salt concentration is much larger than the polyion concentration at the surface critical point, $\kappa \sim \left(\phi^*_\pm\right)^{1/2}$. Thus, $\Delta F_{\text{ads}}/A \sim -\left(\phi^*_\pm\right)^{1/2}\psi_0^2$ and $\psi_0^2 \sim -\Delta\phi^*_\pm/\left(\phi^*_\pm\right)^{1/2}$. Figure IV.6 shows this scaling relationship by plotting $-\Delta\phi^*_\pm/\left(\phi^*_\pm\right)^{1/2}$ versus ψ_0^2, where the linear relationship validates the scaling for small applied potential.

Contact Angle

Finally, we consider wetting behavior on-coexistence. The central quantity in studying on-coexistence wetting is the contact angle. The contact angle stems from the three-phase coexistence between the surface, supernatant, and coacervate phases [79] and is determined from Young's equation.

$$\cos(\theta) = \frac{\gamma_{\text{sup,solid}} - \gamma_{\text{co,solid}}}{\gamma_{\text{sup,co}}} \tag{IV.11}$$

where the terms in the numerator are the supernatant–solid and coacervate–solid surface tension, respectively, and are determined separately from Eq. IV.10 using bulk conditions from coexisting phases from Figure IV.1. Although both terms in the numerator should be the total interfacial tension, the contribution from the pure solvent cancels out upon taking the difference, so that only the excess supernatant–solid and coacervate–solid surface tensions are needed. The denominator in Eq. IV.11 is the interfacial tension, which we calculate using the methods described in our earlier work [30]. Figure IV.17 gives $\gamma_{\text{sup,co}}$ for the phase diagram in Figure IV.1. The contact angle is only defined for partially wet systems. For complete wetting or complete drying, the contact angle will take the values of 0° and 180°, respectively, since one phase will form a macroscopic layer on the surface.

Figure IV.7 shows the contact angle versus the supernatant salt fraction $(\phi_\pm)^{\text{sup}}$ for symmetric and asymmetric nonelectrostatic adsorption. Starting with the symmetric case, negative values of $\beta\eta_{p_\pm}$ correspond to an favorable (attractive) interaction, while positive values are a repulsive interaction with the surface. Increasing the salt concentration toward the bulk critical salt concentration leads to either complete wetting or complete drying. Complete wetting only occurs for $\eta_{p_\pm} < 0$, which indicates that a favorable nonelectrostatic interaction is required for complete wetting in the absence of electrostatic effects. For $\beta\eta_{p_\pm} = -0.05$, the wetting salt concentration is $(\phi_\pm)^{\text{sup}} \approx 0.053$, which is equivalent to the wetting salt concentration in the surface phase diagram in Figure IV.3. Increasing the magnitude of the attractive, or repulsive, polyelectrolyte–surface interactions leads to smaller $\phi_\pm^{\text{wet/dry}}$. Figure IV.7b indicates that complete wetting or drying still occurs when only one component has an interaction with the surface. Compared to the same values of $\beta\eta_{p_+}$ as in Figure IV.7a, the wetting and drying salt concentrations are higher. Such a result is expected since the driving force for adsorption is not as strong when only one component has an attractive, or repulsive, interaction with the surface.

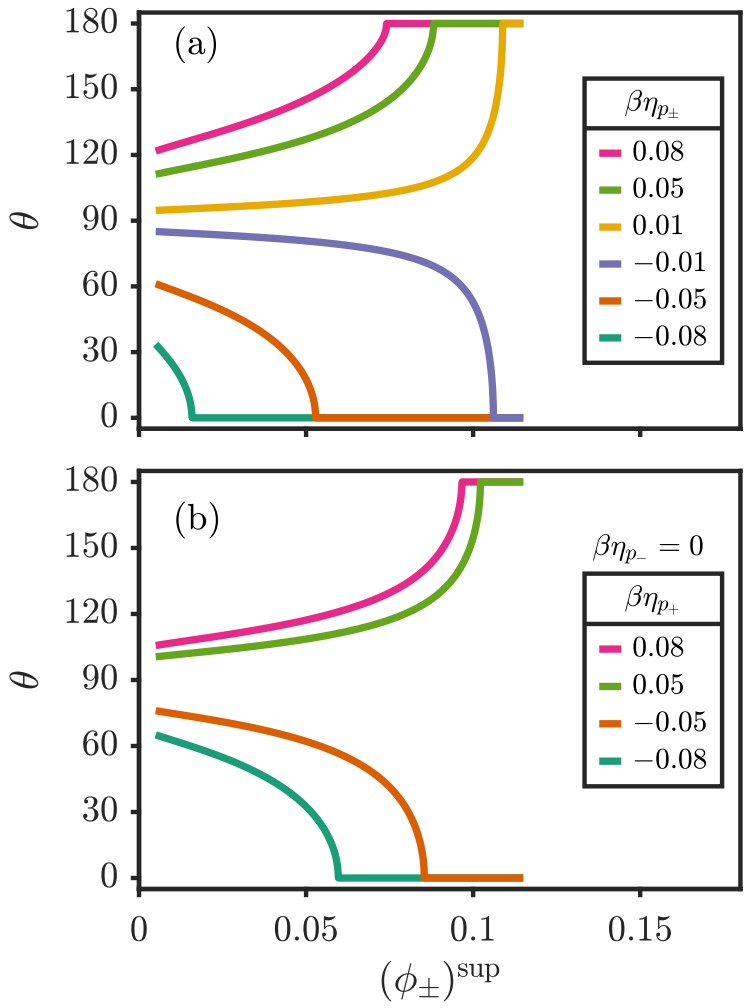

Figure IV.7: Contact angle versus supernatant salt fraction for various (a) symmetric adsorption parameters $\beta\eta_{p_\pm}$ and (b) asymmetric adsorption parameters ($\beta\eta_{p_-} = 0$). Critical salt concentration is $\phi_\pm^{\text{crit}} = 0.115$. Contact angles calculated by Eq. IV.11. In (a) and (b), the electrostatic potential at the surface is zero ($\beta e\psi_0 = 0$). For asymmetric adsorption, the overall potential profile, $\psi(z)$, is non-zero due to the asymmetric interaction with the surface. Coexisting concentrations determined by phase diagram in Figure IV.1.

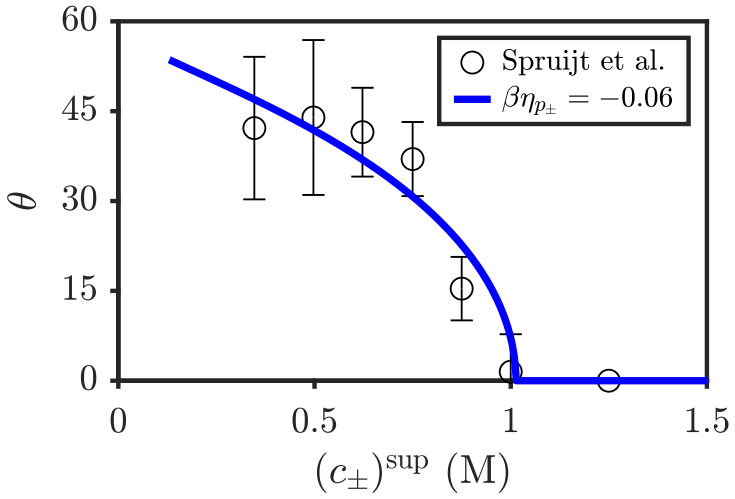

Figure IV.8: Contact angle versus salt concentration in the supernatant phase. Line represents symmetric adsorption with a nonelectrostatic adsorption strength $\beta\eta_{p_\pm} = -0.06$, which was determined by fitting described in the text. Experimental data reproduced from Ref. 23 with permission from the Royal Society of Chemistry.

Qualitatively, the curves featuring complete wetting in Figure IV.7 resemble data reported by Spruijt and coworkers [23]. To make a direct comparison, we assume a length scale of $\sigma = b = 0.4$ nm and fit $\beta\eta_{p_\pm}$ such that the wetting salt concentration is 1 M, which is consistent with the transition to complete wetting in their work. Figure IV.8 shows semi-quantitative agreement between the measured and predicted contact angles. We note that we have assumed symmetric adsorption with no electrostatic potential to minimize the number of fitted parameters. While not shown here, one can also achieve similar agreement using the same fitting approach for asymmetric adsorption ($\eta_{p_+} < 0$, $\eta_{p_-} = 0$).

Applying a positive electrostatic potential to the surface increases the favorability of the surface interaction for the polyanion but penalizes adsorption for the polycation. As seen in the shift of the surface critical point for symmetric adsorption, applying a surface potential actually improves the overall wettability (Figure IV.6). In Figure IV.9, we show the effect of an applied potential on the contact angle for symmetric adsorption. For no applied potential, complete drying occurs upon increasing the salt concentration. With an applied potential of $\beta e\psi_0 = 0.2$, the system exhibits complete wetting. Further increases in the applied potential move the wetting point lower on the phase diagram. The kink in the contact angle for $\beta e\psi_0 = 0.5$ is due to a prewetting transition that occurs for high applied potentials at low salt concentration

(see Figure IV.18). The existence of multiple prewetting transitions is well-known for highly favorable adsorption [89]. Physically, these transitions correspond to layering-type transitions, where the strongly adsorbing component (polyanion here) is highly enriched at the surface. We generally find that additional prewetting transitions occur when $\beta e\psi_0 \geq 0.5$ for almost all of the values of $\eta_{p_\pm}$ studied. While we expect our theory to qualitatively identify layering transitions, fully describing layering transitions requires a more sophisticated treatment of electrostatic correlation and packing effects, which is beyond the scope of this work.

The observation of layering phenomena seen with applied potentials prompts reevaluation of the underlying physical picture of our theory. At the start of Section 3, we claimed that some aspects of wetting behavior are similar when using the assumption of uniformly mixed polyions compared to explicitly considering polyion clusters in the supernatant phase. In Figure IV.19, we compare $\gamma_{\text{sup,solid}}$ from two different representations of the supernatant phase — a solution of uniformly mixed polyelectrolytes and a polyelectrolyte-free solution of salt ions. Both representations have the same osmotic pressure as the coacervate phase. As shown in the Appendix, $\gamma_{\text{sup,solid}}$ is not meaningfully affected by the presence of polyelectrolytes in the supernatant phase, except when there is an applied potential to the surface. In other words, the presence of polyelectrolyte in the supernatant phase does not appreciably influence the contact angle for symmetric and asymmetric nonelectrostatic adsorption without an applied potential. We hypothesize that explicitly considering the nonelectrostatic adsorption of clusters will similarly have little influence on $\gamma_{\text{sup,solid}}$ compared to the $\gamma_{\text{co,solid}}$ so that the contact angles would be unaffected. When applying a surface potential, strong polyelectrolyte adsorption leads to deviations in $\gamma_{\text{sup,solid}}$ from the polyelectrolyte-free case (Figure IV.19b). Figure IV.20 compares the contact angle prediction when using the excess surface tension from the two representations of the supernatant phase. With electrostatic-driven adsorption, we expect polyion clusters would have different adsorption behavior at the coexisting supernatant composition than the uniformly mixed solution. Such differences would be enhanced as the influence of electrostatic effects near the surface increases. We bring these subtleties to the readers' attention to emphasize the limitations and assumptions in our theory. Despite these limitations, we maintain that the essential physics of wetting is captured by the uniformly mixed approach, and we reserve any improved description of adsorption in the supernatant phase to future work.

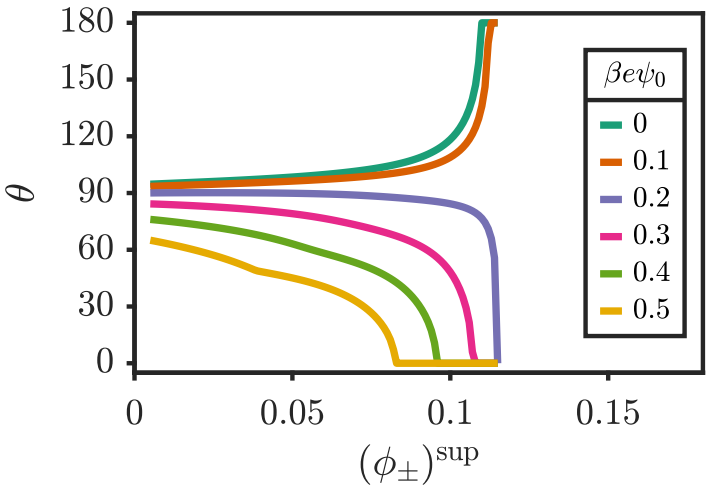

Figure IV.9: Contact angle versus the supernatant salt fraction when applying a surface potential for $\beta\eta_\pm = 0.01$. Critical salt concentration is $\phi_\pm^{\text{crit}} = 0.115$. For reference, 1 $\beta e\psi \approx 22$ mV.

Figure IV.10 shows the contact angle as a function of the applied potential for fixed bulk salt concentrations. In either panel, one can see that increasing the applied surface potential decreases the contact angle, eventually leading to complete wetting. Most notably, in Figure IV.10a, we see that a system with $\beta\eta = 0.03$ initially exhibits complete drying and transitions to complete wetting with an applied potential of less than 15 mV. Lower salt concentrations, like Figure IV.10b, are further from the critical point so the tendency to wet and dry the surface is lessened. In other words, for all values of $\beta\eta_{p_\pm}$ the contact angle moves toward 90° for $\psi_0 = 0$. Upon applying the potential, all systems transition to complete wetting. However, we again note the kinks in the curves that correspond to additional prewetting transitions. The important aspect from the additional prewetting transition is that the effect of the applied potential is diminished, evidenced by the decrease in the magnitude of the slope of the curves after the kink. For $\beta\eta_{p_\pm} = 0.03$, one can see that the applied potential to induce complete wetting occurs closer to $\beta e\psi_0 = 1.3$, which is nearly double the value in Figure IV.10a.

We can explain and quantify how the contact angle changes with the applied potential using a simple thermodynamic argument. Consider varying the applied potential for a given supernatant–coacervate tie-line on the phase diagram. Taking the partial

derivative of the contact angle with respect to the potential

$$\left(\frac{\partial \cos(\theta)}{\partial \psi_0}\right)_{T,A,\{\mu\}} = \frac{1}{\gamma_{\text{sup,co}}}\left[\left(\frac{\partial \gamma_{\text{sup,solid}}}{\partial \psi_0}\right)_{T,A,\{\mu\}} - \left(\frac{\partial \gamma_{\text{co,solid}}}{\partial \psi_0}\right)_{T,A,\{\mu\}}\right] \tag{IV.12}$$

with $\{\mu\}$ signifying the chemical potentials of all species. The derivatives on the right-hand side are related to the surface charge density by the Maxwell relation [60, 90]; thus

$$\left(\frac{\partial \cos(\theta)}{\partial \psi_0}\right)_{T,A,\{\mu\}} = \frac{e\left[(Q_s)^{\text{co}} - (Q_s)^{\text{sup}}\right]}{\gamma_{\text{sup,co}}} \tag{IV.13}$$

where the surface charge densities correspond to that of the coexisting coacervate and supernatant phases each on the solid surface. The second derivative is related to the capacitance of each phase on the solid surface [86].

$$\left(\frac{\partial^2 \cos(\theta)}{\partial \psi_0^2}\right)_{T,A,\{\mu\}} = \frac{e\left[(C)^{\text{co}} - (C)^{\text{sup}}\right]}{\gamma_{\text{sup,co}}} \tag{IV.14}$$

The capacitance generally increases with concentration so that Eq. IV.14 is positive. Together, Equations IV.13 and IV.14 indicate that $\cos(\theta)$ is minimized when the surface charge of the coacervate and supernatant on the surface is the same. For symmetric adsorption, $(Q_s)^{\text{co}} = (Q_s)^{\text{sup}} = 0$ for no applied potential so that the contact angle will always decrease with an applied potential (positive or negative).

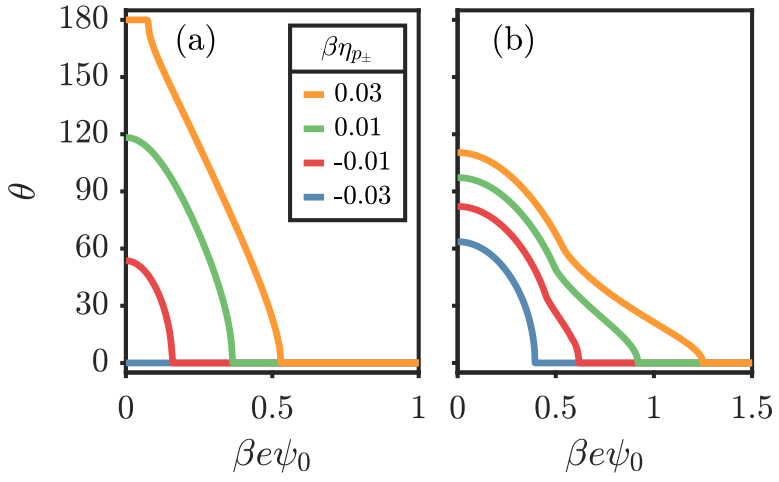

Figure IV.10: Contact angle versus applied surface potential for symmetric adsorption at a fixed salt concentration. Bulk salt concentrations are fixed at (a) $\phi_{\pm}^{\text{B}} = 0.1$ and (b) $\phi_{\pm}^{\text{B}} = 0.0385$ (1 M). For reference, 1 $\beta e\psi \approx 22$ mV.

Near layering transitions, the capacitance of the supernatant phase can be larger than the coacervate phase for the same potential, resulting from the strong adsorption of one polyion type associated with the transition. This phenomena can been seen as positive curvature in the curves in Figure IV.10.

Figure IV.11 shows the wetting/drying salt concentration as a function of the applied potential for various situations. As a reminder, the wetting/drying salt concentration is the salt concentration where the coacervate/supernatant phase completely wets/drys the surface. In Figure IV.11a, wetting and drying salt concentrations are plotted on the same curve and are differentiated by the line styles. The solid curves denote wetting and the dashed ones indicate drying. One can read each curve as a phase diagram, where vertically crossing the curves from low to high salt concentration corresponds to the transition from partial to complete wetting/drying. We can further interpret an increase in $\phi_{\pm}^{\text{dry}}$ or decrease in $\phi_{\pm}^{\text{wet}}$ as improving the overall wettability below $\phi_{\pm}^{\text{wet/dry}}$. For instance, with $\beta\eta_{p_{\pm}} = 0.01$ (magenta curve), by applying no potential, one can only cross the dashed line, corresponding to complete drying. By applying a negative or positive potential, the drying salt concentration increases, eventually passing through the bulk critical point, indicating the system has switched to complete wetting rather than drying. For the same parameters, this transition from a drying salt concentration to a wetting salt concentration is illustrated in Figure IV.9. For all of the curves in the symmetric case in Figure IV.11a, applying a positive or negative potential improves the overall wettability, where drying switches to wetting and/or $\phi_{\pm}^{\text{wet}}$ moves to lower salt concentrations.

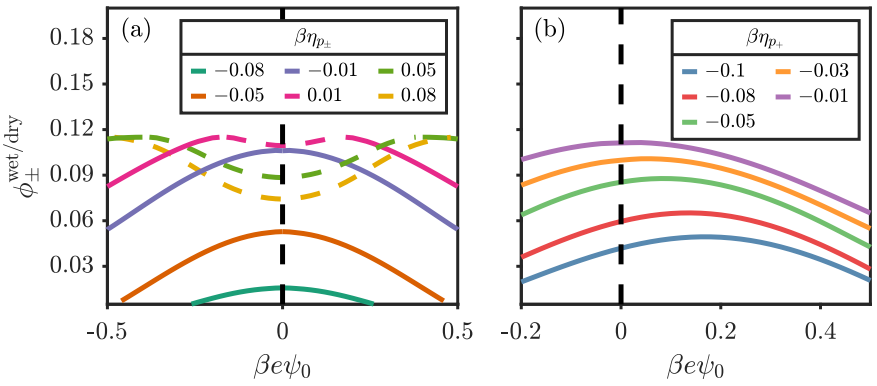

Figure IV.11: Wetting/drying salt concentration $\phi_{\pm}^{\text{wet/dry}}$ versus applied potential for (a) symmetric adsorption and (b) asymmetric adsorption. In (a), dashed lines denote the drying salt concentration, $\phi_{\pm}^{\text{dry}}$. In both panels, solid lines denote the wetting salt concentration, $\phi_{\pm}^{\text{wet}}$.

For asymmetric adsorption in Figure IV.11b, we only plot systems that undergo complete wetting. For all parameters considered, the wetting salt concentration has a maximum at positive potentials. This result can best be explained by Equation IV.13. For no applied potential, polycations adsorb on the surface due to the favorable nonelectrostatic interaction. Polycation adsorption induces a negative surface charge density, and due to the density differences in supernatant and coacervate phases, $(Q_s)^{\mathrm{co}} < (Q_s)^{\mathrm{sup}}$. Because the capacitance of the coacervate is higher than the capacitance of the supernatant $(C)^{\mathrm{co}} > (C)^{\mathrm{sup}}$, applying a positive applied potential will lead to faster changes in $(Q_s)^{\mathrm{co}}$ than $(Q_s)^{\mathrm{sup}}$ so that condition $(Q_s)^{\mathrm{co}} = (Q_s)^{\mathrm{sup}}$ requires a positive applied potential. The net result is a nonmonotonic dependence of the wetting salt concentration on the applied potential. For the conditions in Figure IV.11b, applying a positive potential initially diminishes the wettability (increases contact angles below $\phi_{\pm}^{\mathrm{wet}}$), then improves wettability after the maximum condition. On the other hand, applying a negative potential will only improve the surface wettability.

Conclusions

In this work, we study wetting transitions and contact angles of complex coacervates at solid surfaces. As expected from classical wetting theory, the wettability improves when approaching the bulk critical point. The wetting transition is found to be primarily first order with metastable regions that span multiple orders of magnitude of the polyelectrolyte concentration. Long range electrostatic forces arising from local charge separation can shift the surface critical point to lower salt concentrations, extending the range of second order wetting transitions if there is sufficient nonelectrostatic adsorption asymmetry or an applied surface potential. Many of the results presented here are similar to wetting behavior of simple fluids and polymer blends [91–94]. The essential difference is the presence of electrostatic forces that influence both the phase separation of the polyelectrolytes and possibly their interaction with the surface. The locations of the surface critical point and wetting salt concentration can be tuned by the polymer chemistry (nonelectrostatic interaction) and an applied electrostatic potential on the surface. We rationalize the effect of the electrostatic potential on wettability using arguments from surface thermodynamics.

The issues addressed in this work are relevant to several features seen in nature's underwater adhesives. One aspect is related to symmetric and asymmetric adsorption in biological systems. DOPA residues are prevalent in several of mussel foot proteins [49] compared to the sandcastle worm's adhesive proteins, where DOPA is

primarily present in only one of the proteins [38]. Our results indicate that complete wetting is possible when only one component has nonelectrostatic adsorption but such asymmetry generally requires a more favorable polyion–substrate interaction and the wettability is dependent on the electrostatic potential of the surface. As discussed in the introduction, mussels have the ability to tune the surface characteristics. For example, they induce a pH change from 8 (seawater) to less than 5, which will impart a negative zeta potential on most surfaces. As we highlight in our work, electrostatic manipulation of the surface is a powerful method to tune surface wettability, requiring only potential changes on the order of 10 mV to dramatically affect the contact angle. Conversely, given a surface condition (e.g. fixed pH), there are optimal polycation/polyanion characteristics best suited to wet the substrate. Tuning design parameters requires understanding the delicate interplay of nonelectrostatic adsorption with electrostatic-driven adsorption. Overall, we hope that our work can serve as a guide for designing systems that use complex coacervates on solid surfaces.

Recently, the wetting behavior of protein condensates on solid surfaces has also been associated with the origin of life [95]. The general class of surface-mediated processes in biological systems extends beyond solid surfaces. Many of the principles of wetting a solid, rigid surface can be applied to the wetting of soft, elastic substrates [96, 97]. Zhao *et al.* used a thermodynamic approach to study how membrane surfaces decorated with surface bound molecules improve the wetting of neutral protein condensates [89]. While complex coacervates represent only one type of protein condensate, we expect that extensions of the present work could be used to probe the combined effects of electrostatics and membrane elasticity on the wetting of biological membranes.

We also hope to extend our work to capture some of the physics that our inhomogeneous mean-field theory does not address. As mentioned throughout, treating the supernatant phase as uniformly mixed dismisses the presence of polyion clusters. Forming a coacervate phase on the surface would require the cluster–surface interaction to overcome the translational entropy of the clusters, and in asymmetric adsorption, the energy to rearrange the cluster to facilitate local charge separation [98]. Other important effects not included in this work are strong electrostatic correlation and packing effects near the surface. Substantial adsorption or large applied potentials can lead to layering transitions [76, 99, 100] and other non-intuitive phenomena [85, 101, 102] where the Debye–Hückel treatment of electrostatics and

a point-particle representation are not expected to be accurate. Capturing each of these effects requires a more sophisticated theory, which remains an outstanding challenge.

Appendix
Numerics of Turning Points

Computing the adsorption isotherms with a first order surface transition cannot be done via natural parameter continuation of the bulk polyelectrolyte density due to the presence of turning points. To overcome this, we use pseudo-arclength continuation (PAC) [103, 104] to vary the bulk polyelectrolyte density when computing adsorption isotherms. Such an approach is commonly used to study wetting [105–108]. We will highlight the differences in our approach compared to the usual PAC.

Consider the nonlinear system $\mathbf{F}(\mathbf{X};\lambda) = 0$, where $\mathbf{X}$ can be thought of as the discretized density and electrostatic potential fields, $\mathbf{F}(\mathbf{X};\lambda)$ are the corresponding mean-field equations, and λ is a continuation parameter, such as the bulk polyelectrolyte density. For a given value of λ, one can solve the equation $\mathbf{F}(\mathbf{X};\lambda) = 0$. Natural continuation of λ would proceed by starting with λ_0 and taking steps in $\Delta\lambda$. However, if there are turning points in $||\mathbf{X}||$ versus λ, corresponding to singular points, natural continuation will fail [109]. To address this, we can instead solve the extended system $G = [\mathbf{F}(\mathbf{X}(s),\lambda(s)), N(\mathbf{X}(s),\lambda(s))]$ where λ is now undetermined and $\mathbf{X}$ and λ are parameterized over an arclength variable s. Instead of taking steps of $\Delta\lambda$, one takes steps of the arclength variable of size Δs. The extended system requires specifying a new equation related to the arclength step, $N(\mathbf{X}(s),\lambda(s)) = \dot{\mathbf{x}}_0 \cdot (\mathbf{X} - \mathbf{X}_0) + \dot{\lambda}(\lambda - \lambda_0) - \Delta s$. Here, $\dot{\mathbf{x}}_0 = d\mathbf{X}/ds|_{\mathbf{X}=\mathbf{X}_0}$ and $\dot{\lambda} = d\lambda/ds|_{\lambda=\lambda_0}$ with $||\dot{\mathbf{x}}_0||^2 + |\dot{\lambda}_0|^2 = 1$. The extended system corresponds to finding a solution that lies on the plane perpendicular to $(\dot{\mathbf{x}}_0, \dot{\lambda}_0)$ that intersects the solution curve, which is shown graphically in Figure IV.12.

With access to the Jacobian of the system ($d\mathbf{F}/d\mathbf{X}$), one can obtain the tangent vector $(\dot{\mathbf{x}}_0, \dot{\lambda}_0)$ exactly (up to the sign of $\dot{\lambda}_0$). In this work, the Jacobian is inconvenient. We approximate the tangent vector by taking natural continuation steps (5 usually) in λ using then switch to PAC by using approximating $(\dot{\mathbf{x}}_0, \dot{\lambda}_0)$ based on previous solution points. To solve for the next point, we take a predictor step to the point $(\mathbf{X}_0 + \dot{\mathbf{x}}_0\Delta s, \lambda_0 + \dot{\lambda}_0\Delta s)$ and use Anderson Acceleration to solve the extended system.

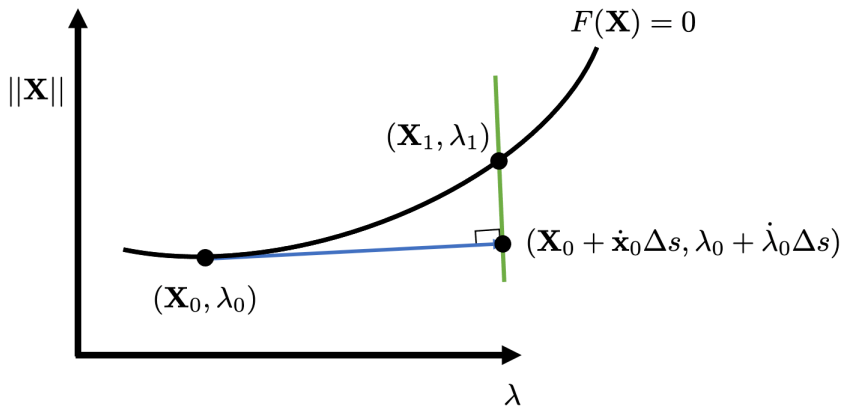

Figure IV.12: Graphical illustration of pseudo-arclength continuation. Continuation proceeds along the solution curve defined by $\mathbf{F}(\mathbf{X}) = 0$ from an initial point $(\mathbf{X}_0, \lambda_0)$ to $(\mathbf{X}_1, \lambda_1)$ by solving the extended system of equations $G = [\mathbf{F}(\mathbf{X}(s), \lambda(s)), N(\mathbf{X}(s), \lambda(s))]$.

Thermodynamic Stability and Turning Points

Figure IV.13 shows a prototypical example of the adsorption isotherm and corresponding excess grand potential energy (equivalent to the surface tension). Each plot is divided into multiple colors that indicate the phase adjacent to the surface. The red lines indicate a thermodynamically unstable region. From thermodynamics of a single component system, thermodynamic stability requires that the 2nd derivative of the free energy with respect to chemical potential be negative [110]. This is true for a multicomponent system if the other chemical potentials are kept constant. In the adsorption process in Figure IV.13, the salt ion chemical potentials change along with the polyelectrolyte chemical potentials so rigorously, one cannot determine stability from Figure IV.13 alone. However, practically, for the conditions here, the change in the chemical potential of the salt ions is small. The 2nd derivative is clearly negative for the blue and black regions and positive for the red region of Figure IV.13b. Further, we can see from Figure IV.13b that there are regions of metastability. For example, there is a section where the free energy (surface tension)

is higher for the supernatant phase, yet a stable phase exists on the surface. The same is true for the coacervate layer. Finally, the crossing of the blue and black curves in Figure IV.13b is the coexistence point of the supernatant and coacervate phase on the surface.

Figure IV.14 shows the surface free energy for one of the adsorption isotherms in Figure 2 of the main text. Namely, for $\beta\eta_{p_\pm} = -0.01$ and overall salt fraction $\phi_\pm^{\mathrm{B}} = 0.1$, the system is below the wetting salt concentration so partial wetting takes place. With partial wetting, it is possible to have a metastable coacervate film on the surface with diverging film thickness, but the film does not cross the supernatant branch to be globally stable.

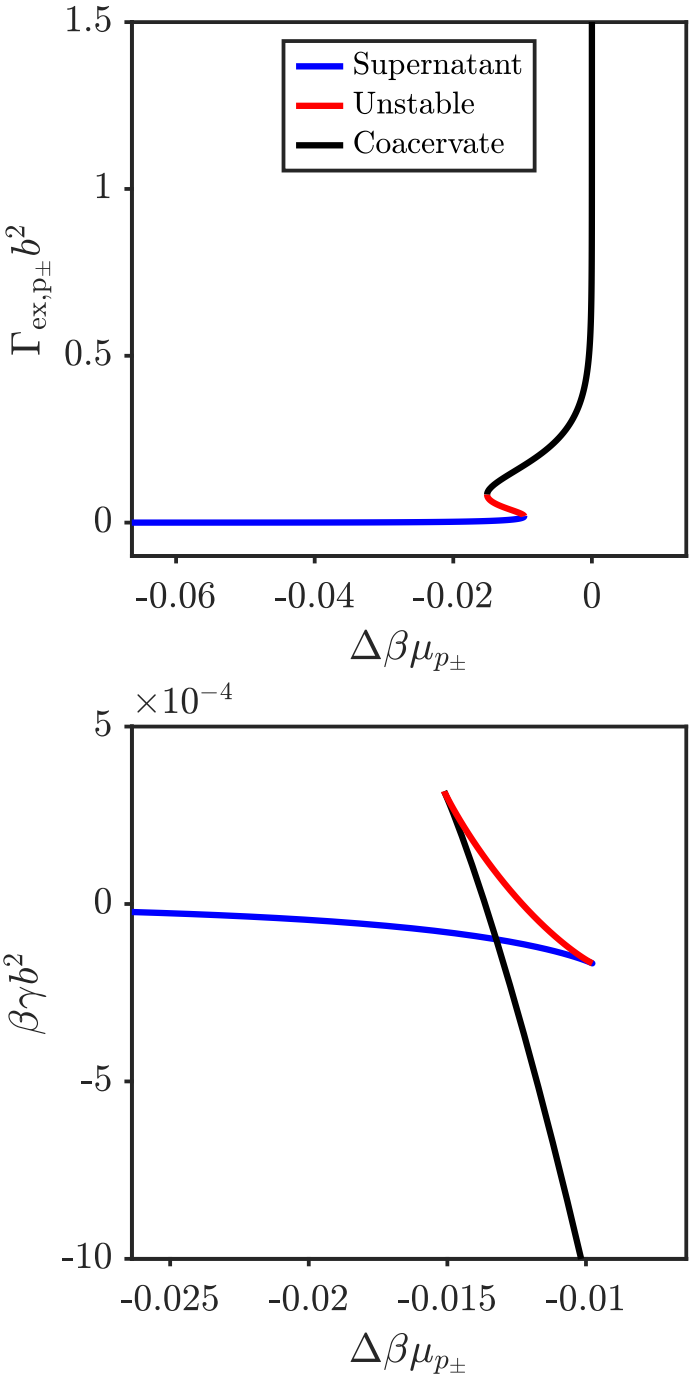

Figure IV.13: Example adsorption isotherm and surface tension for first order transition. (a) Symmetric adsorption isotherm with $\beta\eta_{p_\pm} = -0.05$ for a constant overall salt fraction $\phi_\pm^{\mathrm{B}} = 0.1$. (b) Corresponding surface tension (excess grand potential) for the adsorption isotherm in (a).

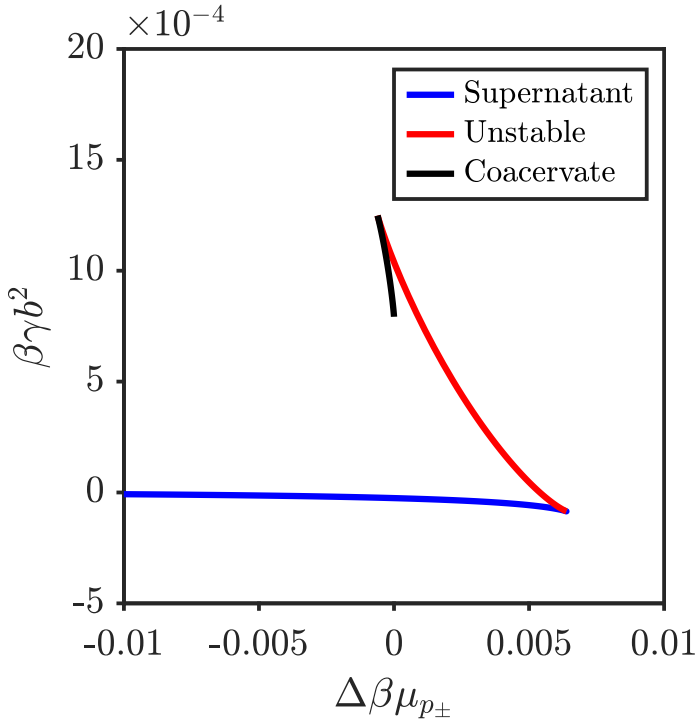

Figure IV.14: Surface tension corresponding to adsorption isotherm with $\beta\eta_{p_\pm} = -0.01$ for a constant overall salt fraction $\phi_\pm^{\mathrm{B}} = 0.1$.

First to Second Order Surface Transition

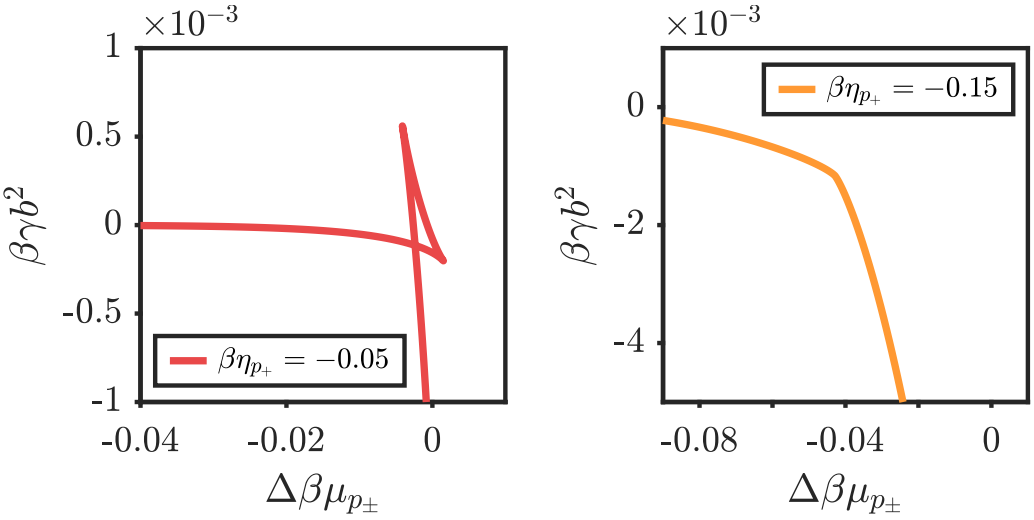

Figure IV.15: Surface tension (surface excess grand potential energy) for (a) $\beta\eta_{p_+} = -0.05$ and (b) $\beta\eta_{p_+} = -0.15$. $\Delta\mu_{p_\pm} = \mu_{p_\pm} - \mu_{p_\pm}^{\text{coex}}$ is a measure of the distance from coexistence. Panel (a) shows the typical surface tension profile for a first order transition, featuring metastable and unstable regions. Panel (b) shows the typical surface tension profile for a second order transition, where the surface tension and first derivative of the surface tension transition smoothly from a supernatant to a coacervate surface phase. Corresponding adsorption isotherms can be found in Figure 4 of the main text.

Symmetric Adsorption with Applied Potential

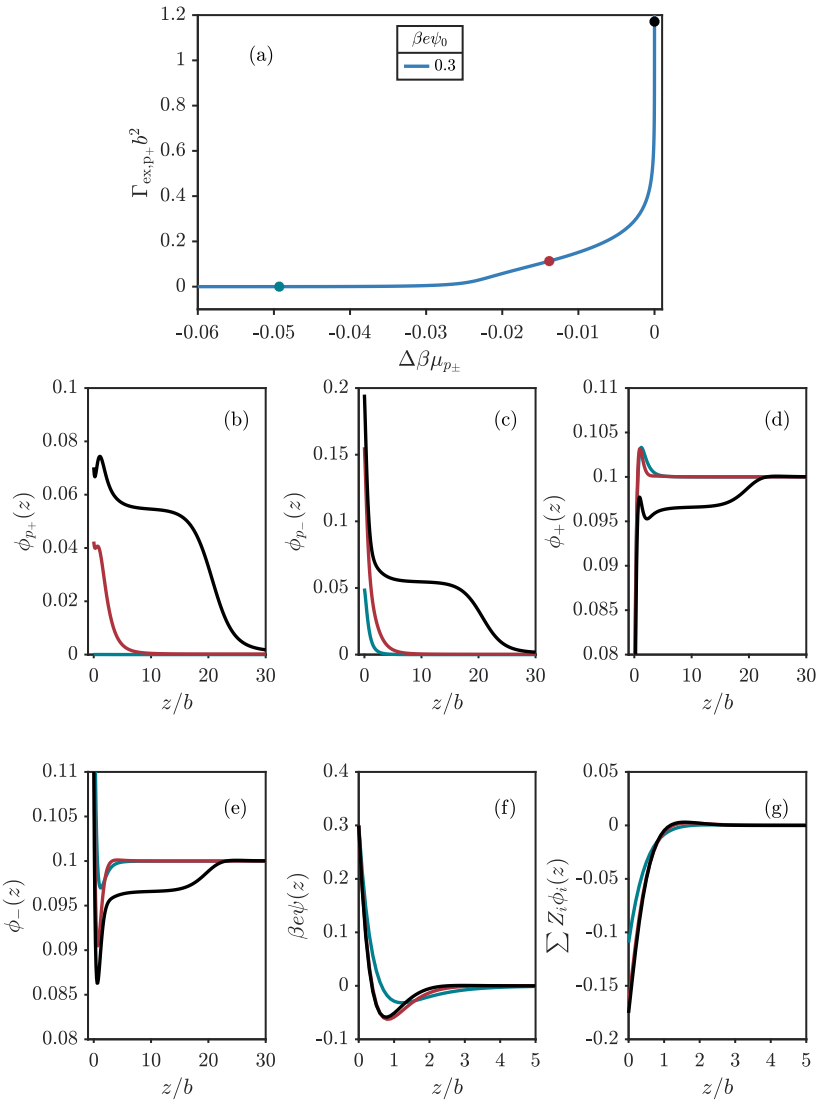

Figure IV.16: Interfacial profiles for an applied potential. (a) Polyelectrolyte adsorption isotherms for $\beta e\psi_0 = 0.3$ at a constant bulk salt concentration of $\phi_\pm^{\mathrm{B}} = 0.1$ with $\beta\eta_{p_\pm} = -0.05$. Corresponding (b) polycation, (c) polyanion, (d) cation, (e) anion, (f) electrostatic potential, and (g) charge density for the solid points in (a). Notably, the surface potential and charge density cross zero in panels (f) and (g), respectively. Based on initially weak adsorption of polycation in (a) and strong adsorption of polyanion in (b) (green curves), we state in the main text that the wetting transition proceeds predominantly from the electrostatic attraction between adsorbed polyanion attracting polycation to the surface.

Interfacial Tension in Contact Angle Calculation

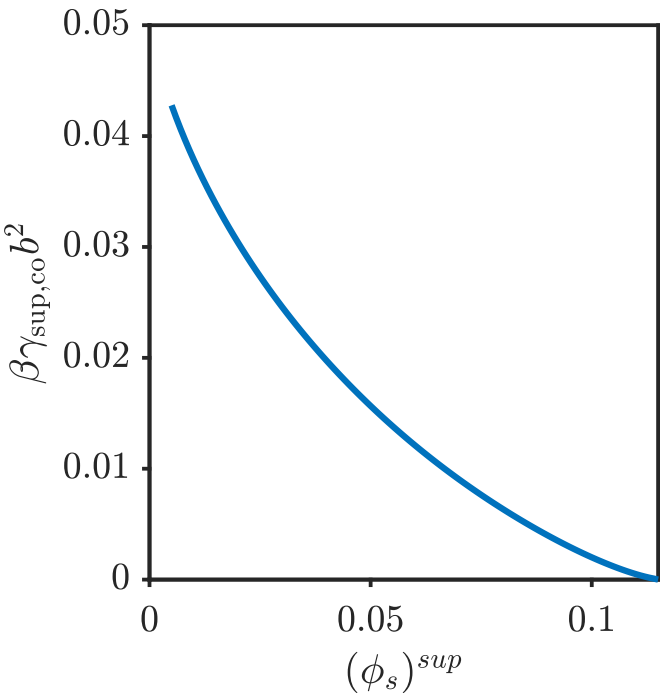

Figure IV.17: Interfacial tension of supernatant–coacervate phase versus the supernatant salt concentration calculated via the same method in Zhang and Wang [30]. The interfacial tension vanishes at the bulk critical point. The parameters in this figure correspond to that of the phase diagram in Figure 1 in the main text.

Additional Prewetting Transition (Layering Transition)

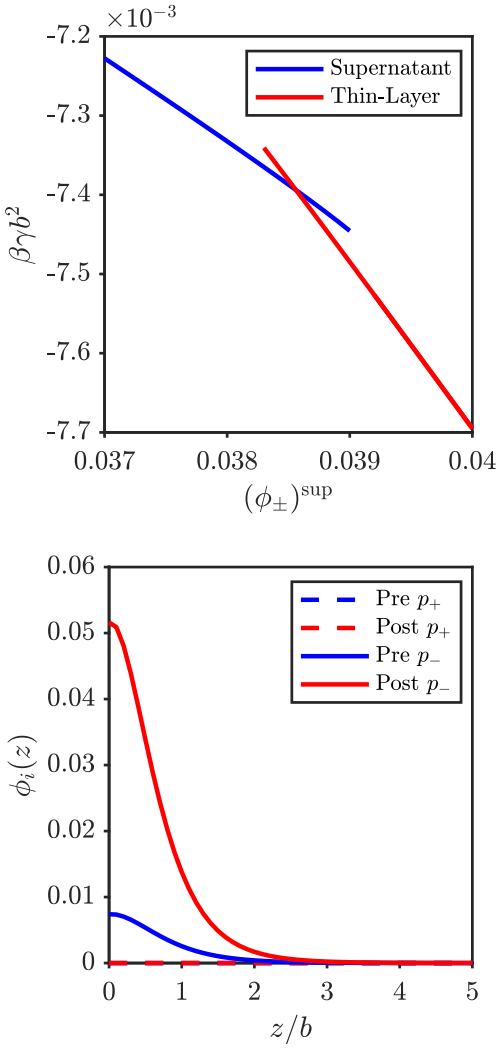

Figure IV.18: Prewetting transition induced by applied potential. (left) Excess grand potential (surface tension) versus supernatant salt concentration for $\beta\eta_{p_\pm} = 0.01$ and $\beta e\psi_0 = 0.5$. (right) Interfacial profile for polycation (dashed) and polyanion (solid) before and after the prewetting transition, corresponding to $(\phi_\pm)^{\text{sup}} = 0.038$ and $(\phi_\pm)^{\text{sup}} = 0.039$, respectively. The before and after profiles overlap for the polycation, indicating the polyanion drives the transition. The wetting salt concentration for these conditions is $\phi_\pm^{\text{wet}} = 0.083$ so the transition occurs below the wetting salt concentration. A first order transition below the wetting salt concentration is an additional prewetting transition. Multiple prewetting transitions of the same kind are possible, which correspond to polyelectrolyte multi-layers forming on the surface.

Effect of Polyelectrolyte Adsorption on Supernatant Surface Tension

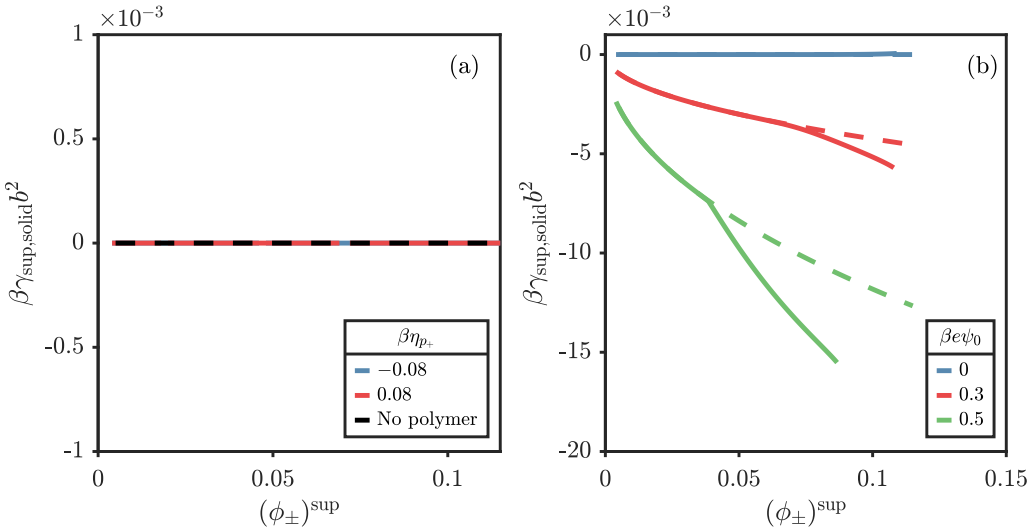

Figure IV.19: Comparison of supernatant descriptions - surface tension. (a) Comparison of $\gamma_{\text{sup,solid}}$ for asymmetric nonelectrostatic adsorption ($\beta\eta_{p\_} = 0$). Solid lines correspond to uniformly mixed description and dashed lines correspond to a polyelectrolyte-free solution at the same osmotic pressure as the coacervate phase. All lines overlap, which indicates that the polyelectrolyte adsorption (or desorption) does not appreciably affect the supernatant–solid surface tension. (b) Comparison of $\gamma_{\text{sup,solid}}$ for symmetric nonelectrostatic adsorption ($\beta\eta_{p_\pm} = 0.01$) for different applied potentials. Solid lines correspond to uniformly mixed description and dashed lines correspond to a polyelectrolyte-free solution at the same osmotic pressure as the coacervate phase. The green and red lines show differing behavior between the uniformly mixed polyelectrolytes and polyelectrolyte-free cases, indicating the effect of polyelectrolyte adsorption on the supernatant–solid surface tension.

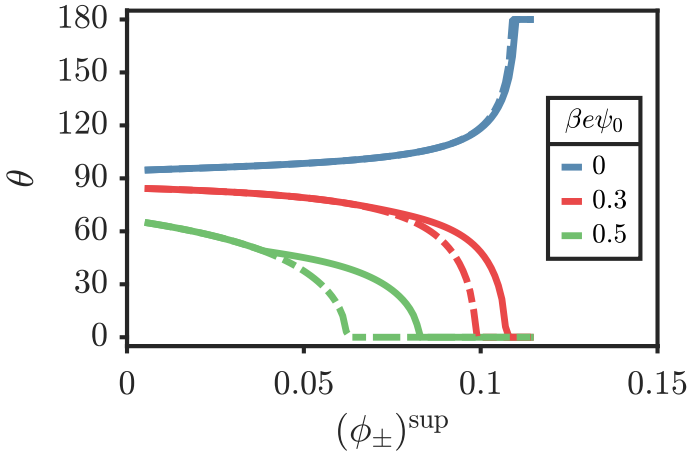

Figure IV.20: Contact angle versus the supernatant salt fraction when applying a surface potential for $\beta\eta_\pm = 0.01$. Critical salt concentration is $\phi_\pm^{\text{crit}} = 0.115$. The calculation of the contact angle uses the supernatant–solid surface tensions from Figure IV.19. Solid lines correspond to uniformly mixed description and dashed lines correspond to a polyelectrolyte-free solution at the same osmotic pressure as the coacervate phase. Again, the effect of the polyelectrolyte adsorption is enhanced as the applied potential increases in magnitude.

IV.2 Extension of Wetting Behavior

There are two natural extensions to the preceding section. The first is to consider the wetting behavior in confinement. Often, one surface cannot support a liquid (coacervate) film, whereas the presence of two surfaces can stabilized the liquid film, which shifts the surface phase diagram for the wetting transition. The second extension is to reconsider the physical picture of the supernatant phase. The theory explored in Section IV.1 considers the supernatant phase to be uniformly mixed. In reality, in dilute solution, polycations and polyanions will pair to form clusters [71, 111]. This section briefly outlines these two extensions.

Capillary Condensation

Phase behavior under confinement greatly differs from bulk systems due to the strong interactions with the surface [112]. The dilute to dense phase transition often occurs at a pressure lower than the saturation pressure. For wetting transitions of polyelectrolyte complex coacervates, the transition already occurs via a prewetting transition below the saturation pressure.

The inclusion of another surface is not expected to introduce any new physics but may have a complex interplay with the prewetting transitions. Figure IV.22 shows

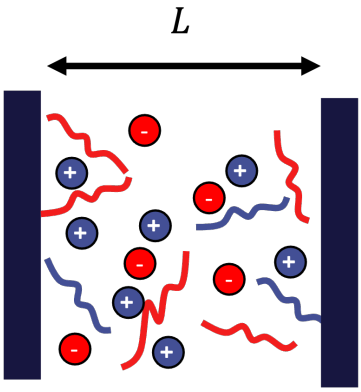

Figure IV.21: Schematic for two-surface system used to study capillary condensation.

polyelectrolyte adsorption isotherms for different pore sizes compared to the result for a single surface. With two surfaces, confinement prevents the film growth from diverging diverging at coexistence. Importantly, as the pore width decreases, the adsorption isotherm begins to qualitatively differ from that of the single surface. For $L = 20b$, the prewetting transition exists around $\Delta\beta\mu_{p_\pm} = -12\times10^{-3}$ and there is an additional surface transition near $\Delta\beta\mu_{p_\pm} = -5\times10^{-3}$. The surface phase transitions are clear from the turning points in adsorption isotherm, which correspond to surface spinodals. The second phase transition is the condensation event that only occurs in the confined system. As the pore width decreases, for example $L = 7b$, only one surface transition remains, which is a combination of the usual prewetting transition and the condensation transition. The polyelectrolytes want to form a thin coacervate layer at the surface but cannot do so without filling the pore. The favorability of adsorbing to both surfaces shifts the prewetting transition further from coexistence.

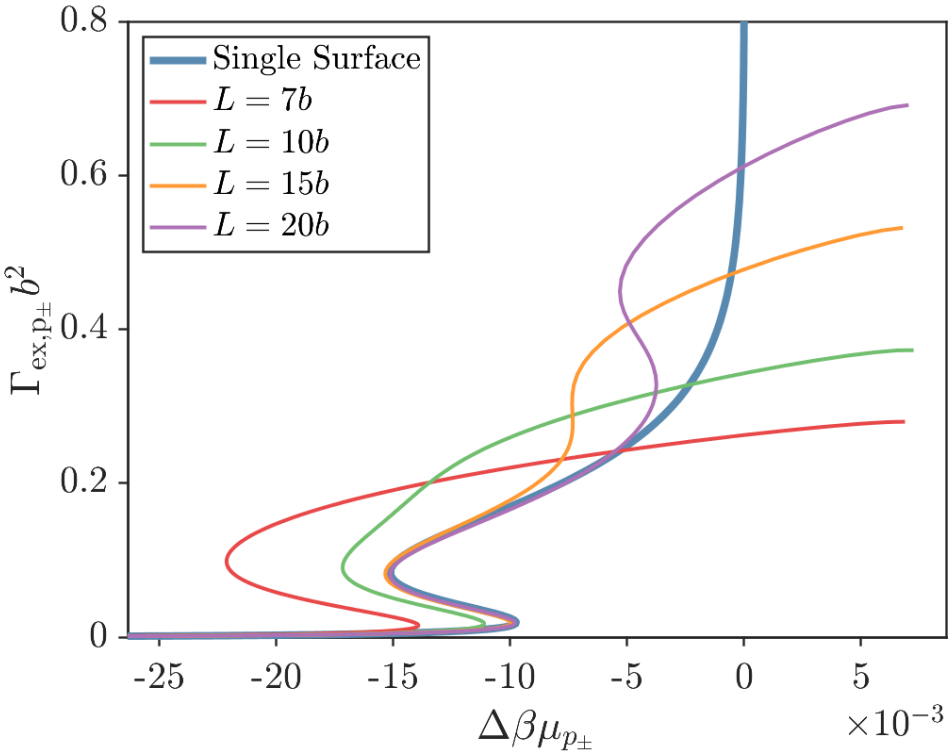

Figure IV.22: Polyelectrolyte adsorption isotherms for various pore separations with $\beta\eta_\pm = -0.05$ at a constant bulk salt concentration of $\phi_\pm^B = 0.1$. $\Delta\beta\mu_{p_\pm} = \beta\mu_{p_\pm} - \beta\mu_{p_\pm}^{coex}$ is a measure of the distance from coexistence. Excess adsorption for two surfaces divided by 2 to compare with single surface.

Clusters in the Supernatant Phase

As discussed in Section IV.1, the assumption that the supernatant phase is made up of uniformly mixed polyelectrolytes is not the correct physical picture. The driving force for complexation is strong in dilute solutions [72]. Zhang and Wang accounted for the formation of neutral polyelectrolyte clusters in the supernatant phase in their work [71]. From their analysis, the presence of clusters (1) leads to a higher overall polymer concentration in the supernatant phase and (2) nearly all of the clusters consist of a single polyanion-polycation pair.

We adjust our theory to account for the cluster-modified supernatant phase. The structure and thermodynamics of the clusters are extensively discussed in Ref. 71. For the purposes of wetting behavior, we only consider single polyanion and polycation pairs forming clusters. The clusters have the form of a spherical globule, as shown in Figure IV.24. Outside of the globule is a salt solution, denoted as a salt reservoir. The concentration of polyion in the cluster generally follows the

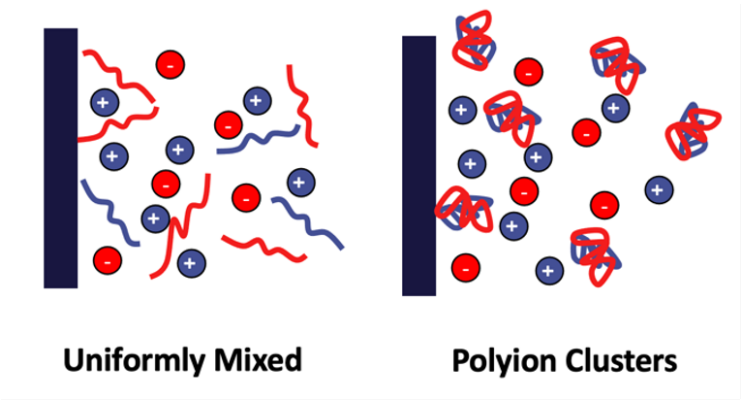

Figure IV.23: Schematic showing difference between uniformly mixed supernatant and a cluster-modified supernatant phase.

same trends for the coacervate phase for bulk phase phase behavior. For instance, increasing the salt concentration decreases the cluster polyion concentration. From the single cluster calculation, the monomer chemical potential can be determined, which is used in determining the inhomogeneous density near a solid surface.

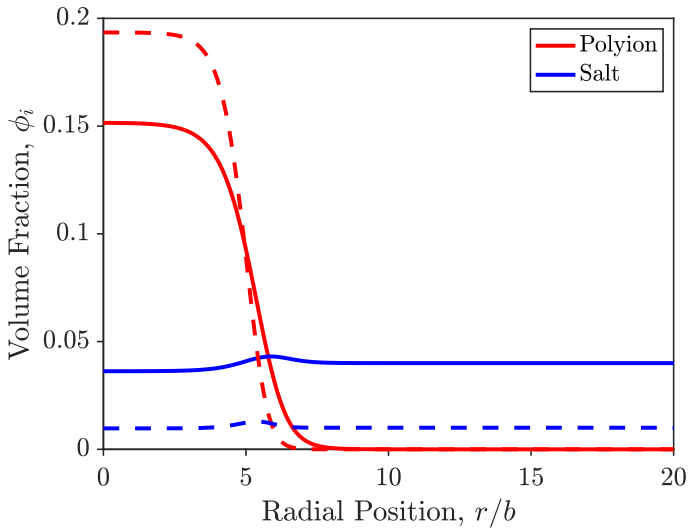

Figure IV.24: Cluster density profile in the supernatant phase. Cluster is symmetric for polycation/polyanion. The chain length is $N = 100$ for a Bjerrum length of $l_b = 1.785b$. The salt reservoir concentration is (solid) $\phi^r_\pm = 0.04$ and (dashed) $\phi^r_\pm = 0.01$.

To study the contact angle with the cluster-modified supernantant phase, the co-existing coacervate condition must be determined. The key assumption in finding coexistence is that the clusters do not contribute to the osmotic pressure of the

supernatant phase. Coexistence is then determined by finding the coacervate phase where the salt chemical potential and the osmotic pressure are equal in each phase. Because of the assumption that the clusters do not contribute to the osmotic pressure, the theory is only valid for relatively low cluster concentration, since, to first order, the contribution to the osmotic pressure increases linearly with the cluster concentration.

To discuss the contact angle results, we compare to Figure IV.20, where the contact angle is shown for the uniformly mixed system and that with no polyelectrolyte in the supernatant phase. Thus, the figure compares the effect of polyelectrolyte adsorption in the supernatant phase on the contact angle. Figure IV.25 shows that the contact angle is relatively unchanged for no applied potential and $\beta e\psi_0 = 0.3$. Only for $\beta e\psi_0 = 0.5$ does the cluster-modified curve start to deviate from the uniformly mixed case. The deviation is the result of strong adsorption of the clusters. The limitations of the cluster-modified theory prevent studying the contact angle to the point of complete wetting. The wetting salt concentration generally occurs close to the critical point, which is too high of a cluster concentration for the cluster-modified theory to be valid. Future development of the theory may overcome this limitation.

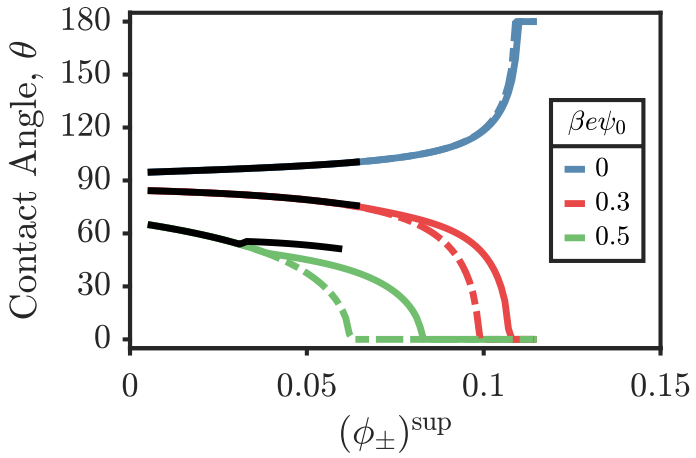

Figure IV.25: Contact angle versus the supernatant salt fraction when applying a surface potential for $\beta\eta_\pm = 0.01$. Critical salt concentration is $\phi_\pm^{\text{crit}} = 0.115$. Solid colored lines correspond to uniformly mixed description and dashed lines correspond to a polyelectrolyte-free solution at the same osmotic pressure as the coacervate phase. Black lines indicate the cluster-modified supernatant phase.

References

(1) Fredrickson, G., *The Equilibrium Theory of Inhomogeneous Polymers*; Oxford University Press: New York, 2007, DOI: 10.1093/acprof:oso/9780198567295.001.0001.

(2) Balzer, C.; Zhang, P.; Wang, Z.-G. *Soft Matter* **2022**, *18*, 6326–6339, DOI: 10.1039/D2SM00859A.

(3) Sing, C. E.; Perry, S. L. *Soft Matter* **2020**, *16*, 2885–2914, DOI: 10.1039/d0sm00001a.

(4) Timilsena, Y. P.; Akanbi, T. O.; Khalid, N.; Adhikari, B.; Barrow, C. J. *International Journal of Biological Macromolecules* **2019**, *121*, 1276–1286, DOI: 10.1016/j.ijbiomac.2018.10.144.

(5) Schmitt, C.; Turgeon, S. L. *Advances in Colloid and Interface Science* **2011**, *167*, 63–70, DOI: 10.1016/j.cis.2010.10.001.

(6) Xiao, Z.; Liu, W.; Zhu, G.; Zhou, R.; Niu, Y. *Journal of the Science of Food and Agriculture* **2014**, *94*, 1482–1494, DOI: 10.1002/jsfa.6491.

(7) Eghbal, N.; Choudhary, R. *LWT - Food Science and Technology* **2018**, *90*, 254–264, DOI: 10.1016/j.lwt.2017.12.036.

(8) Timilsena, Y. P.; Haque, M. A.; Adhikari, B. *Food and Nutrition Sciences* **2020**, *11*, 481–508, DOI: 10.4236/fns.2020.116035.

(9) Cheng, S.; Yuen, C.; Kan, C.; Cheuk, K. *Research Journal of Textile and Apparel* **2008**, *12*, 41–51, DOI: 10.1108/rjta-12-04-2008-b005.

(10) Demirbağ, S.; Aksoy, S. A. *Fibers and Polymers* **2016**, *17*, 408–417, DOI: 10.1007/s12221-016-5113-z.

(11) López, A.; Lis, M. J.; Bezerra, F. M., et al. *Journal of Biomedical Science and Engineering* **2019**, *12*, 377–390, DOI: 10.4236/jbise.2019.128029.

(12) Massella, D.; Giraud, S.; Guan, J.; Ferri, A.; Salaün, F. *Environmental Chemistry Letters* **2019**, *17*, 1787–1800, DOI: 10.1007/s10311-019-00913-w.

(13) Tang, Y.; Scher, H. B.; Jeoh, T. *Innovative Food Science and Emerging Technologies* **2020**, *59*, 102257, DOI: 10.1016/j.ifset.2019.102257.

(14) Burgess, D. J. In *Macromolecular Complexes in Chemistry and Biology*; Springer Berlin Heidelberg: 1994, pp 285–300, DOI: 10.1007/978-3-642-78469-9_17.

(15) Blocher, W. C.; Perry, S. L. *Wiley Interdisciplinary Reviews: Nanomedicine and Nanobiotechnology* **2017**, *9*, e1442, DOI: 10.1002/wnan.1442.

(16) Srivastava, S.; Andreev, M.; Levi, A. E., et al. *Nature Communications* **2017**, *8*, 1–9, DOI: 10.1038/ncomms14131.

(17) Degen, G. D.; Cunha, K. C.; Levine, Z. A.; Waite, J. H.; Shea, J. E. *Journal of Physical Chemistry B* **2021**, *125*, 9999–10008, DOI: 10.1021/acs.jpcb.1c05218.

(18) Veis, A. *Advances in Colloid and Interface Science* **2011**, *167*, 2–11, DOI: 10.1016/j.cis.2011.01.007.

(19) Sing, C. E. *Advances in Colloid and Interface Science* **2017**, *239*, 2–16, DOI: 10.1016/j.cis.2016.04.004.

(20) Rumyantsev, A. M.; Jackson, N. E.; De Pablo, J. J. *Annual Review of Condensed Matter Physics* **2021**, *12*, 155–176, DOI: 10.1146/annurev-conmatphys-042020-113457.

(21) Jho, Y. S.; Yoo, H. Y.; Lin, Y.; Han, S.; Hwang, D. S. *Advances in Colloid and Interface Science* **2017**, *239*, 61–73, DOI: 10.1016/j.cis.2016.07.003.

(22) Prabhu, V. M. *Current Opinion in Colloid and Interface Science* **2021**, *53*, 101422, DOI: 10.1016/j.cocis.2021.101422.

(23) Spruijt, E.; Sprakel, J.; Cohen Stuart, M. A.; Van Der Gucht, J. *Soft Matter* **2010**, *6*, 172–178, DOI: 10.1039/b911541b.

(24) Priftis, D.; Farina, R.; Tirrell, M. *Langmuir* **2012**, *28*, 8721–8729, DOI: 10.1021/la300769d.

(25) Riggleman, R. A.; Kumar, R.; Fredrickson, G. H. *Journal of Chemical Physics* **2012**, *136*, 24903, DOI: 10.1063/1.3674305.

(26) Qin, J.; Priftis, D.; Farina, R., et al. *ACS Macro Letters* **2014**, *3*, 565–568, DOI: 10.1021/mz500190w.

(27) Lytle, T. K.; Salazar, A. J.; Sing, C. E. *Journal of Chemical Physics* **2018**, *149*, 163315, DOI: 10.1063/1.5029934.

(28) Rumyantsev, A. M.; Zhulina, E. B.; Borisov, O. V. *Macromolecules* **2018**, *51*, 3788–3801, DOI: 10.1021/acs.macromol.8b00342.

(29) Ali, S.; Prabhu, V. M. *Macromolecules* **2019**, *52*, 7495–7502, DOI: 10.1021/acs.macromol.9b01491.

(30) Zhang, P.; Wang, Z. G. *Macromolecules* **2021**, *54*, 10994–11007, DOI: 10.1021/acs.macromol.1c01809.

(31) Li, H.; Fauquignon, M.; Haddou, M.; Schatz, C.; Chapel, J. P. *Polymers* **2021**, *13*, 3848, DOI: 10.3390/polym13213848.

(32) Audus, D. J.; Ali, S.; Rumyantsev, A. M., et al. *Physical Review Letters* **2021**, *126*, 237801, DOI: 10.1103/PhysRevLett.126.237801.

(33) Wang, F.; Xu, X.; Zhao, S. *Langmuir* **2019**, *35*, 15267–15274, DOI: 10.1021/acs.langmuir.9b02787.

(34) Lim, S.; Moon, D.; Kim, H. J., et al. *Langmuir* **2014**, *30*, 1108–1115, DOI: 10.1021/la403680z.

(35) Hwang, D. S.; Zeng, H.; Srivastava, A., et al. *Soft Matter* **2010**, *6*, 3232–3236, DOI: 10.1039/c002632h.

(36) Li, Y.; Cheng, J.; Delparastan, P., et al. *Nature Communications* **2020**, *11*, 1–8, DOI: 10.1038/s41467-020-17597-4.

(37) Narayanan, A.; Dhinojwala, A.; Joy, A. *Chemical Society Reviews* **2021**, *50*, 13321–13345, DOI: 10.1039/d1cs00316j.

(38) Shao, H.; Bachus, K. N.; Stewart, R. J. *Macromolecular Bioscience* **2009**, *9*, 464–471, DOI: 10.1002/mabi.200800252.

(39) Kaur, S.; Weerasekare, G. M.; Stewart, R. J. *ACS Applied Materials and Interfaces* **2011**, *3*, 941–944, DOI: 10.1021/am200082v.

(40) Zhang, L.; Lipik, V.; Miserez, A. *Journal of Materials Chemistry B* **2016**, *4*, 1544–1556, DOI: 10.1039/c5tb02298c.

(41) Stewart, R. J.; Wang, C. S.; Song, I. T.; Jones, J. P. *Advances in Colloid and Interface Science* **2017**, *239*, 88–96, DOI: 10.1016/j.cis.2016.06.008.

(42) Vahdati, M.; Cedano-Serrano, F. J.; Creton, C.; Hourdet, D. *ACS Applied Polymer Materials* **2020**, *2*, 3397–3410, DOI: 10.1021/acsapm.0c00479.

(43) Stewart, R. J.; Wang, C. S.; Shao, H. *Advances in Colloid and Interface Science* **2011**, *167*, 85–93, DOI: 10.1016/j.cis.2010.10.009.

(44) Lu, Q.; Danner, E.; Waite, J. H., et al. *Journal of the Royal Society Interface* **2013**, *10*, 20120759, DOI: 10.1098/rsif.2012.0759.

(45) Kim, S.; Huang, J.; Lee, Y., et al. *Proceedings of the National Academy of Sciences of the United States of America* **2016**, *113*, E847–E853, DOI: 10.1073/pnas.1521521113.

(46) Levine, Z. A.; Rapp, M. V.; Wei, W., et al. *Proceedings of the National Academy of Sciences of the United States of America* **2016**, *113*, 4332–4337, DOI: 10.1073/pnas.1603065113.

(47) Yu, Q.; Zheng, Z.; Dong, X., et al. *Soft Matter* **2021**, *17*, 8786–8804, DOI: 10.1039/d1sm00997d.

(48) Narayanan, A.; Kaur, S.; Kumar, N., et al. *Macromolecules* **2021**, *54*, 5417–5428, DOI: 10.1021/acs.macromol.1c00742.

(49) Waite, J. H. *Journal of Experimental Biology* **2017**, *220*, 517–530, DOI: 10.1242/jeb.134056.

(50) Wertheim, M. S. *The Journal of Chemical Physics* **1987**, *87*, 7323–7331, DOI: 10.1063/1.453326.

(51) Zhang, P.; Alsaifi, N. M.; Wu, J.; Wang, Z. G. *Macromolecules* **2016**, *49*, 9720–9730, DOI: 10.1021/acs.macromol.6b02160.

(52) Zhang, P.; Alsaifi, N. M.; Wu, J.; Wang, Z. G. *Journal of Chemical Physics* **2018**, *149*, 163303, DOI: 10.1063/1.5028524.

(53) Ylitalo, A. S.; Balzer, C.; Zhang, P.; Wang, Z. G. *Macromolecules* **2021**, *54*, 11326–11337, DOI: 10.1021/acs.macromol.1c02000.

(54) Lifshitz, I. M.; Grosberg, A. Y.; Khokhlov, A. R. *Reviews of Modern Physics* **1978**, *50*, 683–713, DOI: 10.1103/RevModPhys.50.683.

(55) De Gennes, P. G. *Macromolecules* **1981**, *14*, 1637–1644, DOI: 10.1021/ma50007a007.

(56) Johner, A.; Bonet-Avaloe, J.; Van Der Linden, C. C.; Semenov, A. N.; Joanny, J. F. *Macromolecules* **1996**, *29*, 3629–3638, DOI: 10.1021/ma951637j.

(57) Shafir, A.; Andelman, D. *Physical Review E - Statistical Physics, Plasmas, Fluids, and Related Interdisciplinary Topics* **2004**, *70*, 12, DOI: 10.1103/PhysRevE.70.061804.

(58) Wang, Q. *Macromolecules* **2005**, *38*, 8911–8922, DOI: 10.1021/ma050960b.

(59) Shen, K.; Wang, Z. G. *Journal of Chemical Physics* **2017**, *146*, 84901, DOI: 10.1063/1.4975777.

(60) Bruch, D.; Balzer, C.; Wang, Z.-G. *The Journal of Chemical Physics* **2022**, *156*, 174704, DOI: 10.1063/5.0089260.

(61) Walker, H. F.; Ni, P. *SIAM Journal on Numerical Analysis* **2011**, *49*, 1715–1735, DOI: 10.1137/10078356X.

(62) Overbeek, J. T.; Voorn, M. J. *Journal of Cellular Physiology* **1957**, *49*, 7–26, DOI: 10.1002/jcp.1030490404.

(63) Kudlay, A.; De la Cruz, M. O. *Journal of Chemical Physics* **2004**, *120*, 404–412, DOI: 10.1063/1.1629271.

(64) Potemkin, I. I.; Palyulin, V. V. *Physical Review E - Statistical, Nonlinear, and Soft Matter Physics* **2010**, *81*, 041802, DOI: 10.1103/PhysRevE.81.041802.

(65) Qin, J.; De Pablo, J. J. *Macromolecules* **2016**, *49*, 8789–8800, DOI: 10.1021/acs.macromol.6b02113.

(66) Lytle, T. K.; Sing, C. E. *Soft Matter* **2017**, *13*, 7001–7012, DOI: 10.1039/c7sm01080j.

(67) Zhang, P.; Shen, K.; Alsaifi, N. M.; Wang, Z. G. *Macromolecules* **2018**, *51*, 5586–5593, DOI: 10.1021/acs.macromol.8b00726.

(68) Ou, Z.; Muthukumar, M. *Journal of Chemical Physics* **2006**, *124*, 154902, DOI: 10.1063/1.2178803.

(69) Rumyantsev, A. M.; Potemkin, I. I. *Physical Chemistry Chemical Physics* **2017**, *19*, 27580–27592, DOI: 10.1039/c7cp05300b.

(70) Singh, A. N.; Yethiraj, A. *Journal of Physical Chemistry B* **2020**, *124*, 1285–1292, DOI: 10.1021/acs.jpcb.9b09553.

(71) Zhang, P.; Wang, Z.-G. *Macromolecules* **2022**, *55*, 3910–3923, DOI: 10.1021/ACS.MACROMOL.2C00340.

(72) Chen, S.; Zhang, P.; Wang, Z.-G. *Macromolecules* **2022**, *55*, 3898–3909, DOI: 10.1021/ACS.MACROMOL.2C00339.

(73) Cahn, J. W. *The Journal of Chemical Physics* **1977**, *66*, 3667–3672, DOI: 10.1063/1.434402.

(74) Wu, J. *AIChE Journal* **2006**, *52*, 1169–1193, DOI: 10.1002/aic.10713.

(75) Nakanishi, H.; Fisher, M. E. *Physical Review Letters* **1982**, *49*, 1565–1568, DOI: 10.1103/PhysRevLett.49.1565.

(76) Pandit, R.; Schick, M.; Wortis, M. *Physical Review B* **1982**, *26*, 5112–5140, DOI: 10.1103/PhysRevB.26.5112.

(77) Neitzel, A. E.; Fang, Y. N.; Yu, B., et al. *Macromolecules* **2021**, *54*, 6878–6890, DOI: 10.1021/acs.macromol.1c00703.

(78) Monteillet, H.; Kleijn, J. M.; Sprakel, J.; Leermakers, F. A. *Advances in Colloid and Interface Science* **2017**, *239*, 17–30, DOI: 10.1016/j.cis.2016.07.001.

(79) Bonn, D.; Ross, D. *Reports on Progress in Physics* **2001**, *64*, 1085–1163, DOI: 10.1088/0034-4885/64/9/202.

(80) Yatsyshin, P.; Durán-Olivencia, M. A.; Kalliadasis, S. *Journal of Physics Condensed Matter* **2018**, *30*, 274003, DOI: 10.1088/1361-648X/aac6fa.

(81) Nakanishi, H.; Pincus, P. *The Journal of Chemical Physics* **1983**, *79*, 997–1003, DOI: 10.1063/1.445880.

(82) Teletzke, G. F.; Scriven, L. E.; Davis, H. T. *The Journal of Chemical Physics* **1983**, *78*, 1431–1439, DOI: 10.1063/1.444885.

(83) Andelman, D.; Joanny, J. F. *Comptes Rendus de l'Academie des Sciences - Series IV: Physics, Astrophysics* **2000**, *1*, 1153–1162, DOI: 10.1016/S1296-2147(00)01130-6.

(84) Dobrynin, A. V.; Deshkovski, A.; Rubinstein, M. *Macromolecules* **2001**, *34*, 3421–3436, DOI: 10.1021/ma0013713.

(85) Xie, F.; Nylander, T.; Piculell, L., et al. *Langmuir* **2013**, *29*, 12421–12431, DOI: 10.1021/la4020702.

(86) Quilliet, C.; Berge, B. *Current Opinion in Colloid and Interface Science* **2001**, *6*, 34–39, DOI: 10.1016/S1359-0294(00)00085-6.

(87) Guangze, H.; Jianjia, M. *Continuum Mechanics and Thermodynamics* **2018**, *30*, 817–823, DOI: 10.1007/s00161-018-0644-8.

(88) Vis, M.; Peters, V. F.; Blokhuis, E. M., et al. *Macromolecules* **2015**, *48*, 7335–7345, DOI: 10.1021/acs.macromol.5b01675.

(89) Zhao, X.; Bartolucci, G.; Honigmann, A.; Jülicher, F.; Weber, C. A. *New Journal of Physics* **2021**, *23*, 123003, DOI: 10.1088/1367-2630/ac320b.

(90) Lippmann, G. *Annales de Chimie et de Physique* **1875**, *5*, 494–549.

(91) Teletzke, G. F.; Scriven, L. E.; Davis, H. T. *The Journal of Chemical Physics* **1982**, *77*, 5794–5798, DOI: 10.1063/1.443736.

(92) Jones, R. A. *Polymer* **1994**, *35*, 2160–2166, DOI: 10.1016/0032-3861(94)90244-5.

(93) Genzer, J.; Composto, R. J. *Journal of Chemical Physics* **1997**, *106*, 1257–1263, DOI: 10.1063/1.473222.

(94) Pereira, G. G. *Journal of Chemical Physics* **1997**, *106*, 4282–4290, DOI: 10.1063/1.473130.

(95) Gözen, İ. *Life* **2021**, *11*, 795, DOI: 10.3390/life11080795.

(96) Agudo-Canalejo, J.; Schultz, S. W.; Chino, H., et al. *Nature* **2021**, *591*, 142–146, DOI: 10.1038/s41586-020-2992-3.

(97) Kusumaatmaja, H.; May, A. I.; Knorr, R. L. *Journal of Cell Biology* **2021**, *220*, e202103175, DOI: 10.1083/jcb.202103175.

(98) Gucht, J. v. d.; Spruijt, E.; Lemmers, M.; Cohen Stuart, M. A. *Journal of Colloid and Interface Science* **2011**, *361*, 407–422, DOI: 10.1016/j.jcis.2011.05.080.

(99) Iwamatsu, M. *Journal of Colloid and Interface Science* **1998**, *199*, 177–186, DOI: 10.1006/jcis.1997.5321.

(100) Oleksy, A.; Hansen, J. P. *Molecular Physics* **2009**, *107*, 2609–2624, DOI: 10.1080/00268970903469022.

(101) De Vos, W. M.; Lindhoud, S. *Advances in Colloid and Interface Science* **2019**, *274*, 102040, DOI: 10.1016/j.cis.2019.102040.

(102) Jiang, J. *Macromolecules* **2021**, *54*, 1801–1810, DOI: 10.1021/acs.macromol.0c02472.

(103) Keller, H. B., *Numerical solution of bifurcation and nonlinear eigenvalue problems*; Academic Press: New York, 1977.

(104) Salinger, A. G.; Burroughs, E. A.; Pawlowski, R. P.; Phipps, E. T.; Romero, L. A. *International Journal of Bifurcation and Chaos in Applied Sciences and Engineering* **2005**, *15*, 1015–1032, DOI: 10.1142/S0218127405012508.

(105) Nold, A.; Malijevský, A.; Kalliadasis, S. *Physical Review E - Statistical, Nonlinear, and Soft Matter Physics* **2011**, *84*, 21603, DOI: 10.1103/PhysRevE.84.021603.

(106) Yatsyshin, P.; Savva, N.; Kalliadasis, S. *Journal of Chemical Physics* **2012**, *136*, 124113, DOI: 10.1063/1.3697471.

(107) Yatsyshin, P.; Savva, N.; Kalliadasis, S. *Journal of Chemical Physics* **2015**, *142*, 34708, DOI: 10.1063/1.4905605.

(108) Lin, E. Y.; Frischknecht, A. L.; Winey, K. I.; Riggleman, R. A. *Journal of Chemical Physics* **2021**, *155*, 034701, DOI: 10.1063/5.0052121.

(109) Chan, T. F. *SIAM Journal on Scientific and Statistical Computing* **1984**, *5*, 135–148, DOI: 10.1137/0905010.

(110) Callen, H. B., *Thermodynamics and an Introduction to Thermostatistics*; John Wiley & Sons, Inc.: 1985.

(111) Chen, S.; Wang, Z.-G. *Proceedings of the National Academy of Sciences* **2022**, *119*, e2209975119, DOI: 10.1073/pnas.2209975119.

(112) Yang, G.; Chai, D.; Fan, Z.; Li, X. *Industrial and Engineering Chemistry Research* **2019**, *58*, 19302–19315, DOI: 10.1021/acs.iecr.9b04116.

Chapter V

POLYELECTROLYTE BRUSHES

Polyelectrolyte brushes are fascinating materials that exhibit a rich set of interfacial phenomena. The localization of a high density of charge density at the surface leads to strong stretching of chains away from the surface. Because the polyelectrolytes are fixed to the surface, one can modulate the brush conformations and utilize the surface layer to functionalize surfaces and control surface properties. In this chapter, two different polyelectrolyte brush systems are considered. The first are strong polyelectrolyte brushes that undergo complexation. Such complexation can be used in multi-layer assembly, to enable nanoparticle assembly, and to modify a surface. The brush conformation and other interfacial properties dramatically change upon complexation, which we describe using a simple inhomogeneous thermodynamic theory. As done in the previous chapter, we make connection between surface phase transitions (brush conformation transition) and complexation in a bulk polyelectrolyte solution. The second brush system is that of weak polyelectrolytes. The charge state of weak polyelectrolytes can be modulated by changing solution properties or as we explore, by changing the the electrostatic properties of the surface. We explore the effect of the surface electrostatic potential on the brush height and connect the swelling of the brush to the capacitive performance of the weak polyelectrolyte brush.

I am thankful to Dr. Alejandro Gallegos for many productive discussions on weak polyelectrolyte brushes. His insights helped refine many of the ideas presented in this chapter.

V.1 Complexation in Polyelectrolyte Brushes

Introduction

Polyelectrolyte complexation has long been used as a means to efficiently and robustly self assemble polyelectrolytes [1]. The relative ease and safety of polyelectrolyte multi-layers has particularly led to use in drug delivery [2–4] and other areas where encapsulation is important [5–10]. Complexation-driven self assembly also enables nontrivial morphologies in multicomponent systems, such as in micellar interpolyelectrolyte complexes [11], and so-called *zipper* brushes, where complexation reliably attaches a surface modifier (usually neutral) to surface grafted with polyelectrolyte. More recently, nanoparticles grafted with stimuli responsive polyelectrolytes have gained attention due to ability to control dispersion state and morphology of nanoparticle formulations [12]. All of these applications rely on the thermodynamics of polyelectrolyte complexation, and can be tuned by varying parameters like the electric field [13] or other environmental variables, such as the pH or salt concentration.

Many theoretical descriptions exist for bulk polyelectrolyte complexation, several of which are reviewed by Sing and Perry [14]. Even still, the theoretical description of surface-mediated complexation lags behind. Castelnovo and Joanny developed scaling laws and proposed the mechanism of complexation for the formation of polyelectrolyte multi-layers [15]. Molecular dynamics simulations by Patel *et al.* gave a molecular picture of polyelectroylte multi-layers that highlights the importance of the electrostatic assembly confirms a high degree of penetration upon deposition of each layer [16]. Cao *et al.* showed rich conformational and adsorption properties in the complexation of polyelectrolyte brushes with charged surfactants using Brownian dynamics simulations [17]. Simulations by Sethuraman have looked at the effect of charge sequence and polymer dispersity on the structure of zipper brushes [18, 19]. There is general agreement that complexation plays an essential role in all of studies listed above; however, the connection to bulk phase separation of polyelectrolyte complexes is limited. In our own recent work, we explored the connection between polyelectrolyte complexes wetting solid surfaces and the bulk phase behavior [20]. Recently, Debais and Tagliazucchi demonstrated a unified theory for the description of polyelectrolyte coacervation and layer-by-layber deposition, which generally agreed with experiments [21]. In their work, they dub the complexation in both cases to be “two sides of the same coin.“ In this work, we revisit the thermodynamics of polyelectrolyte complexation near a solid surface by considering complexation in a polyelectrolyte brush.

Theory

We will consider the simplest case of a polycation brush in contact with a polyelectrolyte solution made up of salt and polyanion. For simplicity, we will consider the monomers, salt, and solvent to all have the same effective size (σ). For the monomers, we further state that σ is equal to the Kuhn length b. Thus, all species have the same volume scale $\sigma^3 = b^3 = v$. For the polyelectrolytes, we will consider *fully charged* chains, where each monomer carries a charge of +1 or -1. For generality, we will consider the bulk system to have polycation, polyanion, salt, and solvent. Later, we can specify the bulk concentration of the grafted component to be zero. Much of the theory follows that of Ref. 20.

$$f = f_{id} + f_{ev} + f_{DH} + f_{ch} \tag{V.1}$$

The ideal part is

$$\beta f_{id} v = \sum_{p=p_+,p_-} \frac{\phi_p}{N}\left[\ln\left(\frac{\phi_p}{N}\right) - 1\right] + \sum_{\alpha=+,-} \phi_\alpha\left[\ln\left(\phi_\alpha\right) - 1\right] \tag{V.2}$$

For excluded volume,

$$\beta f_{ev} v = (1 - \sum_i \phi_i)\left[\ln\left(1 - \sum_i \phi_i\right) - 1\right] \tag{V.3}$$

The electrostatic correlation is

$$\beta f_{DH} v = -\frac{1}{4\pi}\left[\ln(1+\kappa\sigma) - \kappa\sigma + \frac{1}{2}\kappa^2\sigma^2\right] \tag{V.4}$$

The contribution from association/chain connectivity

$$\beta f_{ch} v = -\sum_{p=p_+,p_-} \frac{1-N_p}{N_p}\frac{z_p^2 \phi_p l_B/\sigma_p}{1+\kappa\sigma_p} \tag{V.5}$$

For the inhomogeneous theory, we'll use a local approximation using the bulk free energy [20, 22]. The free energy will be formulated using the density functional approach

$$F = F_{id} + F_{ex} \tag{V.6}$$

$$\beta F_{\mathrm{id}} = \sum_{p=p_+,p_-} \int d\mathbf{R}\rho_p(\mathbf{R})\left[\ln(\rho_p(\mathbf{R})v^N) - 1\right] + \sum_{p=p_+,p_-} \int d\mathbf{R}\rho_p(\mathbf{R})\beta V_b(\mathbf{R}) + \sum_\alpha \int d\mathbf{r}\rho_\alpha(\mathbf{r})\left[\ln(\rho_\alpha(\mathbf{r})v) - 1\right] \tag{V.7}$$

where $V_b(\mathbf{R})$ is the bonding potential, which we'll later assign to be Gaussian. The excess free energy is made up of all other parts of the bulk free energy with additional terms corresponding to the charge separation (electrostatic potential). In the grand canonical ensemble, the Euler-Lagrange equations become the following

$$\rho_p(\mathbf{R})v^N = \exp\left\{\beta\Big[\mu_p - V_b(\mathbf{R}) - \sum_{m=1}^{N}\Lambda_p(\mathbf{r_m})\Big]\right\} \tag{V.8}$$

$$\rho_\alpha(\mathbf{r})v = \exp\left\{\beta\left[\mu_\alpha - \Lambda_\alpha(\mathbf{r})\right]\right\} \tag{V.9}$$

$$\epsilon_r\epsilon_0\nabla^2\phi(\mathbf{r}) = \sum_i z_i e\rho_i(\mathbf{r}) \tag{V.10}$$

where Λ_p and Λ_α are effective fields for monomers and small ions, respectively:

$$\Lambda_p(\mathbf{r}) = \frac{\partial f_{\text{ex}}}{\partial\rho_p(\mathbf{r})} + z_p e\phi(\mathbf{r}) \tag{V.11}$$

$$\Lambda_\alpha(\mathbf{r}) = \frac{\partial f_{\text{ex}}}{\partial\rho_\alpha(\mathbf{r})} + z_\alpha e\phi(\mathbf{r}) \tag{V.12}$$

The polymer density is related to the monomer density as

$$\rho_p(\mathbf{r}) = \sum_{m=1}^{N}\int d\mathbf{R}\delta(\mathbf{r}-\mathbf{r}_m)\rho_p(\mathbf{R}) \tag{V.13}$$

The monomer density is then

$$\rho_p(\mathbf{r})v = \exp[\beta\mu_p]\sum_{m=1}^{N}\exp[\beta\Lambda_p(\mathbf{r})]q(\mathbf{r},m)q_c(\mathbf{r},m) \tag{V.14}$$

where $q(\mathbf{r})$ and $q_c(\mathbf{r})$ are chain propagators.

The normalized bond transition probability between two monomers is $\Phi(|\mathbf{r}-\mathbf{r}'|)$. When we have spatial variation in only one direction, we consider the case of grafted and non-grafted polymer chains.

Chain Propagators

When the chains are not grafted, the forward propagator is $q(z,m)$ is symmetric to the complimentary propagator $q_c(z,m)$ since we have a linear homopolymer.

$$q(z,1) = e^{-\beta\Lambda_p(z)} \tag{V.15}$$

$$q(z,i+1) = e^{-\beta\Lambda_p(z)}\int dz'\Phi(z-z')q(z',i) \tag{V.16}$$

$$q_c(z,N) = e^{-\beta\Lambda_p(z)} \tag{V.17}$$

$$q_c(z,i-1) = e^{-\beta\Lambda_p(z)} \int dz' \Phi(z-z') q_c(z',i) \tag{V.18}$$

Only the forward propagator is changed to fix the first bead on the surface $q(z,m)$

$$q(z,1) = e^{-\beta\Lambda_p(z)} \delta(z/b) \tag{V.19}$$

$$q(z,i+1) = e^{-\beta\Lambda_p(z)} \int dz' \Phi(z-z') q(z',i) \tag{V.20}$$

The density of the first bead then becomes

$$\begin{aligned} \rho_p^1(z)v &= \exp[\beta\mu_p] \exp[\beta\Lambda_p(z)] q(z,1) q_c(z,1) \\ &= \exp[\beta\mu_p] q_c(z,1) \delta(z/b) \end{aligned} \tag{V.21}$$

Integrating gives

$$\int dz \rho_p^1(z) v = \sigma_g b^2 = \exp[\beta\mu_p] q_c(z=0,1) \tag{V.22}$$

which determines the chemical potential of the polymer chain.

For a single surface with one-dimensional density variation, the free energy per unit area is

$$\begin{aligned} F =& \frac{1}{\beta} \sum_p \int d\mathbf{R} \rho_p(\mathbf{R}) \Big[\ln(\rho_p(\mathbf{R}) v^N) - 1 \Big] + \frac{1}{\beta} \sum_p \int d\mathbf{R} \rho_p(\mathbf{R}) \beta V_b(\mathbf{R}) \\ &+ \frac{1}{\beta} \sum_\alpha \int d\mathbf{r} \rho_\alpha(\mathbf{r}) \Big[\ln(\rho_\alpha(\mathbf{r}) v) - 1 \Big] \\ &+ \int d\mathbf{r} \Big[f_b^{ex}(\mathbf{r}, \{\phi(\mathbf{r})\}) + e\rho_c(\mathbf{r}) \psi(\mathbf{r}) - \frac{\epsilon_r \epsilon_0}{2} (\nabla\psi)^2 \Big] \end{aligned} \tag{V.23}$$

where $\rho_c(\mathbf{r}) = \rho_{ex} + \sum_i z_i \rho_i(\mathbf{r})$. Using Eq. V.8,

$$\begin{aligned} F =& \frac{1}{\beta} \sum_p \int d\mathbf{R} \rho_p(\mathbf{R}) \Big[\beta\mu_p - \sum_{m=1}^{N} \beta\Lambda_p(\mathbf{r_m}) - 1 \Big] \\ &+ \frac{1}{\beta} \sum_\alpha \int d\mathbf{r} \rho_\alpha(\mathbf{r}) \Big[\ln(\rho_\alpha(\mathbf{r}) v) - 1 \Big] \\ &+ \int d\mathbf{r} \Big[f_b^{ex}(\mathbf{r}, \{\phi(\mathbf{r})\}) + e\rho_c(\mathbf{r}) \psi(\mathbf{r}) - \frac{\epsilon_r \epsilon_0}{2} (\nabla\psi)^2 \Big] \end{aligned} \tag{V.24}$$

We can remove the multidimensional **R** integrals. To consistently treat the polymer and small ions, we also use Eq. V.9

$$\begin{aligned} F = &\frac{1}{\beta}\sum_p \int d\mathbf{r}\rho_p(\mathbf{r})\Big[\beta\mu_p/N - \beta\Lambda_p(\mathbf{r}) - 1/N\Big] \\ &+ \frac{1}{\beta}\sum_\alpha \int d\mathbf{r}\rho_\alpha(\mathbf{r})\Big[\beta\mu_\alpha - \beta\Lambda_\alpha(\mathbf{r}) - 1\Big] \\ &+ \int d\mathbf{r}\Big[f_b^{ex}(\mathbf{r},\{\phi(\mathbf{r})\}) + e\rho_c(\mathbf{r})\psi(\mathbf{r}) - \frac{\epsilon_r\epsilon_0}{2}(\nabla\psi)^2\Big] \end{aligned} \tag{V.25}$$

Using the definitions of $\Lambda_i(\mathbf{r})$, the grand potential energy is

$$\begin{aligned} W &= F - \sum_i \mu_i \mathcal{N}_i \\ &= \int d\mathbf{r}\Big[f_b^{ex}(\mathbf{r},\{\phi(\mathbf{r})\}) - \sum_p \frac{\partial f_b^{ex}}{\partial\rho_p(\mathbf{r})}\rho_p(\mathbf{r}) - \sum_\alpha \frac{\partial f_b^{ex}}{\partial\rho_\alpha(\mathbf{r})}\rho_\alpha(\mathbf{r}) \\ &+ e\rho_{ex}\psi(\mathbf{r}) - \frac{\epsilon_r\epsilon_0}{2}(\nabla\psi)^2 - \frac{1}{\beta}\sum_p \rho_p(\mathbf{r})/N - \frac{1}{\beta}\sum_\alpha \rho_\alpha(\mathbf{r})\Big] \end{aligned} \tag{V.26}$$

If we only consider density variation in one direction (z-direction),

$$\begin{aligned} W = A\int dz\Big[&f_b^{ex}(z,\{\phi(z)\}) - \sum_p \frac{\partial f_b^{ex}}{\partial\rho_p(z)}\rho_p(z) - \sum_\alpha \frac{\partial f_b^{ex}}{\partial\rho_\alpha(z)}\rho_\alpha(z) \\ &+e\rho_{ex}\psi(z) - \frac{\epsilon_r\epsilon_0}{2}\left(\frac{\partial\psi}{\partial z}\right)^2 - \frac{1}{\beta}\rho_p(z)/N - \frac{1}{\beta}\sum_\alpha \rho_\alpha(z)\Big] \end{aligned} \tag{V.27}$$

Assuming the external charge is from a single surface $\rho_{ex} = Q_s\delta(z)/A$, we can write

$$\begin{aligned} W = A\int dz\Big[&f_b^{ex}(z,\{\phi(z)\}) - \sum_p \frac{\partial f_b^{ex}}{\partial\rho_p(z)}\rho_p(z) - \sum_\alpha \frac{\partial f_b^{ex}}{\partial\rho_\alpha(z)}\rho_\alpha(z) \\ &-\frac{\epsilon_r\epsilon_0}{2}\left(\frac{\partial\psi}{\partial z}\right)^2 - \frac{1}{\beta}\rho_p(z)/N - \frac{1}{\beta}\sum_\alpha \rho_\alpha(z)\Big] + eQ_s\psi_0 \end{aligned} \tag{V.28}$$

If the system volume is sufficiently large (rigorously infinite), the osmotic pressure P can be determined from the bulk solution. From Bruch, Balzer, and Wang, then we have

$$\gamma A = W + PV - eQ_s\psi_0 \tag{V.29}$$

Calculating Thermodynamic Quantities

Consider the brush system confined between two surfaces. For a fixed grafting density, the chemical potential of the brushes will change with the separation L.

The appropriate ensemble to calculate the pressure from is a semi-grand potential. Namely, from the grand potential for fixed surface potential Y,

$$P = -\left(\frac{\partial Y}{\partial V}\right)_{T,\{\mu_i\},\psi_0,\psi_L} \tag{V.30}$$

The correct ensemble is the Legendre transform of the above expression

$$P = -\left(\frac{\partial X}{\partial V}\right)_{T,\{\mu_i\}_{i\neq g},\{\sigma_g\},\psi_0,\psi_L} \tag{V.31}$$

where $X = Y + \sum_g \mu_g \sigma_g A$.

Results and Discussion

To reduce the parameter space, all of the results will focus on the simplified case of a strong polycation brush in contact with a monovalent salt solution. We will study the effect of titrating the brush with free polyanion chains. Both the brush and free polyion chains have length $N = 50$, and the Bjerrum length is $l_B = 1.785b$, which corresponds to the dielectric constant of water at room temperature when $b = 0.4$ nm.

Brush Structure and Salt Response

With no free polyanion, a polycation brush grafted to a charge neutral surface will extend to minimize the ion repulsion within the brush. Counterions from the salt solution enter the brush region to neutralize the charge of the brush. Figure V.1 shows the brush profiles for various grafting densities. With increasing grafting density, more salt ions are required to compensate the brush charge, leading to a increasing osmotic pressure in the brush region [23] and thus, brush extension. Figure V.2 shows the plot of $\phi_-(z) - \phi_+(z)$, which is an indication of the charge compensation from small ions. In the bulk, this quantity goes to zero and values greater than zero indicate accumulation of anions.

The brush response to the bulk salt concentration also indicates the scaling regime of the brush [24]. For low salt concentrations, the brush only feels the influence of the counterions that compensate the charge in the brush so the a strong polyelectroylte brush is insensitive to changes in the bulk salt concentration. This regime is the osmotic brush regime. For higher bulk salt concentration, the increasing the bulk salt concentration reduces the osmotic pressure difference between the bulk solution and the brush region, leading to contraction of the brush. This is the salted-brush

regime. The results from the grafting density in Figure V.1 indicate this system is in the salted brush regime for 1 M. Figure V.3 shows the brush height is relatively insensitive to salt until 10 mM, when adding salt begins to contract the brush.

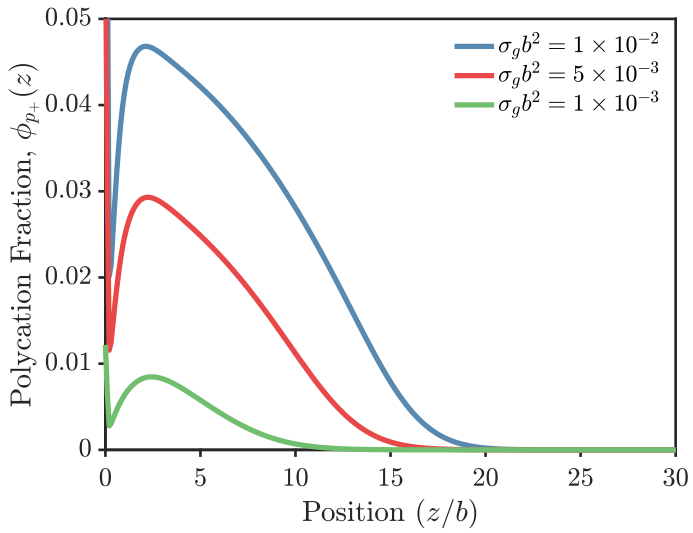

Figure V.1: Density profile for polycation brush grafted to a neutral surface. Bulk salt solution has bulk density $\phi_{\pm} = 0.04$, corresponding to approximately 1 M for $b = 0.4$ nm.

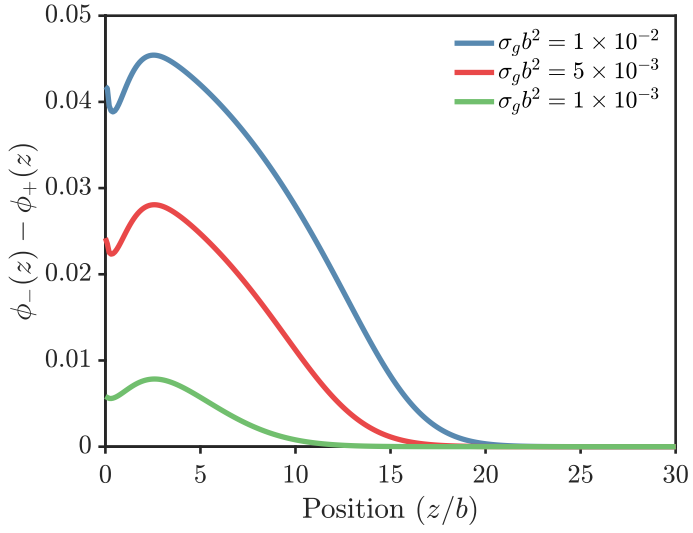

Figure V.2: Charge compensation for brush from small ions corresponding to the system in Figure V.1.

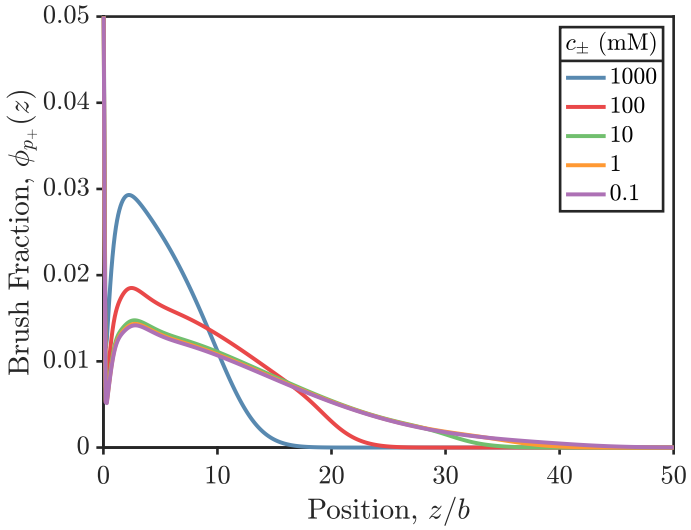

Figure V.3: Density profile for polycation brush grafted to a neutral surface for various bulk salt concentrations. $N = 50$ and $\sigma_g b^2 = 5 \times 10^{-3}$.

Swollen-Collapsed Transition

When adding free polyanion, we expect that anions compensating the brush charge will be replaced by polyanion. A single polyanion chain has more efficacy for compensating the brush charge, and contributes less to the osmotic pressure than a small ion (per charge). Figure V.4 shows the brush and free polyion profiles before and after adding free polyanion. There are two main features of the figure. The first is that, indeed, the brush contracts when adding free polyanion. The second is that the free polyanion profile nearly overlaps with the brush profile. In fact, for the condition shown, there appears to be more free polyanion in the brush region than the brush. This result indicates the strong degree of penetration of the free polyanion.

The displacement of small anions with polyanion in the brush region leads to several interesting phenomena. The small anions are dispelled from the brush and when the free polyanion exceeds the density of polycation brush, small cations are migrate into the brush region (Figure V.5). This behavior is akin to a charge reversal for the brush region. Here, a charge reversal corresponds to a change in sign of the electrostatic potential, since the surface charge density is fixed to be neutral. For no free polyanion, the electrostatic potential in the brush is positive. Adding enough free polyanion eventually leads to a change in sign, which is not shown but is indicated from the small ion profiles in Figure V.5.

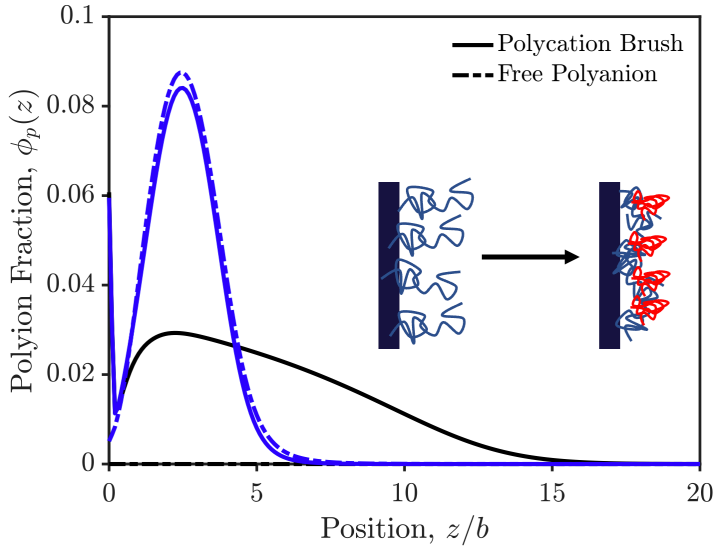

Figure V.4: Density profile for polycation brush grafted to a neutral surface for no free polyanion (black) and $\phi_{p_-} = 1 \times 10^{-5}$ (blue). The grafting density is $\sigma_g b^2 = 5 \times 10^{-3}$ and the bulk salt concentration is $\phi_\pm = 0.04$.

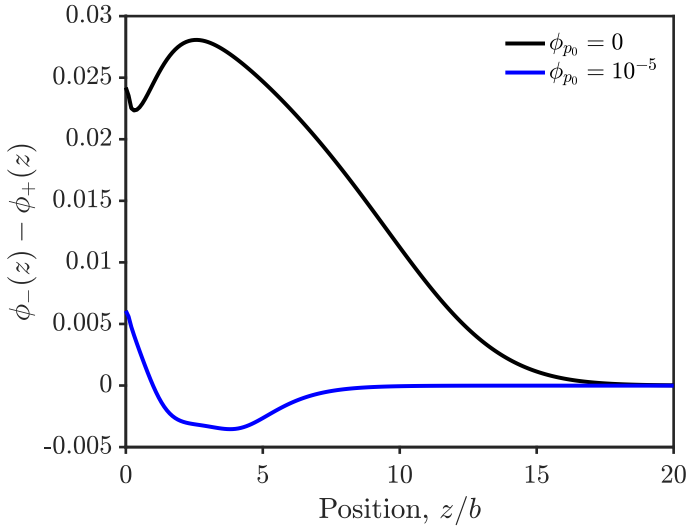

Figure V.5: Charge compensation for brush from small ions for no free polyanion (black) and $\phi_{p_-} = 1 \times 10^{-5}$ (blue). Conditions are the same as Figure V.4.

Now, we shift our focus to the thermodynamics of the swollen-collapsed transition that results from adding free polyanion. To do so, we develop a measure of the complexation of the free polyanion and the polycation brush to be the ratio of the excess number of chains of polyanion to the number of chains of polycation. The excess number of chains of polyanion can be calculated from the excess adsorption.

$$\frac{n_{p_-}^{ex}}{n_{p_+}} = \frac{\int_0^\infty \left(\phi_{p_-}(z) - \phi_{p_-^{bulk}}\right) dz}{N\sigma_g b^2} \tag{V.32}$$

When there is no free polyanion in the brush, this ratio is zero. The excess polyanion chains may exceed the number of polycation chains so the ratio may exceed unity. Figure V.6 shows how the ratio and brush height change upon adding free polyanion. The change in the brush height and the excess polyanion are both continuous and coupled. For the conditions given, there is no effect on the brush until the bulk polyanion exceeds 10^{-12} at which point the complexation rapidly increases and the brush collapses to half of the swollen height.

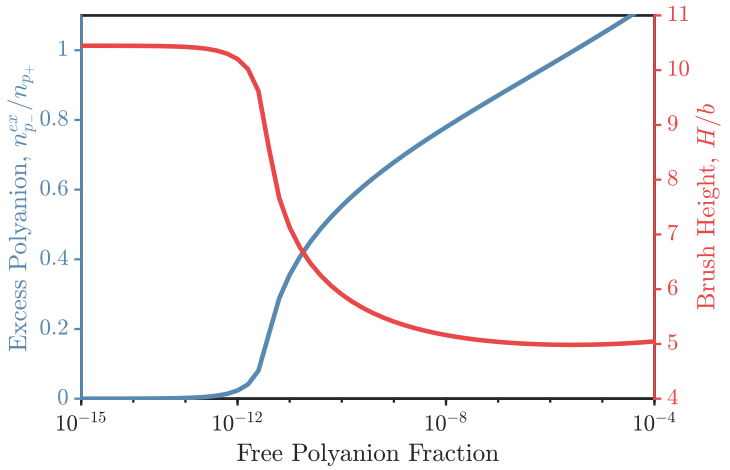

Figure V.6: Ratio of excess polyanion chains (left axis) and the brush height (right axis) as a function of the amount of added bulk free polyanion. The grafting density is 5×10^{-3} and the bulk salt fraction is $\phi_\pm = 0.04$.

The smooth transition from swollen to collapsed in Figure V.6 does not tell the full story. The conformational transition has two distinct surface phases that are driven by the complexation. Figure V.7 shows the excess polyanion chains and the electrostatic potential at the surface for three different grafting densities. For $\sigma_g b^2 = 10^{-2}$, there is a high degree of complexation even at the lowest polyanion fraction, whereas for $\sigma_g b^2 = 10^{-3}$, the complexation measure only increases toward

the highest values of the amount of free polyanion added. Between those two curves, the curve $\sigma_g b^2 = 5 \times 10^{-3}$ shows a typical continuous transition between no polyion penetration into the brush and what is considered full complexation. What is striking in the plot of the surface potential (right-hand plot) is that there are two apparent regimes of the surface electrostatic potential, corresponding to the either the swollen or collapsed states of the brush.

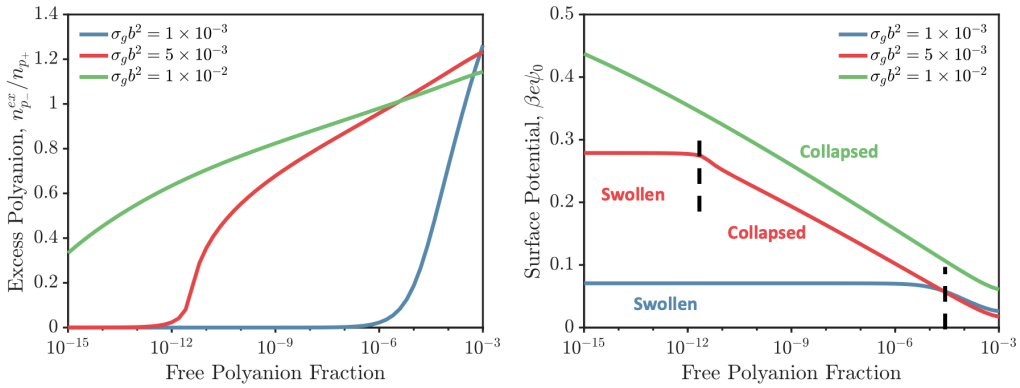

Figure V.7: Ratio of excess polyanion chains (left) and the electrostatic potential at the surface (right) as a function of the amount of added bulk free polyanion for different grafting densities. The bulk salt fraction is $\phi_\pm = 0.04$.

In fact, if one goes searching, there are regions where the transition between swollen and collapsed is first order. The conditions where this transition should occur are that of low salt concentration, where the driving force for complexation is highest, and low grafting density, where small changes in the complexation can drive rapid contraction of the brush. In that regime, Figure V.8 shows coexistence between the two conformational states. A first order transition indicates that there will hysteresis in the brush height upon addition and removal of free polyanion. First order transitions have been seen in finite-length chains in poor solvent conditions [25]; however, from mean field theory, only continuous transitions are expected in this system for finite-length chains. The electrostatic correlation embedded in the theory gives rise to the first-order transition.

All of the results shown so far are for a neutral surface. Practically, one may be interested in tuning the amount of complexation, or at least understanding how various surface properties influence the complexation [13] One such example is the surface electrostatic potential. Intuitively, for a polycation brush, a positive electrostatic potential should encourage negative charge to accumulate in the brush, compared to zero surface potential. Figure V.9 shows the effect of the surface

potential on the swollen-collapsed transition. Changes in much less than 1 V can dramatically shift the transition point for complexation. Further, the behavior of the brush height at fixed potential is nontrivial. For instance, comparing the plots for ψ_0=0, 25, and 50 mV, there is a nonmonotonic dependence on the surface potential, owing to the different degrees of complexation. For applications where the brush height is of central importance, such trends deserve further study.

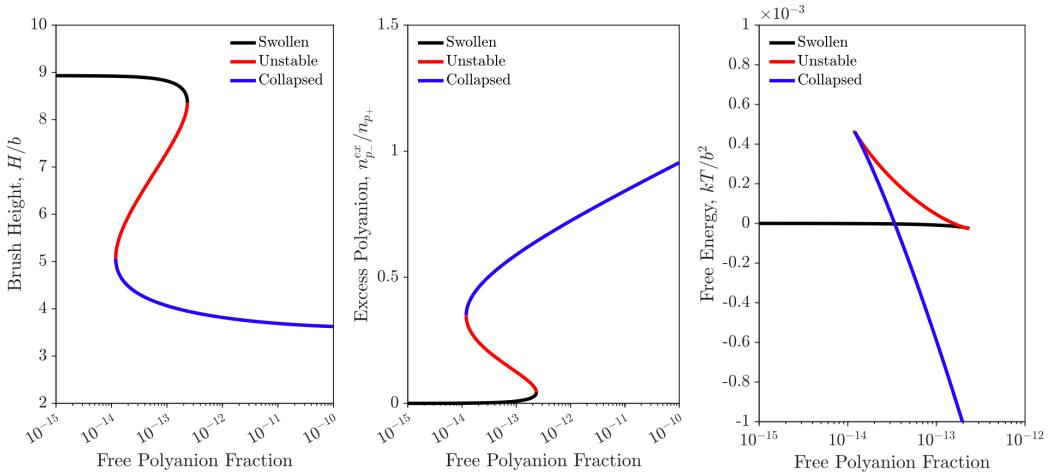

Figure V.8: Brush height (left), ratio of excess polyanion chains (middle) and the excess surface free energy (right) as a function of the amount of added bulk free polyanion. Colors and legend indicate the conformational state of the brush, which are determined from the free energy profile (right). The grafting density is 1×10^{-3} and the bulk salt fraction is $\phi_\pm = 0.01$.

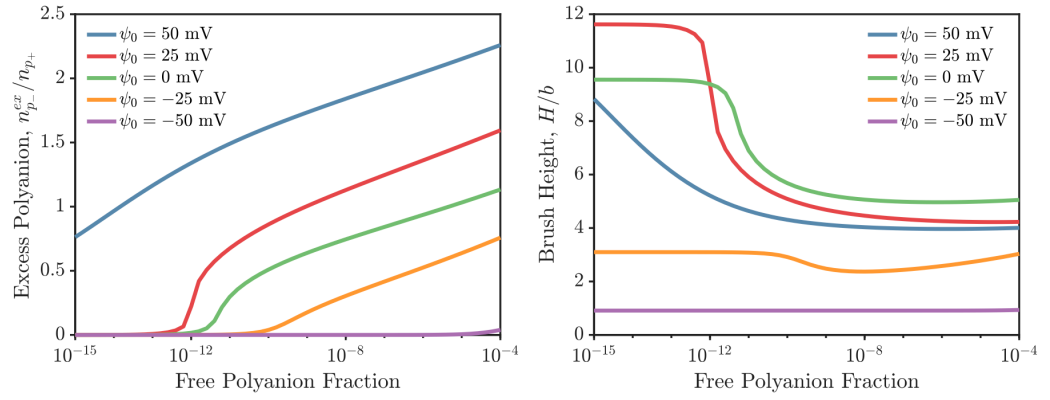

Figure V.9: Ratio of excess polyanion chains as a function of the amount of added bulk free polyanion for various surface potentials. The grafting density is 5×10^{-3} and the bulk salt fraction is $\phi_\pm = 0.04$.

Constructing Phase Diagrams

To what extent is the complexation in the brush similar to complexation in bulk phases? If the transition can be fully understood by the same driving force as that of complex coacervation of bulk phases, then all of the rules-of-thumb and physics for those systems can be applied to the brush system. In experiments, phase diagrams for a variety of charge complexation problems are determined via salt-resistance measurements [26, 27]. A salt resistance measures the salt concentration at which there is no evidence of complexation, which is deemed the barrier a one- and two-phase region. From our theory, we can conduct the same measurements. However, as established above, the conformational transition is usually continuous, making the selection of a single point somewhat fuzzy. A reasonable and physically motivated choice is to pick the salt concentration at which the ratio of excess polyanion to grafted polycation chains is unity. Salt resistance curves are shown in Figure V.10, indicating the points where the ratio crosses unity for a grafting density of $\sigma_g b^2 = 5 \times 10^{-3}$ for fixed amounts of free polyanion in the bulk solution. The basic trend is that a higher amount of salt is required to suppress complexation as the amount of free polyanion increases.

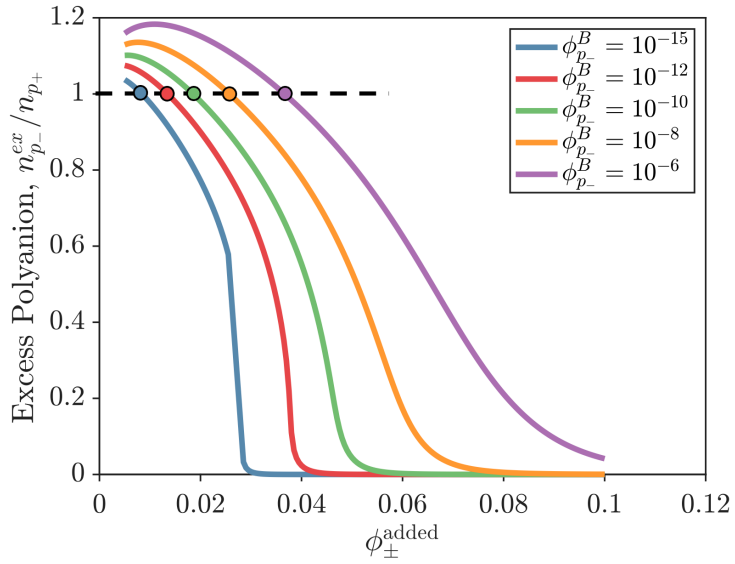

Figure V.10: Salt resistance curves for $\sigma_g b^2 = 5 \times 10^{-3}$ and a neutral surface. The dotted line and points indicate the chosen point where the system transitions.

The chosen transition point on the salt resistance curves was chosen strategically so that we may compare the location of the conformational transition with that of the bulk binodal. In particular, we extract a salt concentration for each value of the

free polyanion and can compare that with the supernatant phase of the bulk binodal. The premise is that the brush region forms a dense, coacervate-like surface phase so that the bulk solution serves the role of a coexisting supernatant phase. The bulk phase diagram for this system can be constructed using the procedures outlined in our previous work [20, 28, 29]. Figure V.11 shows the comparison between phase diagrams. Qualitatively, the conformational transitions follow the same general trend as the bulk phase behavior, which is surprising given (1) the inhomogeniety in the system (i.e. electrostatic potential) and (2) the inability of the brush to form a macroscopic *dense* phase.

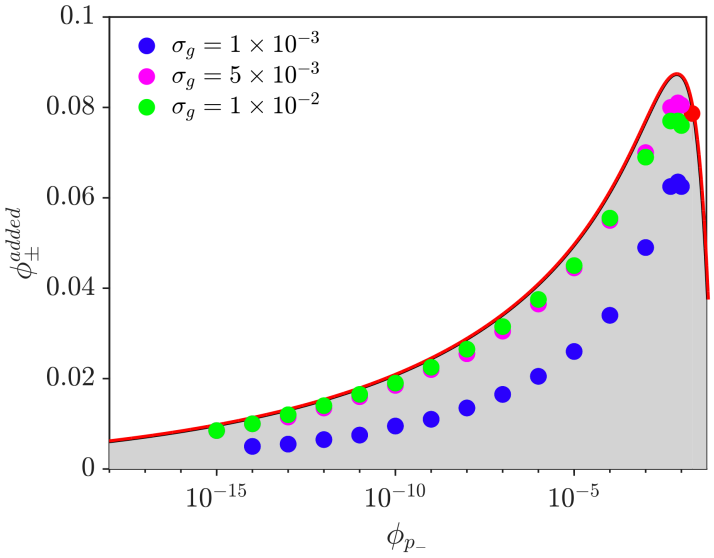

Figure V.11: Comparison of bulk binodal (red line) with conformational transition points extracted from salt resistance curves (points). Two phase region of binodal is shaded in gray. The bulk critical point is marked with a red point.

Conclusion

This work explored the structure and complexation in strong polycation brushes upon titrating with an oppositely charged polyion solution. Penetration of the free polyanion into the polycation brush drives a conformational transition in the brush. The transition is generally continuous but can be first order at low salt concentration, where the driving force for complexation is highest. Various factors influence the transition, including the electrostatic condition of the surface and the salt concentration of the bulk solution in contact with the brush. As seen in previous studies of complex coacervation near a solid surface [30], the electrostatic potential can dramatically shift the ability to complex near the surface.

Much remains unsolved regarding the driving force for complexation, and whether there is a more direct mapping to bulk phase separation. In the brush system, the driving force for polyion penetration into the brush is the release of counterions confined to the brush region. While this hypothesis has been widely proposed for the bulk system [14], the bulk phase behavior is driven by the solvent entropy and electrostatic correlation [28, 31]. Our work will hopefully motivate future studies of the phase behavior near solid surfaces to elucidate this connection further.

Appendix

Nondimensionalizing

The nondimensional form of the free energy is more general and easier to work with numerically. Starting from Eq. V.28. we can start to nondimensionalize the free energy by multiplying by β and using $x = z/b$,

$$\beta W/Ab = \int_0^\infty dx \Big[\beta f_b^{ex}(x,\{\phi(x)\}) - \sum_p \frac{\partial \beta f_b^{ex}}{\partial \rho_p(x)}\rho_p(x) - \sum_\alpha \frac{\partial f_b^{ex}}{\partial \rho_\alpha(x)}\rho_\alpha(x) - \frac{\beta\epsilon_r\epsilon_0}{2b^2}\left(\frac{\partial \psi}{\partial x}\right)^2 - \sum_p \rho_p(x)/N - \sum_\alpha \rho_\alpha(x)\Big] + Q_s\beta e\psi_0/A/b \tag{V.33}$$

$$\beta W/Ab = \int_0^\infty dx \Big[\beta f_b^{ex}(x,\{\phi(x)\}) - \sum_p \frac{\partial \beta f_b^{ex}}{\partial \rho_p(x)}\rho_p(x) - \sum_\alpha \frac{\partial f_b^{ex}}{\partial \rho_\alpha(x)}\rho_\alpha(x) - \frac{\epsilon_r\epsilon_0}{2\beta e^2 b^2}\left(\frac{\partial \beta e\psi}{\partial x}\right)^2 - \sum_p \rho_p(x)/N - \sum_\alpha \rho_\alpha(x)\Big] + Q_s\beta e\psi_0/A/b \tag{V.34}$$

Using the usual definition of the Bjerrum length $l_B = \beta e^2/4\pi\epsilon_r\epsilon_0$ and multiplying the entire expression by $v = b^3$ gives

$$\beta W b^2/A = \int_0^\infty dx \Big[\beta f_b^{ex} v(x,\{\phi(x)\}) - \sum_p \frac{\partial \beta f_b^{ex} v}{\partial \phi_p(x)}\phi_p(x) - \sum_\alpha \frac{\partial f_b^{ex} v}{\partial \phi_\alpha(x)}\phi_\alpha(x) - \frac{1}{8\pi l_B/b}\left(\frac{\partial \beta e\psi}{\partial x}\right)^2 - \sum_p \phi_p(x)/N - \sum_\alpha \phi_\alpha(x)\Big] + Q_s b^2/A\beta e\psi_0 \tag{V.35}$$

V.2 Electroresponsive Weak Polyelectrolyte Brushes

Introduction

Grafting surfaces with polyelectrolytes is a promising route to functionalize surfaces for a wide variety of applications, including lubrication [32, 33], biosensing [34], anti-fouling [35–37], and assembly of nanoparticles [38, 39]. The conformation of a polyelectrolyte brush intimately depends on the charge state of the chains [23, 40]. The charge state of weak polyelectrolytes depends on the local solution conditions [41–45], chemical details of the polymer sequence [46–48], and external forces (e.g. electric fields, confinement, etc.) [49, 50]. In this way, surfaces grafted with weak polyelectrolytes are *smart* materials and the responsiveness to controllable variables enables surface properties to be readily tuned.

The electroresponsiveness of weak polyelectrolyte brushes is a particularly useful knob to turn since changing the electrostatic condition of a surface can be done rather easily in practice through a voltage change. The brush response to an electric field is coupled to all of the solution parameters and the conformations near the surface. Despite several theoretical studies on the electroresponsiveness of polyelectrolyte brushes [51–55], open questions remain about the electroresponsiveness of weak polyelectrolyte brushes [56]. Recently, Senechal *et al.* observed two phenomena without clear origin: (1) applying a negative (positive) electrostatic potential to a polyacid (polybase) leads to brush swelling, and (2) strong hysteresis in the brush height upon cycling the electrostatic potential. The first phenomena has been seen in other experimental studies [57, 58] and observed in the theoretical study by Okrugin *et al*., but has not been fully explained [54]. The second phenomena of hysteresis upon charging and discharging has been seen in other weak polyelectrolyte brush studies when varying the pH [59]. We expect the origin of the hysteresis to be similar in electroresponsive brushes. The open questions for each phenomena deserve an unambiguous mechanistic explanation in order to better design electroresponsive weak polyelectrolyte brushes.

In this work, we focus on the first question above: why does a polyacid brush swell when a negative potential is applied? To answer this question, we develop and apply a simple inhomogeneous thermodynamic theory to study the effect of the surface voltage on the swelling and de-swelling of a weak polyacid. The swelling of a polyacid upon applying a negative potential results from the free salt ions compensating the change in surface charge density. We extend the classical scaling of polyelectrolytes to rationalize this behavior. Finally, we explore implications of

this mechanism by studying the capacitance of the weak polyacid brush, where the brush swelling is coupled to peaks in the capacitance curves.

Theory

No Correlations

In Section III.2, we developed a mean-field theory for weak polyelectrolytes starting from the Hamiltonian. Up until making the saddle-point approximation, that theory is an exact statistical field representation of the underlying microscopic model. Namely, the theory exactly captures all of the correlations, including intrachain correlation. However, we only focused on the mean-field for weak polyelectrolyte adsorption. Here, we include correlations through a different route. We start with a density-explicit free energy in the spirit of classical density functional theory. To begin, we will derive the mean-field theory from III.2 using the DFT approach.

Consider a polyelectrolyte solution made up pH-responsive, linear polyelectrolytes, salt ions and water. Each monomer in the chain is a pH-responsive group whose charge state is determined by local acid-base equilibria. For simplicity, we consider each monomer to have only one dissociable proton (acid residue).

$$HM + H_2O \longleftrightarrow M^- + H_3O^+ \tag{V.36}$$

In the equations above, M is a generic acidic monomer. The reactions above are dictated by the acid-dissociation constant, K_a. Similarly, water can dissociated and at room temperature pure water has $\mathrm{pK_a} = 7$.

$$2H_2O \longleftrightarrow OH^- + H_3O^+ \tag{V.37}$$

We consider the salt ions, denoted + and − to be strong electrolytes with valency z_+, z_- with $z_- < 0$. In the following theory, we make several simplifications. We neglect the size of the bare proton and assume all of the other species have the same size, denoted b. This length scale also sets our volume scale for all species to be $v = b^3$.

From the acid-base relationships, the monomers and water can each take on distinct states - neutral, protonated, or deprotonated. For an acid, only two states are available. To model the protonation and deprotonation, we introduce protonation variables. For example, we use s_i^w to denote the state of a given water molecule i. s_i^w can take on values of -1, 0, or 1, corresponding to deprotonated, neutral, or protonated, respecitvely. Likewise, the monomer state of the j-th monomer on the

i-th chain can be tracked the same way using $s_{i,j}^M$. Such a model is similar to that of Nakamura and Wang [60] in the context of salt-doped block copolymers and more recently, in classical density functional theory by Gallegos, Ong, and Wu [61].

The mean-field free energy is

$$\begin{aligned}
\beta F = &\sum_{\alpha=+,-} \int d\mathbf{r}\, [\rho_\alpha(\mathbf{r}) \ln(\rho_\alpha(\mathbf{r}) v_\alpha) - \rho_\alpha(\mathbf{r})] \\
&+ \int d\mathbf{r} \sum_{s_w} [\rho_w(\mathbf{r}, s_w) \ln(\rho_w(\mathbf{r}, s_w) v_w) - \rho_w(\mathbf{r}, s_w)] \\
&+ \int d\mathbf{R} \sum_{\{s_M\}} \left[\rho_M(\mathbf{R}, \{s_M\}) \ln(\rho_M(\mathbf{R}, \{s_M\}) v_M^N) - \rho_M(\mathbf{R}, \{s_M\})\right] \\
&+ \int d\mathbf{R} \sum_{\{s_M\}} \rho_M(\mathbf{R}, \{s_M\}) \beta V_B(\mathbf{R}, \{s_M\}) \\
&+ \int d\mathbf{r} \sum_{s_w} \rho_w(\mathbf{r}, s_w) \left[\beta \epsilon_w (s_w)^2 - \beta \lambda s_w\right] \\
&+ \int d\mathbf{R} \sum_{\{s_M\}} \rho_M(\mathbf{R}, \{s_M\}) \sum_{i=1}^{N} \left[-\beta \epsilon_M - \beta \lambda\right] s_i^M \\
&+ \int d\mathbf{r} \Big[\rho_c(\mathbf{r}) \psi(\mathbf{r}) - \frac{1}{8\pi l_B} (\nabla \psi)^2\Big] \\
&+ \int d\mathbf{r} \beta \eta(\mathbf{r}) \Big(1 - \sum_{\alpha=+,-} v_\alpha \rho_\alpha(\mathbf{r}) - \sum_{s_w} v_w \rho_w(\mathbf{r}, s_w) - \sum_{i=1}^{N} \sum_{s_i^M} v_M \rho_i^M(\mathbf{r}, s_i^M)\Big)
\end{aligned} \tag{V.38}$$

where $\rho_c(\mathbf{r}) = z_+ \rho_+(\mathbf{r}) + z_- \rho_-(\mathbf{r}) + \sum_{s_w} \rho_w(\mathbf{r}, s_w) s_w + \sum_{i=1}^{N} \sum_{s_i^M} \rho_i^M(\mathbf{r}, s_i^M) s_i^M$. We will lump together the spatial degrees of freedom and the configurations into one variable $\mathbf{X}$.

$$\begin{aligned}
\beta F = &\sum_{\alpha=+,-} \int d\mathbf{r} \rho_\alpha(\mathbf{r}) \left[\ln(\rho_\alpha(\mathbf{r}) v_\alpha) - 1 + z_\alpha \psi(\mathbf{r}) - v_\alpha \beta \eta(\mathbf{r})\right] \\
&+ \int d\mathbf{x} \rho_w(\mathbf{x}) \left[\ln(\rho_w(\mathbf{x}) v_w) - 1 + \beta \epsilon_w (s_w)^2 - \beta \lambda s_w + \psi(\mathbf{r}) s_w - v_w \beta \eta(\mathbf{r})\right] \\
&+ \int d\mathbf{X} \rho_M(\mathbf{X}) \Big[\ln(\rho_M(\mathbf{X}) v_M^N) - 1 + \beta V_B(\mathbf{X}) + \sum_{i=1}^{N} \left[-\beta \epsilon_M - \beta \lambda + \psi(\mathbf{r}_i)\right] s_i^M - \sum_{i=1}^{N} \beta \eta(\mathbf{r}_i)\Big] \\
&+ \int d\mathbf{r} \left[\beta \eta(\mathbf{r}) - \frac{1}{8\pi l_B} \Big(\nabla \psi\Big)^2\right]
\end{aligned} \tag{V.39}$$

Note that $\rho_i^M(\mathbf{r}, s_i^M) = \int d\mathbf{X}' \rho_M(\mathbf{X}') \delta(\mathbf{r} - \mathbf{r}'_i) \delta_{s_i^M, s_i^{M'}}$. Taking the first variation of the grand potential energy Ω, we obtain the mean field equations for the densities

$$\begin{aligned} \frac{\delta\beta\Omega}{\delta\rho_\alpha(\mathbf{r})} &= \ln(\rho_\alpha(\mathbf{r})v_\alpha) + z_\alpha\psi(\mathbf{r}) - v_\alpha\beta\eta(\mathbf{r}) - \beta\mu_\alpha = 0 \\ \rho_\alpha(\mathbf{r})v_\alpha &= \exp\left[\beta\mu_\alpha - z_\alpha\psi(\mathbf{r}) + v_\alpha\beta\eta(\mathbf{r})\right] \end{aligned} \tag{V.40}$$

$$\begin{aligned} \frac{\delta\beta\Omega}{\delta\rho_w(\mathbf{x})} &= \ln(\rho_w(\mathbf{x})v_w) + \beta\epsilon_w(s_w)^2 - \beta\lambda s_w + \psi(\mathbf{r})s_w - v_w\beta\eta(\mathbf{r}) - \beta\mu_w = 0 \\ \rho_w(\mathbf{x})v_w &= \exp\left[\beta\mu_w - \beta\epsilon_w(s_w)^2 + \beta\lambda s_w - \psi(\mathbf{r})s_w + v_w\beta\eta(\mathbf{r})\right] \\ \rho_w(\mathbf{r})v_w = \sum_{s'_w} \rho_w(\mathbf{x})v_w\delta_{s_w,s'_w} &= e^{\beta\mu_w + v_w\beta\eta(\mathbf{r})}\left(1 + e^{-\beta\epsilon_w + \beta\lambda - \psi(\mathbf{r})} + e^{-\beta\epsilon_w - \beta\lambda + \psi(\mathbf{r})}\right) \end{aligned} \tag{V.41}$$

$$\begin{aligned} \frac{\delta\beta\Omega}{\delta\rho_M(\mathbf{X})} &= \ln(\rho_M(\mathbf{X})v_M^N) + \beta V_B(\mathbf{X}) + \sum_{i=1}^N \left[-\beta\epsilon_M - \beta\lambda + \psi(\mathbf{r}_i)\right] s_i^M \\ &\quad - \sum_{i=1}^N \beta\eta(\mathbf{r}_i) - \beta\mu_M = 0 \\ \rho_M(\mathbf{X})v_M^N &= \exp\left[\beta\mu_M - \beta V_B(\mathbf{X}) + \sum_{i=1}^N \left[\beta\epsilon_M + \beta\lambda - \psi(\mathbf{r}_i)\right] s_i^M + \sum_{i=1}^N \beta\eta(\mathbf{r}_i)\right] \end{aligned} \tag{V.42}$$

where the bonding potential is a normalized Gaussian, $\exp[-V_B(\mathbf{X})] = v_M^{N-1} \prod_{j=1}^{N-1} \Phi(|\mathbf{r}_{j+1} - \mathbf{r}_j|)$. The equations become

$$\begin{aligned} \rho_M(\mathbf{X})v_M = e^{\beta\mu_M} e^{\beta\omega(\mathbf{r}_1, s_1^M)} \Phi(|\mathbf{r}_2 - \mathbf{r}_1|) e^{\beta\omega(\mathbf{r}_2, s_2^M)} \Phi(|\mathbf{r}_3 - \mathbf{r}_2|) \times \ldots \\ \ldots \times e^{\beta\omega(\mathbf{r}_{N-1}, s_{N-1}^M)} \Phi(|\mathbf{r}_N - \mathbf{r}_{N-1}|) e^{\beta\omega(\mathbf{r}_N, s_N^M)} \end{aligned} \tag{V.43}$$

where

$$\beta\omega(\mathbf{r}_j, s_j^M) = \left[\beta\epsilon_M + \beta\lambda - \psi(\mathbf{r}_j)\right] s_j^M + \beta\eta(\mathbf{r}_j) \tag{V.44}$$

Solving for the monomer density (configurationally dependent)

$$\begin{aligned} \rho_j^M(\mathbf{r}, s_j^M)v_M = &= \int d\mathbf{X}' \rho_M(\mathbf{X}')v_M \delta(\mathbf{r} - \mathbf{r}'_j) \delta_{s_j^M, s_j^{M'}} \\ &= e^{\beta\mu_M} e^{-\beta\omega(\mathbf{r}, s_j^M)} q(j, \mathbf{r}, s_j^M) q^*(j, \mathbf{r}, s_j^M) \end{aligned} \tag{V.45}$$

where the propagators are defined recursively,

$$q(j, \mathbf{r}, s_j^M) = e^{\beta\omega(\mathbf{r}, s_j^M)} \int d\mathbf{r}' \Phi(|\mathbf{r} - \mathbf{r}'|) \sum_{s_{j-1}^M} q(j-1, \mathbf{r}', s_{j-1}^M) \tag{V.46}$$

$$q^*(j,\mathbf{r},s_j^M) = e^{\beta\omega(\mathbf{r},s_j^M)} \int d\mathbf{r}'\Phi(|\mathbf{r}-\mathbf{r}'|) \sum_{s_{j+1}^M} q(j+1,\mathbf{r}',s_{j+1}^M) \tag{V.47}$$

with the initial conditions $q(1,\mathbf{r},s_1^M) = e^{\beta\omega(\mathbf{r},s_1^M)}$ and $q^*(N,\mathbf{r},s_N^M) = e^{\beta\omega(\mathbf{r},s_N^M)}$. For the brush problem, the first monomer is constrained to the surface so that the propagator is given by

$$q(1,\mathbf{r},s_1^M) = e^{\beta\omega(\mathbf{r},s_1^M)}\delta(x-x_\perp)\delta(y-y_\perp)\delta(z) \tag{V.48}$$

When the spatial variation is only in the z-direction (dimensionless z),

$$q(1,z,s_1^M) = e^{\beta\omega(z,s_1^M)}\delta(z) \tag{V.49}$$

Likewise, we have the condition related to the grafting density

$$\int dx\rho_1^M(x) = b\int dz\rho_1^M(z) = \frac{e^{\beta\mu_M}}{v_M/b}\sum_{s_1^M} q^*(1,0,s_1^M) = \sigma \tag{V.50}$$

so that the chemical potential is determined $e^{\beta\mu_M} = \frac{\sigma v_M/b}{\sum_{s_1^M} q^*(1,0,s_1^M)}$. And the density of all monomers is then

$$\rho_j^M(z,s_j^M) = \frac{\sigma/b}{\sum_{s_1^M} q^*(1,0,s_1^M)} q(j,z,s_j^M)e^{-\beta\omega(z,s_j^M)}q^*(j,z,s_j^M) \tag{V.51}$$

with the first being

$$\rho_1^M(z,s_1^M) = \frac{\sigma/b}{\sum_{s_1^M} q^*(1,0,s_1^M)} q^*(1,z,s_1^M)\delta(z) \tag{V.52}$$

These are all the same mean-field equations as the derivation from field theory in Section III.2. The key difference is that $\xi(\mathbf{r})$ is the composite field for different states. Here, the $\omega(\mathbf{r},s_j^M)$ field is the effective field for each state. By keeping each state separate, we can more easily deal with the sequence dependence in the excess free energy in the next section.

Debye-Hückle Correlations

We use the same general approach as that above to derive the mean field equations with electrostatic correlations.

$$F - F^{\text{no}}_{\text{correlation}} = F_{DH} + F_{DH}^{ch} = \int d\mathbf{r} f_{DH}(\mathbf{r}) + \int d\mathbf{X} f_{DH}^{ch}(\mathbf{X}) \tag{V.53}$$

where the free energy density for disconnected ions and the chain connectivity contribution are given by

$$\beta f_{DH}(\mathbf{r}) = \frac{1}{4\pi d^3}\left[\ln\left(1+\kappa(\mathbf{r})d\right) - \kappa(\mathbf{r})d + \frac{1}{2}\kappa(\mathbf{r})^2 d^2\right] \tag{V.54}$$

where d is the Debye radius (or equivalent estimate) and κ is the inverse Debye length defined as

$$\kappa(\mathbf{r}) = \sqrt{4\pi l_B\left[z_+^2\rho_+(\mathbf{r}) + z_-^2\rho_-(\mathbf{r}) + \sum_{s_w}\rho_w(\mathbf{r},s_w)(s_w)^2 + \sum_{i=1}^{N}\sum_{s_i^M}\rho_i^M(\mathbf{r},s_i^M)(s_i^M)^2\right]} \tag{V.55}$$

For the connectivity,

$$\beta f_{DH}^{ch}(\mathbf{X}) = -\rho(\mathbf{X})\ln\Big(g(\mathbf{X})\Big) \tag{V.56}$$

where $g(\mathbf{X})$ is the distribution function. Using the TPT-1 approximation [62, 63] and the Debye-Hückel approximation for the correlation function[22], we have the following

$$\beta f_{DH}^{ch}(\mathbf{X}) = \rho(\mathbf{X})\sum_{j=1}^{N-1}\frac{s_j^M s_{j+1}^M l_B/d_j}{1+\kappa(\mathbf{r}_j)d_j} = \sum_{j=1}^{N-1}\rho(\mathbf{X})\zeta(\mathbf{r}_j, s_j^M, s_{j+1}^M) \tag{V.57}$$

Taking the variation with respect to the density

$$\begin{aligned}\frac{\delta\beta\Omega}{\delta\rho_\alpha(\mathbf{r})} &= \ln(\rho_\alpha(\mathbf{r})v_\alpha) + z_\alpha\psi(\mathbf{r}) - v_\alpha\beta\eta(\mathbf{r}) + \frac{\delta\beta f_{DH}}{\delta\rho_\alpha(\mathbf{r})} + \frac{\delta\beta f_{DH}^{ch}}{\delta\rho_\alpha(\mathbf{r})} - \beta\mu_\alpha = 0\\ \rho_\alpha(\mathbf{r})v_\alpha &= \exp\left[\beta\mu_\alpha - z_\alpha\psi(\mathbf{r}) + v_\alpha\beta\eta(\mathbf{r}) - \frac{\delta\beta f_{DH}}{\delta\rho_\alpha(\mathbf{r})} - \frac{\delta\beta f_{DH}^{ch}}{\delta\rho_\alpha(\mathbf{r})}\right]\end{aligned} \tag{V.58}$$

$$\begin{aligned}\frac{\delta\beta\Omega}{\delta\rho_w(\mathbf{x})} &= \ln(\rho_w(\mathbf{x})v_w) + \beta\epsilon_w(s_w)^2 - \beta\lambda s_w + \psi(\mathbf{r})s_w - v_w\beta\eta(\mathbf{r}) - \beta\mu_w\\ &\quad + \frac{\delta\beta f_{DH}}{\delta\rho_w(\mathbf{x})} + \frac{\delta\beta f_{DH}^{ch}}{\delta\rho_w(\mathbf{x})} = 0\end{aligned} \tag{V.59}$$

$$\rho_w(\mathbf{x})v_w = \exp\left[\beta\mu_w - \beta\epsilon_w(s_w)^2 + \beta\lambda s_w - \psi(\mathbf{r})s_w + v_w\beta\eta(\mathbf{r}) - \frac{\delta\beta f_{DH}}{\delta\rho_w(\mathbf{x})} - \frac{\delta\beta f_{DH}^{ch}}{\delta\rho_w(\mathbf{x})}\right] \tag{V.60}$$

$$\rho_w(\mathbf{r})v_w = \sum_{s'_w} \rho_w(\mathbf{x})v_w\delta_{s_w,s'_w} \tag{V.61}$$

$$\begin{aligned}\frac{\delta\beta\Omega}{\delta\rho_M(\mathbf{X})} = \ln(\rho_M(\mathbf{X})v_M^N) + \beta V_B(\mathbf{X}) + \sum_{i=1}^{N}\left[-\beta\epsilon_M - \beta\lambda + \psi(\mathbf{r}_i)\right]s_i^M \\ - \sum_{i=1}^{N}\beta\eta(\mathbf{r}_i) + \frac{\delta\beta f_{DH}}{\delta\rho_M(\mathbf{X})} + \frac{\delta\beta f_{DH}^{ch}}{\delta\rho_M(\mathbf{X})} - \beta\mu_M = 0\end{aligned} \tag{V.62}$$

$$\rho_M(\mathbf{X})v_M^N = \exp\left[\beta\mu_M - \beta V_B(\mathbf{X}) + \sum_{i=1}^{N}\left[\beta\epsilon_M + \beta\lambda - \psi(\mathbf{r}_i)\right]s_i^M + \sum_{i=1}^{N}\beta\eta(\mathbf{r}_i) - \frac{\delta\beta f_{DH}}{\delta\rho_M(\mathbf{X})} - \frac{\delta\beta f_{DH}^{ch}}{\delta\rho_M(\mathbf{X})}\right] \tag{V.63}$$

where the local potentials for the excess free energy are given in the Appendix. Substituting the normalized Gaussian potential for the connectivity,

$$\begin{aligned}\rho_M(\mathbf{X})v_M = e^{\beta\mu_M}e^{\beta\omega(\mathbf{r}_1,s_1^M,s_2^M)}\Phi(|\mathbf{r}_2-\mathbf{r}_1|)e^{\beta\omega(\mathbf{r}_2,s_2^M,,s_3^M)}\Phi(|\mathbf{r}_3-\mathbf{r}_2|)\times\ldots \\ \ldots\times e^{\beta\omega(\mathbf{r}_{N-1},s_{N-1}^M,s_N^M)}\Phi(|\mathbf{r}_N-\mathbf{r}_{N-1}|)e^{\beta\omega(\mathbf{r}_N,s_N^M)}\end{aligned} \tag{V.64}$$

where the effective field ω generally depends on $\mathbf{r}_j$, s_j, and s_{j+1}.

$$\begin{aligned}\beta\omega(\mathbf{r}_j,s_j^M,s_{j+1}^M) = \left[\beta\epsilon_M + \beta\lambda - \psi(\mathbf{r}_j)\right]s_j^M + \beta\eta(\mathbf{r}_j) + \frac{(s_j^M)^2\kappa(\mathbf{r}_j)l_B}{2(1+\kappa(\mathbf{r}_j)d)} \\ +\zeta(\mathbf{r}_j,s_j^M,s_{j+1}^M)\left[\frac{\rho(\mathbf{r}_j,s_j^M,s_{j+1}^M)d}{(1+\kappa(\mathbf{r}_j)d)}\frac{2\pi l_B(s_j^M)^2}{\kappa(\mathbf{r}_j)} - 1\right]\end{aligned} \tag{V.65}$$

with the last monomer only depending on its own state

$$\beta\omega(\mathbf{r}_N,s_N^M) = \left[\beta\epsilon_M + \beta\lambda - \psi(\mathbf{r}_j)\right]s_j^M + \beta\eta(\mathbf{r}_j) + \frac{(s_i^M)^2\kappa(\mathbf{r}_j)l_B}{2(1+\kappa(\mathbf{r}_j)d)} \tag{V.66}$$

Writing the one-body density,

$$\begin{aligned}\rho_j^M(\mathbf{r},s_j^M,s_{j+1}^M)v_M = = \int d\mathbf{X}'\rho_M(\mathbf{X}')v_M\delta(\mathbf{r}-\mathbf{r}'_j)\delta_{s_j^M,s_j^{M'}}\delta_{s_{j+1}^M,s_{j+1}^{M'}} \\ = e^{\beta\mu_M}e^{-\beta\omega(\mathbf{r},s_j^M,s_{j+1}^M)}q(j,\mathbf{r},s_j^M,s_{j+1}^M)q^*(j,\mathbf{r},s_j^M,s_{j+1}^M)\end{aligned} \tag{V.67}$$

where the propagators are defined recursively,

$$q(1,\mathbf{r},s_1^M,s_2^M) = e^{\beta\omega(\mathbf{r},s_1^M,s_2^M)} \tag{V.68}$$

$$q(j,\mathbf{r},s_j^M,s_{j+1}^M) = e^{\beta\omega(\mathbf{r},s_j^M,s_{j+1}^M)}\int d\mathbf{r}'\Phi(|\mathbf{r}-\mathbf{r}'|)\sum_{s_{j-1}^M}q(j-1,\mathbf{r}',s_{j-1}^M,s_j^M) \tag{V.69}$$

$$q^*(N, \mathbf{r}, s_N^M) = e^{\beta\omega(\mathbf{r}, s_N^M)} \tag{V.70}$$

$$q^*(N-1, \mathbf{r}, s_{N-1}^M, s_N^M) = e^{\beta\omega(\mathbf{r}, s_{N-1}^M, s_N^M)} \int d\mathbf{r}' \Phi(|\mathbf{r}-\mathbf{r}'|) q(N, \mathbf{r}', s_N^M) \tag{V.71}$$

$$q^*(j, \mathbf{r}, s_j^M, s_{j+1}^M) = e^{\beta\omega(\mathbf{r}, s_j^M, s_{j+1}^M)} \int d\mathbf{r}' \Phi(|\mathbf{r}-\mathbf{r}'|) \sum_{s_{j+2}^M} q(j+1, \mathbf{r}', s_{j+1}^M, s_{j+2}^M) \tag{V.72}$$

One can obtain the total density, or state density, by summing over the configurational variables

$$\begin{aligned} \rho_j^M(\mathbf{r}, s_j^M) &= \sum_{s_{j+1}^M} \rho_j^M(\mathbf{r}, s_j^M, s_{j+1}^M) \\ \rho_j^M(\mathbf{r}) &= \sum_{s_j^M} \rho_j^M(\mathbf{r}, s_j^M) \end{aligned} \tag{V.73}$$

As long as the number of states is relatively small, tracking $\rho_j^M(\mathbf{r}, s_j^M, s_{j+1}^M)$ for each monomer type should not be too intensive.

Grafted Propagators

Starting from the density, where the first monomer is grafted to the surface,

$$\rho_j^M(z, s_j^M, s_{j+1}^M) \nu_M = e^{\beta\mu_M} e^{-\beta\omega(z, s_j^M, s_{j+1}^M)} q(j, z, s_j^M, s_{j+1}^M) q^*(j, z, s_j^M, s_{j+1}^M) \tag{V.74}$$

with

$$\rho_1^M(z, s_1^M, s_2^M) \nu_M = e^{\beta\mu_M} e^{-\beta\omega(z, s_1^M, s_2^M)} q(1, z, s_1^M, s_2^M) q^*(1, z, s_1^M, s_2^M) \tag{V.75}$$

where the propagators are defined recursively,

$$q(1, z, s_1^M, s_2^M) = e^{\beta\omega(z, s_1^M, s_2^M)} \delta(z) \tag{V.76}$$

$$q(2, z, s_2^M, s_3^M) = e^{\beta\omega(z, s_2^M, s_3^M)} \Phi(z) \sum_{s_1^M} e^{\beta\omega(0, s_1^M, s_2^M)} \tag{V.77}$$

$$q(j, z, s_j^M, s_{j+1}^M) = e^{\beta\omega(z, s_j^M, s_{j+1}^M)} \int dz' \Phi(|z-z'|) \sum_{s_{j-1}^M} q(j-1, z', s_{j-1}^M, s_j^M) \tag{V.78}$$

The complimentary propagators are defined the same as above. The grafting condition determines the chemical potential

$$\begin{aligned}\int dz \sum_{s_1^M} \sum_{s_2^M} \rho_1^M(z, s_1^M, s_2^M) v_M &= \sigma b^2 \\ &= e^{\beta\mu_M} \sum_{s_1^M} \sum_{s_2^M} \int dz' e^{-\beta\omega(z', s_1^M, s_2^M)} q(1, z', s_1^M, s_2^M) q^*(1, z', s_1^M, s_2^M) \\ &= e^{\beta\mu_M} \sum_{s_1^M} \sum_{s_2^M} q^*(1, 0, s_1^M, s_2^M)\end{aligned} \tag{V.79}$$

$$e^{\beta\mu_M} = \frac{\sigma b^2}{\sum_{s_1^M} \sum_{s_2^M} q^*(1, 0, s_1^M, s_2^M)} \tag{V.80}$$

The grafted monomer can then be treated as an external, fixed charge where the charge state varies. The charge density arising from the grafted monomer is

$$\begin{aligned}Q_{graft} b^2 = \int dz \sum_{s_1^M} \sum_{s_2^M} \rho_1^M(z, s_1^M, s_2^M) v_M s_1^M &= \sum_{s_1^M} \sum_{s_2^M} e^{\beta\mu_M} q^*(1, 0, s_1^M, s_2^M) s_1^M \\ &= \sigma b^2 \frac{\sum_{s_1^M} \sum_{s_2^M} q^*(1, 0, s_1^M, s_2^M) s_1^M}{\sum_{s_1^M} \sum_{s_2^M} q^*(1, 0, s_1^M, s_2^M)}\end{aligned} \tag{V.81}$$

Results and Discussion

Bulk Titration

We begin by considering the bulk titration behavior of the polyelectrolyte in an electrolyte solution. From the mean-field result, the charge state of the monomers in a uniform bulk solution only depends on the pH and the pK_a. Electrostatic correlations enable the charge state to be dependent on properties like the degree of polymerization and the local salt concentration (Figure V.12). Adding in the Debye–Hückel correlations for disconnected ions favors ionization of the monomers due to the local screening environment. Like-charged ions have less repulsion arising from the ion structuring around each ion. For a connected chain, the correlations at the nearest-neighbor level suppress ionization since there is a penalty for two adjacent monomers to be ionized.

The nearest-neighbor (TPT-1) level approach to the electrostatic contribution to the chain connectivity correlations creates a weak dependence of the charge state

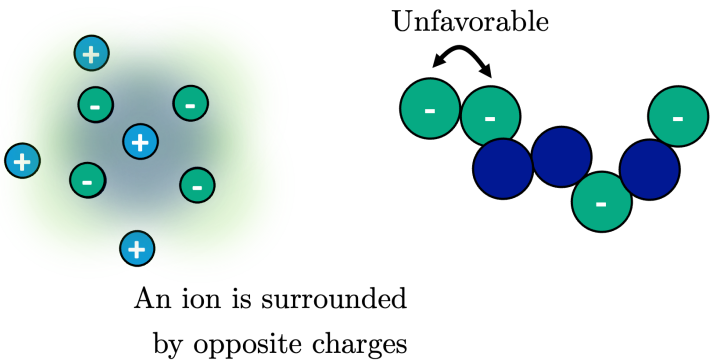

Figure V.12: Bulk titration of polyacid for various degrees of polymerization, N. The mean-field result does not depend on the degree of polymerization. The rest of the curves included the Debye-Hückel correlations.

on the chain length. TPT-1 level treatment of electrostatic correlation is known to underestimate the electrostatic correlation and be relatively insensitive to chain length [64]. Figure V.13 shows the bulk titration behavor for a dilute acid solution for different chain lengths. As expected, increasing the chain length decreases the ionized fraction due to the penalty of adjacent monomers being ionized. The effect saturates rather quickly with $N = 5$ and $N = 100$ being quite similar. The largest effects differences from the mean-field result occur for pH values above the pK_a since the polymer is more likely to be ionized at those conditions. For a

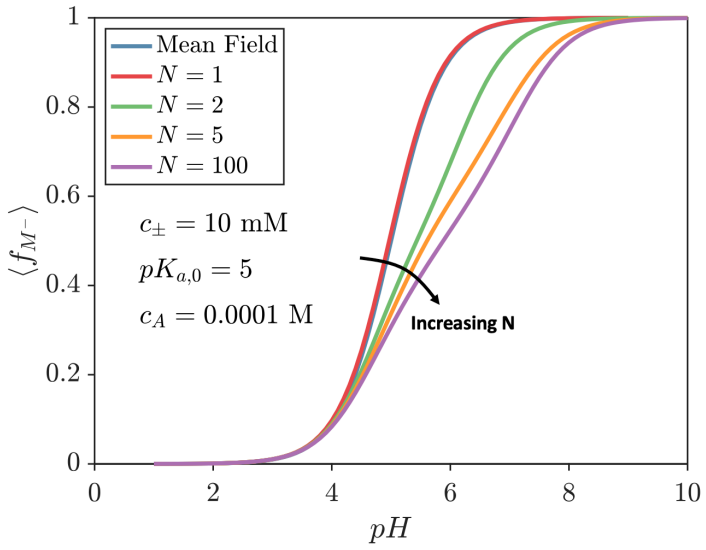

Figure V.13: Bulk titration of polyacid for various chain lengths. The mean-field result does not depend on the degree of polymerization. The rest of the curves included the Debye–Hückel correlations.

fixed chain length, adding salt increases the amount of screening and decreases the penalty for adjacent ionized monomers. Figure V.14 shows that increasing the salt concentration increases the degree of ionization. Even for a 1 M solution, there is still a noticable difference between the mean-field result and that with correlations. These differences will undoubtedly play a role in the brush system, where the strong inhomogeneity induced by the surface creates widely varying local conditions for the weak polyelectrolyte. We briefly offer a comparison to experiments in Figure

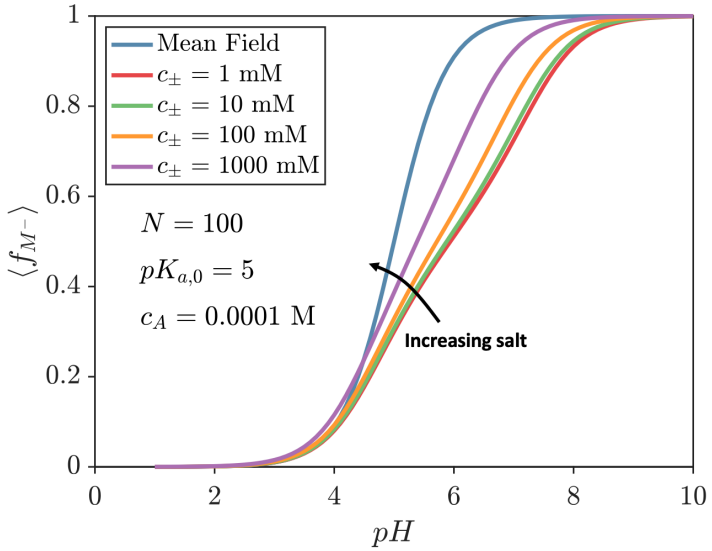

Figure V.14: Bulk titration of polyacid for various salt concentrations. The mean-field result does not depend on the salt concentration. The rest of the curves included the Debye–Hückel correlations.

V.15. The experimental value for the pK_a used was 4.35 [65]. Clearly, the mean-field result fails to capture the correct ionization behavior, overestimating due to the lack of connectivity correlations. The result with correlations yields the correct slope of the titration curve but appears shifted. If one uses a pK_a value of 5.22, the predictions with correlations nearly overlap with the experimental data. For this reason, we are optimistic that even at the Debye–Hückel, we are able to capture the salient physics of ionization in weak polyelectrolytes.

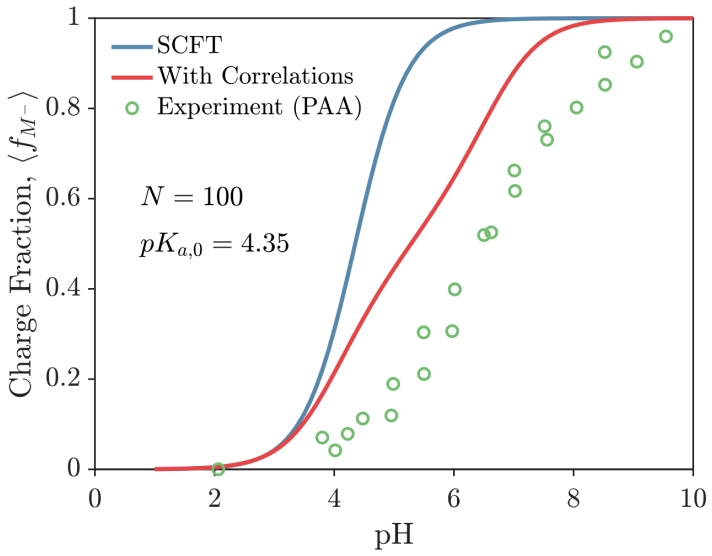

Figure V.15: Comparison of bulk titration behavior across mean-field, Debye–Hückel correlations, and experiment. Experiment values are for poly(acrylic acid) from [66, 67].

Brush Structure

The structure of a polyelectrolyte brush intimately depends on its charge state [24]. A highly charged polyelectrolyte grafted to a surface will tend to extend away from the surface to minimize the ion-ion repulsion with other grafted chains. The chains cannot stretch arbitrarily far owing to the entropic cost of chain stretching – chain conformations are reduced in the extended state. The balance between these two effects gives rise to the equilibrium brush height [23]. Figure V.16 shows a well-known but important result of the brush profile on a charge neutral surface for different values of the pH. For a polyacid, as the pH increases, the average ionization in the brush increases, similar to the bulk titration behavior. Clearly, in Figure V.16, the brush takes on a more extended conformation at a pH of 8 versus that of 3. While not shown, counterions from the salt solution enter the brush region to compensate the charge from the brush. What is important to note is that changing the pH dramatically influences the charge state. For this reason, one can see dramatic changes in the brush conformation by changing the pH. Indeed, the average fraction of ionized monomers in the brush significantly depends on pH. Figure V.17 indicates that in both the mean-field and theory with correlations, the average ionization fraction can span the full range from 0 to nearly fully ionized by changing the pH from 3 to 9. What is somewhat surprising is how similar the

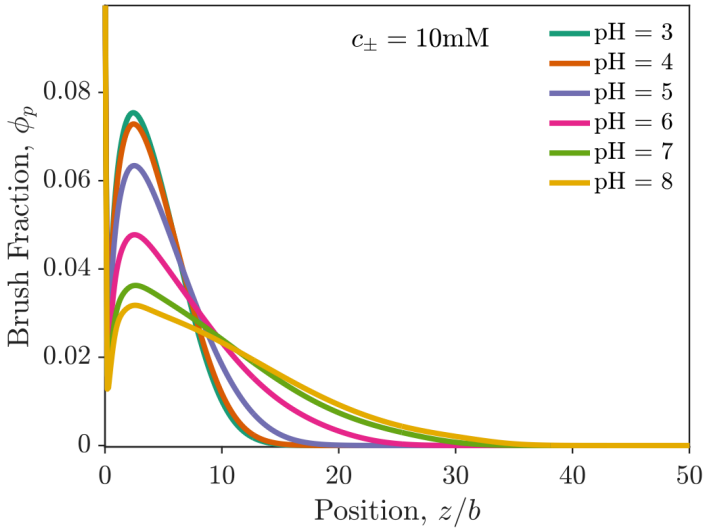

Figure V.16: Polyacid brush density profile near a neutral surface for different values of pH. The salt concentration is 10 mM, the chain length is $N = 50$ and the grafting density is $\sigma_g b^2 = 0.01$.

mean-field result is to the theory with correlations, despite their differences in the bulk titration behavior. The reason is that the local electrostatic potential plays an important role in determining the charge state of each monomer, representing a one-body term on each monomer. The similarity between theories in Figure V.17 is an indication of the strong inhomogeniety in the local electrostatic potential [61]. At a fixed pH, the addition of salt screens the ion-ion repulsion, which generally reduces the penalty for ionization, leading to a higher ionized fraction with increasing salt. There are multiple options for the brush height upon the addition of salt. Figure V.18 shows that adding salt decreases the brush height, which indicates that we are in the salted brush regime [68]. The onset of the salted brush regime is known to occur in the range of 10 mM [59].

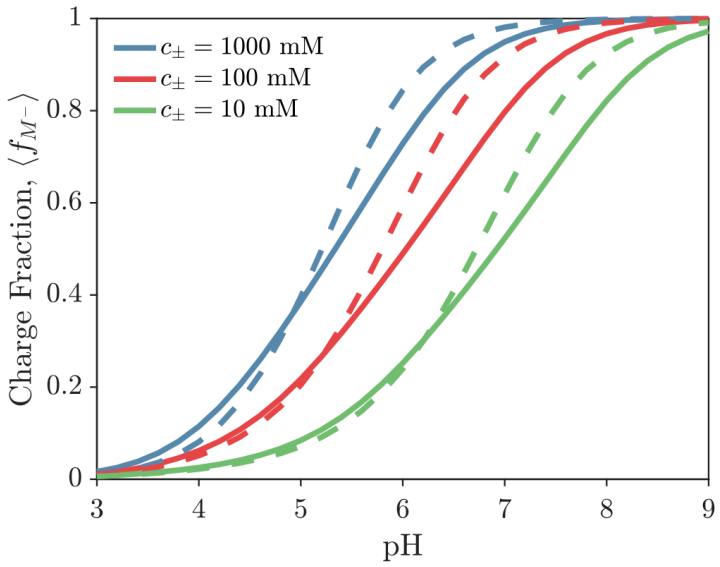

Figure V.17: Average fraction of ionized monomers for a polyacid brush grafted to a neutral surface versus the solution pH. The chain length is $N = 50$ and the grafting density is $\sigma_g b^2 = 0.01$.

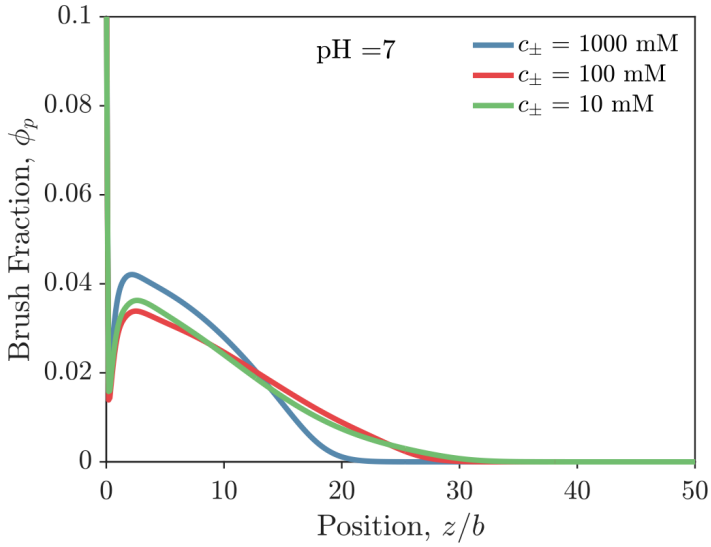

Figure V.18: Polyacid brush density profile near a neutral surface for different salt concentrations. The pH is 7, the chain length is $N = 50$ and the grafting density is $\sigma_g b^2 = 0.01$.

Electrostatic Manipulation

Up to this point, we have considered polyacid brushes grafted to neutral surfaces. For the electroresponsive behavior, the guiding parameter is the electrostatic potential

at the surface. When the surface is neutral, a grafted polyacid will induce a negative surface potential. The point of zero potential usually refers to a positively charged surface. Figure V.19 shows the effect of the surface potential on the brush height. The abscissa in the plot is given as the negative value of the applied potential since that is language of the motivating experimental work [56]. There are a few clear trends. for any given pH: (1) a more negative applied potential swells the polyacid brush and (2) the brush height rapidly changes in the range of zero potential, mostly in the range of $-\Delta V \approx 0.05$ V. At the same time, the average ionized fraction in the brush monotonically decreases for negative potentials. The central question posed in Ref. 56 is founded on this question: how can the brush swell if the ionized fraction decreases?

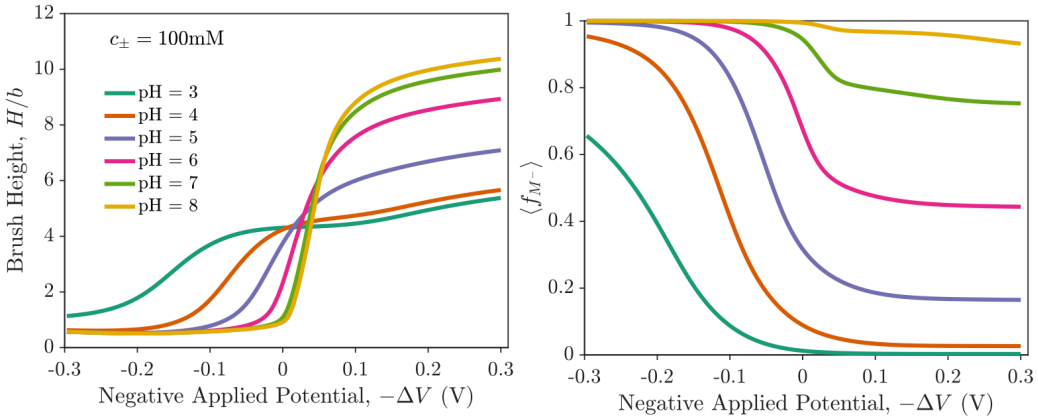

Figure V.19: Effect of applied potential on the brush conformation and charge. (left) Brush height and (right) average ionized fraction as a function of the negative of the applied electrostatic potential on the surface. The chain length is $N = 20$ and the grafting density is $\sigma_g b^2 = 0.01$.

To answer this question, we turn to classical scaling arguments of polyelectrolyte brushes [69]. Many of the main ideas that follow have been extensively considered by Borisov and coworkers [54, 70]; however, the open question calls for a simple explanation. Viewing the problem through a *brush-centric* lens does not work — the surface condition plays an essential role. When a negative potential is applied to a surface, the surface charge density will decrease since the capacitance must be positive. When the surface charge density decreases, the polyacid will either be less attracted to a positively charged surface or will be more repelled from a negatively charged surface. This explanation captures the essential physics. From scaling in the salted brush regime, the equilibrium height of the brush is determined

by the balance of ion-ion repulsion in the brush region and the stretching of the brush. Dividing the system into a bulk solution in contact with a brush region, the ion-ion repulsion in the brush region can be directly related to the difference in the osmotic pressure between the bulk solution and the brush region. The force of chain stretching is $f_{el} \sim H/Nb^2 \sim b\sigma/\phi_{\text{brush}}$ and the ion-ion repulsion for a neutral surface is $f_{ion-ion} \sim \frac{f^2\phi_{\text{brush}}^2}{\sigma_g b^6 C_s}$, where $\phi_{\text{brush}} = Nb^3\sigma_g/H$ is the average monomer volume fraction in the brush region. The balance of these two forces leads to the classic scaling relation for the brush height, $H \sim Nb^{2/3}\sigma_g^{1/3}C_s^{-1/3}f^{2/3}$. From this relationship, applying a negative potential decreases the average ionization f and the brush should contract. In the brush region if one includes the contribution from the surface charge density, the scaling relationship changes. To add this contribution, we treat it similarly to the fixed, immobilied charge of the monomers in the brush region so that the ions in the bulk solution *see* a charge of Q_s/H from the surface. The ion-ion repulsion is then $f_{ion-ion} \sim \frac{f^2\phi_{\text{brush}}^2\left(1-\frac{Q_s}{Nf\sigma_g}\right)^2}{\sigma_g b^6 C_s}$ for a polyacid where $f > 0$. The brush height scaling becomes $H \sim Nb^{2/3}\sigma_g^{1/3}C_s^{-1/3}\left(f-\frac{Q_s}{N\sigma}\right)^{2/3}$.

The scaling analysis above indicates that the brush height is determined by the effective charge fraction, $f - \frac{Q_s}{N\sigma}$, that the counterions in the bulk solution see in the brush region. For a fixed charge fraction for a negatively charged polyelectrolyte, the effective charge fraction is clearly monotonic with the surface charge density. Namely, the effective charge fraction increases with a negatively charged surface and decreases with a positively charged surface. Of course, the scaling analysis above is not applicable in the regime where the polyelectrolyte is fully collapsed on the surface. In that case, the relevant force balance is the attraction of the brush to the surface and the force required to confine the brush to a thin surface layer [71]. For weak polyelectrolytes, the charge fraction f decreases as $-Q_s$ increases, leading to a competition between change in ionization and the change in surface charge density. In other words, when applying a negative potential to the surface, the energy can either go toward neutralizing monomers or confining more small ions in the brush region. One can also coarsely work out a condition on the capacitance from the scaling relationship, where brush extension upon applying a negative potential will occur when $C_d > N\sigma\frac{\partial f}{\partial \Delta V}$. The dependence of f on the surface potential is not obvious, but can be calculated numerically. Figure V.20 shows that the effective charge fraction for the polyacid brush considered here is monotonically increasing with the negative applied potential, indicating that the brush should swell. While not shown, the same trend is true for salt concentrations of 10mM and 1000mM as well.

We do not expect the scaling exponents to be accurate for this system because we are considering short chains and the electrostatic correlations adjust the expression for the ion-ion repulsion. Other brush systems also have shown scaling that deviates from the predicted scaling, even at the mean field level [72].

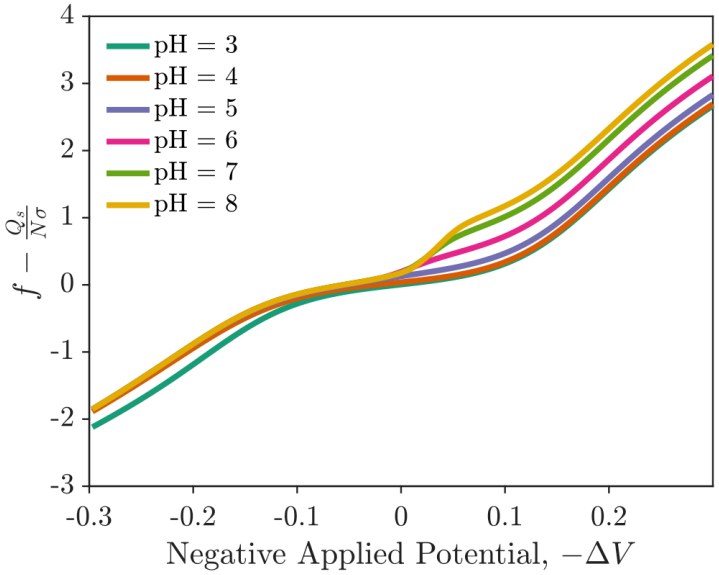

Figure V.20: Effective fraction as a function of the negative of the applied electrostatic potential on the surface. The chain length is $N = 20$ and the grafting density is $\sigma_g b^2 = 0.01$.

Having established the swelling behavior from pure electrostatic arguments, we investigate some implications of the electroresponsiveness. Namely, we will analyze the capacitance of the polyacid brush in different solvent conditions. Figure V.21 shows the brush height when applying a negative potential and the corresponding capacitance for two different solvent conditions. The Appendix shows how we incorporate the solvent quality into our theory. Looking at the left-hand panels, the region where the brush height rapidly changes corresponds to a peak in the differential capacitance. The reason for this is that as the brush expands, counterions rush into the brush region, potentially leading to a large change in the charge stored in the EDL. So for the polyacid brush, the brush height response to the potential is intimately connected to the capacitance performance. The right-hand panels show the same plots for the brush in a better solvent $\chi = 5.0$. Increasing the solvent quality increases the ability of the brush to extend, where the brush can resist electrostatic forces that may collapse the brush on the surface. The net result is that the brush height changes more slowly when applying a surface potential. For the capacitance,

a less dramatic change in the brush height leads to a less dramatic peak in the capacitance. So for capacitance applications, the optimal conditions are to have a poor enough solvent to cause rapid extension upon charging without having too poor of a solvent, where the electrostatic forces cannot overcome the barrier to extend the brush.

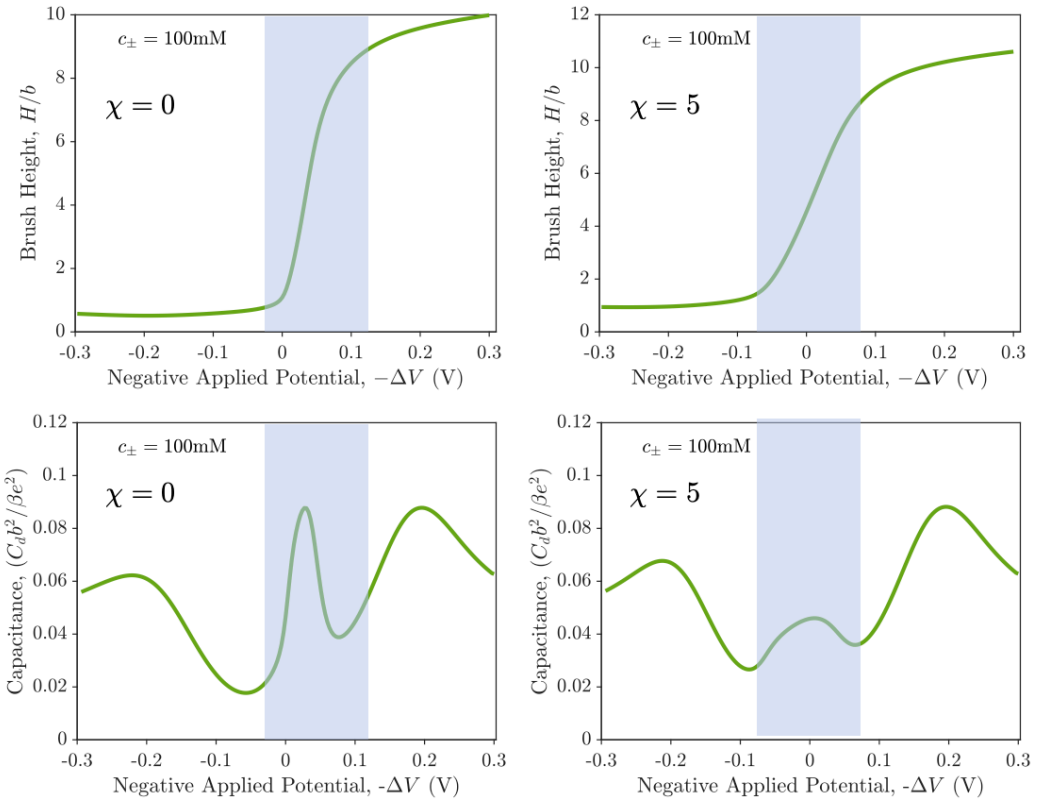

Figure V.21: Brush extension and capacitance as a function of the negative of the applied electrostatic potential for different solvent qualities. The chain length is $N = 20$ and the grafting density is $\sigma_g b^2 = 0.01$.

The capacitance has a nontrivial dependence on the pH and the salt concentration. For each individual pH and salt concentration, the peak of interesting the capacitance can be understood using the argument above. Figure V.22 shows the varying behavior in the capacitance with pH and salt concentration. A benefit of the analysis above is that one can tune the capacitance by understanding the electroresponse of the brush height, rather than having to measure surface properties that may be difficult to access experimentally.

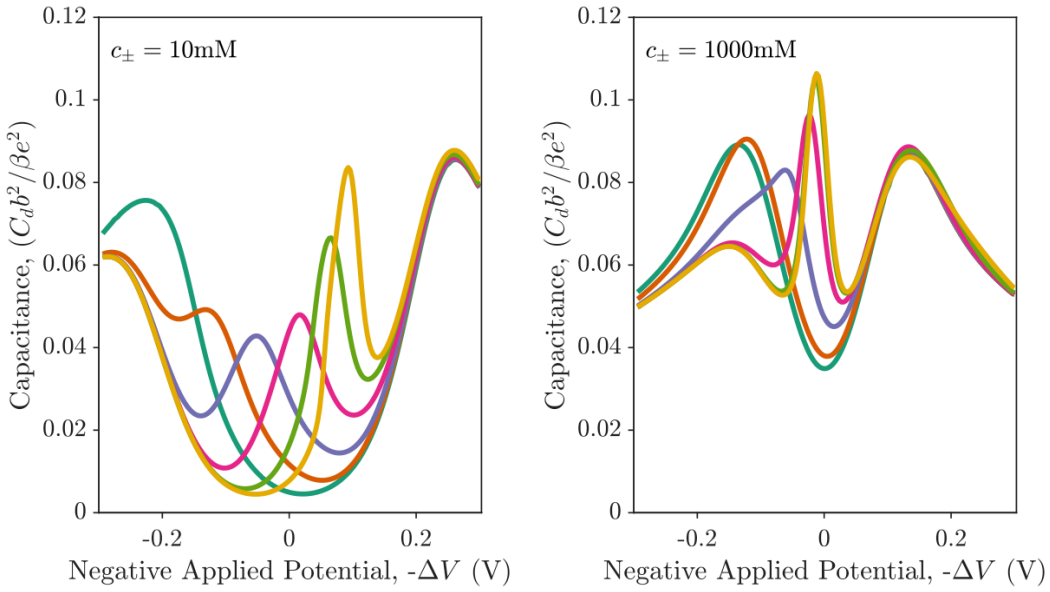

Figure V.22: Capacitance for different values of pH. The chain length is $N = 20$ and the grafting density is $\sigma_g b^2 = 0.01$.

Conclusion

For weak polyelectrolyte brushes, the interplay of the charge state, solution conditions, and electrostatic interaction with the surface lead to a variety of brush conformations. Recent experiments described an apparent paradox where applying a negative potential to a polyacid swells the brush. One may expect that a negative potential should decrease the ionized fraction and contract the brush. This brush-centric view neglects the role of the fixed, immobilized surface charges. We rationalize the experimental observations through a scaling analysis that includes the surface charges and provide numerical results from an inhomogeneous thermodynamic theory. The mechanism for the brush swelling is related to the surface charge compensation by the small ions. Future work in this area includes elucidating the origin of hysteresis upon charging and discharging a surface with a weak polyelectrolyte brush, as seen in Ref. 56. Nonelectrostatic effects likely play an important role in the conformation persisting in a metastable collapsed or swollen state.

Appendix

Potentials for Debye-Hückle Correlations

For clarity, we explicitly calculate the local chemical potential when all of the species are the same size

$$\frac{\delta\beta f_{DH}}{\delta\rho_\alpha(\mathbf{r})} = -\frac{z_\alpha^2\kappa(\mathbf{r})l_B}{2(1+\kappa(\mathbf{r})d)} \tag{V.82}$$

$$\frac{\delta\beta f_{DH}}{\delta\rho_w(\mathbf{x})} = -\frac{(s_w)^2\kappa(\mathbf{r})l_B}{2(1+\kappa(\mathbf{r})d)} \tag{V.83}$$

$$\frac{\delta\beta f_{DH}}{\delta\rho_M(\mathbf{X})} = -\sum_{j=1}^{N}\frac{(s_j^M)^2\kappa(\mathbf{r}_j)l_B}{2(1+\kappa(\mathbf{r}_j)d)} \tag{V.84}$$

$$\frac{\delta\beta f_{DH}^{ch}}{\delta\rho_\alpha(\mathbf{r})} = -\sum_{j=1}^{N-1}\sum_{\{s_j^M\}}\sum_{\{s_{j+1}^M\}}\rho(\mathbf{r},s_j^M,s_{j+1}^M)\frac{\zeta(\mathbf{r},s_j^M,s_{j+1}^M)d}{(1+\kappa(\mathbf{r})d)}\frac{2\pi l_B z_\alpha^2}{\kappa(\mathbf{r})} \tag{V.85}$$

$$\frac{\delta\beta f_{DH}^{ch}}{\delta\rho_w(\mathbf{x})} = -\sum_{j=1}^{N-1}\sum_{\{s_j^M\}}\sum_{\{s_{j+1}^M\}}\rho(\mathbf{r},s_j^M,s_{j+1}^M)\frac{\zeta(\mathbf{r},s_j^M,s_{j+1}^M)d}{(1+\kappa(\mathbf{r})d)}\frac{2\pi l_B (s_w)^2}{\kappa(\mathbf{r})} \tag{V.86}$$

$$\frac{\delta\beta f_{DH}^{ch}}{\delta\rho_M(\mathbf{X})} = \sum_{j=1}^{N-1}\zeta(\mathbf{r},s_j^M,s_{j+1}^M) - \sum_{j=1}^{N-1}\rho(\mathbf{r},s_j^M,s_{j+1}^M)\frac{\zeta(\mathbf{r},s_j^M,s_{j+1}^M)d}{(1+\kappa(\mathbf{r})d)}\frac{2\pi l_B (s_j^M)^2}{\kappa(\mathbf{r})} \tag{V.87}$$

$$\frac{\delta\beta f_{DH}^{ch}}{\delta\rho_M(\mathbf{X})} = \sum_{j=1}^{N-1}\zeta(\mathbf{r},s_j^M,s_{j+1}^M)\left[1-\frac{\rho(\mathbf{r},s_j^M,s_{j+1}^M)\;d}{(1+\kappa(\mathbf{r})d)}\frac{2\pi l_B (s_j^M)^2}{\kappa(\mathbf{r})}\right] \tag{V.88}$$

Free energy and potentials for χ-parameters

For a single component, the χ potential can be written as

$$F_\chi = \chi\int d\mathbf{r}'\rho(\mathbf{r}')^2 \tag{V.89}$$

Taking the variation with respect to the total density

$$\begin{aligned}
\frac{\delta F_\chi}{\delta\rho(\mathbf{X})} &= 2\chi \int d\mathbf{r}'\rho(\mathbf{r}')\frac{\delta\rho(\mathbf{r}')}{\delta\rho(\mathbf{X})} = 2\chi \int d\mathbf{r}'\rho(\mathbf{r}') \sum_{j=1}^{N} \int d\mathbf{r}'_j \frac{\delta\rho(\mathbf{r}')}{\delta\rho_j(\mathbf{r}'_j)}\frac{\delta\rho_j(\mathbf{r}'_j)}{\delta\rho(\mathbf{X})} \\
&= 2\chi \int d\mathbf{r}'\rho(\mathbf{r}') \sum_{j=1}^{N} \frac{\delta\rho_j(\mathbf{r}')}{\delta\rho(\mathbf{X})} \\
&= 2\chi \int d\mathbf{r}'\rho(\mathbf{r}') \sum_{j=1}^{N} \delta(\mathbf{r}' - \mathbf{r}) \\
&= 2\chi \sum_{j=1}^{N} \int d\mathbf{r}'\rho(\mathbf{r}')\delta(\mathbf{r}' - \mathbf{r}) \\
&= 2\chi \sum_{j=1}^{N} \rho(\mathbf{r})
\end{aligned} \tag{V.90}$$

For relevance to the free energy,

$$\begin{aligned}
-\int d\mathbf{X}'\rho(\mathbf{X}')\frac{\delta F_\chi}{\delta\rho(\mathbf{X}')} &= -2\chi N \int d\mathbf{X}'\rho(\mathbf{X}') \sum_{k=1}^{N} \rho_k(\mathbf{r}'_k) \\
&= -2\chi N \sum_{k=1}^{N} \int d\mathbf{r}'_k\rho_k(\mathbf{r}'_k) \int d\mathbf{X}''\rho(\mathbf{X}'')\delta(\mathbf{r}'_k - \mathbf{r}'') \\
&= -2\chi N \sum_{k=1}^{N} \int d\mathbf{r}'_k\rho_k^2(\mathbf{r}'_k)
\end{aligned} \tag{V.91}$$

We can also treat a χ-parameter that is only applied to specific states. For example, to model hydrogen bonding, one could define a χ-parameter between the protonated form of acid and (any) water,

$$F_{\chi_H} = \chi_H \int d\mathbf{r}' \left[\rho_w(\mathbf{r}') + \rho_M(\mathbf{r}', 0)\right]^2 \tag{V.92}$$

Taking the variation with respect to the total density

$$\begin{aligned}
\frac{\delta F_\chi}{\delta\rho(\mathbf{X})} &= 2\chi_H \int d\mathbf{r}' \left[\rho_w(\mathbf{r}') + \rho_M(\mathbf{r}', 0)\right] \left(\frac{\delta\rho_w(\mathbf{r}')}{\delta\rho(\mathbf{X})} + \frac{\delta\rho_M(\mathbf{r}', 0)}{\delta\rho(\mathbf{X})}\right) \\
&= 2\chi_H \int d\mathbf{r}' \left[\rho_w(\mathbf{r}') + \rho_M(\mathbf{r}', 0)\right] \sum_{j=1}^{N} \delta(\mathbf{r} - \mathbf{r}')\delta_{s_j,0} \\
&= 2\chi_H \sum_{j=1}^{N} \left[\rho_w(\mathbf{r}') + \rho_M(\mathbf{r}', 0)\right] \delta_{s_j,0}
\end{aligned} \tag{V.93}$$

$$\begin{aligned}\frac{\delta F_\chi}{\delta \rho_w(\mathbf{x})} &= 2\chi_H \int d\mathbf{r}' \left[\rho_w(\mathbf{r}') + \rho_M(\mathbf{r}', 0)\right] \left(\frac{\delta \rho_w(\mathbf{r}')}{\delta \rho_w(\mathbf{x})} + \frac{\delta \rho_M(\mathbf{r}', 0)}{\delta \rho_w(\mathbf{x})}\right) \\ &= 2\chi_H \int d\mathbf{r}' \left[\rho_w(\mathbf{r}') + \rho_M(\mathbf{r}', 0)\right] \sum_{s'_W} \delta(\mathbf{r} - \mathbf{r}') \delta_{s_w, s'_w} \\ &= 2\chi_H \left[\rho_w(\mathbf{r}) + \rho_M(\mathbf{r}, 0)\right]\end{aligned} \tag{V.94}$$

References

(1) Izumrudov, V. A.; Mussabayeva, B. K.; Murzagulova, K. B. *Russian Chemical Reviews* **2018**, *87*, 192, DOI: 10.1070/RCR4767.

(2) Burgess, D. J. In *Macromolecular Complexes in Chemistry and Biology*; Springer Berlin Heidelberg: 1994, pp 285–300, DOI: 10.1007/978-3-642-78469-9_17.

(3) Blocher, W. C.; Perry, S. L. *Wiley Interdisciplinary Reviews: Nanomedicine and Nanobiotechnology* **2017**, *9*, e1442, DOI: 10.1002/wnan.1442.

(4) Timilsena, Y. P.; Akanbi, T. O.; Khalid, N.; Adhikari, B.; Barrow, C. J. *International Journal of Biological Macromolecules* **2019**, *121*, 1276–1286, DOI: 10.1016/j.ijbiomac.2018.10.144.

(5) Schmitt, C.; Turgeon, S. L. *Advances in Colloid and Interface Science* **2011**, *167*, 63–70, DOI: 10.1016/j.cis.2010.10.001.

(6) Xiao, Z.; Liu, W.; Zhu, G.; Zhou, R.; Niu, Y. *Journal of the Science of Food and Agriculture* **2014**, *94*, 1482–1494, DOI: 10.1002/jsfa.6491.

(7) Eghbal, N.; Choudhary, R. *LWT - Food Science and Technology* **2018**, *90*, 254–264, DOI: 10.1016/j.lwt.2017.12.036.

(8) Massella, D.; Giraud, S.; Guan, J.; Ferri, A.; Salaün, F. *Environmental Chemistry Letters* **2019**, *17*, 1787–1800, DOI: 10.1007/s10311-019-00913-w.

(9) Timilsena, Y. P.; Haque, M. A.; Adhikari, B. *Food and Nutrition Sciences* **2020**, *11*, 481–508, DOI: 10.4236/fns.2020.116035.

(10) Tang, Y.; Scher, H. B.; Jeoh, T. *Innovative Food Science and Emerging Technologies* **2020**, *59*, 102257, DOI: 10.1016/j.ifset.2019.102257.

(11) Synatschke, C. V.; Löbling, T. I.; Förtsch, M., et al. *Macromolecules* **2013**, *46*, 6466–6474, DOI: 10.1021/ma400934n.

(12) Pothukuchi, R. P.; Radhakrishna, M. *Soft Matter* **2022**, *18*, 6124–6137, DOI: 10.1039/D2SM00650B.

(13) Ko, Y. H.; Kim, Y. H.; Park, J., et al. *Macromolecules* **2011**, *44*, 2866–2872, DOI: 10.1021/ma102112a.

(14) Sing, C. E.; Perry, S. L. *Soft Matter* **2020**, *16*, 2885–2914, DOI: 10.1039/d0sm00001a.

(15) Castelnovo, M.; Joanny, J.-F. *Langmuir* **2000**, *16*, 7524–7532, DOI: 10.1021/la000211h.

(16) Patel, P. A.; Jeon, J.; Mather, P. T.; Dobrynin, A. V. *Langmuir* **2005**, *21*, 6113–6122, DOI: 10.1021/LA050432T.

(17) Cao, Q.; Zuo, C.; Li, L. *Physical Chemistry Chemical Physics* **2011**, *13*, 9706–9715, DOI: 10.1039/C0CP02171G.

(18) Sethuraman, V.; McGovern, M.; Morse, D. C.; Dorfman, K. D. *Soft Matter* **2019**, *15*, 5431–5442, DOI: 10.1039/C9SM00581A.

(19) Sethuraman, V.; Zheng, D.; Morse, D. C.; Dorfman, K. D. *Macromolecules* **2022**, *55*, 3030–3038, DOI: 10.1021/acs.macromol.1c02623.

(20) Balzer, C.; Zhang, P.; Wang, Z.-G. *Soft Matter* **2022**, *18*, 6326–6339, DOI: 10.1039/D2SM00859A.

(21) Debais, G.; Tagliazucchi, M. *Macromolecules* **2022**, *55*, 5263–5275, DOI: 10.1021/acs.macromol.2c00250.

(22) Zhang, P.; Wang, Z. G. *Macromolecules* **2021**, *54*, 10994–11007, DOI: 10.1021/acs.macromol.1c01809.

(23) Zhulina, E. B.; Birshtein, T. M.; Borisov, O. V. *Macromolecules* **1995**, *28*, 1491–1499, DOI: 10.1021/ma00109a021.

(24) Borisov, O. V.; Zhulina, E. B.; Birshtein, T. M. *Macromolecules* **1994**, *27*, 4795–4803, DOI: 10.1021/ma00095a021.

(25) Pryamitsyn, V. A.; Leermakers, F. A. M.; Fleer, G. J.; Zhulina, E. B. *Macromolecules* **1996**, *29*, 8260–8270, DOI: 10.1021/ma9607832.

(26) Huang, J.; Laaser, J. E. *ACS Macro Letters* **2021**, *10*, 1029–1034, DOI: 10.1021/acsmacrolett.1c00382.

(27) Madinya, J. J.; Chang, L. W.; Perry, S. L.; Sing, C. E. *Molecular Systems Design and Engineering* **2020**, *5*, 632–644, DOI: 10.1039/c9me00074g.

(28) Ylitalo, A. S.; Balzer, C.; Zhang, P.; Wang, Z. G. *Macromolecules* **2021**, *54*, 11326–11337, DOI: 10.1021/acs.macromol.1c02000.

(29) Zhang, L.; Lipik, V.; Miserez, A. *Journal of Materials Chemistry B* **2016**, *4*, 1544–1556, DOI: 10.1039/c5tb02298c.

(30) Balzer, C.; Jiang, J.; Marson, R. L.; Ginzburg, V. V.; Wang, Z.-G. *Langmuir* **2021**, *37*, 5483–5493, DOI: 10.1021/acs.langmuir.1c00139.

(31) Zhang, P.; Shen, K.; Alsaifi, N. M.; Wang, Z. G. *Macromolecules* **2018**, *51*, 5586–5593, DOI: 10.1021/acs.macromol.8b00726.

(32) Kreer, T. *Soft Matter* **2016**, *12*, 3479–3501, DOI: 10.1039/C5SM02919H.

(33) Zhulina, E. B.; Rubinstein, M. *Macromolecules* **2014**, *47*, 5825–5838, DOI: 10.1021/ma500772a.

(34) Ali, M.; Yameen, B.; Neumann, R., et al. *Journal of the American Chemical Society* **2008**, *130*, 16351–16357, DOI: 10.1021/ja8071258.

(35) Ma, S.; Ye, Q.; Pei, X.; Wang, D.; Zhou, F. *Advanced Materials Interfaces* **2015**, *2*, 1500257, DOI: 10.1002/admi.201500257.

(36) Higaki, Y.; Kobayashi, M.; Murakami, D.; Takahara, A. *Polymer Journal* **2016**, *48*, 325–331, DOI: 10.1038/pj.2015.137.

(37) Borzęcka, N. H.; Kozłowska, I.; Gac, J. M.; Bojarska, M. *Applied Surface Science* **2020**, *506*, 144658, DOI: 10.1016/j.apsusc.2019.144658.

(38) Pincus, P. **1991**, 2912–2919, DOI: 10.1021/ma00010a043.

(39) Marins, J. A.; Montagnon, T.; Ezzaier, H., et al. *ACS Applied Nano Materials* **2018**, *1*, 6760–6772, DOI: 10.1021/acsanm.8b01558.

(40) Borukhov, I.; Andelman, D.; Borrega, R., et al. **2000**, DOI: 10.1021/jp001892s.

(41) Kern, W. *Zeitschrift für Physikalische Chemie* **1939**, *184A*, 197–210, DOI: 10.1515/zpch-1939-18416.

(42) Wang, S.; Granick, S.; Zhao, J. *The Journal of Chemical Physics* **2008**, *129*, 241102, DOI: 10.1063/1.3055596.

(43) Nová, L.; Uhlík, F.; Košovan, P. *Physical Chemistry Chemical Physics* **2017**, *19*, 14376–14387, DOI: 10.1039/c7cp00265c.

(44) Zhulina, E. B.; Rubinstein, M. *Soft Matter* **2012**, *8*, 9376–9383, DOI: 10.1039/C2SM25863C.

(45) Nap, R. J.; Szleifer, I. *Journal of Chemical Physics* **2018**, *149*, 163309, DOI: 10.1063/1.5029377.

(46) Ferrand-Drake Del Castillo, G.; Hailes, R. L.; Dahlin, A. *Journal of Physical Chemistry Letters* **2020**, *11*, 5212–5218, DOI: 10.1021/acs.jpclett.0c01289.

(47) Lunkad, R.; Murmiliuk, A.; Tošner, Z.; Štěpánek, M.; Košovan, P. *Polymers* **2021**, *13*, 214, DOI: 10.3390/polym13020214.

(48) Gallegos, A.; Ong, G. M. C.; Wu, J. *Soft Matter* **2021**, *17*, 9221–9234, DOI: 10.1039/D1SM00848J.

(49) Chen, G.; Das, S. *The Journal of Physical Chemistry B* **2016**, *120*, 6848–6857, DOI: 10.1021/acs.jpcb.6b04636.

(50) Sachar, H. S.; Pial, T. H.; Desai, P. R., et al. *Matter* **2020**, *2*, 1509–1521, DOI: 10.1016/j.matt.2020.02.022.

(51) Yamamoto, T.; Pincus, P. A. *Europhysics Letters* **2011**, *95*, 48003, DOI: 10.1209/0295-5075/95/48003.

(52) Ho, Y.-F.; Shendruk, T. N.; Slater, G. W.; Hsiao, P.-Y. *Langmuir* **2013**, *29*, 2359–2370, DOI: 10.1021/la304267f.

(53) Longo, G. S.; Olvera de la Cruz, M.; Szleifer, I. *Soft Matter* **2016**, *12*, 8359–8366, DOI: 10.1039/C6SM01172A.

(54) Okrugin, B. M.; Richter, R. P.; Leermakers, F. A. M., et al. *Polymers* **2020**, *12*, 898, DOI: 10.3390/polym12040898.

(55) Perez Sirkin, Y. A.; Szleifer, I.; Tagliazucchi, M. *Macromolecules* **2020**, *53*, 2616–2626, DOI: 10.1021/acs.macromol.0c00082.

(56) Senechal, V.; Rodriguez-Hernandez, J.; Drummond, C. *Macromolecules* **2022**, acs.macromol.1c02377, DOI: 10.1021/acs.macromol.1c02377.

(57) Weir, M. P.; Heriot, S. Y.; Martin, S. J., et al. *Langmuir* **2011**, *27*, 11000–11007, DOI: 10.1021/la201343w.

(58) Borisova, O. V.; Billon, L.; Richter, R. P.; Reimhult, E.; Borisov, O. V. *Langmuir* **2015**, *31*, 7684–7694, DOI: 10.1021/acs.langmuir.5b01993.

(59) Hollingsworth, N.; Larson, R. G. *Polymers* **2021**, *13*, 812, DOI: 10.3390/polym13050812.

(60) Nakamura, I.; Wang, Z. G. *Soft Matter* **2012**, *8*, 9356–9367, DOI: 10.1039/c2sm25606a.

(61) Gallegos, A.; Ong, G. M. C.; Wu, J. *The Journal of Chemical Physics* **2021**, *155*, 241102, DOI: 10.1063/5.0066774.

(62) Wertheim, M. S. *Journal of Statistical Physics* **1984**, *35*, 35–47, DOI: 10.1007/BF01017363.

(63) Wertheim, M. S. *The Journal of Chemical Physics* **1987**, *87*, 7323–7331, DOI: 10.1063/1.453326.

(64) Shen, K.; Wang, Z. G. *Journal of Chemical Physics* **2017**, *146*, 84901, DOI: 10.1063/1.4975777.

(65) Ghasemi, M.; Larson, R. G. *Progress in Polymer Science* **2021**, *112*, 101322, DOI: 10.1016/J.PROGPOLYMSCI.2020.101322.

(66) Petrov, A. I.; Antipov, A. A.; Sukhorukov, G. B. *Macromolecules* **2003**, *36*, 10079–10086, DOI: 10.1021/ma034516p.

(67) Choi, J.; Rubner, M. F. **2005**, DOI: 10.1021/ma048596o.

(68) Israëls, R.; Leermakers, F. A.; Fleer, G. J. *Macromolecules* **1994**, *27*, 3087–3093, DOI: 10.1021/MA00089A028/ASSET/MA00089A028.FP.PNG_V03.

(69) Israels, R.; Leermakers, F. A. M.; Fleer, G. J.; Zhulina, E. B. *Macromolecules* **1994**, *27*, 3249–3261, DOI: 10.1021/ma00090a018.

(70) Borisov, O. V.; Leermakers, F. A. M.; Fleer, G. J.; Zhulina, E. B. *The Journal of Chemical Physics* **2001**, *114*, 7700–7712, DOI: 10.1063/1.1360244.

(71) Borisov, O. V.; Boulakh, A. B.; Zhulina, E. B. *The European Physical Journal E* **2003**, *12*, 543–551, DOI: 10.1140/epje/e2004-00026-3.

(72) Seki, H.; Suzuki, Y. Y.; Orland, H. *Journal of the Physical Society of Japan* **2007**, *76*, 104601, DOI: 10.1143/JPSJ.76.104601.